



HAL
open science

Application of encapsulated nickel nanoparticle catalysts to the reforming of a model producer gas derived from biomass gasification

David Laprune

► **To cite this version:**

David Laprune. Application of encapsulated nickel nanoparticle catalysts to the reforming of a model producer gas derived from biomass gasification. Catalysis. Université de Lyon, 2017. English. NNT : 2017LYSE1129 . tel-01782399

HAL Id: tel-01782399

<https://theses.hal.science/tel-01782399>

Submitted on 2 May 2018

HAL is a multi-disciplinary open access archive for the deposit and dissemination of scientific research documents, whether they are published or not. The documents may come from teaching and research institutions in France or abroad, or from public or private research centers.

L'archive ouverte pluridisciplinaire **HAL**, est destinée au dépôt et à la diffusion de documents scientifiques de niveau recherche, publiés ou non, émanant des établissements d'enseignement et de recherche français ou étrangers, des laboratoires publics ou privés.



N°d'ordre: 2017LYSE1129

THESE de DOCTORAT DE L'UNIVERSITE DE LYON

opérée au sein de
l'Université Claude Bernard Lyon 1

Ecole Doctorale N° 206
Ecole Doctorale de Chimie de Lyon

Spécialité de doctorat : Chimie

Soutenue publiquement le 05/07/2017, par :

David LAPRUNE

Application de catalyseurs encapsulés à base de nickel au réformage d'un gaz modèle issu de la gazéification de la biomasse

Devant le jury composé de :

Fongarland, Pascal	Professeur, Université Lyon 1, LGPC	Président
Roger, Anne-Cécile Prelot, Bénédicte	Professeur, Université de Strasbourg, ICPEES Chargé de Recherche, CNRS, ICGM	Rapporteure Rapporteure
Meunier, Frédéric Farrusseng, David	Chargé de Recherche, CNRS, IRCELYON Directeur de Recherche, CNRS, IRCELYON	Directeur de thèse Co-directeur de thèse
Bedel, Laurent	Ingénieur de recherche, CEA	Examineur

UNIVERSITE CLAUDE BERNARD - LYON 1

Président de l'Université

Président du Conseil Académique

Vice-président du Conseil d'Administration

Vice-président du Conseil Formation et Vie Universitaire

Vice-président de la Commission Recherche

Directrice Générale des Services

M. le Professeur Frédéric FLEURY

M. le Professeur Hamda BEN HADID

M. le Professeur Didier REVEL

M. le Professeur Philippe CHEVALIER

M. Fabrice VALLÉE

Mme Dominique MARCHAND

COMPOSANTES SANTE

Faculté de Médecine Lyon Est – Claude Bernard

Faculté de Médecine et de Maïeutique Lyon Sud – Charles Mérieux

Faculté d'Odontologie

Institut des Sciences Pharmaceutiques et Biologiques

Institut des Sciences et Techniques de la Réadaptation

Département de formation et Centre de Recherche en Biologie Humaine

Directeur : M. le Professeur G.RODE

Directeur : Mme la Professeure C. BURILLON

Directeur : M. le Professeur D. BOURGEOIS

Directeur : Mme la Professeure C. VINCIGUERRA

Directeur : M. X. PERROT

Directeur : Mme la Professeure A-M. SCHOTT

COMPOSANTES ET DEPARTEMENTS DE SCIENCES ET TECHNOLOGIE

Faculté des Sciences et Technologies

Département Biologie

Département Chimie Biochimie

Département GEP

Département Informatique

Département Mathématiques

Département Mécanique

Département Physique

UFR Sciences et Techniques des Activités Physiques et Sportives

Observatoire des Sciences de l'Univers de Lyon

Polytech Lyon

Ecole Supérieure de Chimie Physique Electronique

Institut Universitaire de Technologie de Lyon 1

Ecole Supérieure du Professorat et de l'Education

Institut de Science Financière et d'Assurances

Directeur : M. F. DE MARCHI

Directeur : M. le Professeur F. THEVENARD

Directeur : Mme C. FELIX

Directeur : M. Hassan HAMMOURI

Directeur : M. le Professeur S. AKKOUCHE

Directeur : M. le Professeur G. TOMANOV

Directeur : M. le Professeur H. BEN HADID

Directeur : M. le Professeur J-C PLENET

Directeur : M. Y.VANPOULLE

Directeur : M. B. GUIDERDONI

Directeur : M. le Professeur E.PERRIN

Directeur : M. G. PIGNAULT

Directeur : M. le Professeur C. VITON

Directeur : M. le Professeur A. MOUGNIOTTE

Directeur : M. N. LEBOISNE

An eye for an eye makes the whole world blind

Mohandas K. Gandhi

Acknowledgements

I would like to start by thanking Stéphane Daniel and Catherine Pinel for making my stay at the Institut de Recherche sur la Catalyse et l'Environnement de Lyon possible and for giving me access to the laboratory and research facilities.

The 3 year (and a $\frac{1}{4}$) PhD period was an important and highly enjoyable step in my life that helped me at growing as a research scientist and this would not have been possible without the help of my supervisors: Frédéric Meunier, David Farrusseng and Alain Tuel. Thank you all for the trust you have placed in me during our first interview and for giving me the opportunity to start and discover the path of research at IRCELYON.

Thank you Fred for your continuous guidance, patience, kindness and the knowledge passed to me. Your infallible motivation and impressive devotion to sciences have been a great source of inspiration to me. I am very grateful to David for your strong support, the insightful discussions and for the scientific background that you taught me. Finally, thank you Alain for the nice discussions on zeolite science and for your continuous interest and strong belief in my work.

Special thanks go to the jury members of this thesis: Prof. Pascal Fongarland, Prof. Anne-Cécile Roger, Dr. Bénédicte Prelot and Laurent Bedel. Thank you for having accepted to review this work.

I also want to thank the IRCELYON staff who contributed to this work: Mimoun Aouine, Laurence Burel, Pascale Mascunan, Noelle Cristin, Bernadette Jouguet, Françoise Bosselet and Yoann Aizac. Thank you Lucian Roiban, Thierry Epicier and Siddardha Koneti from Mateis laboratory for your kind contribution in microscopy. Finally, I am grateful to Emmanuel Landrison and Florian Chapon for your strong technical support and for making my experiments possible.

I would like to express my sincere thanks to Shiwen Li who guided me at the beginning of my PhD. Thank you Shiwen for your fruitful help and your incredible kindness.

I send my gratitude to Christina Theodoridi who I had the chance to closely work with during a part of my PhD. Your contribution to this work, your determination and open-mindedness were a lot appreciated and never forgotten.

These 3 years has been rich in events and an excellent opportunity to meet great people. I especially want to thank Mathilde, Cindy and Maxime for being such wonderful friends and for standing by me when I needed it most. Your friendship is priceless. Particular thanks go to Laurent, Alex M., Davide, Alejandra, Ana-Rita, Yoldes, Jérémy, Jérôme, Cécile, Alex L., Céline, Caroline, Anaëlle, Joffrey, Elia, Elie and Aleksandra for their support and kindness. Also, thanks to all ING team members, I am glad to have been part of a group in which eagerness and team-spirit are the watchwords. Thanks to the ATEC for organizing many entertaining side events. Not to forget my oldest friend Etienne who kindly reread this manuscript and corrected my English.

At last, I thank my family for their infallible support and for always having believed in me more than I did. Thank you for your devotion to helping me in making my expectations come true.

Abstract

Europe is facing climate and energy challenges and aims at increasing the utilization of biomass in the production of renewable fuels. Many technological difficulties remain, for instance, biomass gasification produces a syngas rich in tars and H₂S that can lead to catalyst poisoning in downstream reactors. Our goal was to develop stable catalysts that could fully reform producer gas. Nickel nanoparticles encapsulated inside hollow silicalite-1 single crystals were studied. The encapsulation was expected to limit particle sintering and coking under harsh reforming conditions. These particles could still sinter within each single crystal. The synthesis of a novel hollow structure ("multi-hollow", i.e. a single zeolite crystal with multiple mesoporous cavities) was developed. The size-exclusion of large aromatic compounds from the sample was demonstrated. This material also enabled improving the initial dispersion of metal nanoparticles. The sample activity was yet adversely affected by two main factors associated with the preparation steps, i.e. the formation of a silica over-layer and phosphorus-poisoning. During the reforming of a simulated producer gas, the silicalite-1 membrane could not prevent tar-related deactivation of embedded nickel particles, because those were cracked at typical reforming temperatures into smaller aromatic compounds, which could diffuse throughout the MFI-type layer. The preparation of Rh-based multi-hollow analogues could not be achieved. Alumina-supported Rh and Ni-based catalysts were then tested. H₂S induced a large drop of the reforming activity and Rh catalysts were the least impacted by coking and S-poisoning. Methane reforming rate were proportional to the Rh metal surface area. The use of high reaction temperatures (>875 °C) was shown to be necessary to limit deactivation by coking.

Resumé

L'Europe est confrontée à des défis climatiques et énergétiques et vise à accroître l'utilisation de la biomasse dans la production d'énergies renouvelables. De nombreuses difficultés technologiques persistent, par exemple, la gazéification de la biomasse produit un gaz de synthèse riche en goudrons et H₂S qui peuvent conduire à une désactivation des catalyseurs dans les réacteurs en aval. Notre objectif a été de développer des catalyseurs stables qui peuvent réformer complètement ces hydrocarbures contenus dans le gaz de synthèse. Des nanoparticules de nickel encapsulées dans des monocristaux de silicalite-1 creusée formant une cavité unique ("single-hollow") ont été étudiées. L'encapsulation a pour but de limiter le frittage des particules et le cokage dans des conditions de reformage difficiles. Le frittage de ces particules au sein de chaque monocristal a cependant été observé. La synthèse d'une nouvelle structure creusée (c'est-à-dire un monocristal de zéolites avec de multiples cavités mésoporeuses, nommé "multi-hollow") a été développée. L'exclusion en taille de composés aromatiques larges par la membrane l'échantillon a été démontré. Ce matériau a également permis d'améliorer la dispersion initiale des nanoparticules métalliques. L'activité de l'échantillon a cependant été affectée par deux facteurs principaux associés aux étapes de préparation, c'est-à-dire la formation d'une couche de silice à la surface des particules et d'un empoisonnement au phosphore. Au cours du réformage d'un gaz de synthèse model riche en hydrocarbures, la membrane silicalite-1 n'a pu empêcher la désactivation due aux goudrons des particules de nickel encapsulées, car ceux-ci craquent aux températures typiques de reformage en composés aromatiques plus petits, susceptibles de se diffuser à travers la paroi de type MFI. La préparation de matériaux analogues à base de Rh n'a pas pu être réalisée. Des catalyseurs à base de Rh et de Ni supportés sur alumine ont ensuite été testés. Nous avons montré que le H₂S induit une chute significative de l'activité en reformage et que les catalyseurs au Rh sont les moins influencés par le cokage et l'empoisonnement au S. L'activité en reformage du méthane était proportionnelle à la surface spécifique en Rh. Une température de réaction élevée (> 875 °C) a été jugée nécessaire pour limiter la désactivation par cokage.

Content

Acknowledgements	4
Abstract	5
Resumé.....	5
Content	6
List of abbreviations	11
Chapter 1 - Introduction.....	13
1. Context of this work.....	13
1.1. Introduction to FASTCARD.....	13
1.2. FASTCARD WP1 - Hydrocarbon reforming	17
2. State of the art	20
2.1. Hydrocarbon reforming.....	20
2.1.1. Reforming history at a glance	20
2.1.2. Steam methane reforming process	21
2.1.3. Bio-syngas production	22
2.1.4. Producer gas reforming.....	26
2.1.5. Thermodynamic study of producer gas reforming	28
2.2. Catalysis.....	31
2.2.1. Heterogeneously catalyzed gas-phase reaction	31
2.2.2. Catalytic reforming	33
2.2.3. Catalyst deactivation	37
2.3. Zeolites	44
2.3.1. Introduction to zeolites	45
2.3.2. Structural modifications	46
2.3.3. Metal particles encapsulation in zeolite catalysts	48
2.3.4. Pioneered achievements on hollow zeolites at IRCELYON.....	50
3. Aim of this PhD work.....	51
Chapter 2 - Experimental.....	53

1. Material syntheses	53
1.1. Silicalite-1 nanocrystals	53
1.2. Ni@silicalite-1 synthesis	53
1.2.1. Ni impregnation	53
1.2.2. Encapsulation of Ni in a Single Hollow structure (Ni@Sil-1 SH)	54
1.2.3. Encapsulation of Ni in a Multi Hollow structure (Ni@Sil-1 MH)	54
1.2.4. Citric acid treatment	55
1.2.5. Preparation of a supported Ni/silicalite-1 catalyst	55
2. Characterization techniques	55
2.1. Elementary analysis (ICP-OES)	55
2.2. Powder X-Ray Diffraction (XRD)	56
2.3. Nitrogen adsorption/desorption	56
2.4. Transmission Electronic Microscopy (TEM)	57
2.4.1. Sample preparation for TEM observation	57
2.4.2. TEM apparatus	57
2.4.3. Statistical study of nanoparticles based on TEM images	58
2.4.4. Energy Dispersive X-Ray Spectroscopy (EDX) measurement	59
2.4.5. Environmental Transmission Electron Microscopy (ETEM)	59
2.5. Hydrogen chemisorption	60
2.6. Thermogravimetric Analysis (TGA)	60
2.7. Temperature Programmed Reduction (TPR)	60
2.8. Carbon-Hydrogen-Oxygen-Nitrogen-Sulfur (CHONS)	61
2.9. Diffuse Reflectance Infrared FT-IR Spectroscopy (DRIFTS)	61
3. Catalytic reactions	62
3.1. Catalytic data treatments	62
3.2. Arene hydrogenation	63
3.3. Methane reforming	64
3.3.1. Experimental set-up	65
3.3.2. Analytical set-up	68
3.4. CO methanation	70
3.4.1. Evaluation of the molecular sieving property	70

3.4.2. Estimation of the accessible nickel surface area	71
3.5. Evaluation of transport phenomena	71
3.5.1. External mass transport limitations.....	72
3.5.2. Internal mass transport limitations	72
3.5.3. External heat transfer limitations	73
3.5.4. Internal heat transfer limitations.....	74
3.5.5. Radial heat transfer limitations.....	74

Chapter 3 - Size-selectivity of metal particles encapsulated in hollow silicalite-1 zeolites

1. Introduction.....	75
2. Results and discussion	76
2.1. Preparation of Ni particles encapsulated in single hollow silicalite-1 material (Ni@Sil-1 SH)	76
2.1.1. Post-impregnation method.....	76
2.1.2. Impregnation followed by the formation of hollow structures method	77
2.1.3. Citric acid treatment.....	80
2.2. Characterization of the zeolitic samples.....	82
2.2.1. Thermogravimetric analyses	82
2.2.2. Environmental Transmission Electron Microscopy.....	84
2.2.3. X-ray diffraction	86
2.2.4. Nitrogen physisorption.....	87
2.2.5. Infrared spectroscopy.....	89
2.3. Extension of the preparation method to Rh and NiPt	90
2.3.1. Preparation of Rh particles encapsulated in single hollow silicalite-1.....	90
2.3.2. Preparation of NiPt particles encapsulated in single hollow silicalite-1	91
2.4. Catalytic results	93
2.4.1. Arene hydrogenation.....	93
2.4.2. CO methanation in presence of pyrene	95
2.4.3. Sintering test	97
3. Conclusions.....	98

Chapter 4 - Highly dispersed Ni nanoparticles via the refinement of the confining hollow structure.....

1. Introduction.....	101
2. Characterization of multi hollow catalysts.....	103
2.1. Ni-free silicalite-1 hollow crystals.....	103
2.2. Ni-loaded silicalite-1 hollow crystals	107
2.2.1. X-ray diffraction	109
2.2.2. Thermogravimetric analyses.....	111
2.2.3. Nitrogen physisorption.....	113
3. Catalytic properties of multi hollow catalysts	115
3.1. Selectivity in arene hydrogenation.....	115
3.2. Stability in steam methane reforming at 700 °C	116
3.3. Activity in CO methanation at 300 °C.....	119
4. Multi Hollow catalysts prepared by a P-free desilicating agent	122
4.1. Synthesis of Ni@silicalite-1 TBA	122
4.2. Characterization of Ni@silicalite-1 TBA.....	123
4.2.1. Thermogravimetric analyses.....	125
4.2.2. X-ray diffraction	125
4.2.3. Nitrogen physisorption.....	126
4.3. Catalytic properties of Ni@silicalite-1 TBA.....	127
5. Conclusions.....	127

Chapter 5 - Effect of tars on the activity of Ni@Sil-1 SH catalysts in the reforming of producer gas..... 129

1. Introduction.....	129
2. Experimental procedure	131
2.1. Choice of catalysts.....	131
2.2. Properties of commercial catalysts	131
2.3. Reforming tests	132
3. Catalytic results	134
3.1. Reforming activity in presence of a 2-ring aromatic	134
3.1.1. Catalytic activities and stabilities	134
3.1.2. Characterizations of used samples	137

3.2. Reforming activity in presence of a 1-ring aromatic	142
3.3. Reforming activity in presence of a 4-ring aromatic	144
4. Conclusions.....	145
Chapter 6 - Effects of tars and H₂S on the reforming of a model producer gas	147
1. Introduction.....	147
2. Experimental procedure	149
2.1. Choice and properties of catalysts	149
2.2. Reforming tests	150
3. Catalytic results	152
3.1. Impact of C ₁₄ H ₁₀ and H ₂ S on the activity in CH ₄ reforming	152
3.1.1. Measurements of reaction rates at 850, 875 and 900 °C	152
3.1.2. Tar conversion and cracking product production at 850, 875 and 900 °C.....	155
3.2. Characterization of used samples	156
3.3. Evaluation of the loss in Ni active sites in reforming due to S.....	159
3.4. Assessment of transport limitations during reforming.....	160
4. Conclusions.....	164
References.....	166
Conclusions	175
Perspectives	178
Publications.....	180

List of abbreviations

/	Stands for “supported on”
@	Stands for “encapsulated in”
BET	Brunauer-Emmett-Teller
BTL	Biomass To Liquid
C_{balance}	Carbon balance
CHONS	Carbon-Hydrogen-Oxygen-Nitrogen-Sulfur
CitAc	Stands for “treated with citric acid”
CTL	Coal To Liquid
d_{NW}	Normal Weighted mean diameter
d_{SW}	Surface Weighted mean diameter
DRIFTS	Diffuse Reflectance Infrared Fourier Transform Spectroscopy
E_{app}	Apparent Activation Energy
ECN	Energy research Centre of the Netherlands
EDX	Energy Dispersive X-Ray Spectroscopy
EELS	Electron Energy Loss Spectroscopy
ETEM	Environmental Transmission Electron Microscopy
EU	European Union
FASTCARD	FAST industrialisation by CAtalysts Research and Development
FCC	Fluid Catalytic Cracking
FFT	Fast Fourier Transform
FID	Flame Ionization Detector
FTS	Fischer-Tropsch Synthesis
GHG	Greenhouse Gas
GHSV	Gas Hourly Space Velocity
GTL	Gas To Liquid
HAADF	High Angle Annular Dark Field
HC	Hydrocarbon
HR	High Resolution
ICP-OES	Inductively-Coupled Plasma Optical Emission Spectroscopy
IWI	Incipient Wetness Impregnation
JCPDS	Joint Committee on Powder Diffraction Standards
LCS	Low Coordination Sites
MFC	Mass Flow Controller

MFI	Mobil Five
MH	Multi Hollow
MP	Melting Point
MSI	Metal-Support Interactions
NP	Nanoparticle
PAH	Polycyclic Aromatic Hydrocarbons
PDID	Pulsed Discharge Ionization Detector
PGM	Platinum Group Metal
PSA	Pressure Swing Adsorption
RDS	Rate Determining Step
S/C	Steam to Carbon
SDA	Structure Directing Agent
SH	Single Hollow
Sil-1	Silicalite-1
SMR	Steam Methane Reforming
SP	Set Point
STEM	Scanning Transmission Electron Microscopy
TBAOH	Tetrabutylammonium Hydroxide
TBPOH	Tetrabutylphosphonium Hydroxide
TCD	Thermal Conductivity Detector
TEM	Transmission Electronic Microscopy
TEOS	Tetraethyl Orthosilicate
TGA	Thermogravimetric Analysis
TOF	Turn-Over Frequency
TPABR	Tetrapropylammonium Bromide
TPAOH	Tetrapropylammonium Hydroxide
TPR	Temperature-Programmed Reduction
WGS	Water Gas Shift
WHSV	Weight Hourly Space Velocity
WP	Work Package
XRD	X-Ray Diffraction

Chapter 1 - Introduction

1. Context of this work

This PhD work was supported by the European Union Seventh Framework Programme FP7-NMP-2013, under Grant Agreement number 604277 (FAST industrialisation by CAtalysts Research and Development, acronym FASTCARD, <https://www.sintef.no/fastcard/>).

1.1. Introduction to FASTCARD

In the context of setting a more sustainable future, the European Union (EU) is looking at cost-efficient ways to make its economy less energy-consuming and more climate-friendly. In 2008, the EU has voted three ambitious objectives on energy and climate to be reached by year 2020. The so-called 20-20-20 targets consist in attaining:

- 20% increase of renewable energy in the total energy consumption
- 20% decrease of greenhouse gas emissions (from year 1990 levels)
- 20% increase in energy efficiency

One of the ways to increase the uptake of renewable energy and at the same time to reduce greenhouse gas emissions is the substitution of traditional feedstock by bio-resources (biomass). The European production of first-generation biofuels, such as biodiesel and bioethanol, is based on well-established technologies and has kept increasing over the last few years (Figure 1.1). Bioethanol is produced by hydrolysis and fermentation of plants rich in carbohydrates (sugar cane, sugar beet, wheat, maize, corn, barley, etc.), while the production of biodiesel is based on the transesterification of vegetable oil originating from various sources.^[1] Transesterification is a catalyzed process.

Today, heterogeneous catalysis plays a pivotal role in the conversion of fossil resources to fuel for transports. For example, fluid catalytic cracking (FCC) is a major conversion process that produces the majority of the world's gasoline from heavy fossil oil (worldwide FCC capacity in 2013: ~ 14 million bpd).^[2] In addition, emerging synthetic diesel fuels can be produced from coal (coal to liquid process, CTL) or natural gas (gas to liquid process, GTL) using the catalytic Fischer-Tropsch technology (worldwide CTL and GTL capacities in 2013: ~ 160 000 and 220 000 bpd, respectively).^[3]

Second-generation biofuels are seen as a promising way to reach the 20-20-20 targets. In comparison with the first-generation, this new generation of advanced biofuels is expected to have a significantly lower carbon footprint, not to compete with food crops and to offer better engine performance.^[4] Second-generation biofuels are made from lignocellulosic material that makes up the majority of the cheap and abundant non-food materials available from plants. However, their production, via gasification or pyrolysis processes, is still in the early stages of research and development.

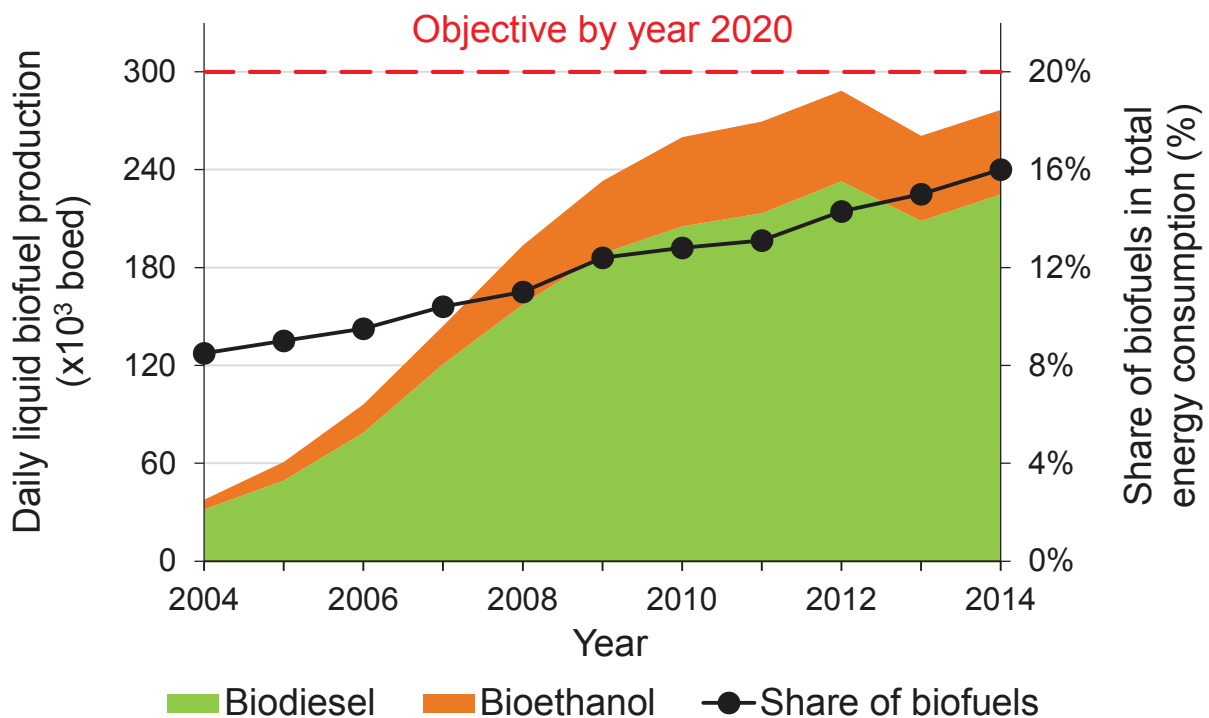


Figure 1.1 Left axis: Daily production of biodiesel and bioethanol in the EU since 2004 (in barrels of oil equivalent). Right axis: Share of biofuels in gross final consumption of energy in the EU since 2004 (%).^[5]

The recent demand of the EU for producing second-generation biofuels generates challenges in catalyst development. So far, the implementation at industrial level of appropriate catalysts has been hindered by economic reasons when scaling up from laboratory benches to demonstration units. These reasons constitutes real barriers and lows down industrialization and commercial implementation. In comparison with more traditional fossil resources (coal, oil and natural gas), the catalytic conversion of biomass is highly complex due to its large amount of oxygen, nitrogen and sulfur containing molecules and its huge variability depending on its origin (waste, paper, wood, grass, straw, etc.). This level of complexity warrants the need to design new catalysts with enhanced properties in terms of robustness, flexibility and reliability before going to the industrial scale.

In addition, when compared with classical feedstocks (i.e. fossil oil and natural gas), biomass is much more reactive towards catalytic conversion and needs additional catalytic steps for stabilizing and conditioning. The gasification of biomass produces hydrocarbons (C_1 , C_2 and C_3 hydrocarbons (HC), mono- and poly-aromatics) that represent 50% of the energy contained within the feedstock, which would be wasted if not converted to useful fuel. The liquefaction of biomass through pyrolysis leads to very unstable sugar and oxygenated aromatics containing liquids that must be stabilized to an optimal level by hydrotreatment before post-processing. These critical pre-treatment steps have their own energy requirements which present special challenges for an implementation at the industrial scale. It is therefore important to address issues dealing with catalytic stabilizing and conditioning of bio-based intermediates in order to increase the overall energy efficiencies of the value chains from biomass to biofuels and achieve a low carbon footprint.

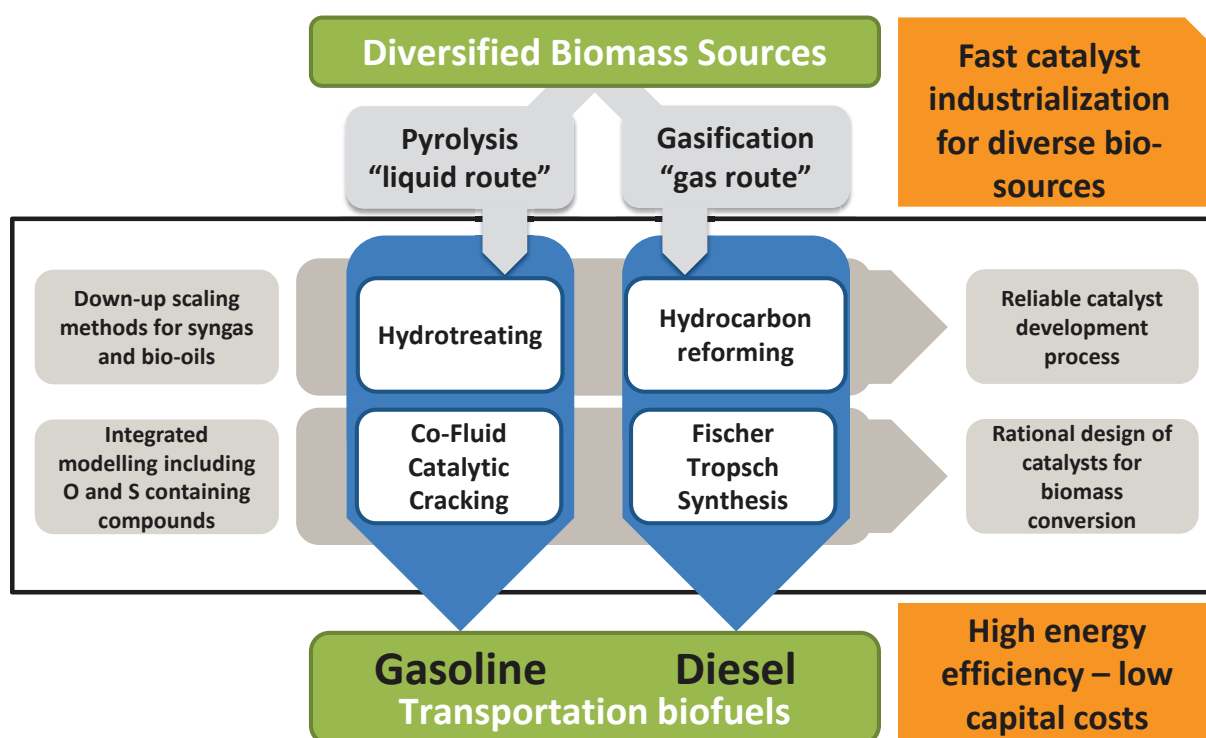


Figure 1.2 FASTCARD concept.

To meet the short term European 20-20-20 objectives and long term targets of the European Energy Roadmap 2050,^[6] the FASTCARD project is aiming at achieving a faster industrial implementation of biomass conversion to advanced biofuels in the European Union by developing new catalysts and methodologies.^[7] The objective of this European collaboration is to bring further knowledge and better technical performance of the catalysts, hence decreasing technological risk and reducing costs and time needed for further industrialization. FASTCARD focuses on accelerating the two major value chains for the catalytic conversion of biomass to advanced biofuels (Figure 1.2):

- **The liquid route (via biomass pyrolysis):** Hydrotreating of pyrolysis oil and subsequent co-FCC processing.
- **The gas route (via biomass gasification):** Hydrocarbon reforming of the HC-rich *syngas* (synthesis gas, a fuel gas mixture consisting primarily of H₂ and CO) and subsequent CO₂-rich Fischer-Tropsch synthesis (CO₂ FTS).

These two catalysis-based routes are complementary, as the pyrolysis chain can lead to the timely achievement of the 20-20-20 objectives, whereas the gasification chain focuses on the long term perspective of sustainability according to Energy Roadmap 2050. The two value chains involve four key catalytic steps, making use of two major classes of catalyst families: metal-supported and acid catalysts for the gas and liquid routes, respectively. FASTCARD activities are divided in four different work-packages (WP), each of them being dedicated to one of these four relevant catalytic processes:

- **Hydrocarbon reforming (WP1):** Development of advanced steam reforming catalysts suitable for a two-step catalytic reforming process (that consists of a pre-reformer and a subsequent steam reformer). Developing poison-resistant and sintering-resistant nanocatalysts for the steam methane reforming reaction is one of the major challenges of this work package.
- **CO₂ Fischer-Tropsch (WP2):** Development of advanced CO₂-tolerant iron-based Fischer-Tropsch catalysts with enhanced robustness (with respect to reaction temperatures higher than 250 °C), flexibility (regarding the variability of the syngas composition that contains a significant CO₂ level) and durability. One aim is to improve the catalyst selectivity to produce optimum gasoline type hydrocarbons, allowing downstream upgrading processes to be removed or simplified.
- **Hydrotreating (WP3):** Development of optimal catalysts for the two key steps of the hydrotreating process: bio-oil stabilization and hydrodeoxygenation for further upgrading by co-feeding in existing FCC plants. Challenges to address are to:
 - Develop catalysts that can operate at reduced hydrogen and pressure requirements for selective removal of the reactive precursors causing oil destabilization
 - Tailor the catalyst activity and durability for deeper oxygen removal by hydrodeoxygenation with minimum consumption of hydrogen to reach optimum oil properties
- **Co-FCC (WP4):** Development of a catalyst able to co-process hydrotreated bio-oils and crude oil distillates in a FCC unit. The catalyst development consists of adapting the active components of existing Faujasite-based FCC catalysts to make them compatible with the bio-based co-feed with maximized oxygen content.

1.2. FASTCARD WP1 - Hydrocarbon reforming

Fluidized bed gasification at typically 800 °C is an appropriate technology for biomass gasification in the FASTCAR context. Not only is it efficient due to the low gasifying temperature, but it also does not require substantial pre-treatment of the biomass feedstock, making it fuel flexible. However, the produced syngas during the gasification contains large amounts of hydrocarbons that may represent up to 50% of the energy value of the syngas. These hydrocarbons are mainly composed of (in order of decreasing concentration): methane, ethylene, benzene, tars (poly-aromatic HCs). These molecules need to be further reformed into H₂ and CO to make the syngas suitable for biofuel production. This can be done by catalytic reforming, where the temperature level is kept low and thus avoiding high efficiency penalties. The process is schematized in Figure 1.3.

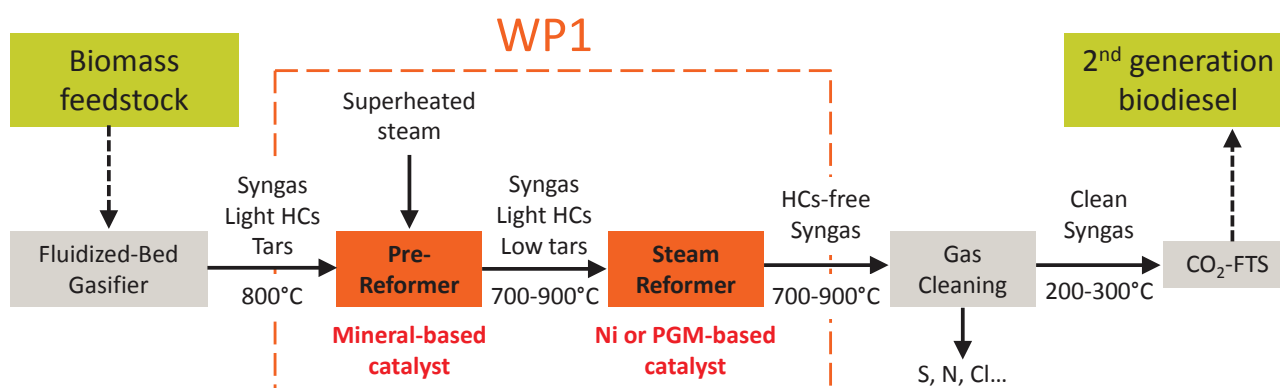


Figure 1.3 Process flow scheme of the gas route.

Fluidized bed gasification technologies are relatively mature and available commercially for many different fuels. Catalytic hydrocarbon reforming is conventional for fossil fuels like natural gas and naphtha. Reforming catalysts are generally nickel (Ni) based (noble metal catalysts exist, but are considered too expensive). Combining commercially available fluidized bed gasification and catalytic reforming therefore offer a highly efficient way to produce clean biofuels. The combination however, comes with several challenges that mainly relate to catalyst deactivation due to poisoning by sulfur and coking. Actually Ni-supported catalysts are prone to coking and irreversible poisoning with sulfur under reforming conditions at 700-900 °C. This is a challenge when using clean wood, but is even more challenging when gasifying more contaminated and thus less expensive biomass feedstocks. Combinations of cheap feedstock and full hydrocarbon reforming to syngas for biofuels production do not exist yet.

Developing catalysts to be operated downstream of fluidized bed biomass gasification (where sulfur poisoning and coking pose the main challenge) is the task of WP1. In practice, this would mean a limitation of the type of fuel to clean biomass (i.e. low-sulfur level) and a limitation of the gasifier operating conditions to those producing little tars (i.e. high temperature $> 1000\text{ }^{\circ}\text{C}$). Such limitations that imply expensive feedstock and loss in energy efficiency are not acceptable in the context of FASTCARD. WP1 is aiming at optimizing the reforming process to generate flexibility in how to operate the gasifier (meaning lower-cost fuels and lower-temperature gasification).

Along these lines, FASTCARD proposes using a combination of two reforming steps in series. This process is composed of (Figure 1.3):

- **A pre-reformer:** the raw producer gas from fluidized bed gasifier is treated in a low-cost mineral-based catalyst bed at $700\text{-}900\text{ }^{\circ}\text{C}$. This reduces the content of tars and sulfur, which are poisons for the second step. The endothermic pre-reforming process benefits from the high temperature of the producer gas that comes out of the gasifier at ca. $800\text{ }^{\circ}\text{C}$. Additional superheated steam can be injected at reactor inlet to reach the desired steam-to-carbon (S/C) ratio.
- **A steam reformer:** The partly cleaned gas is further treated in a Ni-based or PGM-based (Platinum Group Metal) reformer for complete reforming to syngas. A conventional reactor design that consists of steel tubes with packed reactor bed located in a furnace is considered.

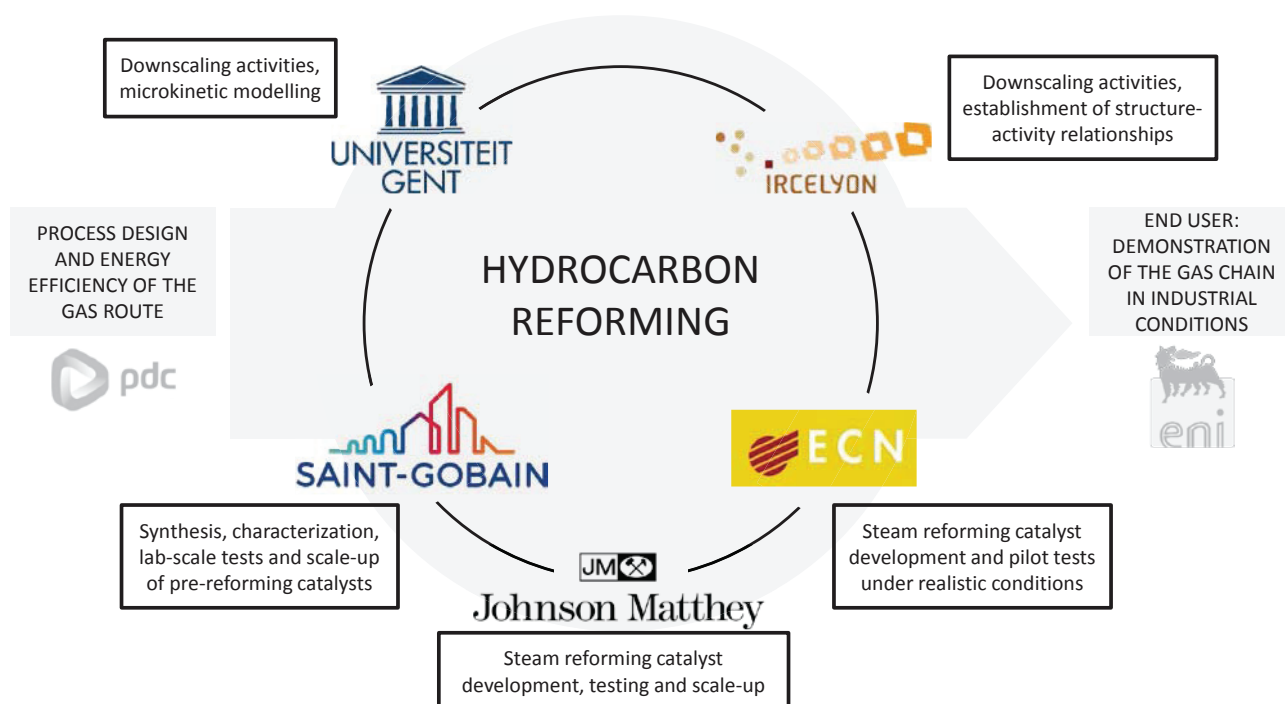


Figure 1.4 Activities of the partners involved in FASTCARD WP1.

This unique and flexible approach combines a robust pre-reforming step by cheap minerals-based catalyst (but with limited methane reforming efficiency) with a full reforming step by metal-based catalyst (but with high sensitivity for poisons). The two-step catalytic reforming relies on the development of catalysts and supports with innovative design. The general objectives of WP1 are:

- To conduct realistic benchmarking tests of state-of-the-art catalysts prior to downscaling
- To develop new catalyst formulations and to study their activity/stability (via accelerated ageing studies and high throughput testing) at small scale level. The objectives for the catalysts are:
 - **pre-reformer catalyst:** conversion of at least 50% of tars
 - **reformer catalyst:** reduction of metal loadings (if PGM-based) and full conversion of HCs at moderate temperature in presence of H₂S up to 100 ppmv (particle per million by volume)
- To develop a microkinetic model that predicts the behavior with respect to sulfur and coke deposition under realistic conditions for optimized catalysts
- To demonstrate that best candidate catalysts are producible using scalable industrial processes
- To conduct 200-hour tests under realistic conditions of newly scaled-up candidates such that deactivation of the catalyst is less than 5%

Among the fifteen European participants composing the FASTCARD consortium, five industrial (ECN, Johnson Matthey, Saint-Gobain) and academic (University of Ghent, IRCELYON) partners are involved in WP1. The partners step in at different stages of the catalyst development, as described in Figure 1.4. The complementary skills and facilities available in this collaboration are favourable to bring advancements in fundamental understanding (academic inputs) along with catalyst manufacture and pilot demonstration (industrial inputs). The involvement of IRCELYON within WP1 mainly consists in:

- Building up testing facilities and procedures at laboratory scale in order to evaluate catalyst formulations using representative feed compositions
- Developing well size-controlled metal nanoparticles of pure Ni metal and PGM metals using the “ship-in-a-bottle” synthesis
- Establishing quantitative structure-activity relationships for the steam reforming reactions via metal-based catalyst characterization and evaluation

2. State of the art

2.1. Hydrocarbon reforming

Reforming is an advanced and mature technology in the energy sector. For decades, this process has been widely employed to convert hydrocarbons originating from various sources (mostly fossil) into a mixture of H_2 , CO and CO_2 . The produced syngas is a key intermediate in the chemical industry which is used in a number of highly selective syntheses of an extensive range of chemicals and fuels.

2.1.1. Reforming history at a glance

Catalytic interaction between hydrocarbons and metals is believed to have been first observed as early as in 1817.^[8] Among the few studies reported during the following century, Mond claimed the application of nickel for this process in 1889. In 1924, the first detailed study of the catalytic reaction between steam and methane was described by Neumann and Jacob.

The first nickel catalyst for the purpose of reforming was patented in 1913 by BASF.^[8] Industrial interests and the number of patents increased from then. At that time, natural gas was abundantly available and seen as a promising feedstock for the production of ammonia and methanol. In 1927, IG Farben patented a reforming catalyst to be placed in an externally heated steel tube. This company shared developments with Standard Oil, and in 1930 the first steam reformer was commissioned to produce hydrogen at Baton Rouge, Louisiana. In Europe, the first steam reformer was commissioned 6 years later by ICI in Billingham, UK.^[9] During the fifties, light distillate naphtha became an economical feedstock in Europe. In 1962, the first naphtha reforming plant was built in Heysham, UK. Since then, thanks to technological breakthroughs that resulted from new catalyst development and process efficiency improvements, the steam reforming process has been perfected and is now well implanted.^[10] The interest towards this technology is shown by the growing number of scientific publications in the specialized literature. While less than 30 articles related to steam reforming were published each year in the 1970's, more than 750 scientific articles were released in 2016 (Scopus database).

Today, steam reforming of natural gas is one of the main sources for syngas production. Depending on the end use, the syngas can be subjected to several downstream processes to produce pure hydrogen (Figure 1.5). Hydrogen is a key feedstock used in refineries for crude oil upgrading and for the synthesis of ammonia.^[11,12] Its worldwide production is estimated to be 50 million metric tons

per year, half of it being produced from steam reforming of natural gas. Another important application of natural gas-derived syngas is the methanol synthesis.^[13] In 2015, global demand of this key alcohol intermediate reached 70 million metric tons. Methanol is mostly produced from steam reforming of natural gas, as the produced syngas composition is adapted to its synthesis. However, coal gasification is becoming a major syngas production process for the manufacture of methanol in China, which has more than 50 such plants in operation, with dozens more in construction or planning. Finally, the recent resurgence of interest for the Gas-To-Liquid (GTL) technology has increased the demand in syngas. In 2011, the world largest GTL plant (Pearl, Shell) started operating in Ras Laffan, Qatar. The two train production facilities are equipped with steam reformers to convert natural gas into GTL products (140 000 barrels/day). Nevertheless, the impact of crude-oil price on GTL product prices is a major obstacle to widespread commercialization of GTL.

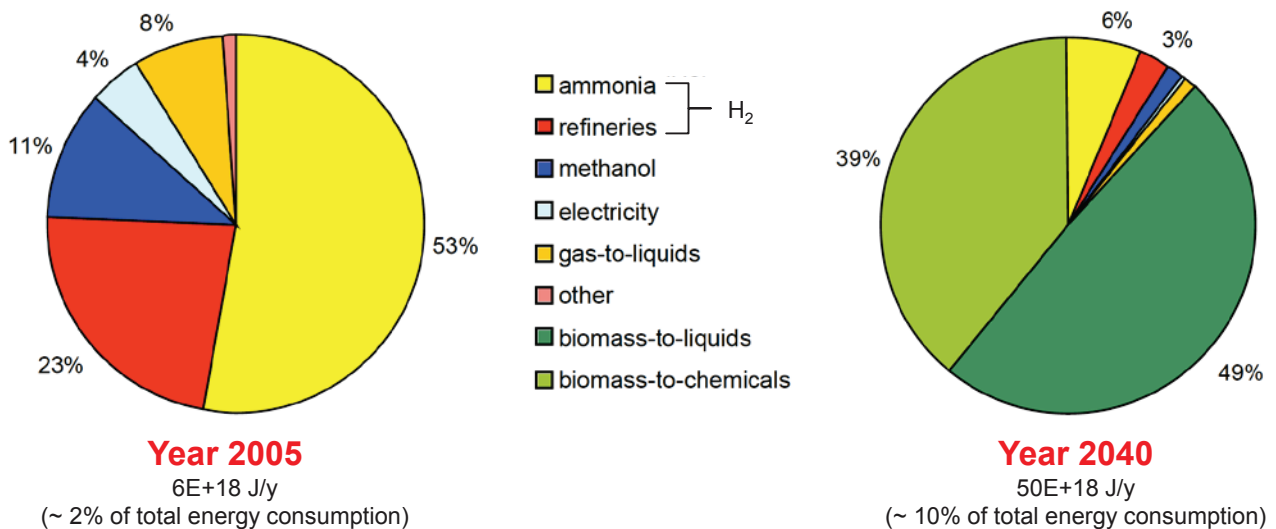


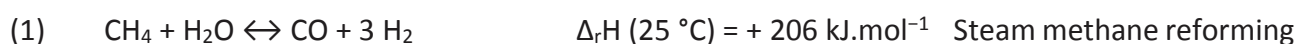
Figure 1.5 Past and future world syngas market.^[14]

2.1.2. Steam methane reforming process

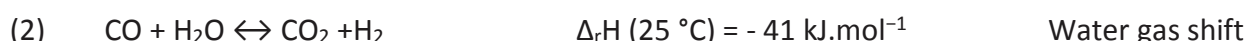
A broad variety of reforming processes (steam reforming, partial oxidation, autothermal reforming, dry reforming, etc.) has been developed to fit a large range of requirements needed in downstream processes. While pure H₂ production from reforming requires a syngas with a high H₂/CO ratio (over than 2.5-3), a syngas with a low H₂/CO ratio (lower than 2-2.5) is needed for the synthesis of GTL products and methanol.

Steam reforming produces a syngas with a H₂/CO ratio in the range of about 2.2 to 4.8 depending on the feed composition.^[13] This reforming application is often conducted with natural gas. Hydrogen production via methane reforming proceeds in several steps, described as follows:^[15]

1. **Pre-treatment:** Sulfur compounds must be removed in order to avoid downstream catalyst poisoning. The raw feed is mixed with recycled H₂ and organic sulfur compounds are converted into H₂S over a hydrogenation catalyst. A second step consists in the removal of H₂S by adsorption. The sulfur content in fuel streams is usually kept under 1 ppmv.
2. **Steam methane reforming (SMR, Equation 1):** The desulfurized feed is first preheated before entering the catalyst reformer tubes. Then the feed passes through the catalytic bed in a multi-tubular reformer reactor. Usually steam reforming is performed at 800-900 °C, above 20 bar, and with a S/C ratio of around 2.5-3 to ensure coke-free operations.^[13] The reaction is highly endothermic.



3. **Water gas shift (WGS, Equation 2):** The outlet gas is cooled by steam production before entering a shift converter. CO and steam are converted into CO₂ and H₂ which leads to higher hydrogen yield. The reaction is slightly exothermic.



4. **Purification:** The shifted gas is cooled to room temperature. Removal of steam and CO₂ from H₂ is carried out through condensation and Pressure Swing Adsorption (PSA), respectively. High purity hydrogen can be obtained (above 99.95%).^[16]

2.1.3. Bio-syngas production

Liquid fuels can be produced from natural gas by first producing syngas and then converting the syngas to liquid fuels via the GTL process. Natural gas, while plentiful, is a fossil fuel and thus contributes to greenhouse gas (GHG) emissions. For sustainable reasons, there is a push to produce renewable fuels from biomass (Figure 1.5). In the Biomass-To-Liquid (BTL) process, liquid fuels can be produced from biomass by first converting it to bio-syngas via gasification.

Gasification technology, in combination with gas cleaning and catalytic reforming of the raw gas offers the possibility to convert biomass into a bio-syngas adapted for the production of Fischer-Tropsch biodiesel or other biofuels and chemicals. While several gasification technologies have been considered at the laboratory level,^[4,17–20] a limited number of demonstration plants is under operation (e.g. GoBiGas).^[21] As an example due to its relation to the FASTCARD project, the bio-syngas pilot plant of the Energy research Centre of the Netherlands (ECN) is based on indirect fluidized bed gasification (MILENA) and includes the following steps (Figure 1.6):^[22,23]

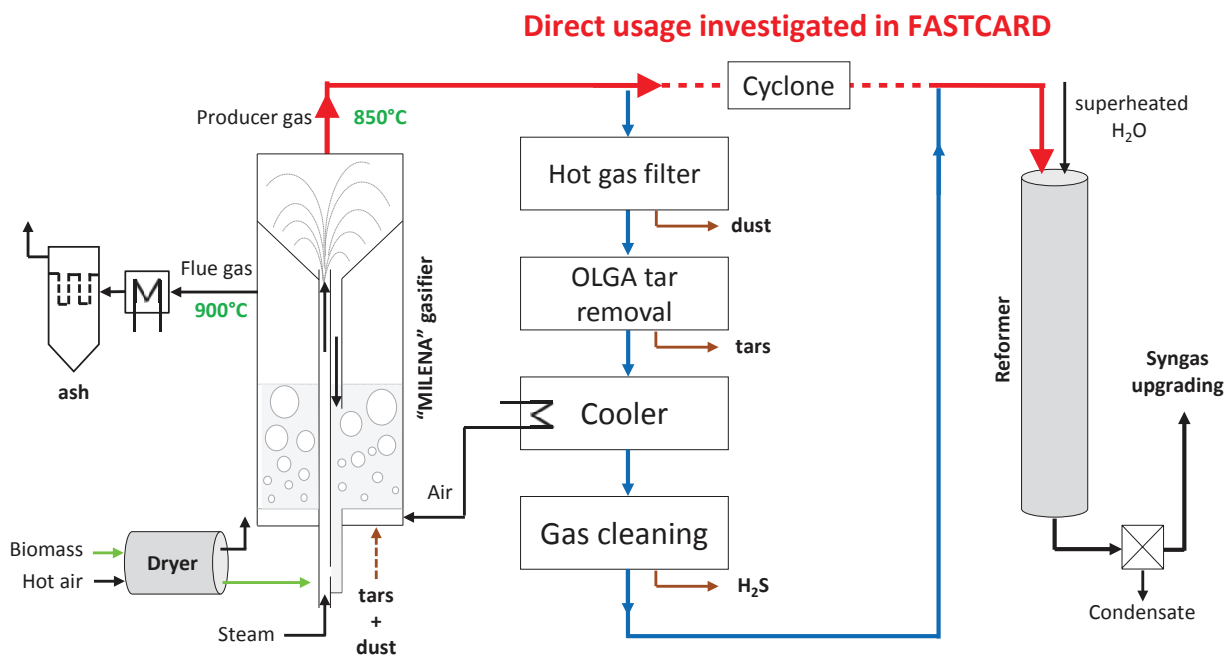
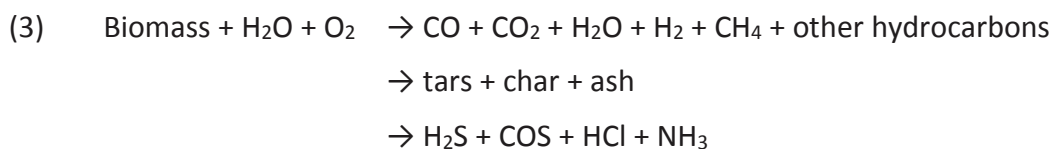


Figure 1.6 Simplified layout of the actual bio-syngas demonstration plant at ECN (blue arrows) and the alternative gas cleaning-free process design under investigation within the FASTCARD project (red arrows).

- Gasification:** In MILENA gasifier, dried biomass and superheated steam are fed into the riser.^[24] Fluidized bed material enters the riser from the combustion area and heats the biomass to 850 °C. The heated biomass particles are partially converted into gas. The volume created by the gas results in a vertical velocity in the riser carrying over the bed material together with the degasified biomass particles (char). The upper part of the gasifier reduces the vertical velocity of the gas causing the bed material and char to separate from the gas and to fall down into the downcomer. The downcomer transports bed material and char from the gasification section into the combustor. Tars and dust, separated from the producer gas, are also brought to the combustor. Char, tars and dust are burned with air to heat the bed material to approximately 925 °C. No additional heat input is required. The producer gas (Table 1.1) leaves the reactor from the top and is sent to the gas cleaning section. A generalized reaction describing biomass gasification is described in Equation 1:



- Gas cleaning:** Producer gas conditioning is necessary to prevent the downstream reforming catalyst from deactivating. In the actual bio-syngas demonstration plant at ECN, a hot gas filter is first used to remove the dust (Figure 1.6). This dust stream contains ash, small bed material particles and char. Tars are then stripped of the producer gas in a gas cleaning unit (named "OLGA") based on scrubbing with liquid oil. Tars and dust can be recycled to the combustion area. The producer gas is then cooled in heat exchanger; the heat is used to pre-heat combustion air. In the next gas cleaning unit, S-containing molecules are removed by hydrodesulphurization and subsequent commercial adsorbent materials (typically ZnO and active carbon filters).
- Reforming:** In the actual configuration used at ECN, the contaminant-free producer gas is mixed with superheated steam to ensure a sufficient H/C ratio and prevent coke formation. Light hydrocarbons and remaining traces of tars are converted in the reforming unit to H₂, CO and CO₂. Furthermore, NH₃ (which is a strong poison for the downstream Fischer-Tropsch catalyst)^[25,26] contained in the feed gas is converted into N₂. Both thermal and catalytic reforming options are being investigated at ECN. In WP1, direct reforming of the raw producer gas using advanced catalysts resistant to H₂S is being investigated as an alternative to the actual bio-syngas plant configuration (Figure 1.6). This would enable direct upgrading of the tars without intermediate gas cleaning steps and energy savings.

Table 1.1 Typical producer gas composition obtained at ECN.

Component	Concentration mol% _{dry}			
CO	28			
H ₂	27			
CO ₂	25			
CH ₄	10			
C ₂ H ₂	0.2			
C ₂ H ₄	3.4			
C ₂ H ₆	0.2			
C ₆ H ₆	1.0			
C ₇ H ₈	0.1			
N ₂	3.1			
Tars	18	g.m ⁻³ _{dry}		
		Tar class	Description	Concentration mg.m ⁻³ _{dry}
		Class 2	heterocyclic aromatics	982
		Class 3	1 ring aromatics	197
		Class 4	2-3 rings polyaromatics	11406
		Class 5	4-5 rings polyaromatics	2147
		Unknowns	-	3642

Table 1.1 summarizes the producer gas composition obtained at ECN while operating the gasifier at 880 °C using olivine as bed material and using beech wood as feedstock.^[27] The corresponding tar composition is detailed in Figure 1.7. On a dry basis, H₂, CO, CO₂ and CH₄ are the most prominent molecules present in the gas. On a wet basis and under similar gasification conditions, the steam content can be up to 40 mol%.^[28] The relative share of H₂, CO, CO₂ and CH₄ depend on several factors: the operating temperature, the amount of steam added to the riser, the amount of steam added to the combustor, the catalytic activity of the bed material that influences the water-gas-shift equilibrium, etc. Among the hydrocarbons detected in the gas stream, methane is by far the most present. The remainder is mainly composed of C₂ and 1-ring (mostly benzene (C₆H₆) and toluene (C₇H₈)) hydrocarbons.

The producer gas also contains inorganic contaminants due to the presence of S, Cl and N-containing molecules in the feedstock.^[29] It is assumed that approximately 50% of the sulfur in the biomass fuel ends up in the product gas, of which 90% as H₂S and 10% as COS (no CS₂), the rest is retained in the char. For chlorine, it is assumed that 20% of the fuel chlorine ends up as HCl in the gas, the remainder is removed as chloride salts in the cyclone. For fuel nitrogen, a conversion of 50% into NH₃ is assumed (no HCN), the other part is converted into N₂ or retained in the char. Concentrations in H₂S, HCl and NH₃ are typically in the range of 0-200, 0-100 and 0-2000 ppmv, respectively.^[28]

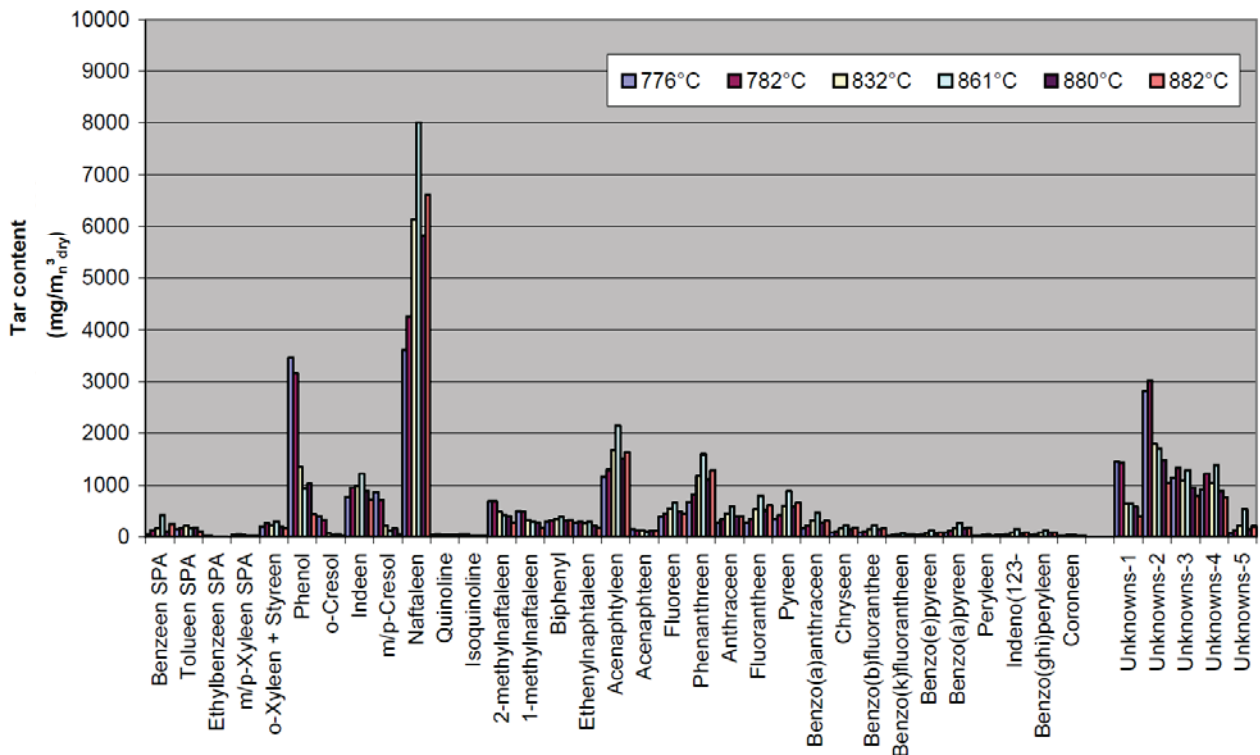


Figure 1.7 Tar composition in producer gas obtained for various gasification temperatures at ECN.

The producer gas also contains organic contaminants, called tars. All fluidized bed and fixed-bed gasifiers produce tar-containing gas. The presence of tars is an important technical barriers in the biomass gasification development. Tar buildup causes pipe plugging and filter fouling, resulting in serious operational issues. Tars are a complex mixture of condensable hydrocarbons, which includes single ring to 5-ring aromatic compounds along with other oxygen-containing hydrocarbons and complex polycyclic aromatic hydrocarbons (PAH). Tars are generally defined as all organic contaminants with a molecular weight larger than benzene (toluene often is excluded).^[30] Based on the molecular weight of tar compounds, ECN proposed a classification of tar components into five groups, as shown in Table 1.1.^[31] Naphthalene always is a major contributor to the total tar content.^[32,33] In the case of ECN process (Figure 1.8), at a gasification temperature of 880 °C, naphthalene (C₁₀H₈), phenanthrene (C₁₄H₁₀) and pyrene (C₁₆H₁₀) are the main representative compounds of 2-ring, 3-ring and 4-ring PAH, respectively (Figure 1.7). It is worth noting that at higher gasification temperatures the total tar content in the producer gas is lower, while the fraction of heavy tar compounds (classes 4 and 5) is higher.

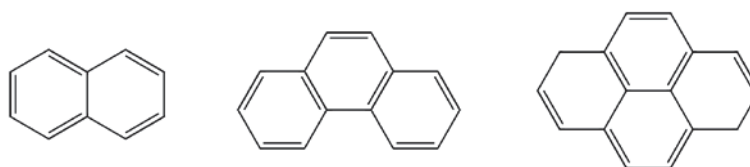


Figure 1.8 From left to right, chemical structures of naphthalene, phenanthrene and pyrene.

2.1.4. Producer gas reforming

This study aims at developing advanced reforming catalysts for the direct conversion of producer gas into a HC-free bio-syngas, in absence of the intermediate gas cleaning steps. In this catalytic process, both light hydrocarbons and tars have to be reformed to increase syngas yield. Sufficiently active and stable reforming catalysts are expected to operate in presence of organic (tars) and inorganic (mostly H₂S) contaminants.

Catalytic reforming of post-gasification HCs is a technically and economically interesting approach for gas cleaning. First, the catalytic steam reforming of light hydrocarbons is a well-known technology.^[8] Second, it has the potential to increase conversion efficiencies while simultaneously eliminating the need for the collection/disposal of tars and for intermediate heat exchangers.^[7] However, HCs elimination reactions are known to be kinetically limited. Therefore, the reaction rates can be increased by increasing the temperature and/or using a catalyst. Catalysts can only increase the rate of a reaction that is thermodynamically feasible. The main reactions that occurs in the reformer can be divided in two categories and are summarized as follows:^[32–35]

HC decomposing reactions:

- | | | |
|-----|--|------------------|
| (4) | $C_nH_m + n H_2O \rightarrow n CO + (n + \frac{1}{2} m) H_2$ | Steam reforming |
| (5) | $C_nH_m + n CO_2 \rightarrow 2n CO + \frac{1}{2} m H_2$ | Dry reforming |
| (6) | $p C_nH_m \rightarrow q C_xH_y + r H_2$ | Cracking |
| (7) | $C_nH_m \rightarrow n C^* + \frac{1}{2} m H_2$ | Carbon formation |

Equilibrium reactions:

- | | | | |
|------|---|--|-----------------|
| (2) | $CO + H_2O \leftrightarrow CO_2 + H_2$ | $\Delta_rH (25\text{ }^\circ\text{C}) = -41\text{ kJ.mol}^{-1}$ | Water gas shift |
| (8) | $CO + 3 H_2 \leftrightarrow CH_4 + H_2O$ | $\Delta_rH (25\text{ }^\circ\text{C}) = -223\text{ kJ.mol}^{-1}$ | Methanation (1) |
| (9) | $C^* + 2 H_2 \leftrightarrow CH_4$ | $\Delta_rH (25\text{ }^\circ\text{C}) = -87\text{ kJ.mol}^{-1}$ | Methanation (2) |
| (10) | $CO + H_2 \leftrightarrow H_2O + C^*$ | $\Delta_rH (25\text{ }^\circ\text{C}) = -136\text{ kJ.mol}^{-1}$ | Water gas (1) |
| (11) | $CO_2 + 2 H_2 \leftrightarrow 2 H_2O + C^*$ | $\Delta_rH (25\text{ }^\circ\text{C}) = -103\text{ kJ.mol}^{-1}$ | Water gas (2) |
| (12) | $2 CO \leftrightarrow C^* + CO_2$ | $\Delta_rH (25\text{ }^\circ\text{C}) = -172\text{ kJ.mol}^{-1}$ | Boudouard |

HC decomposing reactions are endothermic reaction that mix steam (Equation 4) and dry (Equation 5) reforming. This dual approach, called bi-reforming or combined-reforming, is promising for potential industrial application in syngas production, as the H_2/CO ratio can be easily adjusted by controlling H_2O/CO_2 in the feed, and the coke deposition can be lowered due to the addition of steam.^[36–39] Some studies have shown that steam and dry reforming reactions are catalyzed by group VIII metals.^[40,41] Calculations performed by Simell et al. showed that dry reforming was more thermodynamically favored than steam reforming at temperatures above 830-850 °C.^[40] The cracking reaction (Equation 6) is a simplification, where lighter HCs (C_xH_y) are formed from heavier ones (C_nH_m). This decomposition can be much more complex and many different paths are possible. Coll et al. reported that, in general, the more aromatic rings, the lower the decomposition rate, although naphthalene, which has only two rings, is one of the less reactive tar model compounds.^[42] At the typical reaction temperatures (700-1000 °C), all HCs higher than CH_4 decompose irreversibly, whereas CH_4 , H_2O , CO and H_2 reach the thermodynamic WGS equilibrium (Equation 2). While the formation of coke (C^*) through the Boudouard (Equation 12) and water gas (Equations 10 and 11) reactions is exothermic and favored at lower temperatures, carbon deposition becomes increasingly important at higher temperatures via HC cracking (Equations 7 and 9). The tendency of carbon to deposit depends on the nature of the surface carbon species. Rostrup-Nielsen et al. had reported that the more unsaturated the HC, the more extensive the carbon deposition.^[8] Coll et al. also observed that the larger the number of aromatic rings in the molecule, the stronger the tendency to coke formation.^[42] Thermodynamic approach and catalytic reforming mechanisms will be discussed more in details in sections 2.1.5 and 2.2.2.3 of this chapter, respectively.

2.1.5. Thermodynamic study of producer gas reforming

As discussed in section 2.1.4, producer gas reforming is actually a combination of different reactions. The involved reactions will be described in this section along with thermodynamic calculations. This thermodynamic study was carried out with the chemical reaction and equilibrium software HSC. This computational tool determines equilibrium gas-phase compositions based on Gibbs free enthalpy minimization. The choice of the feed gas composition (Table 1.2), which is a simplified version of a typical reformat gas composition, is based on our experimental conditions (see section 3.3.1 of chapter 2). The system pressure is set at 2.2 bar, in agreement with our test conditions.

Table 1.2 Feed gas composition used for the simulations of reforming equilibria.

Compound		CO	H ₂	CO ₂	H ₂ O	CH ₄	N ₂	Ar
Experimental	(mL min ⁻¹)	25	20	12.5	48.75	11.25	2.5	5
feed rate	(10 ⁻³ mol min ⁻¹)	1.12	0.89	0.56	2.17	0.50	0.11	0.22

Le Chatelier's principle states that raising the temperature favors endothermic reactions, like HC decomposing reactions. In contrast, raising the temperature will favor the reverse direction of the exothermic equilibrium reactions. The effect of the temperature on the equilibrium composition is presented in Figure 1.9. In Figure 1.10, the calculations of the conversion in CH₄ and the H₂/CO molar ratio at the thermodynamic equilibrium are plotted as a function of the temperature.

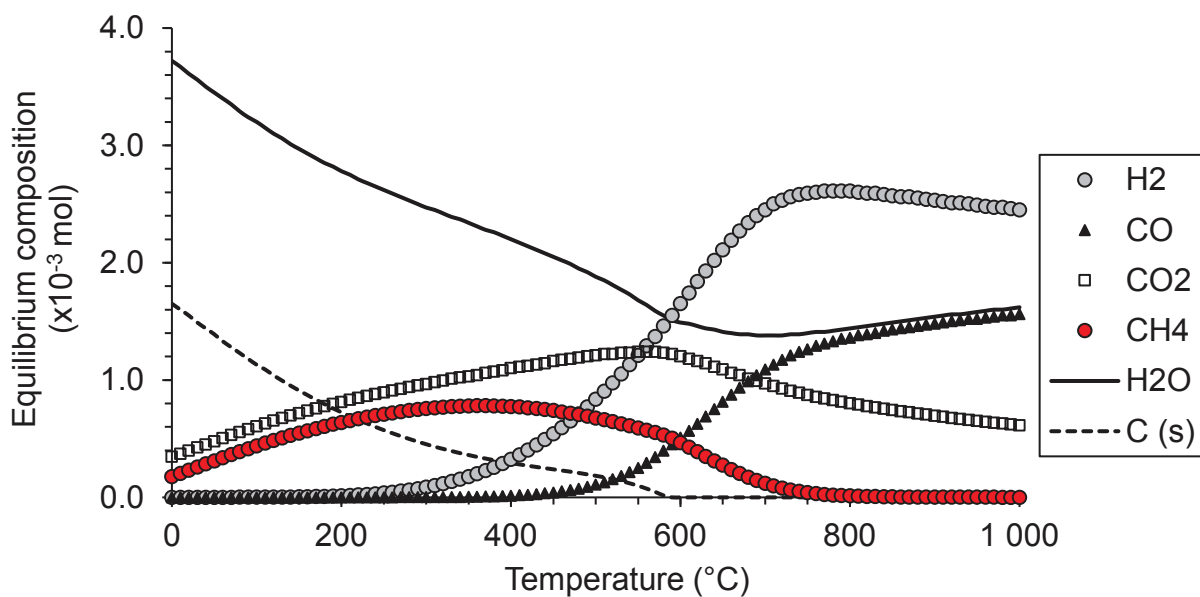


Figure 1.9 Equilibrium compositions between 0 and 1000 °C under test conditions.

As expected at higher temperatures, the amount of syngas produced from CH₄ reforming increases up to almost complete conversion of CH₄ while the H₂/CO ratio decreases because of the reverse Water Gas Shift reaction (Equation 2). In a typical temperature range that is the most adapted for reforming to be performed (700-1000 °C where at least 75 % conversion in CH₄ is observed), a H₂/CO ratio of 1.5-2.5 is thermodynamically favored. This ratio can be highly desirable for target downstream processes, like the iron-based Fischer-Tropsch synthesis.^[43] Still in this temperature range, H₂O and CO₂ are observable in non-negligible concentrations that are higher than 21 mol% and 9 mol% on a wet basis, respectively. The presence of H₂O even at reforming equilibrium is used to the advantage of the combined reforming process by lowering the severity of the operating conditions of CO₂ reforming.^[44] Indeed, the presence of H₂O enhances carbon gasification (Equations 10 and 11). While HC decomposition favors coke formation at high temperatures (Equation 7 and 9), from the thermodynamic views no carbon deposition is expected at 600 °C or above (Figure 1.9).

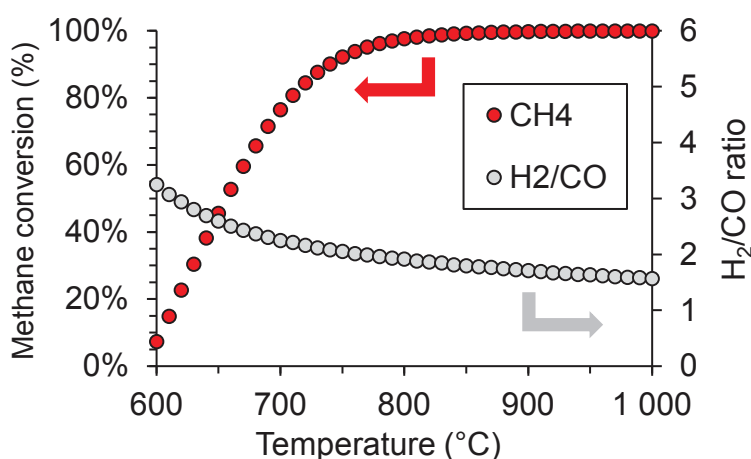


Figure 1.10 Methane conversion (left axis) and H₂/CO molar ratio (right axis) calculated at the thermodynamic equilibrium at 2.2 bar as a function of the temperature.

Pressure is known to have a major influence on the conversion of HCs in reforming. HC decomposing reaction are accompanied by a volume expansion: the mol number of gas products is higher than that of gas reactants. As Le Chatelier's principle states, increasing the pressure favors the side of the equilibrium with the least number of gaseous molecules. Thus, the CH₄ conversion calculated at 2.2 bar (Figure 1.10) is thermodynamically less favored than when operating at atmospheric pressure: a 95 % conversion in CH₄ is reached from 770 °C and 720 °C when operating at 2.2 bar and 1 bar, respectively. However, in practice methane reformers operate with H₂O partial pressures of up to 20-40 bar.^[10] These conditions generate a high S/C ratio that decreases the amount of unreacted CH₄ and reduces the risk of coke formation when too little oxidant is present.

Figure 1.11 presents the equilibrium constants of the steam (Equation 3) and dry (Equation 4) reforming reactions calculated at temperatures ranging from 0 to 1000 °C. In addition to methane and toluene, three tar model compounds were selected: naphthalene, phenanthrene and pyrene.

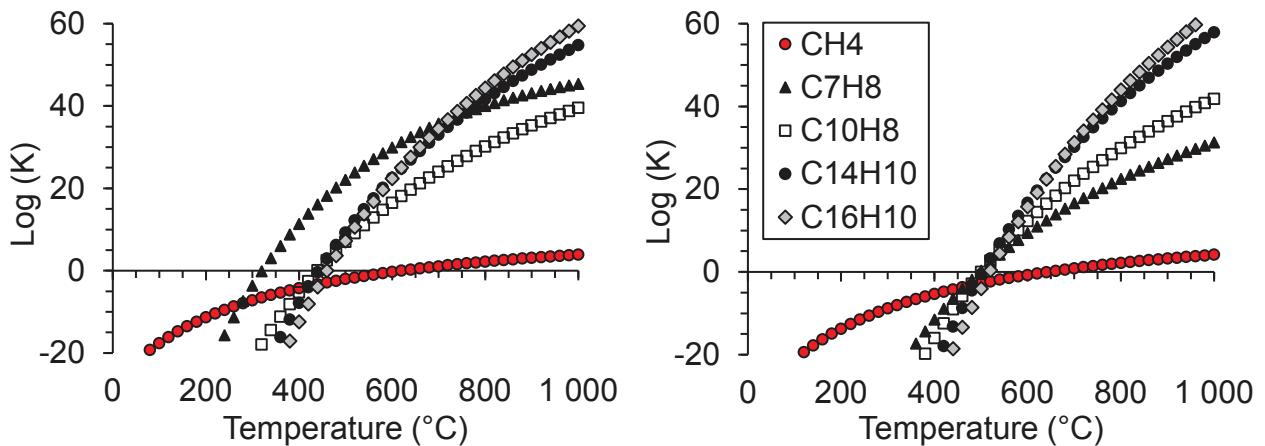


Figure 1.11 Equilibrium constants for the steam (left) and dry (right) reforming of various HCs.

Formation of CO and H₂ by steam and dry reforming of CH₄ is favored (Log K > 0) when T > 620 °C and T > 640 °C, respectively. At 700-1000 °C, the conversion of heavier HCs to CO and H₂ is much more favored than that of CH₄. H₂O and CO₂ reforming are thus favored from lower temperatures, i.e. T > 440-460 °C and T > 500-520 °C, respectively (except steam toluene reforming that is expected from T > 320 °C). These data stress that dry reforming is more thermodynamically favored than steam reforming at temperatures above 820 °C. In addition, it is observed that the more aromatic rings, the higher the propensity to be reformed.

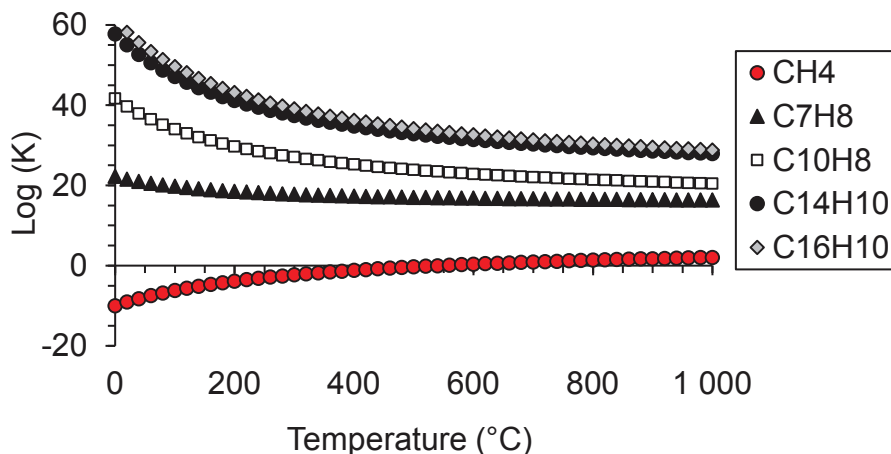


Figure 1.12 Equilibrium constants for the carbon formation reaction (Equation 7) from different HCs.

Figure 1.12 presents the equilibrium constants of the carbon formation reaction (Equation 7) for the same five HCs. Coke formation is expected from CH₄ decomposition when T > 540 °C. Toluene and tar model compounds are potential coking agent at temperatures ranging from 0 to 1000 °C. It is observed that the more aromatic rings, the higher the propensity to form carbon deposit.

2.2. Catalysis

Steam methane reforming has been widely studied. As high temperatures are needed to achieve high conversions of CH₄ from the thermodynamic aspect, reformers generally operate at lower temperatures using a catalyst. Throughout the years, it has been carried out over different supported catalysts that were chosen to both enhance the catalyst activity and improve its resistance to deactivation. While a growing interest toward tar reforming is observed in the literature, very few studies have been performed on producer gas reforming.

2.2.1. Heterogeneously catalyzed gas-phase reaction

Catalysis was defined for the first time in 1985 by Ostwald as follows:^[45] "*a catalyst accelerates a chemical reaction without affecting the position of equilibrium*". This acceleration originates from a change in the reaction pathways along with a decrease in the energy barrier of reaction.

The two main domains of catalysis are heterogeneous and homogeneous catalysis. In the case of catalyzed reforming processes, only heterogeneous catalysis is involved since the feed is gaseous or liquid and the catalyst a solid material. Heterogeneous catalytic processes involve purely physical as well as purely chemical steps which occur in the following order:

- 1 - Diffusion of the reactant(s) into the boundary layer to the catalyst
- 2 - Diffusion of the reactant(s) through the pores
- 3 - Adsorption of the reactant(s) on the inner pore surface
- 4 - Chemical reaction on the active site
- 5 - Desorption of the product(s) from the catalyst surface
- 6 - Diffusion of the product(s) out of the pores
- 7 - Diffusion of the product(s) through the boundary layer to the gas phase

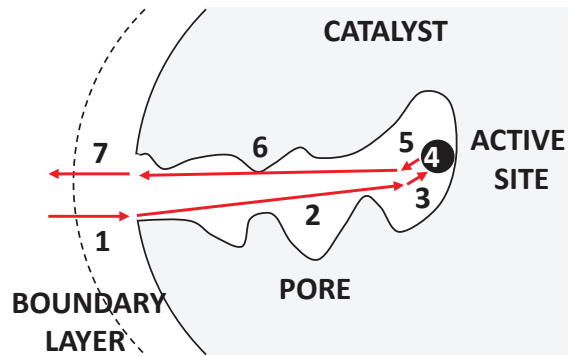


Figure 1.13 Scheme of the different steps involved in a heterogeneous catalytic process.

Depending on transport and reaction rates, the effective reaction rate observed during the catalytic reaction follows three different regimes:^[46]

- **Kinetic limitation:** the reaction rate is slow in comparison with the diffusion rates
- **Diffusion limitation in pores:** the diffusion rate in pores is slow compared with the diffusion rate in the gas film and the kinetic reaction rate
- **Diffusion limitation in the gas film:** the diffusion rate in the gas film is slow compared with the kinetic reaction rate and the diffusion rate in pores.

Ideally, the resistance effect of diffusion limitations in the gas film and pores is reduced as much as possible to maximize the effective reaction rate. If mass transfer problems are encountered in a catalytic reaction, various strategies are employed to minimize their effects:^[46]

- **Mass transfer limitation in pores:** the internal mass-transfer coefficient can be increased by decreasing the catalyst particle size and improving the pore geometry.
- **Mass transfer limitation in the gas film:** the external mass transfer coefficient can be increased by decreasing the catalyst particle size and increasing the fluid velocity.

In addition to mass transport effects, heat transfer throughout the catalyst particle and the gas film can affect the effective reaction rate. Heat transport phenomena are generally related to the heat of reaction and result in a temperature gradient. This intrusion of gradients causes severe deviations from the ideal isothermal performance. Thus, heat transport limitations are significantly altering the local temperature and can promote side reactions. Deviations from isothermicity can be lowered by decreasing the catalyst particle size or by diluting the catalyst bed with inert particles.

2.2.2. Catalytic reforming

2.2.2.1. Metal

Methane reforming has been mainly studied over Rh, Ni, Ru, Pt, Pd and Ir. Different studies have investigated the order of activity over different pure transition metals. There appears to be a general consensus on this order, for both H₂O and CO₂ reforming:^[47-49]

$$\text{Rh, Ru} > \text{Ni, Ir} > \text{Pd, Pt}$$

Although it should be noted that Wei and Iglesia have observed otherwise:^[50]

$$\text{Pt} > \text{Ir} > \text{Rh} > \text{Ru, Ni}$$

Catalytic reforming of methane is traditionally performed over Ni-based catalysts since those present acceptable activity and low costs. Noble metals such as Rh, Ru, Pd, Ir and Pt are less prone to deactivation (for instance surface poisoning or oxidation) but are usually too expensive to be used in conventional industrial reformers.^[51]

The activity of a catalyst is related to the metal surface area. This implies that the catalytic activity benefits from a high dispersion of the metal particles. Dispersions for Ni catalysts are of 2-5 %, with metal particles of 20-50 nm in general.^[8] There is an optimum Ni-loading beyond which an increase in metal content does not produce any increase in activity, usually around 15-20 wt%.

The structure of the Ni surface strongly influences the catalytic activity. Steam and dry reforming are structure-sensitive reactions. In fact, Ni particles are polycrystalline and composed of a number of single crystals.^[52] Schouten et al. reported that Ni (110) and (100) surfaces are much more active for methane dissociation than the highly packed Ni (111) surface.^[53-55] The coordination number of surface metal atoms is 7, 8 and 9 for Ni (110), Ni (100) and Ni (111), respectively. Less coordinated Ni metal atoms are thus more reactive than metal atoms in the higher coordinated surface terrace sites. This agrees with the conclusions of Wei and Iglesia who found that CH₄ reforming turnover rates increased as the size of Ni particles decreased.^[56] This observation suggests that coordinatively unsaturated Ni surface atoms (that are more present in smaller clusters) activate C-H bonds more effectively than atoms on lower-index surfaces. The same conclusion was observed on noble metals.^[50,57,58] This is confirmed by the results of the theoretical studies performed by Rostrup-Nielsen et al., which indicate that steps are much more reactive than the close-packed surface.^[59]

Bi-metallic catalysts have also been studied for the reforming of methane.^[60] The addition of a second metal leads to geometric and electronic modifications. Geometric modifications will usually result in a better metal dispersion and thus higher active surface. Electronic modifications will have an effect on adsorption/desorption of reactants and products which can affect activity and selectivity. Therefore, positive interactions between the two metals generally allow to increase activity, improve resistance to deactivation and extend the lifetime of the catalysts. In 2011, the effect of noble metal addition on Ni catalysts for the SMR reaction was reviewed by Li et al.^[61] These effects on the catalytic performances can be summarized as:

- Higher activity (improved Ni dispersion, retarded Ni sintering and increased CH₄ activation)
- Suppression of Ni oxidation (resulting in the suppression of hot spot formation)
- Limited carbon formation and higher resistance to sulfur poisoning
- Self-activation behavior

Producer gas reforming has been less extensively studied. Tomishige et al. evaluated the activity of various metals supported on CeO₂-SiO₂ for steam reforming of biomass-derived tars. They found the order of activity at 650 °C (at iso metal loading in mol) to be:^[62]



Developing metal-based reforming catalysis to convert producer gas is a challenge due to the high propensity of tars to form coke and the presence of S-containing agents. So far, research has mainly focused on improving Ni/ γ -Al₂O₃ materials developed by sol-gel method, a synthesis pathway that enable high metal-support interactions which limit sintering and coke deactivation.^[32] Addition of a cheap element as a doping agent for the metal or the support has been studied to find synergistic influences (Figure 1.14). Noble metal addition (Pt, Pd, Rh, Ru, Re, or Ir) has also been considered to improve the resistance of Ni-based catalysts against deactivation. Yung et al. reviewed and classified the different elements used for catalytic tar reforming. The authors ranked the performances of the different active sites, promoters and supports. Some elements were classified as catalyst poisons.^[63]

2.2.2.2. Support

The choice of the support is fundamental for HC reforming. The support should be stable under the reaction conditions and should provide a high surface area for the metal. It will determine important features such as the dispersion of the metal particles, the resistance to sintering or the resistance to carbon formation.^[64] It can thus affect the activity of the catalyst and may even participate in the reaction. A high porosity should also result in a long contact-time between reactants and catalyst.

Acidic supports are expected to facilitate the decomposition of HCs, but they will also promote cracking and polymerization, producing carbon that can lead to catalyst deactivation. Supports possessing a strong Lewis basicity are thus preferred. Basicity is expected to favor carbon gasification. Therefore, the addition of basic metal oxides such as Li, K, Mg, and Ca to a catalyst supported on alumina (Al_2O_3) has proven to prevent carbon deposition (Figure 1.14). Furthermore, supports with a basic nature are known to enhance the activation of steam.^[65,66]

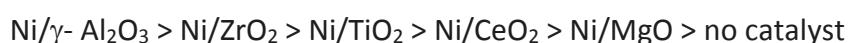
1																	2
H																	He
3	4											5	6	7	8	9	10
Li	Be											B	C	N	O	F	Ne
11	12											13	14	15	16	17	18
Na	Mg											Al	Si	P	S	Cl	Ar
19	20	21	22	23	24	25	26	27	28	29	30	31	32	33	34	35	36
K	Ca	Sc	Ti	V	Cr	Mn	Fe	Co	Ni	Cu	Zn	Ga	Ge	As	Se	Br	Kr
37	38	39	40	41	42	43	44	45	46	47	48	49	50	51	52	53	54
Rb	Sr	Y	Zr	Nb	Mo	Tc	Ru	Rh	Pd	Ag	Cd	In	Sn	Sb	Te	I	Xe
55	56	*	72	73	74	75	76	77	78	79	80	81	82	83	84	85	86
Cs	Ba		Hf	Ta	W	Re	Os	Ir	Pt	Au	Hg	Tl	Pb	Bi	Po	At	Rn
87	88																
Fr	Ra																
		*	57	58	59	60	61	62	63	64	65	66	67	68	69	70	71
		Lanthanides	La	Ce	Pr	Nd	Pm	Sm	Eu	Gd	Tb	Dy	Ho	Er	Tm	Yb	Lu

bold text	=	tested as base catalyst		=	biomass-derived poisons
	=	good promoter		=	good support
	=	moderate promoter		=	moderate support
	=	poor promoter		=	poor support

Figure 1.14 Overview of elements used as active site, promoter or support for producer gas reforming.^[63]

One of the most employed supports for methane reforming reactions is Al_2O_3 for its advanced features. However, Yokota et al. reported that a 0.5 wt% Rh/ $\gamma\text{-Al}_2\text{O}_3$ catalyst is less active than a 0.5 wt% Rh/ SiO_2 for the dry reforming of CH_4 at 700 °C, despite the higher dispersion of Rh on $\gamma\text{-Al}_2\text{O}_3$. In fact, stronger metal-support interactions (MSI) exist for Rh on $\gamma\text{-Al}_2\text{O}_3$. Accordingly, the $\gamma\text{-Al}_2\text{O}_3$ system tends to maximize its number of metal-support bonds, resulting in a higher dispersion. Then, as a consequence of this stronger MSI, Rh loses its metallic character that can dissociate CH_4 .^[67]

Regarding Ni-based tar reforming catalysts, different reviews agree on $\gamma\text{-Al}_2\text{O}_3$ as the best support. For example, Miyazawa et al. studied the H_2O reforming of a tar mixture derived from the pyrolysis of wood with different supports and found that the order of activity at 600 °C was the following:^[68]



However, when the temperature is too high ($> 800\text{ }^{\circ}\text{C}$), $\alpha\text{-Al}_2\text{O}_3$ phase formation can occur. The catalytic activity is much lower for $\alpha\text{-Al}_2\text{O}_3$ compared to the $\gamma\text{-Al}_2\text{O}_3$ phase principally because of the drastic pore volume and surface area reduction.

2.2.2.3. Reaction Mechanisms

Xu and Froment studied the steam reforming of methane over $\text{Ni/MgAl}_2\text{O}_4$ catalyst and proposed the following mechanism (Figure 1.15):^[69]

- H_2O reacts with surface Ni atoms, yielding adsorbed oxygen and gaseous H_2 . The gaseous H_2 formed is directly released in the gas phase and/or is in equilibrium with adsorbed H and H_2 .
- CH_4 is adsorbed on surface nickel atoms and either reacts with the adsorbed oxygen or dissociates to form chemisorbed radicals, CH_x ($x = 0\text{-}3$). The adsorbed oxygen and the carbon-containing radicals react to form chemisorbed CH_2O , CHO , CO or CO_2 . CO and CO_2 are formed out of CHO and CH_2O species.

Here, the reactions of carbon-intermediates with adsorbed oxygen are rate determining steps (RDS). However, Wei and Iglesia proposed otherwise.^[56] They found that reaction rates were proportional to CH_4 partial pressure but independent of the co-reactant pressure. Hence, they suggested a sole kinetic relevance of the CH_4 activation step over Ni and noble metals (Figure 1.15). The equilibrated nature of the other steps suggests that WGS reaction (Equation 2) is also at equilibrium. Remarkably, no involvement of the support in the activation of co-reactants was found to be kinetically relevant.

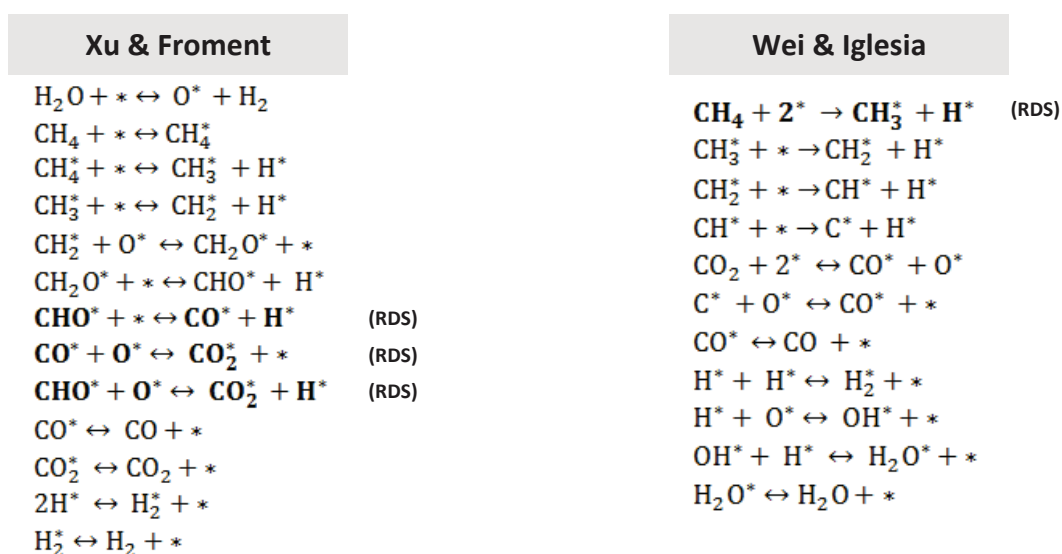


Figure 1.15 Reaction schemes for the SMR reaction proposed Froment (left) and Iglesia (right). * denotes a surface site.

Due to the complexity of real tars, most researchers used model tar compounds to study the catalytic properties of their materials. However, only few kinetic studies of tar reforming have been carried out on metal-based catalysts.

Mechanisms and kinetics of the thermal conversion of HC model compounds (naphthalene, toluene and benzene) in presence of H_2 and H_2O was studied by Jess et al.^[70] A simplified reaction scheme is shown in Figure 1.16. They concluded that benzene is the major intermediate component of the thermal decomposition of naphthalene ($T > 1000\text{ }^\circ\text{C}$). In consecutive reaction steps, benzene is cracked in lighter HCs, mostly methane and ethylene. All organic cracking products are then further converted to CO and H_2 in the presence of steam. The rate of benzene and naphthalene decomposition reactions are first and zeroth order with respect to the HC and steam, respectively. A negative reaction order in H_2 was measured for both aromatic compounds.

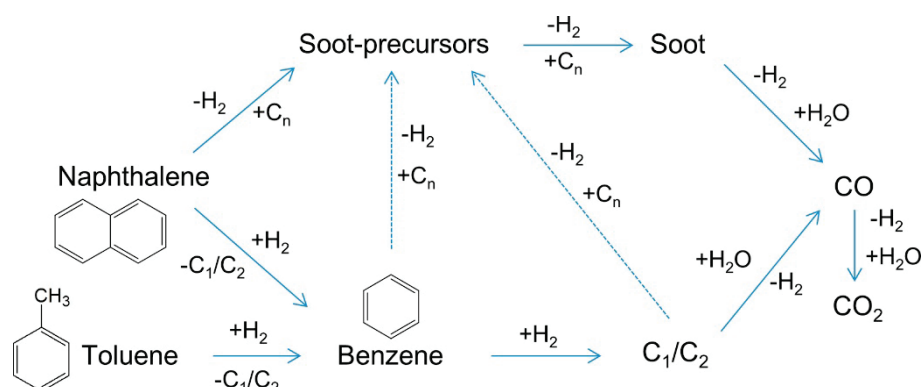


Figure 1.16 Reaction scheme of thermal conversion of naphthalene in presence of H_2O and H_2 .^[35]

Kaisalo et al. studied the kinetics of the benzene steam reforming on a Ni/Al_2O_3 catalyst from 750 to 900 $^\circ\text{C}$.^[71] The reaction order for benzene is close to one, while for H_2O , the reaction order is close to zero. In the reaction conditions, benzene is fully steam reformed, no HC is detected within the products. CO_2 addition to the feed stream has a rate enhancing effect for benzene steam reforming.

2.2.3. Catalyst deactivation

There can be many reasons for reforming catalysts to deactivate. It should be stressed that a distinction between thermal deactivation (i.e. sintering) and poisoning (i.e. contamination of the active surface atoms by the sorption of C-, S- or P-containing agents) exists. Understanding the causes of deactivation and developing new catalysts that are more resistant are constant concerns.

2.2.3.4. Sintering

Sintering refers to the agglomeration and the growth of the crystallites of the active phase. It also refers to support collapse leading to the loss of surface area. Both phenomena result in the loss of active surface and thus a decrease in activity.^[72]

Sintering is a thermal degradation that is favored by high temperatures and high steam pressures.^[52,73,74] This deactivation is irreversible or difficult to reverse. It also depends on the nature of the metal, the metal content, the initial crystallite size, the particle size distribution and the nature of the support.^[75,76] According to the Rule of Tammann, sintering is expected at temperatures above half of the melting temperature of the metal (i.e. above 590 °C for metallic Ni).

Three mechanisms for the metal particle growth have been proposed (Figure 1.17):

- **Particle migration:** entire crystallites migrate over the support followed by coalescence.
- **Atom migration (Ostwald ripening):** metal atoms emitted from one crystallite migrate over the support and are captured by another crystallite.
- **Vapour transport:** atom emission at high temperatures through the gas phase (promoted by reactants which form compounds with the metal in general).

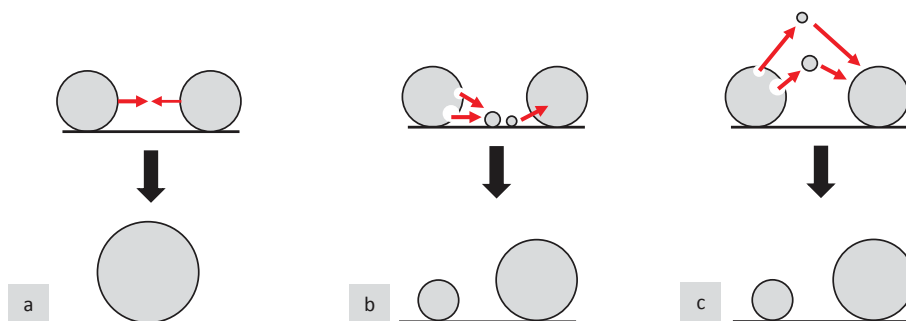


Figure 1.17 Scheme of sintering processes: coalescence (a), Ostwald ripening (b) and vapour transport (c).

The driving force for sintering is the difference in particle surface energy, which varies inversely with particle size. Surface energy minimization dictates that initial stage sintering acts to reduce surface area, so small size particles tend to sinter more than larger ones. In addition, the thermal energy requirements to induce motion of small crystallites is less than for larger clusters. Sehested et al. studied the mechanism for sintering of various Ni/MgAl₂O₄ reforming catalysts under a high steam pressure at 500 °C.^[77] They concluded on the basis of the particle size distributions that sintering occurred via the crystallite migration and coalescence mechanism. In a later study, the authors demonstrated that the sintering of the Ni particles is initially fast and will slow down as the Ni particles grow in size.^[76]

Limiting sintering is crucial to preserve the nickel surface area on which depends the reforming activity. In addition, nickel particle growth also influences the resistance toward poisoning by carbon and sulfur. Coking tendency is affected by the nickel particle size and the ability for sulfur absorption is related to the nickel surface area.^[52] For years, strengthening MSIs has been the cornerstone in research to prevent deactivation due to particle agglomeration. Thereby, particular attention has been devoted to study the role of the nature of the support,^[78–82] the nickel impregnation method,^[83–85] the thermal treatments,^[86–89] and the addition of promoters on sintering.^[90–93]

More recently, a growing interest for the nano-confining of Ni particles as a potential solutions against sintering has been observed.^[94,95] Encapsulation strategy is achieved by introducing a coating to stabilize the metallic particles. On the basis of the morphology, the catalysts with encapsulation structures can be classified into four groups (Figure 1.18).

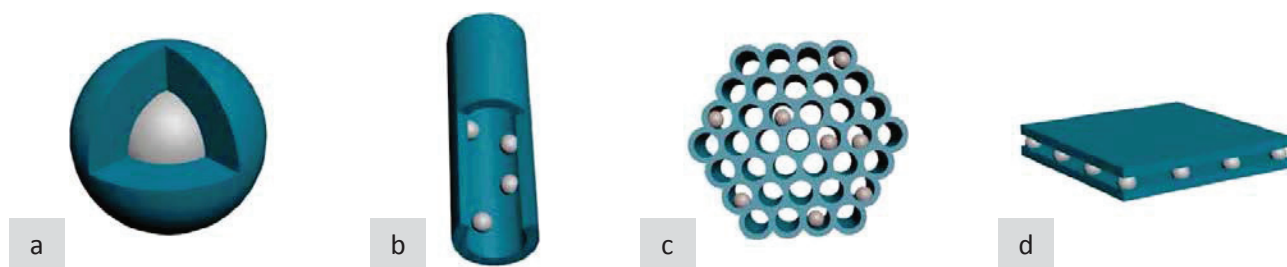


Figure 1.18 Core@shell (a), core@tube (b), mesoporous (c) and lamellar (d) encapsulated structures.^[95]

Embedding metal nanoparticles (NPs) in well-defined cavities or channels exerts a spatial restriction on the metal content hampering its sintering.^[96] In addition, the confining environment provided by the support offers a high surface area for the dispersion of active metals and often leads to different activities with respect to the conventional supported catalysts. Among these encapsulation strategies, the Ni@SiO₂ core-shell structure has been the most studied in reforming, as highlighted below:

- Wang et al. reported the preparation of core-shell structured Ni@SiO₂ catalysts by an emulsion method.^[97] In comparison with supported Ni/SiO₂ counterpart, the sample showed higher and more stable performances in the dry reforming of CH₄. The amorphous silica layer inhibited the sintering of the Ni content and the preserved small Ni NPs minimized carbon deposit.
- Park et al. reported the synthesis of a highly-loaded Ni@SiO₂ core-shell type material (named “yolk-shell”) that consists of Ni cores inside mesoporous hollow silica shells.^[98] Despite a poor metallic dispersion, the catalyst exhibits a higher activity and an enhanced thermal stability in the steam reforming of CH₄ with respect to a supported Ni/MCF sample.

- Zhang et al. prepared a nanostructured Ni@SiO₂ core-shell catalyst in which micropores and mesopores were created in the originally amorphous silica shell.^[99] Surprisingly, in the dry reforming of CH₄ over 24 h at 750 °C, chemisorption measurements reveal that the initial Ni surface area was preserved while microscopic observations exhibit an increase in Ni particle size, suggesting that sintering occurs inside the shells that contains multiple NPs. In addition, the formation of amorphous carbon and a loss of porosity of the silica shells were observed.
- A core-shell Ni-Cu@SiO₂ was prepared by Wu et al.^[100] In the dry reforming of CH₄ at 700 °C, most of the core-shell nanostructures was preserved. The silica shells prevent sintering and preserve the monodispersion of the nanoalloy cores.
- Li et al. reported the synthesis of a Ni-yolk@Ni@SiO₂ nanocomposite that consists of a Ni@SiO₂ yolk-shell structure in which satellite Ni NPs surround the Ni yolk within the silica shell.^[101] The satellite Ni was formed upon reduction of Ni phyllosilicate species at the strongly-bonded Ni-silica interface and provided a high thermal stability to the material in dry reforming of CH₄. The authors showed that formation of this original structure was highly shell thickness-dependent.

2.2.3.5. Carbon formation

Carbon formation is commonly described as the principal cause of deactivation during HC reforming reactions. Ni-based catalysts are particularly prone to carbon deposition that leads to deactivation. The potential for coking is the highest when the S/C ratio in the feed is low. The stoichiometry of the CO₂ reforming reaction leads to a low H/C ratio which favors carbon formation. The general propensity for coke formation of HC species is aromatic > olefinic > paraffinic.^[10]

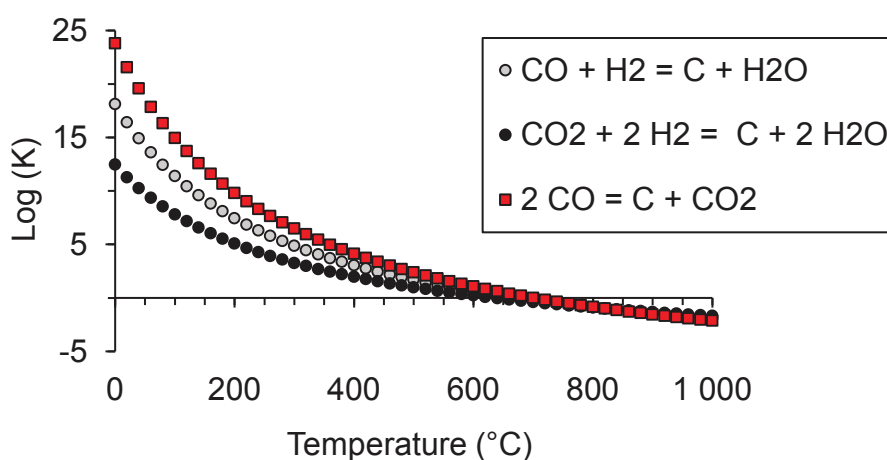


Figure 1.19 Equilibrium constants for the carbon formation equilibrated reactions using HSC software.

Carbon formation can occur through three main different reactions: water gas (Equations 10 and 11), Boudouard (Equation 12) and HC cracking (Equations 7 and 9). The two former reactions are thermodynamically favored when $T < 700\text{ °C}$ (Figure 1.19). The thermodynamic of cracking reactions depends on the nature of the HC (Figure 1.12). Because of the endothermic nature of the reforming reactions, high catalyst activity leads to a lower temperature at the reaction site, resulting in a higher risk for carbon formation. Three types of carbon can be observed in a reforming unit: pyrolytic, encapsulated and whisker carbon as presented in Table 1.3 and illustrated in Figure 1.20.

Table 1.3 Different routes for carbon formation in HC reforming.^[8,52]

Type of carbon	Pyrolytic	Encapsulated "gum"	Whisker
Formation process	Thermal cracking of HCs: deposition of C-precursors on catalysts	Slow polymerization of CH_x radicals on Ni surface into an encapsulating film or deposit into few concentric layers	Diffusion of C through Ni particles: nucleation and whisker growth from the support interface with Ni crystal at top
Temperature of formation	> 600 °C	< 500 °C	> 450 °C
Nature	Coke (amorphous)	Graphite (crystalline)	Graphite (crystalline)
Parameters	High temperatures Low S/C ratio High pressures Acidity of catalyst Low catalytic activity	Low temperatures Low S/C ratio Low H/C ratio Aromatics in feed	High temperatures Low S/C ratio Weak H_2O adsorption
Consequences	Encapsulation of catalyst particles: deactivation and increase of pressure drop	Progressive deactivation	No deactivation of Ni surface: breakdown of catalyst and increase of pressure drop

As observed in Table 1.3, carbon formation depends on many parameters. Bengaard et al. studied thoroughly the formation of graphite during methane SR over Ni catalysts.^[59] They arrived at the generally accepted conclusion that the nucleation of graphite is extremely structure sensitive. Step sites are much more reactive than close-packed facets. When the metal particles are very small, the step edges become too small for graphite nucleation to proceed. Therefore, the smaller the particle, the lower the ability to grow graphite.

Carbon formation can be reduced through proper design of the catalyst. Addition of promoters is used to inhibit carbon formation. Adding small amounts of an alkali metal to the catalyst introduces basicity into the support, which lowers its acidic nature and thus limits carbon formation by HC cracking. However, Benggaard et al. concluded that the major carbon-preventing effect of potassium is to adsorb and block the Ni sites (-K-O-K-O- rows are formed along these sites) and hence remove the sites for graphite nucleation.^[59] However, this complete step coverage by K-based rows strongly decreases the activity in HC reforming. In comparison, Au and S promotion of Ni catalysts is more efficient as these adatoms spread out along the steps, blocking a sufficient number of sites to prevent graphite nucleation. Alloying Ni by addition of a noble metal is also a solution to lower carbon formation.^[60,61] Guo et al. explained that the presence of Rh in a Ni-Rh surface alloy increases the energy barriers of the C-C bond formation and the C diffusion through the particle.^[102]

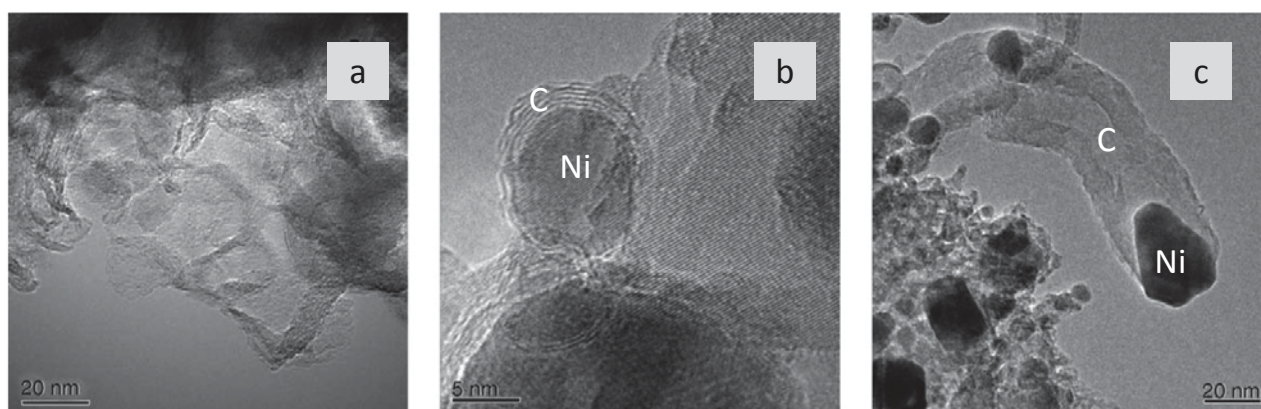
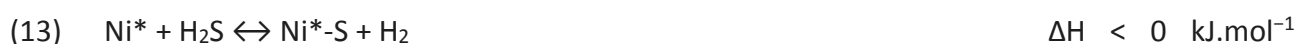


Figure 1.20 TEM images of pyrolytic (a), encapsulating (b) and whisker (c) carbon on a Ni-based catalyst.^[52]

In the reforming of a producer gas generated from a circulating fluidized bed gasifier, Albertazzi et al. studied the formation of carbon on a commercial Ni/MgAl₂O₄.^[103] From temperature programmed oxidation (TPO) measurements of the post mortem samples, they detected the formation of CO₂ at two different temperatures. The first peak, centred at 350 °C, was assigned to amorphous pyrolytic carbon. The second one, centred at 650 °C and showing a higher intensity, was attributed to graphite formation from tars. This assumption was verified by Josuinkas et al. when analysing used Ni-based catalysts after steam reforming of aromatic model compounds (naphthalene, toluene, benzene). Only one peak at temperatures of 600-630 °C was measured and ascribed to the oxidation of carbon whiskers.^[104] However, they noticed that the nature of the carbon formed was related to the nature of aromatic compound. The formation of whiskers as the main type of carbon deposit in the steam reforming of toluene was confirmed by Kiennemann and co-workers from TPO and TEM analyses.^[105]

2.2.3.6. Sulfur poisoning

Catalyst poisons act by blocking active surface sites. Among the various existing contaminants (Si, P, As, Pb, Li, Na, K), sulfur is the most severe poison for group VIII metal reforming catalysts.^[72] Ni is the most vulnerable metal of this group to sulfur poisoning. For this reason, sulfur must be removed down to a low level from the feed before entering the reformer. Inside the reformer, remaining S-containing compounds are converted into H₂S, which chemisorbs strongly and dissociatively on the Ni surface atom (Ni*) through the reaction:



The heat of adsorption of sulfur is negative and decreases with decreasing S coverage.^[106] At zero coverage an enthalpy of adsorption of - 250 kJ mol⁻¹ was estimated by extrapolation, while at high coverage an enthalpy below - 125 kJ mol⁻¹ is expected. At saturation, the S/Ni surface stoichiometry is approximately 0.5. This means that even at high S coverage, surface Ni-S bonds are more stable than bulk Ni-S bonds, as equilibrium data indicate an enthalpy of - 75 kJ mol⁻¹ for the formation of bulk Ni₃S₂. Hence, formation of nickel sulfide is only observed at much higher S levels than normally experienced in a reformer. The surface coverage of sulfur (θ_s) on Ni depends on the temperature and the partial pressures of H₂S and H₂. It can be estimated in certain conditions as follows:^[73]

$$(14) \quad \theta_s = 1.45 + (4.17 \cdot \ln(P_{\text{H}_2\text{S}}/P_{\text{H}_2}) - 9.53) \cdot T \cdot 10^{-5}$$

Sulfur has a strong impact on the reaction rate (r) in reforming. It was shown that the intrinsic activity of a catalyst decreases rapidly with the coverage of unpoisoned sites in the third power as expressed below (r_0 is the activity when $\theta_s = 0$):^[8]

$$(15) \quad r(\theta_s) = r_0 \cdot (1 - \theta_s)^3$$

The effect of S on the reaction rate can be lowered by increasing the temperature, by increasing the H₂ pressure or by modifying the physicochemical properties of the catalyst. Modification of the active metal to create electron-deficient metallic sites lowers the strength of the M*-S bond. According to Arcoya et al., the sulfur resistance of group VIII metals is related to the surface electronic state of the metal and increases in the following order:^[107]



Hence Rh is likely more resistant to S poisoning than Ni, although some theoretical studies state that Rh is more S-sensitive than Ni due to its higher binding energy.^[108] In the steam reforming of heavy HCs, Lakhapatri et al. evaluated Ni and Rh-based catalysts supported on γ -Al₂O₃ using 1000 ppmv of thiophene in the feed stream.^[109] Catalysts were fairly stable in the absence of thiophene, but the addition of sulfur led to significant deactivation. No bulk sulfides were observed and only surface adsorption was seen. In addition, the authors observed that Rh/Ni mixed metal catalysts resulted in the formation of Rh-Ni alloy species that were shown to better resist S adsorption to some extent.^[110] Tomishige et al. studied the partial oxidation of tar obtained from the gasification of a woody feedstock in a fluidized bed reactor using a 20wt.%Ni commercial steam reforming catalyst and a 1wt.%Rh/CeO₂/SiO₂ catalyst with and without H₂S in the feed stream.^[111] Both catalysts showed a decrease in the rate of bio-syngas formation upon the addition of H₂S, although the Rh catalyst was more stable than the Ni catalyst, which severely deactivated. The synergistic effect of alloying Ni with Rh in lowering S deactivation was confirmed by Xie et al. who studied the steam reforming of heavy HCs on a 10wt.%Ni-2wt.%Rh/CeO₂/SiO₂ catalyst.^[112]

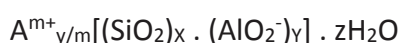
In the reforming of a simulated producer gas containing 100 ppmv of H₂S, Simell and co-workers reported the activity of various metal-supported catalysts.^[41] They observed that a 0.5 wt.% Rh/ZrO₂ was significantly more active in the conversion of ethylene and tar model compounds (naphthalene and toluene) than a 8 wt.% Ni/ZrO₂ catalyst at 800 °C. At 900 °C, similar observations were made and both Rh and Ni were the most active metals among Ir, Pd, Ru and Pt. More surprising, all metals showed a similar activity in methane reforming, being below 10% conversion. Recently, Steele et al. observed that both Ni and Rh-based catalysts were capable of giving significant tar conversions in the presence of 100 ppmv H₂S at temperatures of 700-900 °C though little CH₄ conversion was observed.^[113] Both toluene and naphthalene compounds were converted to similar extents and the only HC product observed was benzene. Rh based catalysts at significantly lower metal loading gave superior activity to the high surface area Ni catalysts. Furthermore, the S- deactivation was found to be fully reversible and was attributed to a site-blocking mechanism.

2.3. Zeolites

Zeolites are crystalline microporous aluminosilicates of alkaline or alkaline earth metals. More than 200 different structures exist which are either natural or synthetic. These solids are widely used in ion-exchange, adsorption, separation and many catalytic processes. Since the industrial application of faujasites in fluid catalytic cracking of heavy petroleum distillates in 1962, zeolites have been one of the most widely used catalysts in industry.^[114–116]

2.3.1. Introduction to zeolites

The elementary building units of zeolites are $[\text{SiO}_4]^{4-}$ and $[\text{AlO}_4]^{5-}$ tetrahedra. Adjacent tetrahedra are linked at their corners via a common oxygen atom, and this results in an inorganic macromolecule with a structurally distinct three-dimensional framework. The net formulae of the tetrahedra are SiO_2 and AlO_2^- , hence one negative charge resides at each tetrahedron in the framework which has aluminium in its centre. The framework of a zeolite contains channels, channel intersections and/or cages with dimensions from ca. 0.2 to 1 nm (Figure 1.21 Structure of the MFI framework including its micropore system and channel dimension Figure 1.21). Inside these voids, water molecules and small cations (generally Na, K, Ca or Mg) are present to compensate the negative framework charge, if any. The chemical composition of a zeolite can hence be represented by a formula as follows (A is a cation with the charge m, (x+y) is the number of tetrahedra per crystallographic unit cell):



X/Y represents the framework silicon/aluminum (Si/Al) ratio. This ratio determines the exchange capacity of the zeolite and its acidic character. Lowenstein's rule states that two contiguous tetrahedra containing aluminum on tetrahedral positions are forbidden, thus the Si/Al ratio ranges from 1 to infinite. Zeolites are classified by the Structure Commission of the International Zeolite Association (IZA) assigning a three-letter code to each framework topology irrespective of composition.^[117] MFI (for Mobil Five) is an illustrative code of the framework structure of both ZSM-5 (Si/Al \geq 1) and Silicalite-1 zeolites (all-silica analogue, Si/Al = ∞). The MFI framework is built from the pentasil unit (Figure 1.21). These units are connected to form two sets of 10-ring channels that intersect perpendicularly: straight channels (0.56 x 0.53 nm opening) and sinusoidal channels (0.55 x 0.51 nm opening). These channels can host catalytic active sites which are either acidic or metallic.

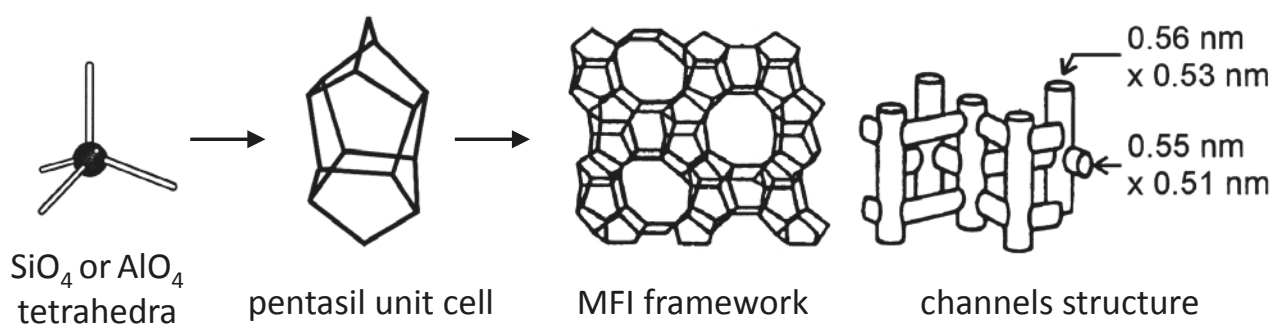


Figure 1.21 Structure of the MFI framework including its micropore system and channel dimension.^[116]

2.3.2. Structural modifications

The presence of active sites confined in well-defined micropores may expose zeolites to mass transfer limitations that lower the catalytic rates. This phenomena restricts the catalyst utilization to a certain depth under the crystal surface. The percentage of zeolite effectively used in a reaction can be represented by the effectiveness factor (η) which increases when the Thiele modulus value (ϕ) decreases. When $\phi \approx 0$, zeolite is fully used without diffusion limitations: the observed reaction rate is equal to the intrinsic reaction rate. From the equation of the Thiele modulus, ϕ can be lowered by shortening the characteristic diffusion length (L)(Figure 1.22). Hence, improving mass transfer properties can be achieved by the synthesis of small crystals or by developing hierarchical systems which are zeolite crystals with multiple levels of porosity. Such solids can be obtained either by direct synthesis of small size zeolites or by post-synthesis treatments such as dealumination or desilication. Nanosized zeolites can be obtained by controlling crystallization parameters or acting on the nature of the template, which can restrict the crystal growth or affect the crystallization in a specific direction (ie. templating approach). Post-synthesis treatments rely on the preferential extraction of one of the constituents from the zeolite framework (ie. “top-down” approach).^[118–124]

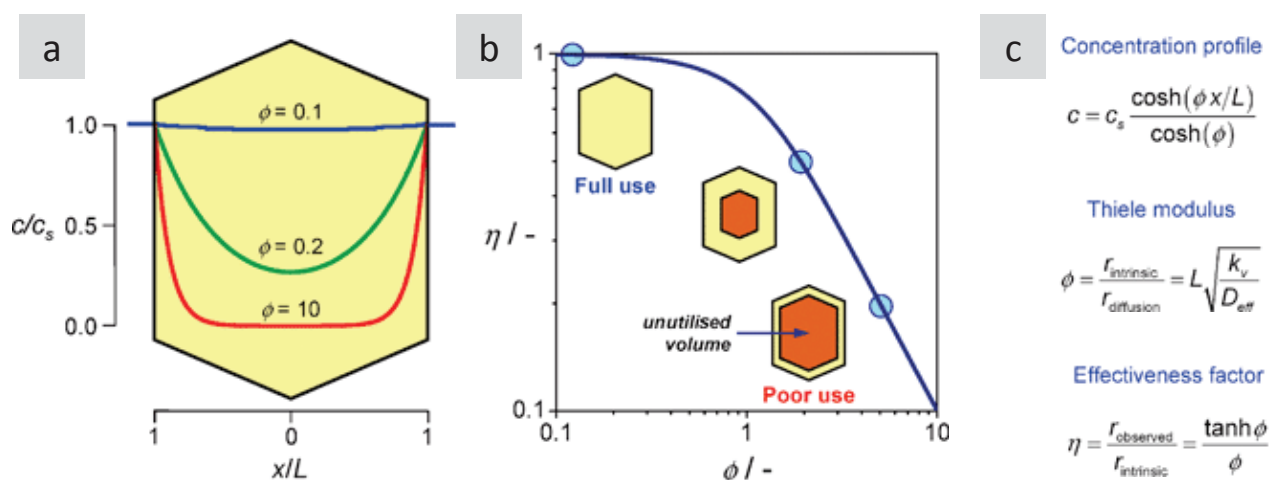


Figure 1.22 Concentration profile of a reactant across a zeolite crystal at different values of Thiele modulus (a), dependence of the effectiveness factor on the Thiele modulus (b) and related equations (c).^[119]

2.3.2.1. Dealumination

Dealumination is performed either by acid treatment or high temperature steaming (above 500 °C) to introduce mesopores in zeolites.^[125] During the treatment, part of aluminum species is removed from framework positions, with formation of silanol (Si-OH bond) nests. In high temperature steaming, those nests are generally refilled by Si species resulting from a partial dissolution of the

framework by water vapor at high temperature. However, breaking Al-O-Si bonds also leads to changes in zeolite acidic properties, such as strength, concentration and distribution of acid sites. Moreover, formation of acid sites (mainly Lewis acid sites) resulting from extra-framework aluminum also needs to be taken into account. In contrast, desilication is another strategy to create mesopores as well as to preserve Brønsted acid sites.

2.3.2.2. Desilication

Desilication is achieved by selective removal of silicon from the zeolite framework under alkaline pH conditions. The hydrolysis of Si-O-Si bonds results in a partial dissolution of the zeolite framework with formation of mesopores, while silicon atoms in Al-O-Si bonds are stabilized by framework aluminum species. Thus framework Al plays an important role in desilication since it stabilizes the zeolite structure and prevents a complete dissolution. Moreover, the differences in solubility between silica-rich and aluminum-rich parts have been widely used to create materials with special architectures such as hollow crystals. Groen et al. studied the desilication ZSM-5 crystals with an Al gradient (Al-rich surface and Si-rich core). The preferential desilication of the Si-rich core produces intra-crystalline cavities without changing the original microporosity and is function of the Si/Al ratio. The porosity is confirmed by a hysteresis in the N₂ physisorption isotherm with a closure point at $P/P^{\circ} \approx 0.42$, characteristic of cavities connected to the outer surface by the zeolite micropores. [126–130] Other studies have reported the benefits of desilication on the catalytic performances.

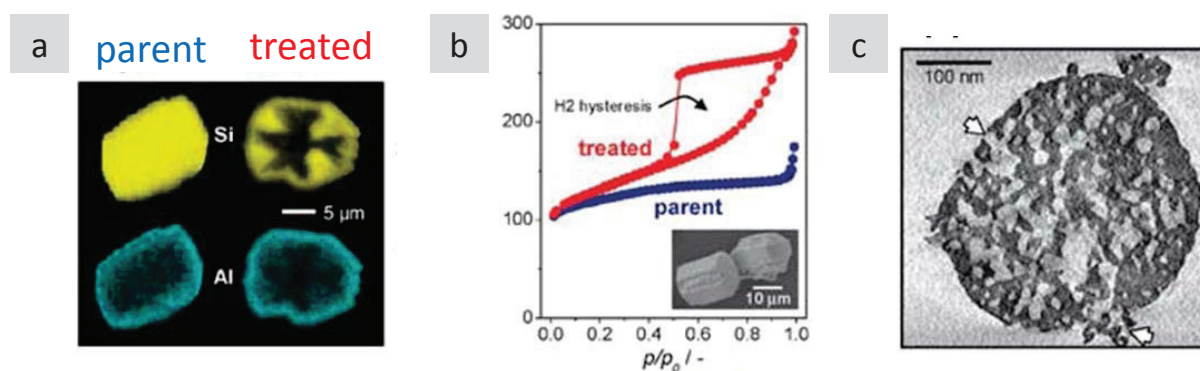


Figure 1.23 SEM-EDX images of parent and alkaline treated ZSM-5 crystals (a), N₂ physisorption isotherms of corresponding crystals (b) and TEM images of alkaline treated small ZSM-5 (c). [130]

Desilication has also been performed on all-silica zeolites such as silicalite-1. [131] Weidenthaler et al. have reported the synthesis of Au particles encapsulated in mesoporous silicalite-1 materials obtained by a desilication-reassembly process. Encapsulated Au particles showed a higher thermal stability, activity and selectivity in the gas-phase oxidation of ethanol than the supported analogue.

2.3.3. Metal particles encapsulation in zeolite catalysts

As mentioned in part 2.2.3.4, sintering can be hampered by encapsulation of particles in core shell or yolk shell nanostructures. However, in the presented examples, shells are mesoporous which are useless in terms of molecular sieving at the sub-nanometer scale. Selectivity of the shell at molecular level can be achieved using metallic particles embedded in or covered by zeolite. Particles are only accessible through the zeolite micropore system while zeolite themselves protect the nanoparticles against sintering. Such catalysts, which combine sinter-resistant nanoparticles with a shape selective zeolite, may find applications in selective catalysis and material science.

2.3.3.1. Encapsulation by direct synthesis

Metal particles such as Pt, Pd, Rh, Ir, Re, and Ag can be encapsulated in zeolites by direct addition of the corresponding metal precursor in the synthesis gel followed by reduction.^[132,133] This method was used by Iglesia et al. to synthesize particles of different metals in small pore zeolites, such as GIS and ANA. Particles were efficiently protected by the zeolite from bulk poisoning molecules such as thiophene and toluene in the hydrogenation of ethane over these catalysts.

In a related process, Au particles encapsulated in silicalite-1 have been synthesized by crystallizing the zeolite in the presence of gold colloids (Figure 1.24).^[134] Au nanoparticles with a diameter around 2 nm are thermally stable upon calcination at 550 °C for 3 hours. Compared to a standard Au/TiO₂ supported catalyst, Au@silicalite-1 shows a high reactant size selectivity and sintering resistance in the oxidation of substituted aromatics in methanol. However, a significant proportion of Au particles are located on the outer surface of the crystals and the particle size distribution is broad with a significant portion of particles larger than 10nm.

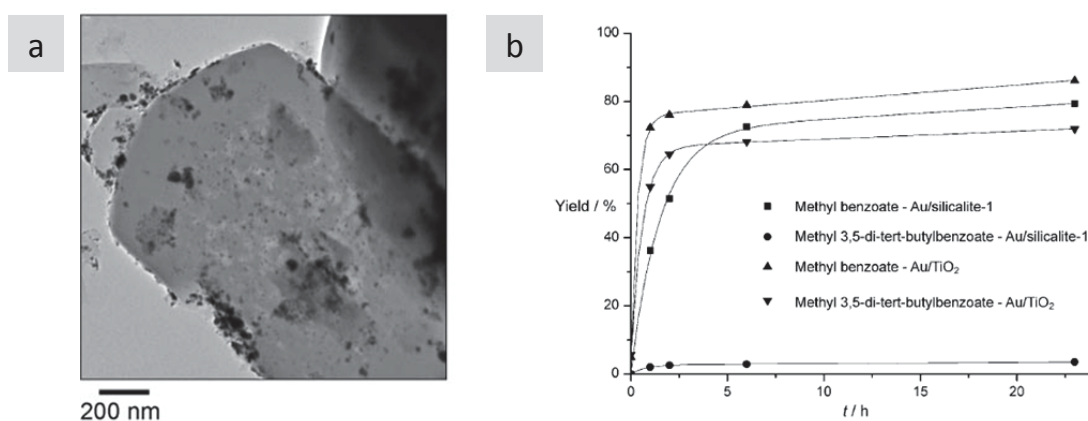


Figure 1.24 TEM image of Au@silicalite-1 materials (a) and activity in methanol production (b, circle).^[134]

2.3.3.2. Encapsulation by post synthesis

Post synthesis incorporation of metals and/or oxides in zeolites is usually achieved by wet impregnation or ion exchange methods, followed by drying and reduction steps. Wet impregnation consists in filling the pores of the zeolites with a solution containing a metal precursor.^[135] When the volume of solution is equal or less than the total pore volume of the support, the technique is referred to as incipient wetness impregnation (IWI). In the ion exchange process, cations of the zeolite are replaced by metallic ions (for example Ni^{2+}). However, this method cannot be performed on neutral zeolites such as silicalite-1.

Au/Y zeolites prepared by wet impregnation followed by a reduction process show that Au particles are encapsulated in the cages of the zeolite with a diameter around 1 nm. This catalyst showed high stability and efficiency in the catalytic oxidation of 5-hydroxymethyl-2-furfural (HMF).^[136]

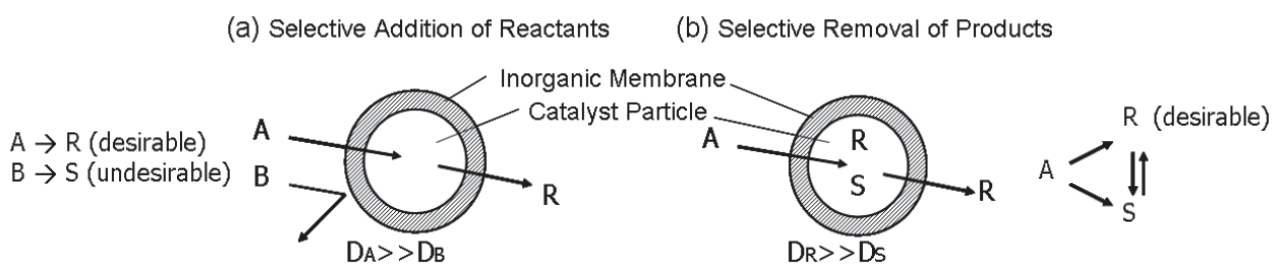


Figure 1.25 Principle of operation of a catalyst coated with a perm-selective hollow zeolite membrane^[137]

Another option to achieve the combination of zeolite properties and sinter-stable particles is to form hollow zeolite structures by metal nanoparticle encapsulation inside a zeolite layer. The reactant and product selectivity of metal catalysts is controlled by the zeolite shell that acts as a selective membrane by molecular sieving mechanisms (Figure 1.25).^[123,124,138]

Tang et al. developed the synthesis of hollow silicalite-1 and Beta in the presence of hard templates such as mesoporous silica or polystyrene beads.^[139–142] Small zeolite particles are gathered around the bead to form a compact zeolite shell, and then templates are removed either by dissolution or by calcination. Pt and Ag particles can also be encapsulated into these shells by using template-supported nanoparticles and these solids showed much better selectivity and stability than supported catalysts in liquid oxidation reactions.^[142] Hollow zeolite shells obtained by this method are polycrystalline with a thickness approximately 200 nm, which composed from aggregation of small zeolite particles. Shells are thick enough to still show diffusion limitations and they are probably less efficient as membrane as compared to single crystals.

2.3.4. Pioneered achievements on hollow zeolites at IRCELYON

Tuel et al. have reported the preparation of hollow MFI-type zeolites (pore size ≈ 0.55 nm) with wall thickness of approximately 20 to 30 nm by dissolution/recrystallization of bulk crystals in the presence of TPAOH (Figure 1.26).^[143–145] By contrast to a standard dissolution using NaOH, dissolved species could recrystallize on the outer surface of the crystals, thus leading to uniform structures with well-defined edges. As a consequence, no zeolite is lost during the process (dissolved species could recrystallize) and the overall composition is unchanged. It is interesting to note that the mechanism of dissolution/recrystallization is intrinsically different from a conventional desilication: the method does not necessitate the presence of Al in the crystals and dissolution preferentially occurs in defect-rich areas, typically the center of the crystals.

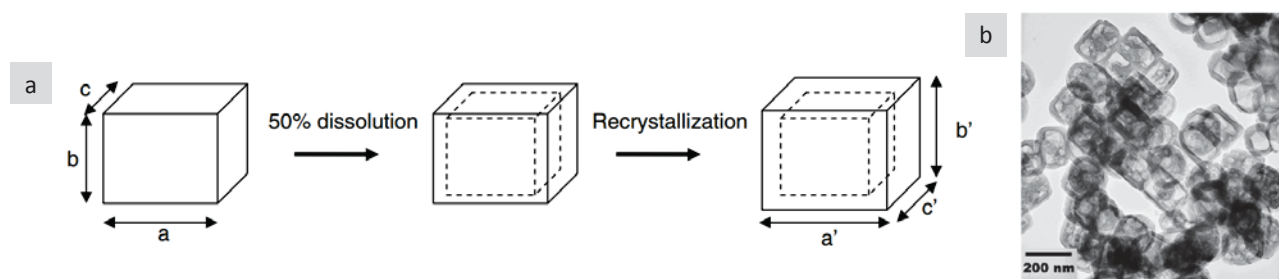


Figure 1.26 Scheme of the dissolution/recrystallization process (a) and TEM image (b) of hollow zeolites.

More recently, Li et al. have succeeded in the preparation of noble (Au, Pt, Pd and Ag) metal particles encapsulated in these hollow “nanoboxes”. The embedding was achieved by impregnating original MFI zeolite crystals with the metallic precursors prior to the TPAOH treatment and subsequent thermal treatments. Each hollow shell obtained contains a unique metallic particle and a desired particle size (2–15 nm) can be achieved by adjusting the concentration of metal precursor used for impregnation (Figure 1.27).^[146–148] Moreover, the method has been extended to nanoalloys such as PdPt, PtAg, PdAg, and AuAg by impregnating with mixture of metallic precursors.^[149]

The microporous shells can totally prevent particle sintering at high temperature both in reductive (750 °C in H₂) and oxidative atmospheres, even under more harsh conditions in the presence of H₂O (500 °C in O₂ + H₂O). Concerning the application in catalytic reactions, Pt particles in hollow materials show outstanding properties in terms of size selectivity in the hydrogenation of substituted aromatics. Toluene (0.61 nm) can easily reach the embedded particle whereas mesitylene (0.87 nm) cannot. Moreover, in the case of toluene, the catalytic activity is not altered by mass transport through the thin microporous shell. Pt particles in silicalite-1 are also able to selectively oxidize CO in the presence of propylene, a poison for Pt-supported catalysts. The activity can be attributed to the presence of the zeolite membrane which reduces the access of the alkenes to nanoparticles.

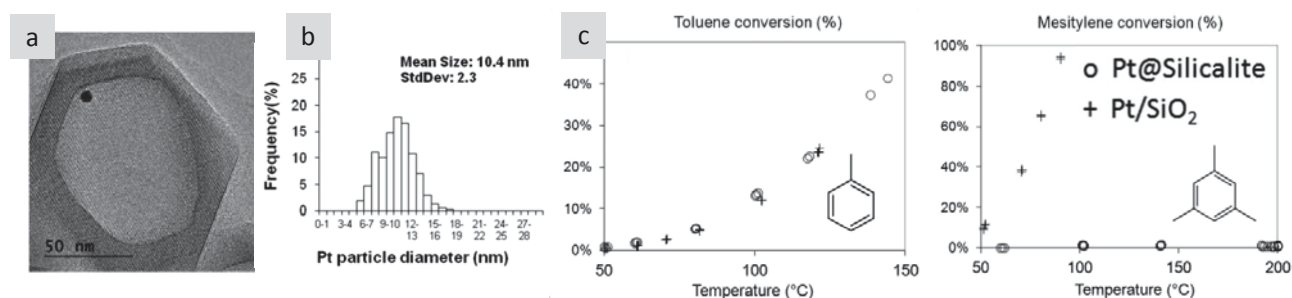


Figure 1.27 HRTEM image (a), particle size distribution after reduction in H₂ at 750 °C (b) and activity in toluene and mesitylene hydrogenation (c).^[147]

3. Aim of this PhD work

Based on the work previously reported by Li et al., this PhD work deals with the reforming of a simulated producer gas over hollow zeolite catalysts in which metal nanoparticles are encapsulated in single crystal shells. The advanced structure of these composite materials is expected to:

- Highly disperse particles and be highly active in the reforming of small size HCs
- Limit sintering of metal nanoparticles under high temperatures and high steam content
- Prevent carbon deposition from tar decomposition by size exclusion of large HCs
- Provide enhanced resistance to sulfur and carbon poisoning by the synergic effect of nanoalloy

At the beginning of this work, nickel has been selected as the metal of interest for the preparation of yolk-shell materials. For the composition of the nanoshell, silicalite-1 was preferred to ZSM-5 for two reasons:

- The acidic properties of ZSM-5 would favor carbon deposition
- The high temperatures and high steam content of the reaction would induce ZSM-5 steaming

Different strategies have also been examined to improve the characteristics of the hollow zeolite and the encapsulation method. In addition to nickel, we have tried to extend the synthesis to rhodium. The final aim was to synthesize for the first time a nanoalloy constituted of both a transition metal (Ni) and a noble metal (Rh) encapsulated inside a hollow silicalite-1 membrane.

In the frame of the FASTCARD project, supported mono and bi-metallic catalysts prepared by WP1 partners were also evaluated in the reforming of producer gas. A screening test was carried out to unravel structural-activity relationships and emphasized the most promising formulations. This PhD thesis is consisted of six chapters:

- Chapter 1: State of the art which focuses on the challenges in the catalytic reforming of producer gas and the use of zeolite as protective carriers for metals.
- Chapter 2: Experimental part which includes the preparation methods of the various materials, characterization techniques and catalytic reactions.
- Chapter 3: Preparation of nickel nanoparticles in single hollow silicalite-1. Molecular sieving was demonstrated in the hydrogenation of light aromatics and in the methanation of CO in presence of pyrene. Extension to noble metal encapsulation for preparing nanoalloys was investigated.
- Chapter 4: Enhancement of the metallic dispersion of nickel by encapsulation in multi-hollow silicalite-1 single crystals. The impact of the encapsulation method on the molecular sieving, sintering resistance and catalytic activity were evaluated using model reactions.
- Chapter 5: Evaluation of the catalytic and structural stability of Ni@silicalite-1 in the reforming of a model producer gas using naphthalene and pyrene as tar model compounds.
- Chapter 6: Screening of supported Ni and Rh catalysts in the reforming of methane in presence of hydrogen sulfide and phenanthrene as representative sources of S and C related poisoning, respectively. Study of structure-activity features, apparent kinetics and transport phenomena.

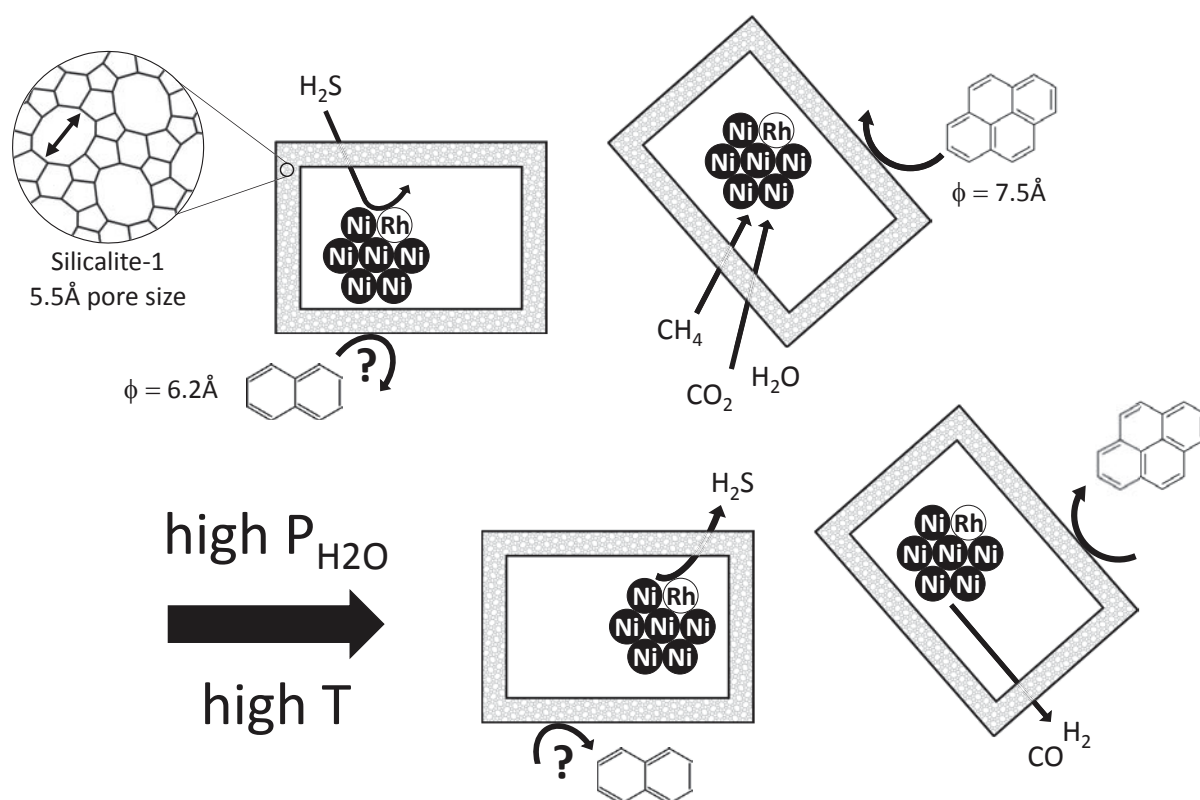


Figure 1.28 Schematic concept of the application of Ni@silicalite-1 in the reforming of producer gas.

Chapter 2 - Experimental

1. Material syntheses

The synthesis of metal nanoparticles encapsulated in silicalite-1 catalyst is a multi-step process as presented in Figure 2.1. In this experimental part, we will focus on the preparation of Ni-based samples loaded at 5% in weight. This synthesis protocol can be extended to different Ni loadings or to different metals. The materials are denoted 5%Ni@Sil-1, with “@” meaning “encapsulated in”, while the use of “/” means “supported on”. Silicalite-1 is denoted “Sil-1” for short.

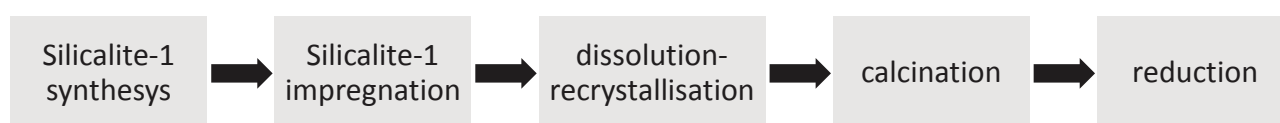


Figure 2.1 Diagram of the principal synthesis method for the preparation of Ni@silicalite-1 catalysts.

1.1. Silicalite-1 nanocrystals

Original silicalite-1 was synthesized from the crystallization of gels containing TEOS (tetraethyl orthosilicate, Aldrich, 98%), TPAOH (tetrapropylammonium hydroxide, 1 M solution) and H₂O. The 1 M solution of TPAOH is prepared from TPABr (tetrapropylammonium bromide, Alfa Aesar, 98%) solution by exchange with Ag₂O (Alfa Aesar, 99.99%) for 5 minutes in absence of light. Precipitated AgBr is then removed by filtration. The resulting gel (SiO₂-0.4TPAOH-35H₂O in composition) was stirred at room temperature overnight to fully hydrolyze the TEOS and then transferred into a Teflon-lined autoclave. After being heated at 170 °C under static conditions for 72 h, the autoclave was then cooled down to room temperature and the solid was centrifuged, washed with water until pH = 7 and dried overnight at 90 °C. The resulting solid was calcined for 12 h at 525 °C in air yielding plain single crystals of approximately 200 nm × 150 nm × 140 nm in size referred to as Sil-1.

1.2. Ni@silicalite-1 synthesis

1.2.1. Ni impregnation

Nickel impregnation into silicalite-1 was performed by the wet impregnation method. The bulk Sil-1 was first desorbed under vacuum at 300 C overnight, purged with argon and impregnated with an aqueous solution of Ni(NO₃)₂·6H₂O (99.999%, Sigma-Aldrich) with a volume (2 ml g_{Sil-1}⁻¹) higher than

the microporous volume ($0.2 \text{ ml g}_{\text{sil-1}}^{-1}$ according to Figure 3.15) to permit complete solvation of the precursor. The concentration of the solution is estimated by the theoretical Ni loading in the zeolite (426 mmol L^{-1} to reach a 5 wt% loading). The mixture was stirred at $50 \text{ }^\circ\text{C}$ until complete evaporation of water to reach the $\text{Ni}(\text{NO}_3)_2/\text{Sil-1}$. The resulting green powder was dried for 12 h at $90 \text{ }^\circ\text{C}$.

1.2.2. Encapsulation of Ni in a Single Hollow structure (Ni@Sil-1 SH)

The hollow structure was obtained by treating 1 gram of $\text{Ni}(\text{NO}_3)_2/\text{Sil-1}$ with an aqueous solution of TPAOH (7.5 ml; 0.55 M; pH = 13.6) in a Teflon-lined autoclave at $170 \text{ }^\circ\text{C}$ under rotating conditions for 24 h. During this process, the highly defective core of the silicalite-1 crystal is preferentially dissolved and silica species recrystallize on the outer surface in the presence of TPA^+ cations (Figure 2.2). The solution was then cooled down, recovered by centrifugation, washed with water until pH = 7, dried overnight at $90 \text{ }^\circ\text{C}$ and calcined in air at $450 \text{ }^\circ\text{C}$ for 6 h to obtain the 5%NiO@Sil-1 SH. Finally the solid was reduced at $750 \text{ }^\circ\text{C}$ under H_2 for 3 h with a heating rate of $2.5 \text{ }^\circ\text{C min}^{-1}$ to yield the 5%Ni@Sil-1 SH. A Ni-free single hollow silicalite-1 sample was prepared according to the same procedure without any Ni impregnation.

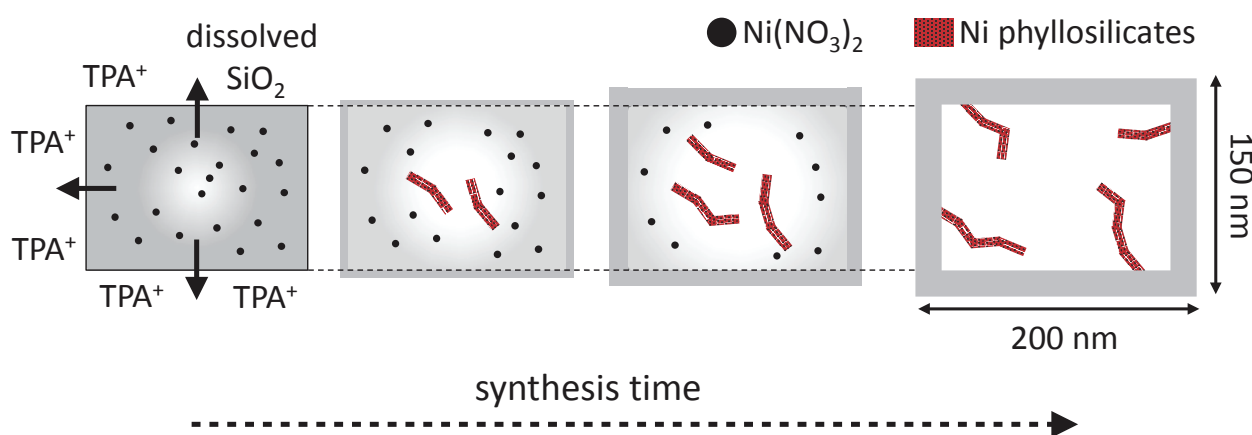


Figure 2.2 Dissolution-recrystallization process of the impregnated silicalite-1 in presence of TPAOH.

1.2.3. Encapsulation of Ni in a Multi Hollow structure (Ni@Sil-1 MH)

Similarly to the synthetic approach of the single hollow, the multi hollow structure was formed under hydrothermal conditions in presence of a phosphonium-containing structure-directing agent. Post-synthesis desilication was conducted by treating $\text{Ni}(\text{NO}_3)_2/\text{Sil-1}$ with a commercial TBPOH (tetrabutylphosphonium hydroxide, 40 wt.% in H_2O , Sigma-Aldrich) solution. 1 gram of powder was added to a solution made of 3.5 mL of the commercial TBPOH mixed with 1 mL of H_2O (4.5 ml; 1.125 M; pH = 13.7). The mixture was then transferred into a Teflon-lined autoclave and heated at $115 \text{ }^\circ\text{C}$

under rotating conditions for 96 h. The solution was then cooled down, washed with water until pH = 7 and dried overnight at 90 °C. Finally the powder was successively calcined in air at 450 °C for 6 h to obtain the 5%NiO@Sil-1 MH and reduced at 750 °C under H₂ for 3 h with a heating rate of 2.5 °C min⁻¹ to yield the 5%Ni@Sil-1 MH. A Ni-free multi hollow silicalite-1 sample was prepared according to the same procedure without any Ni impregnation.

1.2.4. Citric acid treatment

Both single and multi-hollow samples were treated similarly to selectively remove the nickel particles that were not entrapped during the encapsulation procedure. 0.5 gram of NiO@silicalite-1 was added to 50 mL of a 0.5 mol/L aqueous solution of citric acid (≥ 99.0%, Sigma-Aldrich). The mixture was stirred vigorously at 80 °C for 2 h. The solution was then centrifuged and washed with water until pH = 7 and dried overnight at 90 °C. Finally the solid was reduced at 750 °C under H₂ for 2 h to yield samples referred to as CitAc Ni@Sil-1 SH and MH. Prior to nitrogen physisorption measurements, these samples were further calcined in air at 550 °C for 6 h to remove carbon traces due to the thermal decomposition of the residual citrates.

1.2.5. Preparation of a supported Ni/silicalite-1 catalyst

A catalyst named 5%Ni/Sil-1 was produced by direct calcination and reduction of Ni(NO₃)₂/Sil-1. The calcination is carried out in air at 450 °C for 6 h. The reduction is performed at 750 °C under H₂ for 3 h with a heating rate of 2.5 °C min⁻¹. This catalyst is used as a supported reference material for catalytic tests in which nickel particles are not encapsulated inside a hollow silicalite-1 shell.

2. Characterization techniques

2.1. Elementary analysis (ICP-OES)

Elementary analysis is carried out by Inductively-Coupled Plasma Optical Emission Spectroscopy (HORIBA Jobin Yvon Activa ICP-OES). The reduced samples are first dissolved in an acid solution (mixture of HF, H₂SO₄ and HNO₃ solutions for Ni catalysts; mixture of HF, H₂SO₄ and aqua regia solutions for noble metal catalysts) which is then introduced into the spectrometer. Excited atoms and ions produced from each element emit a characteristic radiation whose intensity is measured. This intensity is then correlated to the amount of each element. ICP technique is used to detect the metal contents in both hollow zeolite and supported materials.

2.2. Powder X-Ray Diffraction (XRD)

X-ray diffraction (XRD) patterns of the solid are recorded on a diffractometer (D8 advance A25 from Bruker) using $\text{CuK}\alpha_1$ radiation at $\lambda = 1.5406 \text{ \AA}$ and equipped with a Ni filter and 1-D fast multistrip detector (LynxEye, 192 channels on 2.95°). Diffractograms are collected at room temperature under air, from 4 to 90° (2θ) with 0.02° step and 0.5s per step for a total acquisition time of 32 min . This technique is used for crystallinity calculation, phase identification and metal particle size estimation.

Relative loss in crystallinity of silicalite-1-based catalysts during reforming at high temperatures was calculated following a standard method.^[150] The crystallinity is calculated as the ratio of intensity of a portion of the XRD pattern of the sample to intensity of the corresponding portion of the pattern of the reference sample (ie. a fully crystalline plain silicalite-1 sample).

$$(16) \quad \% \text{Crystallinity}_{\text{sample}} = (\text{Area}_{\text{sample } 2\theta=22.5-25^\circ} / \text{Area}_{\text{reference } 2\theta=22.5-25^\circ}) \times 100$$

$$(17) \quad \text{Loss in crystallinity} = (\% \text{Crystallinity}_{\text{fresh sample}} - \% \text{Crystallinity}_{\text{used sample}}) / \% \text{Crystallinity}_{\text{fresh sample}}$$

When possible (i.e. in case of high metal content, large particle size and/or supported catalyst), the metallic crystallite sizes were estimated from peak half-widths using the Scherrer formula with corrections for instrumental line broadening:

$$(18) \quad d = (0.89 \lambda) / (\beta \cos \theta) * (180) / \pi$$

where d is the average size of the crystalline grains (\AA), λ is the wavelength of incident x-ray (\AA), β is the full width at half maximum of the diffraction peak (degrees) and θ is the Bragg angle (degrees).

2.3. Nitrogen adsorption/desorption

N_2 physisorption isotherms are measured at 77 K on a BELSORP-mini (BEL Japan) sorption apparatus. Approximately 100 mg of sample is degassed in a cell at 300°C for 3 hours prior to adsorption. Apparent surface area is calculated using the BET method in the relative pressure range of $0-0.12\text{q}$. The t-plot analysis is not considered here, in view of the debate on the validity of the t-plot method to assess microporosity in hierarchical materials.^[151] The microporous volume is determined as the volume of N_2 adsorbed when the slope of the adsorption branch becomes lower than $10^3 \text{ cm}^3 \text{ g}^{-1}$.

From isotherms of hollow zeolites, the hysteresis loop with an abrupt closure at P/P^0 around 0.42 characterizes internal porosity connected to outer surface via entrances smaller than 4nm . Hence,

the presence of a hysteresis loop is generally taken as an indication of the presence of cavities in the crystals. The difference in N_2 uptake between the adsorption and the desorption branches of the isotherms beyond this closure point (typically at $P/P^0 = 0.5$) is an indication of the volume of N_2 entrapped inside the hollow zeolite. The total pore volume is estimated from the N_2 uptake at $P/P^0 = 0.9$ on the desorption branch, not to take into account the inter-particle mesoporosity which can be significant in the case of small crystals. Under these conditions, the total pore volume value corresponds to the microporous volume and the entrapped meso/macroporous volume of the zeolite.

2.4. Transmission Electronic Microscopy (TEM)

TEM images of metal nanoparticles in hollow zeolites and reference catalysts are obtained on a JEOL 2010 LaB₆ microscope operating at 200 kV. The resolution of electronic microscopy is much higher than the optical ones due to the very short De Broglie wavelength of electrons (resolution of 0.19 nm in Jeol 2010 microscopy).

2.4.1. Sample preparation for TEM observation

Sample preparation involves grinding of a catalyst in ethanol in a mortar and depositing a drop of the suspension on a Cu TEM holey carbon grid. This procedure allows for a very thin layer of the sample to deposit on the grid, avoiding overlap between catalyst particles and making it easier to image the metal particles in thin hollow zeolite or on the support.

2.4.2. TEM apparatus

A picture and scheme of the TEM equipment is showed in Figure 2.3. An electron beam is emitted by an electron gun containing an emission source (LaB₆ single crystal in JEOL 2010) connected to a high voltage source (200 Kv in JEOL 2010) under vacuum. The beam is converged by the different electromagnetic lenses of the TEM, typically the condenser, objective and projector lenses. The condenser lenses are responsible for primary beam formation and focus the beam on the sample. When passing through the sample, electrons are scattered due to collisions with the atoms in the sample and the beam is focused by the objective lenses to form the image of the sample. The projector lenses magnify the image and project them on an imaging device (a CCD camera in the case of JEOL 2010). The images are then recorded using Digital Micrograph software.

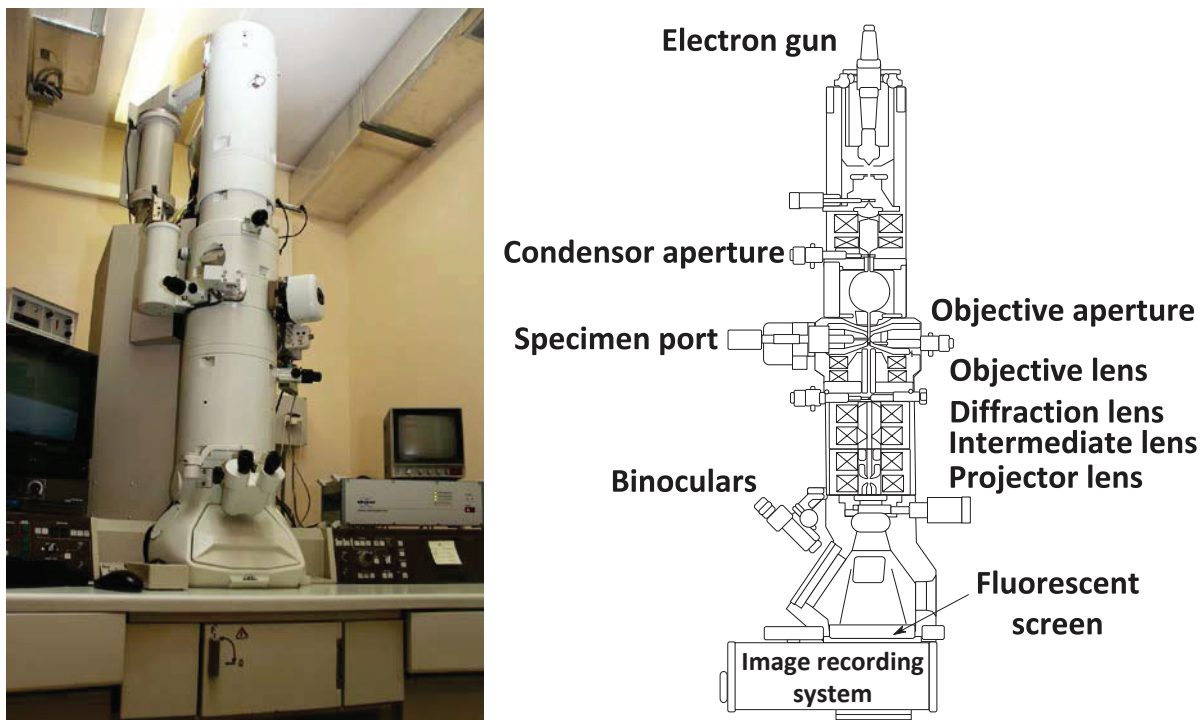


Figure 2.3 Picture (left) and scheme (right) of JEOL 2010 TEM apparatus.

The resolution of the TEM is determined by the speed and wavelength of the electrons. The magnification of the TEM is determined by the ratio of the distances between the specimen and the image plane of the objective lens; the contrast is due to the absorption of electrons by the solid depending on the thickness and composition of the material. JEOL 2010 can also operate under high resolution (HR-TEM) mode for direct imaging of the atomic structure of the sample. In this mode, the image formation is based on a different principle than conventional ones.

In this work, microscopy has been frequently used for the characterization of the particular structure of yolk-shell materials in the nanometer range. Moreover, TEM images have been used to evaluate particle size distribution, using Image J software. High resolution has been used for analyzing crystal structure of zeolite and nanoparticles at an atomic resolution scale.

2.4.3. Statistical study of nanoparticles based on TEM images

From TEM images, particle size distributions (for metal containing samples) are obtained counting 500 particles using Image J software.^[152] Each distribution is modeled using a normal law centered on the number weighted mean diameter d_{10} (defined as $d_{NW} = \sum n_i d_i / \sum n_i$ where n_i is the number of particles with diameter d_i) and broadened by the experimental standard deviation. The surface weighted (or Sauter) mean diameter d_{32} (defined as $d_{SW} = \sum n_i d_i^3 / \sum n_i d_i^2$) is estimated from the size distribution. d_{SW} represents the size of a particle that has the same surface/volume ratio as the

entire distribution. This mean diameter is inversely related to the specific surface area of metal and is of interest in applications where the surface area is the determining factor. The dispersion of metal nanoparticles is estimated from d_{sw} using a cuboctahedral model and a calculation method according to Van Hardeveld and Hartog.^[153] This model is used to evaluate the dispersion by considering the percentage of surface atoms among the overall atoms in each metal particle.

2.4.4. Energy Dispersive X-Ray Spectroscopy (EDX) measurement

JEOL 2010 microscope is equipped with an EDX Link ISIS analyzer (Oxford Instruments). It is possible to identify the elements present in the sample by performing EDX. When the electron beam passes through the sample, X-rays are generated and emitted from the sample. X-rays escaping from the sample can be detected and measured from the characteristic spectrum of each element. In addition, the number of photons emitted is proportional to the mass concentration of this species. Hence, EDX can provide precise constitution of a part of the sample at the nanometer scale.

2.4.5. Environmental Transmission Electron Microscopy (ETEM)

ETEM analysis was performed on a Titan G2 environmental microscope (FEI) operating between 80-300 kV. This apparatus allows measurements under gas pressure below 20 mbar and heating until 1000 °C by using individual evacuating vacuum stages in the microscope column. This allows for large pressure differences between the specimen area and electron source area, which requires high vacuum conditions for the electron beam. Here, the reduction of nickel phyllosilicates has been investigated on NiO@Sil-1 SH under a hydrogen pressure of 5.5 mbar up to 750 °C. The heating rate was adjusted manually. The oxidation states of nickel prior and after reduction were studied by *in situ* electron energy loss spectroscopy (EELS) under STEM conditions.

Scanning transmission electron microscopy (STEM) mode can be operated on Titan G2 using objective lenses above the sample to make the incident electron beam convergent. EELS and high angle annular dark field (HAADF) are possible on this mode. HAADF images show little or no diffraction effects, this imaging technique is particularly adapted to tomography reconstruction as it generates strong contrast between heavy metal particles and inorganic supports. In this work, single-tilt tomography has been performed on CitAc Ni@Sil-1 MH under vacuum with a continuous tilting series from +/- 72° and image acquisition each 2°.

2.5. Hydrogen chemisorption

Metal surface areas were measured by hydrogen chemisorption at 35 °C using an ASAP 2010 (Micromeritics). The sample holder was loaded with 0.1-0.5 g of catalyst. Prior to the measurement, the catalyst sample was reduced *in situ* in flowing hydrogen at 700 °C for 2 h. After reduction, the sample was evacuated for 2 h at 350 °C before cooling down to 35 °C. Two successive adsorption isotherms, separated by a second evacuation of 1 h at 35 °C, were then measured, according to the method described by Iglesia.^[56] The amount of hydrogen chemisorbed was obtained by correcting the total H₂ uptake (1st isotherm) with that of weakly adsorbed H₂ (2nd isotherm).

Ni (respectively Rh) surface areas (S_M) are calculated assuming a H/Ni_{surface} = 1 (resp. H/Rh_{surface} = 2) ratio and a Ni (resp. Rh) atom area of $6.51 \times 10^{-20} \text{ m}^2$ (resp. $7.58 \times 10^{-20} \text{ m}^2$).^[154–156] Specific surface areas are converted to mean particle diameters (d_{mean}) and metallic dispersions (D) assuming a spherical particle shape, resulting in:

$$(19) \quad d_{\text{mean}} = 60000 / (\rho * S_M)$$

$$(20) \quad D = 6 * ((v_M / a_M) / d_{\text{mean}}) * 100$$

where ρ is the metal mass density, a_M is the area occupied by a surface atom and v_M is the volume occupied by a bulk atom.

2.6. Thermogravimetric Analysis (TGA)

Thermogravimetric analyses were performed on a TGA/DSC MX1 microbalance (Mettler Toledo). Typically 5 mg of catalyst is placed in a Al₂O₃ sample holder and heated in pure O₂ atmosphere at 50 mL min⁻¹ up to 900 °C at a heating rate of 5 °C min⁻¹. This technique is used for quantifying the amount of carbon-based compounds deposited on the sample.

2.7. Temperature Programmed Reduction (TPR)

Temperature-programmed reduction was performed on a Setsys Evolution 1200 TGA apparatus (Setaram). Approximately 50 mg of sample was treated under a 50 mL min⁻¹ flow rate of 5% H₂/Ar up to 900 °C using a heating rate of 10 °C min⁻¹. The resulting water signal was recorded on a coupled Omnistar mass spectrometer (Pfeiffer). This technique is used for analyzing the temperatures of reduction of nickel phyllosilicates formed during the desilicating treatments.

2.8. Carbon-Hydrogen-Oxygen-Nitrogen-Sulfur (CHONS)

Sulfur content adsorbed at the surface of the used samples was quantified by a Flash 2000 CHONS analyzer (Thermo Scientific). A known mass of catalyst is placed in the combustion chamber under a O_2/He gas mixture flow and heated up to $1800\text{ }^\circ\text{C}$. Resulting combustion products are separated by gas chromatography where SO_2 is quantified by a thermal conductivity detector. Carbon deposits were not quantified as the corresponding CO_2 flows were below the detection limit of the TCD.

2.9. Diffuse Reflectance Infrared FT-IR Spectroscopy (DRIFTS)

Analyses of the catalyst surface were carried in a modified high temperature-low pressure DRIFTS reaction cell (Spectra-Tech) fitted with KBr windows. The reaction cell was modified to eliminate bed by-pass by inserting some PTFE tape between the ceramic crucible and the metallic base plate (Figure 2.4). The cell was placed in a collector assembly and fitted in a Tensor 27 FT-IR spectrometer (Bruker) equipped with a mercury cadmium telluride (MCT) detector cooled with liquid nitrogen. Approximately 5 mg of catalyst powder was deposited onto a silicon carbide (SiC) bed inside the crucible. Quartz wool plug was used to hold the sample bed. The infrared spectra were recorded with a resolution of 4 cm^{-1} . The spectra were monitored and analyzed using the OPUS software.

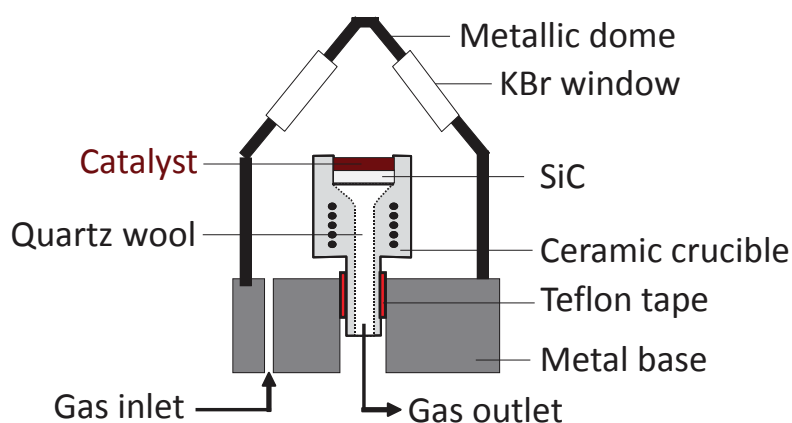


Figure 2.4 Scheme of the DRIFTS reaction cell.

Here, DRIFTS was used to estimate the relative amount of silanol hydroxyl groups on silicalite-1 at the different stages of the CitAc Ni@Sil-1 SH preparation. Samples were first degassed *in situ* at $300\text{ }^\circ\text{C}$ for 1 h in a 50 mL min^{-1} flow rate of He. Spectra in the O-H stretching area were subsequently recorded at $300\text{ }^\circ\text{C}$ by accumulating 256 scans. Spectra were corrected with the spectrum of pure H_2O and normalized using the area of the silica overtone band at 1875 cm^{-1} . DRIFTS was also used to study the adsorption capacity of metallic samples before and after reforming in presence of H_2S

using CO as a molecular probe. Samples were first reduced at 450 °C in 35 mL min⁻¹ H₂ diluted in 20 mL min⁻¹ He. After 1 h, the temperature was set to 250 °C and 1 mL min⁻¹ CO was added to the feed stream. Spectra of adsorbed CO were recorded by accumulating 32 scans.

3. Catalytic reactions

3.1. Catalytic data treatments

Most reaction conditions were described in terms of space velocity, either on a mass (WHSV) or on a volume (GHSV) basis of catalyst, and sometimes in terms of contact time (τ):^[45]

$$(21) \quad \text{WHSV} = M_{\text{flow}} / m_{\text{cata}} \quad \text{Weight hourly space velocity (h}^{-1}\text{)}$$

$$(22) \quad \text{GHSV} = V_{\text{flow}} / V_{\text{cata}} \quad \text{Gas hourly space velocity (h}^{-1}\text{)}$$

$$(23) \quad \tau = 1 / \text{GHSV} \quad \text{Contact time (h)}$$

Where M_{flow} and V_{flow} are respectively the mass (kg h⁻¹) and volumetric (m³ h⁻¹) flow rates of feed; m_{cata} and v_{cata} are respectively the mass (kg) and volume (m³) of catalyst.

The catalytic performances were analysed and discussed in terms of conversion, activity (called reaction rate), turn-over frequency (TOF), apparent activation energy (E_{app}) and carbon balance according to the following calculations:^[45]

$$(24) \quad X_{\text{CxHy}} = 100 * (F_{\text{CxHy inlet}} - F_{\text{CxHy outlet}}) / F_{\text{CxHy inlet}} \quad \text{CxHy conversion (\%)}$$

$$(25) \quad A_{\text{CxHy}} = (F_{\text{CxHy inlet}} - F_{\text{CxHy outlet}}) / m_{\text{cata}} \quad \text{Mean reaction rate (\mu mol}_{\text{CxHy}} \text{ s}^{-1} \text{ g}_{\text{cata}}^{-1}\text{)}$$

$$(26) \quad \text{TOF}_{\text{CxHy}} = (F_{\text{CxHy inlet}} - F_{\text{CxHy outlet}}) / (m_{\text{cata}} * S_{\text{metal}}) \quad \text{Turn-over frequency (s}^{-1}\text{)}$$

$$(27) \quad E_{\text{app}} = - R * T * \ln (\text{TOF}_{\text{CxHy}} / A) \quad \text{Apparent activation energy (J mol}^{-1}\text{)}$$

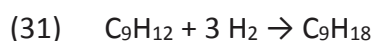
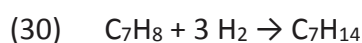
$$(28) \quad C_{\text{balance}} = 100 * (\sum F_{\text{carbon outlet}} / \sum F_{\text{carbon inlet}}) \quad \text{Carbon balance (\%)}$$

$$(29) \quad R_{\text{H}_2/\text{CO}} = F_{\text{H}_2 \text{ outlet}} / F_{\text{CO outlet}} \quad \text{H}_2/\text{CO ratio}$$

Where F_{inlet} and F_{outlet} are respectively the molar flow rates ($\mu\text{mol s}^{-1}$) at reactor inlet and outlet, m_{cata} is the mass (g) of catalyst, S_{metal} is the metallic surface ($\mu\text{mol}_{\text{metal surface atom}} \text{ g}_{\text{cata}}^{-1}$), R is the gas constant (8.314 J mol⁻¹ K⁻¹), T is the oven temperature set-point (K) and A is the pre-exponential factor (s⁻¹ for a 1st order reaction).

3.2. Arene hydrogenation

Toluene and mesitylene (i.e. 1,3,5-trimethylbenzene) hydrogenation tests were carried out using a fixed-bed continuous-flow reactor consisting of a quartz tube (length 400 mm, 4 mm ID, 6 mm OD) containing the powdered catalyst held between quartz wool plugs. The system was operated at atmospheric pressure and the samples were reduced *in situ* at 500 °C in pure H₂ for 60 min before the catalytic tests. Aromatic reactants were fed individually using a saturator kept at 0 °C, leading to partial pressures of 912 and 62 Pa for toluene and mesitylene, respectively. A flow of 20 mL/min of pure H₂ was used as reactant carrier gas and fed through one saturator at a time. The catalyst powders were crushed and sieved and the fraction 100-200 microns was selected. Between 60-180 mg of catalyst was used, depending on the activity of the sample, to remain under differential conditions. The gas hourly space velocity (GHSV) was so varied between 6700 and 20000 h⁻¹, approximating the catalyst density as being unity.



FT-IR spectroscopy is commonly used as an analytical technique to investigate complex reaction mixtures. Here, the reactor effluent was analyzed using a 10 cm path-length FT-IR gas cell fitted in a Tensor 27 FT-IR spectrophotometer (Bruker). Typically 32 scans were collected at a resolution of 4 cm⁻¹ and averaged. The conversion of the arene reactants was determined through integration of spectral regions corresponding to the C-H stretching vibration modes.^[147,157,158] The IR spectra of toluene and mesitylene are shown in Figure 2.5 (spectra in red). Spectra in blue are those of the corresponding reactor effluents at a conversion of ca. 9 %. The spectra of the reaction products (black spectra) could be obtained by removing the contribution of the reactants and corresponded to that of methylcyclohexane in the case of toluene (Figure 2.5, a) and to that of the two stereoisomers of 1,3,5-trimethylcyclohexane in the case of mesitylene (Figure 2.5, b). No other reaction products could be observed in the conditions used.

The area comprised over the range 3000-3200 cm⁻¹ was integrated to quantify the concentration of the reactants, as this region only contained a contribution from the arenes. The change of arene concentration was then calculated, also taking into account the reduction of number of moles of gases according to Equations 30 and 31. Only data points for which the arene conversion was below 20% were considered to calculate rates, apparent activation energies and turn-over frequencies.

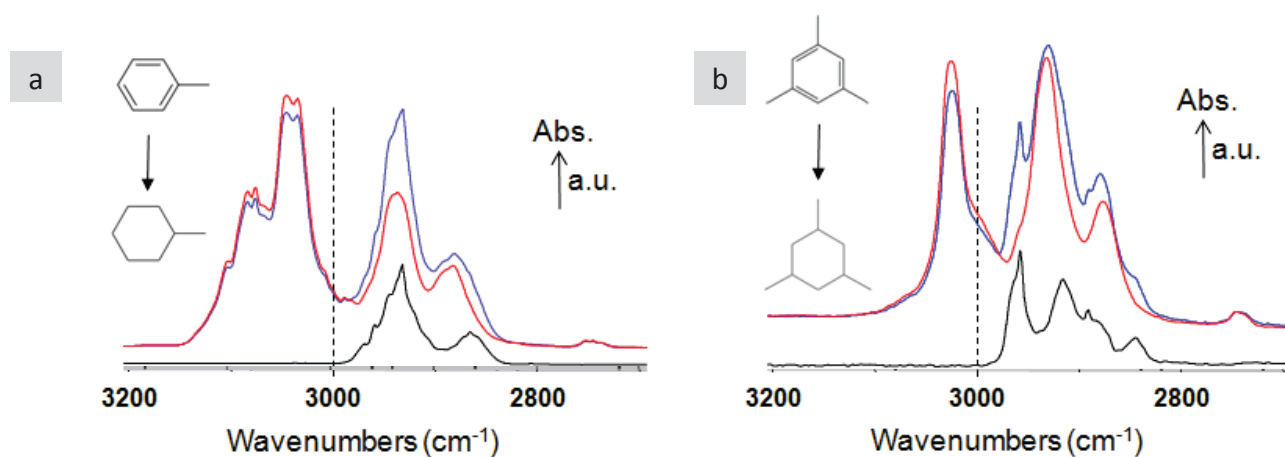


Figure 2.5 FT-IR transmission spectra recorded during the hydrogenation of toluene (a) and mesitylene (b).

3.3. Methane reforming

CH_4 reforming experiments were performed on a lab-scale system which was developed at the beginning of this PhD work in the frame of FASTCARD (Figure 2.6). The system was designed to carry out gas-phase catalytic tests with co-feeding of compounds which are either liquid or solid at room temperature. Experimental reforming conditions will be more precisely described in each chapter.

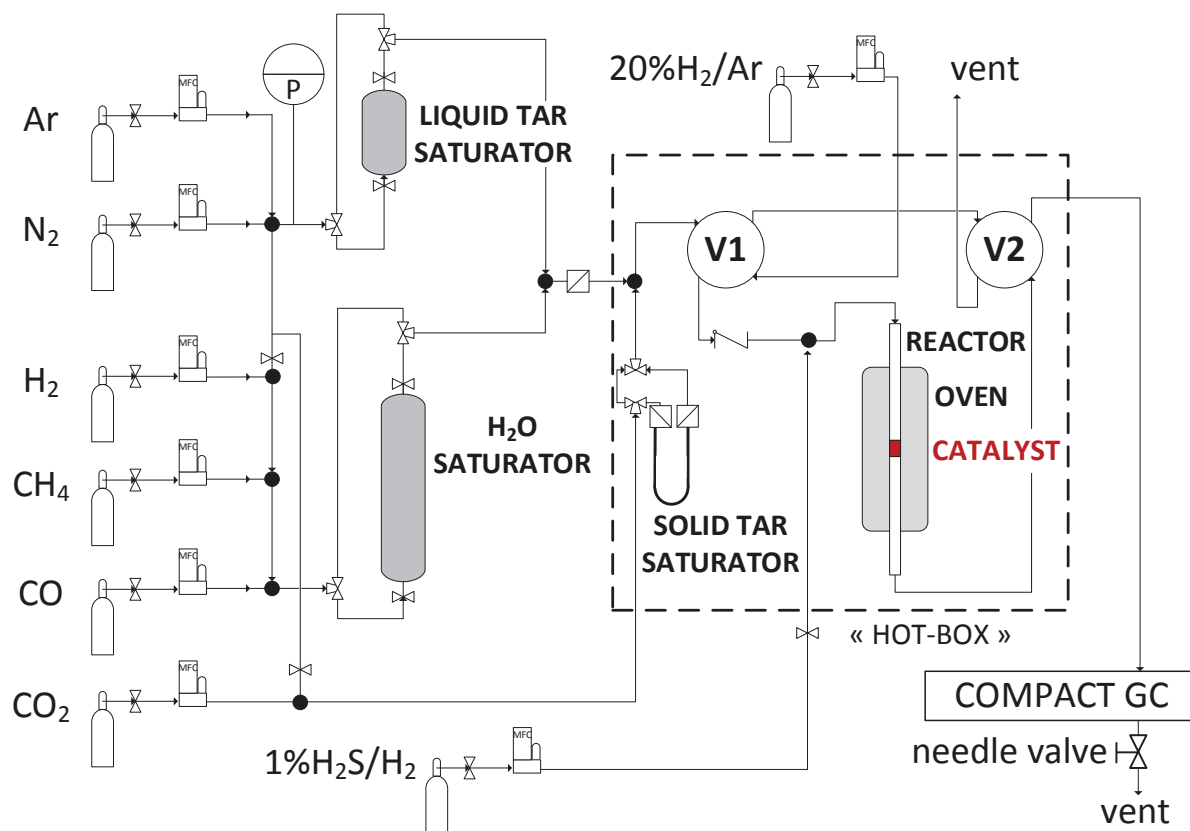


Figure 2.6 Schematic layout of the experimental setup.

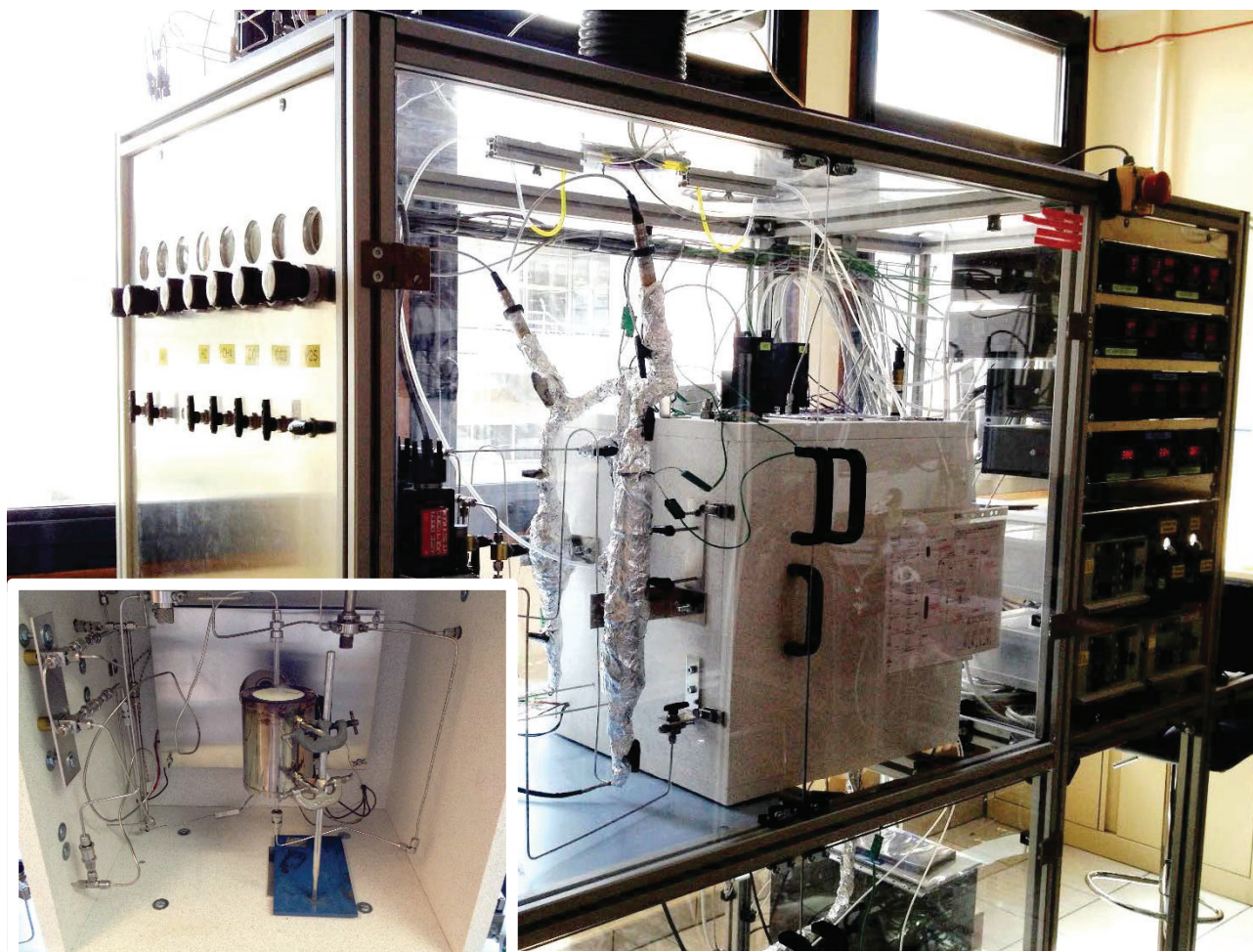


Figure 2.7 Pictures of the experimental setup. The inside of the hot-box in which are placed the reactor, the solid tar saturator and the two automated switching valves is presented in the bottom left inset.

3.3.1. Experimental set-up

Reforming tests were carried out in a fixed-bed continuous-flow reactor consisting of a quartz tube (length 300 mm, 4 mm inside and 6 mm outside diameter) containing between 10 and 100 mg of non-diluted catalyst powder held between plugs of quartz wool. The typical bed height varied between 0.5 and 20 mm, depending on the mass and nature of catalyst. Prior to testing, both powdered and shaped catalysts were crushed and sieved to obtain particle sizes ranging from 100 to 200 μm . Hence, the reactor could not be considered in a plug-flow regime. The catalytic bed was located in the isothermal region of a tube furnace placed inside a pre-heating hot-box. The reaction temperature was monitored by a thermocouple placed in the furnace outside the reactor. Catalysts were reduced *in situ* at the temperature of the reaction (between 700 and 900 $^{\circ}\text{C}$) with a heating rate varying between 400 and 600 $^{\circ}\text{C h}^{-1}$, for 2 h in a 200 mL min^{-1} flow rate of 20 vol.% H_2/Ar mixture.

Figure 2.8 shows the temperature profile of the 13.5 cm-long reactor measured at 700, 800, 900 °C. A thermocouple was placed inside and moved along the empty reactor under an Ar gas flow. The temperature was considered homogeneous ($\Delta T < 1\%$) between 5 and 7.25 cm, independently of the oven set point (SP). Hence, the catalytic bed should be placed in this zone and its height should not be over 2.25 cm. The difference between the oven SP and the reactor temperature was observed to increase with the SP and was taken into account to heat the reactor at the desired temperature.

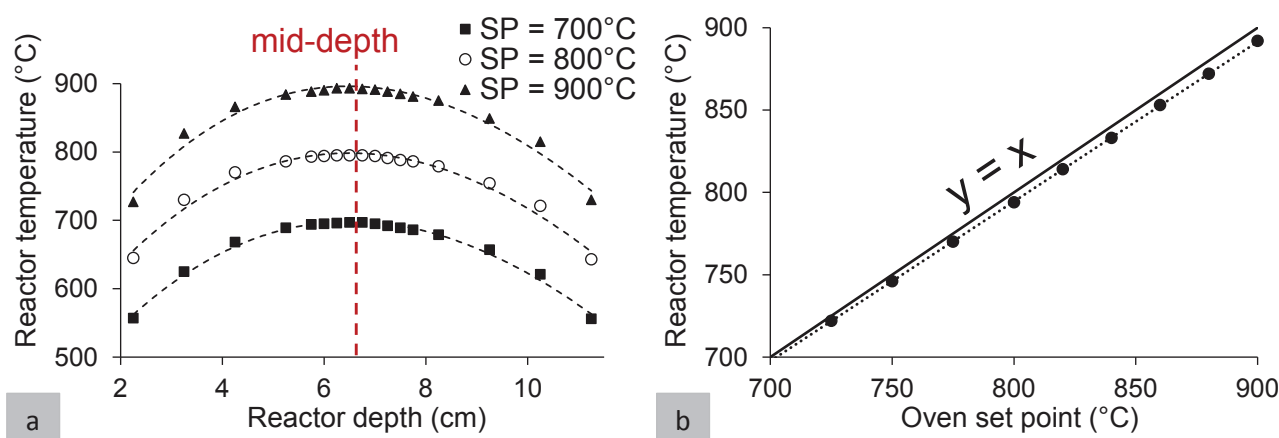


Figure 2.8 Reactor temperature as a function of the reactor depth (a) and the oven set point (b).

To conduct realistic tests, catalysts were tested under a supply of realistic producer gas. This simulated bio-syngas stream was set on the real reformat gas conditions (Table 2.1) obtained from MILENA pilot gasifier at ECN in the frame of FASTCARD. This composition was obtained operating the gasifier at 850 °C and using olivine as bed material. The feedstock used by ECN, as a standard solid biomass fuel representing clean biomass, was clean beech wood in the form of small chips. For a better understanding of catalyst deactivation, the reformat gas composition from MILENA was simplified and adapted to our study (Table 2.2). CH₄ being both the most present and the most difficult HC to decompose, C₂-C₃ components were not added to the gas stream and were replaced with Ar in equal volume fraction. For safety reasons, toluene (Aldrich, $\geq 99.9\%$) was selected to be representative of mono-aromatic tar generated from biomass gasification instead of benzene. Naphthalene (Aldrich, 99%), phenanthrene (Aldrich, 98%) and pyrene (Aldrich, 98%) are respectively the most important 2-ring, 3-ring and 4-ring PAH formed during gasification and were chosen to be representative of their molecular class. H₂S (Air Liquide, 1vol.% in H₂), the major sulfur-containing molecule, was selected to represent sulfur-based contaminants. Ultra-pure permanent gases were provided by Air Liquide (N50 (> 99.999 %) quality for Ar, N₂ and H₂; N45 (> 99.995 %) quality for CO, CO₂ and CH₄).

Table 2.1 Producer gas composition from fluidized bed gasification of beech wood obtained at ECN

Component	Volume %	Tar	MW	Concentration		
			g mol ⁻¹	mg Nm ⁻³	ppmv	
CO	20	Phenol	94	2890	688	
H ₂	16	Indene	116	1750	338	
CO ₂	10	m/p-Cresol	108	500	104	
H ₂ O	39	Naphthalene	128	8070	1411	
CH ₄	9	2-methylnaphthalene	142	770	121	
N ₂	1	1-methylnaphthalene	142	540	85	
C ₂ H ₂	0.2	Acenaphthylene	152	2200	324	
C ₂ H ₄	2.9	Fluorene	166	810	109	
C ₂ H ₆	0.2	Phenanthrene	178	1610	202	
C ₃ H ₆	0.1	Anthracene	178	650	82	
C ₆ H ₆	0.7	Fluoranthene	202	730	81	
C ₇ H ₈	0.1	Pyrene	202	890	99	
S-, N-, Cl- containing compounds	tar	0.7	Minor tars (< 500 mg Nm ⁻³)	-	3570	-
	others	0.1	Unknown tars	-	8260	-
	H ₂ S (ppmv)	180	Total		33240	

Brooks Instrument mass flow controllers (MFC) were used to control gas flow rates of H₂, CH₄, CO, CO₂, N₂ and Ar. The overall system pressure was set at $P_{\text{total}} = 2.2$ bar using a needle valve located downstream the on-line analyzer. A pressure sensor was placed upstream of the reactor to check for a possible pressure increase due to bed blocking. Pure water (18 MΩ.cm at 25 °C) was contained in a 500 cm³ stainless steel gas cylinder placed vertically in which some sand powder was added to its bottom to favor the vapor-liquid interphase. Water was vaporized with the H₂ + CH₄ + CO carrier gas mixture flowing from bottom to top and the temperature was set at 99 °C with a surrounding heating cable to obtain the desired flow rates of steam. Similarly, liquid tar (toluene) was contained in a 150 cm³ stainless steel gas cylinder heated at 82 °C and was vaporized with the N₂ + Ar gas mixture. Solid tars (naphthalene, phenanthrene or pyrene) were placed in a U-shaped ¼" stainless steel tube saturator and held between plugs of quartz wool inside the hot-box. Hot-box temperature and carrier gas were selected to feed the desired concentration of tar. Pyrene concentration was limited to 5 ppmv due to experimental constraints.

Table 2.2 Simplified feed gas composition for catalytic reforming tests

Compound	CO	H ₂	CO ₂	H ₂ O	CH ₄	N ₂	Ar	Poisoning compounds (if any)	
								Tar (ppmv)	Sulfur (ppmv)
vol.%	20	16	10	39	9	2	4	Toluene 10 000 Naphthalene 1 400 Phenanthrene 200 Pyrene 5	H ₂ S 200
ml min ⁻¹	25	20	12.5	48.8	11.3	2.5	5		

For a defined carrier gas flow rate (F_{carrier}) and total system pressure (P_{total} , in bar), concentration (C_i) in steam and tar at reactor inlet was achieved by monitoring their respective partial pressure (P_i , in bar), as described in Equation 32. The partial pressure was controlled by the temperature of the saturator (T_{sat} , in K), as described in Equation 33. Antoine equation parameters (A,B,C) were obtained from the National Institute of Standards and Technology (NIST) website (Table 2.3).^[159] Preliminary tests confirmed these calculations, revealing the high accuracy of these saturating systems.

$$(32) \quad C_i = F_i / F_{\text{total}} = (F_{\text{carrier}} * (P_i / P_{\text{total}}) / (1 - P_i / P_{\text{total}})) / F_{\text{total}}$$

$$(33) \quad \text{LOG}_{10} (P_i) = A - B / (T_{\text{sat}} + C)$$

The total gas flow rate of reactants was 125 mL min⁻¹ (Table 2.2). The corresponding weight hourly space velocity (WHSV) was so varied between 69 and 689 h⁻¹. The GHSV varied between 75000 and 750000 h⁻¹, assuming catalyst density to be unity. These high space velocity values were selected to prevent total conversion of HCs, providing insights in terms of activity and stability of the different catalysts. Furthermore, these conditions allowed an accelerated ageing in terms of poison exposure on a reasonable timescale.

Table 2.3 Antoine equation parameters^[159]

Compound	A	B	C
Steam	5.08354	1663.125	-45.622
Toluene	4.07827	1343.943	-53.773
Naphthalene	4.27117	1831.571	-61.329
Phenanthrene	4.51922	2428.448	-70.96
Pyrene	2.68713	1086.824	-262.849

3.3.2. Analytical set-up

Reactor effluent was analyzed online with a Compact GC (CGC, Global Analyzer Solutions). Gas lines from saturators to analyser were heated so that steam and tar condensation were prevented. The three-channel analyzer was equipped with three columns coupled with TCD, FID and PDID detectors enabling the quantification of permanent gases (N₂, H₂, CO, CO₂ and CH₄), HCs (CH₄ and heavier) and the detection of traces (H₂S), respectively. N₂ signal was used as an internal standard for the TCD channel to convert other surface areas (A) into molar flows (F) (Equation 34). Quantitative analyses of permanent gases were performed by calibrating the CGC using different partial pressures of

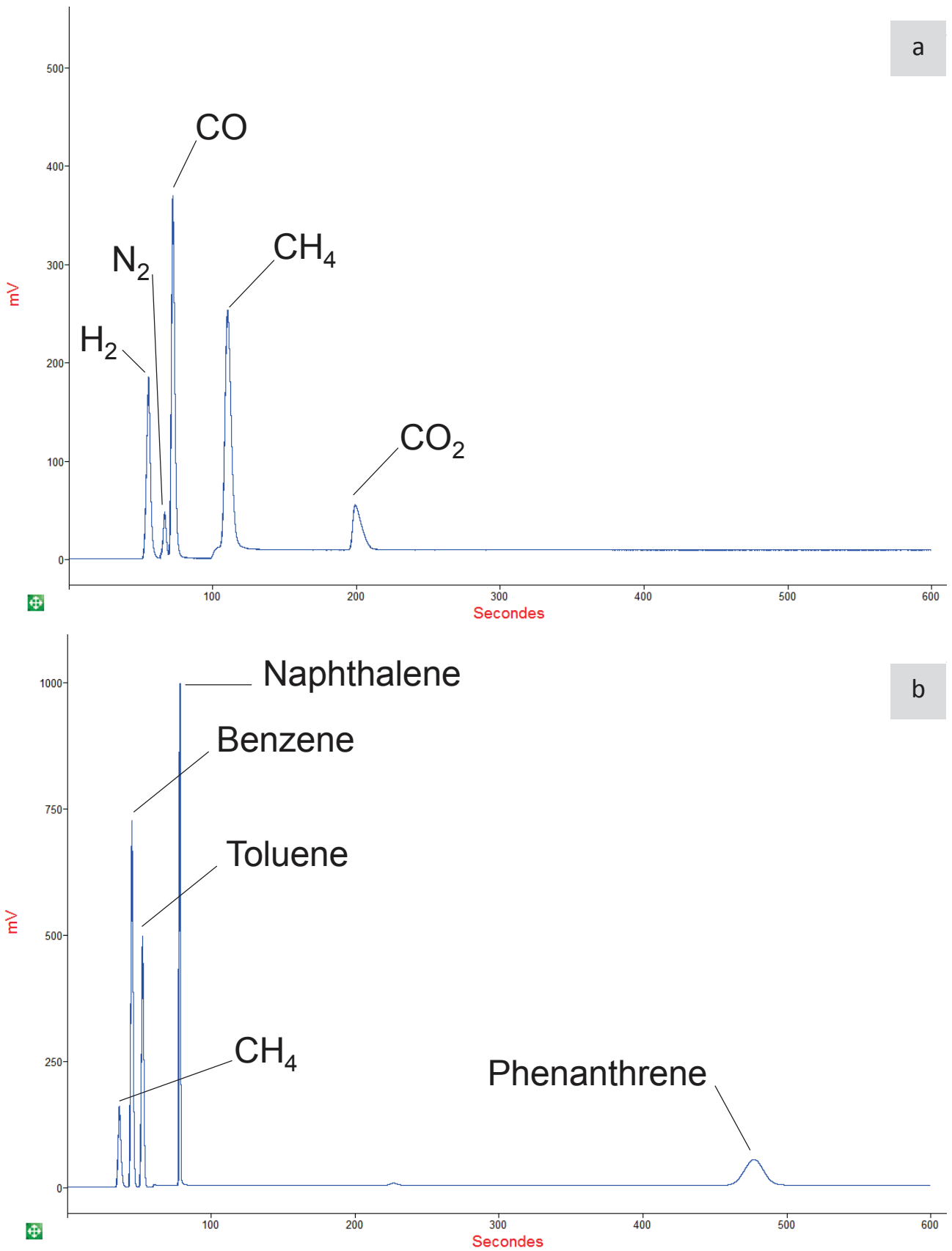


Figure 2.9 Typical gas chromatograms with corresponding compounds obtained on TCD (a) and FID (b) channels during methane reforming tests in presence of tars.

compounds diluted in N₂. H₂O was back-flushed and its quantification was not performed. Similarly, CH₄ signal was used as an internal standard for the FID channel (the CH₄ molar flow rate being itself determined from the TCD channel) to quantify heavier HCs (Equation 35). On this channel, HCs of interest were quantified by determining their response factor (R) relative to CH₄ at P_{total} = 2.2 bar.

$$(34) \quad F_{\text{CH}_4} = R_{\text{N}_2/\text{CH}_4} * (A_{\text{CH}_4} / A_{\text{N}_2}) * F_{\text{N}_2} \quad \text{TCD channel}$$

$$(35) \quad F_{\text{C}_x\text{H}_y} = R_{\text{CH}_4/\text{C}_x\text{H}_y} * (A_{\text{C}_x\text{H}_y} / A_{\text{CH}_4}) * F_{\text{CH}_4} \quad \text{FID channel}$$

3.4. CO methanation

The structure-insensitive CO methanation (Equation 36) was used as a model reaction to get insights into the structural features of the catalysts. Methanation is highly exothermic, hence experimental conditions were adapted for maintaining CO conversion low enough to avoid light-off phenomena.



Activity in methanation was measured for two different purposes:

- Evaluate the molecular sieving property of Ni@Sil-1 at an intermediate temperature (300 °C)
- Estimate the accessible metal surface sites of a catalyst using methanation as a probe reaction

The experimental set-up used for this reaction is a simplified version of the lab-scale unit presented in Figure 2.6 and described in part 3.3.1. Light-off phenomena were considered inexistent if the reactor temperature was close to the oven set-point ($\Delta T < 2$ °C). The analytical device was similar to that reported in part 0. For the sake of accuracy of flow rate quantification on the TCD channel, methanation activity was expressed in $\mu\text{mol}_{\text{CH}_4} \text{ s}^{-1} \text{ g}_{\text{cata}}^{-1}$.

3.4.1. Evaluation of the molecular sieving property

Similarly to reforming, methanation tests were carried out in a fixed-bed continuous-flow quartz reactor containing between 25 and 50 mg of sieved (100-200 μm) catalyst powder held with quartz wool. Pyrene was selected as a tar model compound, placed in the U-shaped $\frac{1}{4}$ " saturator heated at 151 °C and vaporized with the N₂ + Ar carrier gas mixture, resulting in a concentration of 5 ppmv. Prior to testing, catalysts were reduced *in situ* at 700 °C with a heating rate of 400 °C/h for 2 h in a 200 mL min⁻¹ flow rate of 20 vol.% H₂/Ar mixture.

Table 2.4 Feed gas composition for catalytic methanation tests in presence of pyrene

Compound	CO	H ₂	N ₂	Ar	Tar (if any) (ppmv)
ml min ⁻¹	5	42.5	2.5	2.5	Pyrene 5

The catalytic activity was then measured at 300 °C, dwelling 18 h at this temperature under an H₂-rich (H₂/CO = 8.5) methanation feed (Table 2.4). Pyrene was only introduced in the feed stream between t = 2 h and up to t = 5 h. The total system pressure was controlled at P_{total} = 1.4 bar. The reversibility of the deactivation was then studied by maintaining the catalyst under a pyrene-free feed for up to 13 h.

3.4.2. Estimation of the accessible nickel surface area

CO methanation is known to be structure-insensitive displaying TOFs values independent from the size and morphology of Ni particles.^[160–162] Preliminary CO methanation experiments performed at 300 °C under an H₂-rich feed (Table 2.5) using various supported catalysts with different Ni loadings and particle size exhibited all a TOF of ca. 0.35 s⁻¹. These data were in good agreement with the ones reported in the literature and will be presented in chapter 3.^[163]

Table 2.5 Feed gas composition for activity measurements in CO methanation

Compound	CO	H ₂	N ₂
ml min ⁻¹	5	42.5	2.5

In some cases, activity in CO methanation at 300 °C was used to derive the Ni specific surface area assuming a TOF of 0.35 s⁻¹ for each active site. These *in situ* measurements were carried out before and after a reforming test to respectively estimate the metal area of the fresh and used samples, hence unravelling the loss of active sites during reforming.

3.5. Evaluation of transport phenomena

A spreadsheet developed by the Eurokin consortium was used to assess transport limitations in the gas-solid fixed-bed reactor while reforming.^[164] This section discusses the evaluation of the mass and heat transfer limitations and gives criteria that should be respected in order to operate in conditions where the reforming rates are only determined by the intrinsic kinetics of the 1st order reaction.^[165,166]

3.5.1. External mass transport limitations

To make sure that the reaction rate is determined by catalytic reactions rather than by the diffusion of the reactants from the bulk to the external surface of the catalyst, Equation 37 must be satisfied:

$$(37) \quad \mathbf{Ca} = \frac{C_{A \text{ bulk}} - C_{A \text{ surface}}}{C_{A \text{ bulk}}} = \frac{R_{\text{app}} * d_p}{6 * k_G * C_{A \text{ bulk}}} < \mathbf{0.05}$$

Where Ca is the Carberry number (dimensionless)

$C_{A \text{ bulk}}$ is the concentration of reactant A in the bulk ($\text{mol m}^{-3}_{\text{gas}}$)

$C_{A \text{ surface}}$ is the concentration of A at the external surface of the catalyst ($\text{mol m}^{-3}_{\text{gas}}$)

R_{app} is the apparent rate of reaction per volume of catalyst ($\text{mol m}^{-3}_{\text{cat}} \text{s}^{-1}$)

d_p is the diameter of the spherical pellet (m)

k_G is the external mass transfer coefficient (m s^{-1}) which can be calculated from the Sherwood number (Sh) in the range $0.1 < Re < 100$:

$$(38) \quad \text{Sh} = \frac{k_G * d_p}{D_{A \text{ m}}} = 2 + 1.8 \text{Re}^{1/2} \text{Sc}^{1/3}$$

Both Reynolds number (Re) and the Schmidt number (Sc) can be calculated as follows:

$$(39) \quad \text{Re} = \frac{u_v * \rho_G * d_p}{\mu_G} \quad \text{and} \quad (40) \quad \text{Sc} = \frac{\mu_G}{\rho_G * D_{A \text{ m}}}$$

Where $D_{A \text{ m}}$ is the molecular diffusivity of A in the gas mixture ($\text{m}^2 \text{s}^{-1}$)

u_v is the superficial velocity (m s^{-1})

ρ_G is the density of the gas mixture (kg m^{-3})

μ_G is the viscosity of the gas mixture ($\text{kg m}^{-1} \text{s}^{-1}$)

3.5.2. Internal mass transport limitations

To make sure that the reaction rate is not determined by the diffusion of the reactants from the external surface to the catalytic surface, the Weisz-Prater criterion must be respected (Equation 41):

$$(41) \quad \omega = \left(\frac{d_p}{6}\right)^2 * \frac{R_{\text{app}}}{D_{A \text{ eff}} * C_{A \text{ surface}}} < \mathbf{0.08}$$

Where ω is the Weisz modulus (dimensionless)

$D_{A \text{ eff}}$ is the effective diffusivity inside the pellet ($\text{m}^2 \text{s}^{-1}$) which can be calculated as follows:

$$(42) \quad \frac{1}{D_{A \text{ eff}}} = \frac{\tau_p}{\varepsilon_p} * \left(\frac{1}{D_{A \text{ m}}} + \frac{1}{D_{A \text{ k}}}\right)$$

Where ε_p refers to the pellet porosity (dimensionless) and τ_p to the pellet tortuosity (dimensionless).

Knudsen diffusion coefficient ($D_{A \text{ k}}$) can be calculated from the following equations:

$$(43) \quad D_{Ak} = \frac{2}{3} r * \sqrt{\frac{8 * R * T}{\pi * m_A}} \quad \text{and} \quad (44) \quad r = 2 \frac{\varepsilon_p}{\rho_p * S_{int}}$$

Where r is the average pore radius of the pellet (m)

R is the gas constant ($\text{J mol}^{-1} \text{K}^{-1}$)

T is the temperature of the gas mixture in the bulk (K)

m_A is the molecular mass of A (kg mol^{-1})

ρ_p is the pellet density ($\text{kg m}^{-3}_{\text{cat}}$)

S_{int} is the specific internal surface area of the pellet ($\text{m}^2 \text{g}^{-1}$)

The Weisz modulus was preferred to the Thiele counterpart to estimate internal mass transport limitations. The Thiele modulus (ϕ) requires the knowledge of the intrinsic reaction rate while the Weisz criterion is expressed in observable reaction rate term. These two parameters are linked by the effectiveness factor (η) that relates the diffusive and intrinsic reaction rates:

$$(45) \quad \omega = \eta * \phi^2$$

3.5.3. External heat transfer limitations

The effects of heat transfer are analogous to those of mass transfer. Heat transfer limitations throughout the film surrounding the catalyst particle can be evaluated. The criterion for external maximum temperature difference ΔT_{film} over the film surrounding the spherical catalyst particles is expressed as follows:

$$(46) \quad \Delta T_{\text{film}} = \frac{R_{app} * |\Delta H| * d_p}{6 \alpha_p} < \frac{0.05 * R * T^2}{E_{app}}$$

Where ΔT_{film} is the temperature difference over the film surrounding the pellet (K)

ΔH is the reaction enthalpy (J mol_A^{-1})

E_{app} is the apparent activation energy of the reaction (J mol^{-1})

α_p is the heat transfer coefficient between the pellet and the gas mixture ($\text{W m}^{-2} \text{K}^{-1}$):

$$(47) \quad \alpha_p = \frac{Nu * \lambda_G}{d_p}$$

Where λ_G is the thermal conductivity of the gas mixture [$\text{W m}^{-1} \text{K}^{-1}$]

Nu is the Nusselt number which can be calculated in the range $0.1 < Re < 100$ as follows:

$$(48) \quad Nu = 2 + 1.1 Re^{0.6} Pr^{1/3} \quad \text{and} \quad (49) \quad Pr = \frac{C_{pG} * \mu_G}{\lambda_G}$$

Where Pr is the Prandtl number (dimensionless)

$C_{p,G}$ is the heat capacity of the gas mixture ($J\ kg^{-1}\ K^{-1}$)

μ_G is the viscosity of the gas mixture ($kg\ m^{-1}\ s^{-1}$)

3.5.4. Internal heat transfer limitations

Heat transfer limitations throughout the catalyst particle can also affect the reaction rate. The maximum temperature difference ΔT_{int} between the edge and the centre of the particle is expressed as follows:

$$(50) \quad \Delta T_{int} = \frac{R_{app} * |\Delta H| * d_p^2}{60 * \lambda_p} < \frac{0.05 * R * T^2}{E_{app}}$$

Where ΔT_{film} is the temperature difference between the surface and the centre of the pellet (K)

λ_p is the thermal conductivity of the catalyst particle ($W\ m^{-1}\ K^{-1}$)

3.5.5. Radial heat transfer limitations

Radial heat transport from the near wall to the centreline of the bed can cause severe deviations from the isothermal operation. This transport is not limiting if the following criterion is valid:

$$(51) \quad \Delta T_{rad} = \frac{R_{app} * |\Delta H| * (1 - \epsilon_b) * (1 - b) * d_t^2}{32 * \lambda_{r,eff}} < \frac{0.05 * R * T_w^2}{E_{app}}$$

Where ΔT_{rad} is the temperature difference between the bed near the wall and the bed centre (K)

b is the volume of inert material as fraction of total solids volume ($m^3_{inert}\ m^{-3}_{inert+cat}$)

ϵ_b is the bed porosity ($m^3_{void}\ m^{-3}_{bed}$)

$\lambda_{r,eff}$ is the effective radial thermal conductivity in the bed ($W\ m^{-1}\ K^{-1}$)

T_w is the temperature of the wall (K)

Chapter 3 - Size-selectivity of metal particles encapsulated in hollow silicalite-1 zeolites

1. Introduction

Size-selective membranes and catalysts find important applications in separation, sensing and catalytic technologies. Catalytic hydrogenation is an ubiquitous reaction and is used for instance in the synthesis of fine chemicals and fuel upgrading, with substrate sizes that are similar to that of zeolite pores.^[167-170] The possibility to prepare metal nanoparticles embedded inside zeolite single crystal nanoboxes was recently reported by our group.^[123,124,146-149,171] The use of noble metals typically led to single nanoparticles with a well-defined size embedded in silicalite-1 nanoboxes.^[146,147] The total size exclusion of mesitylene (kinetic diameter = 8.7 Å) from the MFI-type silicalite-1 hollow nanocrystals was demonstrated and led to a Pt-based catalyst that was highly active for the hydrogenation of toluene (kinetic diameter = 5.8 Å) and totally inactive for that of mesitylene.^[147] In addition, these nanoboxes can act as nanoreactors in which the nanoparticles are encapsulated and protected from sintering by coalescence.^[123,124,171]

Herein, we have extended the concept of yolk-shell materials to transition metal nanoparticles encapsulated in single-crystal hollow zeolite shells, in which the thin hollow shell protects metal particles from sintering and also serves as molecular sieve. In this chapter, we report the preparation and the upgrading of nickel nanoparticles encapsulated inside hollow silicalite-1 (5%Ni@Sil-1 SH, SH for single hollow). The synthesis was extended to the preparation of Rh@silicalite-1 material, with the aim of encapsulating a nanoalloy of transition and noble metals (NiRh@silicalite-1). The attempts to include Rh inside the membrane were not successful, hence we decided to focus our attention on the synthesis of NiPt@silicalite-1 nanoalloys. In the preparation of Ni@silicalite-1, we show that metal nanoparticles can also be formed outside of the silicalite-1 nanoboxes when attempting to prepare high metal loadings, leading to less size-selective catalysts. The presence of metal nanoparticles outside the nanoboxes can be particularly detrimental if the reactants are converted into deactivating molecules that can poison or block the nanobox surface or pores, as when dealing with reforming or dehydrogenation reactions.

We demonstrate in this chapter that a simple citric acid-based treatment can selectively leach out most external Ni nanoparticles, while leaving a significant amount of nanoparticles located inside the nanoboxes. The leached sample (CitAc Ni@Sil-1 SH) exhibited an improved selectivity in the hydrogenation of toluene as compared to that of the bulkier mesitylene. In addition, the molecular sieving property of this sample at sub-nanometer scale was verified during the methanation of CO at 300 °C where the Ni particles were shown to be resistant to pyrene poisoning. Additionally, the sintering resistance was evaluated in the reforming of a model producer gas (Table 2.2) over both 5%Ni@Sil-1 SH and CitAc Ni@Sil-1 SH samples.

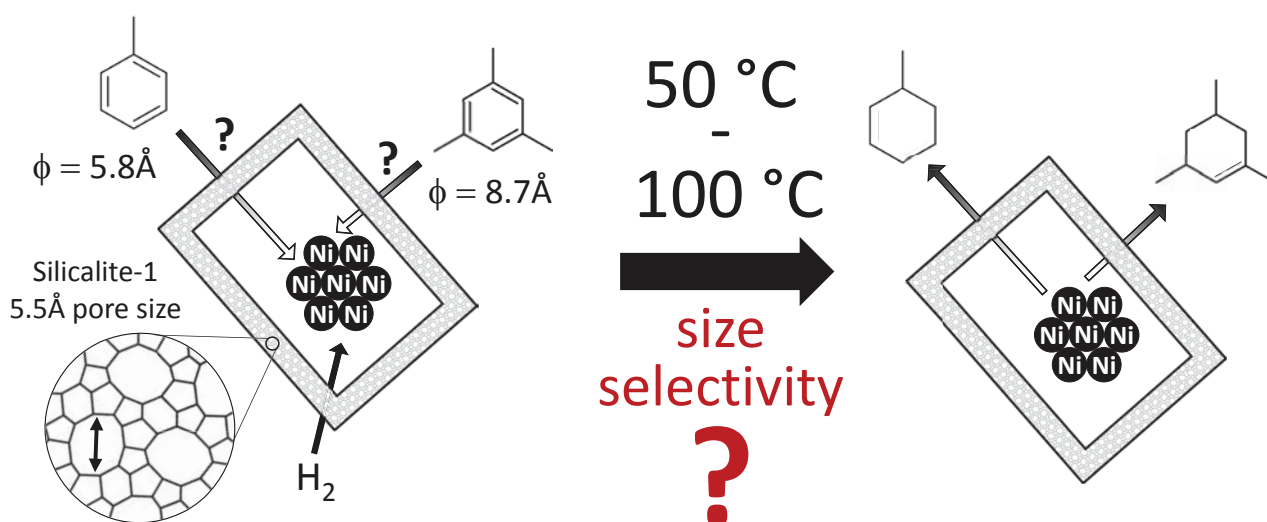


Figure 3.1 Scheme of the potential size-selectivity property of CitAc Ni@Sil-1 SH catalyst.

2. Results and discussion

2.1. Preparation of Ni particles encapsulated in single hollow silicalite-1 material (Ni@Sil-1 SH)

2.1.1. Post-impregnation method

We have impregnated hollow silicalite-1 with an aqueous solution ($0.2 \text{ ml g}_{\text{sil-1}}^{-1}$) of $\text{Ni}(\text{NO}_3)_2 \cdot 6\text{H}_2\text{O}$ and then calcined the solid in air at 450 °C for 6 h. The corresponding final material was denoted PI 0.5%Ni@Sil-1 (PI for post impregnation), 0.5% represents the nominal Ni loading. TEM images of the catalyst are given in Figure 3.2. The pictures clearly show that NiO particles are not homogeneously distributed, some nanoboxes being empty while others contain many particles with sizes ranging from approximately 4 to 25 nm. Moreover, only a few of these particles are inside

zeolite cavities, most of those being large and outside the crystals. Therefore, the post-impregnation method was not further studied in the case of Ni.

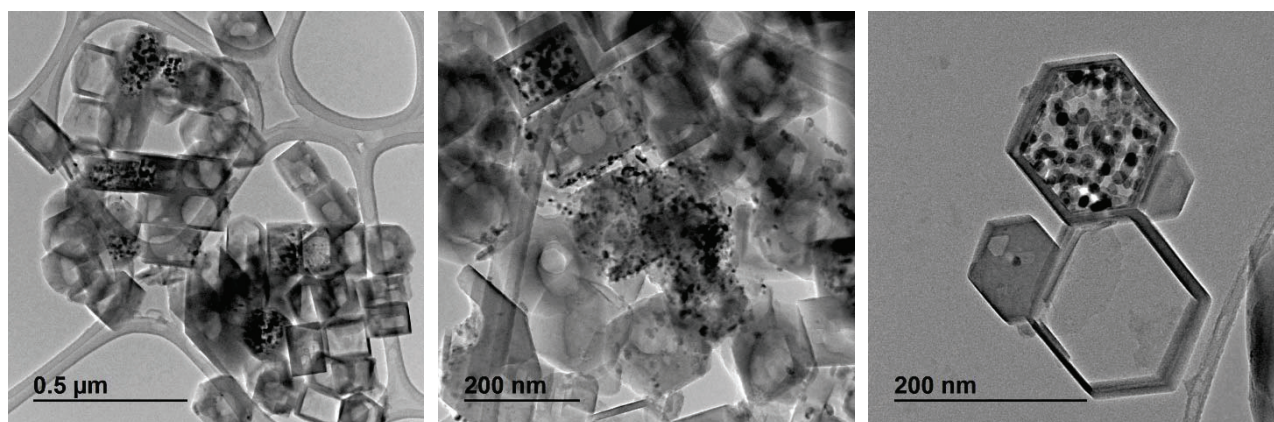


Figure 3.2 TEM images of PI 0.5%@Sil-1 sample.

2.1.2. Impregnation followed by the formation of hollow structures method

Another synthesis method to prepare Ni@Sil-1 SH has been developed that consists of three steps (synthesis details in section 1.2 of chapter 2; the recipe is given for a particular concentration, yielding a final material with 5 wt.% Ni). In the following, we thoroughly describe the synthesis and characterization of a 5%Ni@Sil-1 SH sample which were prepared as follows:

1. Impregnation of bulk silicalite-1 crystals with Ni aqueous solution
2. Hollow zeolites are then formed by a dissolution-recrystallization process under hydrothermal conditions in the presence of TPAOH at 170 °C
3. The sample is calcined at 450 °C in order to remove the template and organic residues, and reduced at 750 °C for 3 h in H₂

As reported by Tuel et al., silicalite-1 crystals are not stable at high temperature under highly alkaline pH conditions.^[143–145] Zeolite crystals are partially dissolved, preferentially in the middle, which is the region where the density of framework defects sites is maximum. However, when dissolution is performed with TPAOH under appropriate conditions, dissolved species can recrystallize on the surface, leading to regular hollow crystals with well-defined cavities and walls. A significant fraction (> 50%) of the original crystal was dissolved and recrystallized during the process.^[143,144]

The direct application of this synthesis procedure previously developed for noble metal nanoparticles encapsulated in silicalite-1 to nickel did not yield the oxide nanoparticles, as was expected.^[146,147] After the TPAOH treatment and subsequent calcination, hollow crystals did not

contain particles, contrary to the case of noble metals.^[146,147] The color of the sample was gray, which indicated the presence of some Ni species, and TEM pictures surprisingly revealed the presence of dark long fibers covering the internal and external surfaces of the boxes (Figure 3.3).

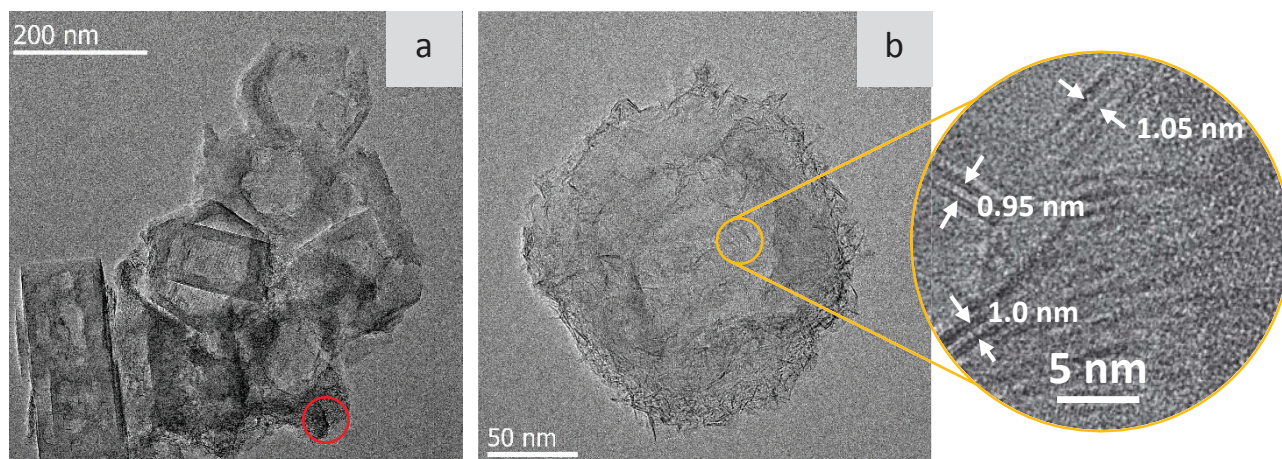


Figure 3.3 TEM images of NiO@Sil-1 SH using a magnification of $\times 15000$ (a) and $\times 45000$ (b). The zone analyzed by EDX in (a) is indicated by a red circle. The zoom in on a region of (b) using HRTEM reveals the nickel phyllosilicates: white arrows indicate the silicate layers used for interlayer distance determination.

This type of fibrous structure is often found in Ni/SiO₂ catalysts upon specific preparation methods and corresponds to nickel phyllosilicates. Nickel phyllosilicates can be formed under hydrothermal conditions in basic media leading to various compounds depending on subsequent thermal treatment (further information are given in section 2.2.1).^[172,173] As fibers were not observed in the absence of Ni, we assumed that they were formed during the TPAOH treatment when partial dissolution of the zeolite occurred. In order to characterize the observed fibers, EDX and high-resolution TEM measurements were carried out on 5%NiO@Sil-1 SH. An EDX analysis realized on layers located outside the nanoboxes (Figure 3.3a) indicated a weight composition of 31% Ni, 30% Si and 39% O, corresponding to NiSi₂O₅, the Si₂O₅²⁻ unit being characteristic of phyllosilicates according to the Nickel-Strunz classification.^[174] The nickel phyllosilicate structure was confirmed by HR TEM measurements of the interlayer distance of 1.00 ± 0.05 nm, which corresponds to the value generally reported for these structures (zoom of Figure 3.3b).^[84]

These layered compounds could be converted to metal nanoparticles upon reduction at 750 °C, yielding yolk-shell type materials. Figure 3.4 shows some typical TEM micrographs of the reduced samples and the corresponding Ni nanoparticle size distributions are shown in Figure 3.5. TEM pictures of the reference catalyst named 5%Ni/Sil-1, which was produced by direct calcination and reduction of Ni(NO₃)₂/Sil-1 under the same conditions as 5%Ni@Sil-1 SH, are also presented.

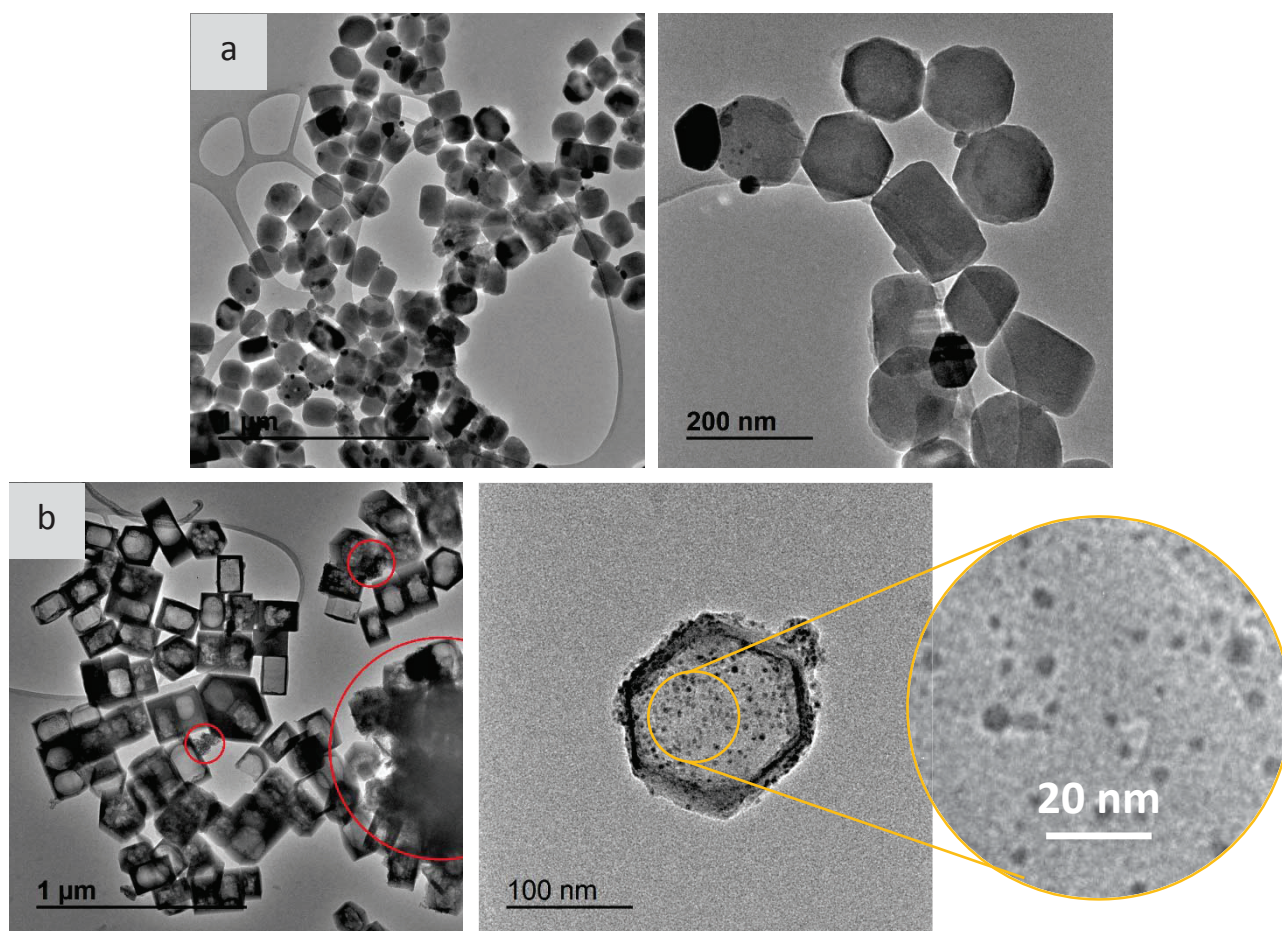


Figure 3.4 TEM images of reduced 5%Ni/Sil-1 (a) and 5%Ni@Sil-1 SH (b) using various magnifications. Red circles indicate the presence of nickel nanoparticles (confirmed by EDX) outside the zeolite nanoboxes.

The silicalite-1 plain crystals and the corresponding nanoboxes exhibited regular shapes with sizes between 150 and 200 nm and with wall thickness around 20 to 30 nm. Most of the Ni appeared as large nanoparticles ($d_{sw} = 46$ nm) located outside of the silicalite-1 plain crystals in the case of the 5%Ni/Sil-1 (Figure 3.4a). In contrast, the nanobox-based samples 5%Ni@Sil-1 SH exhibited significantly smaller nanoparticles, with d_{sw} of 7.9 nm considering both internal and external particles (Figure 3.4b). In the case of noble metal encapsulation in hollow silicalite-1, Au and Pt@Sil-1 SH materials showed a single particle inside the big unique cavity of the crystal.^[146,147] In contrast, for Ni containing hollow silicalite-1, many particles are observed in the internal cavities. In addition, phyllosilicates located at the center of the crystal could somewhat limit the dissolution process resulting in, for some of the crystals, the formation of several cavities instead of one single large cavity as observed in the case of noble metal-based materials. A large number of Ni nanoparticles clearly appeared to be located outside of the nanoboxes in the case of the 5%Ni@Sil-1 SH, such as those visible on the nanobox edges. These external particles are probably resulting from the reduction of phyllosilicates that were bonded to the external surface of the nanoboxes (Figure 3.3).

The presence of many particles outside hollow crystals suggested that the maximum incorporation level of Ni species inside the silicalite-1 had been exceeded. The exact Ni loading measured by ICP on the 5%Ni@Sil-1 SH was close to the nominal values (i.e. 6.2 wt.%(Table 3.1).

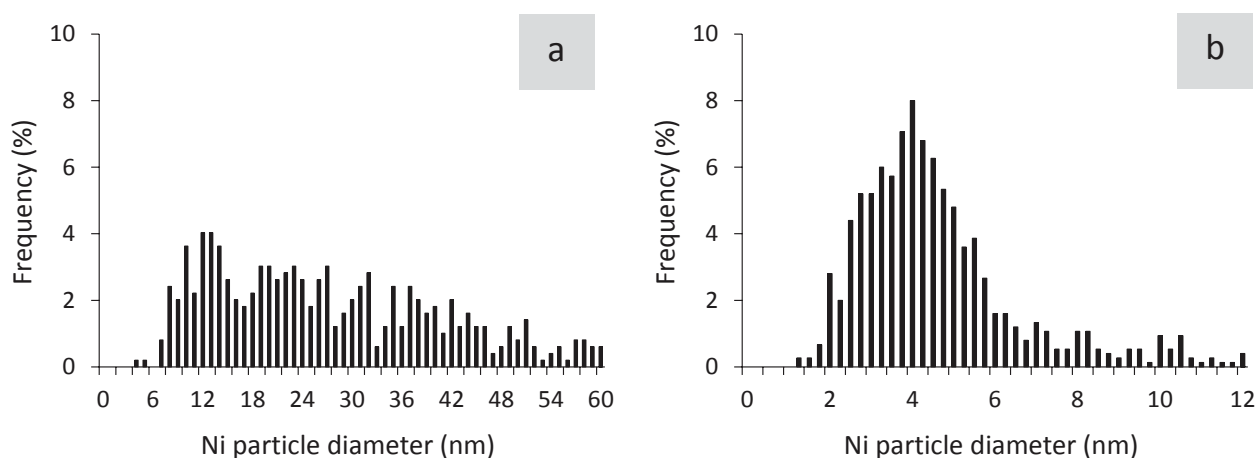


Figure 3.5 Particle size distributions of reduced (a) 5%Ni/Sil-1 and 5%Ni@Sil-1 SH. 500 nanoparticles were measured for each sample.

2.1.3. Citric acid treatment

Obuchi and co-workers have previously reported a method to selectively remove Pt nanoparticles located outside ZSM-5 (aluminosilicate zeolite with MFI-type framework) crystals based on a complex procedure involving the use of tetraethylammonium halide salts and halogens.^[175] Citric acid is known to act as a chelating agent of transition metals to provide complexing citrate ligands with M^{2+} species.^[176] The calcined NiO@Sil-1 SH was then treated with an aqueous solution of citric acid at 80 °C for 2 h, washed and reduced in H_2 at 750 °C to reach the CitAc Ni@Sil-1 SH. The objective was to attempt removing selectively Ni^{2+} species located outside hollow crystals to fully benefit from the size-selectivity of the zeolite membrane.

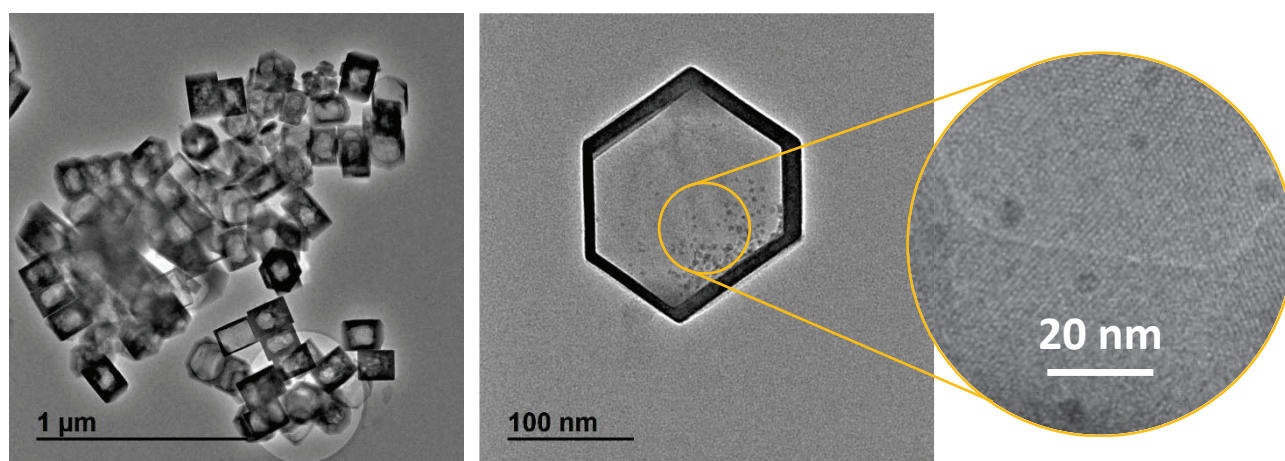


Figure 3.6 TEM images of reduced CitAc Ni@Sil-1 SH using various magnifications.

In contrast to 5%Ni@Sil-1 SH, almost no nanoparticles were present on the edges of the CitAc Ni@Sil-1 SH (Figure 3.7), suggesting that most of those visible were actually located inside the nanobox. Yet, an analysis of a large number of TEM pictures revealed that some agglomerated Ni nanoparticles could still be observed within the CitAc Ni@Sil-1 SH sample (Figure 3.7b). The TEM analysis indicates that the citric acid treatment led to the removal of most of the Ni species located outside of the nanoboxes, while leaving a significant amount of smaller Ni nanoparticles inside the nanobox.

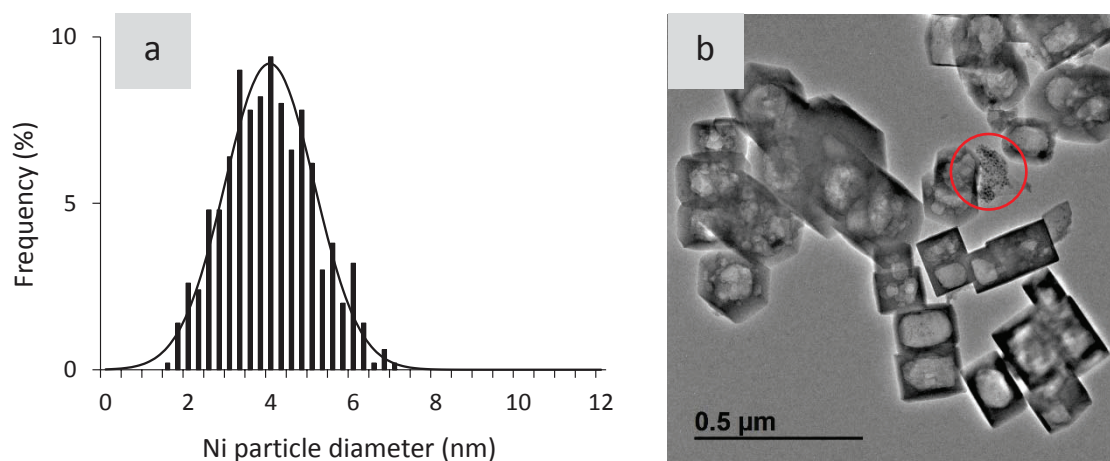


Figure 3.7 (a) Particle size distribution (500 nanoparticles counted) and (b) TEM image of reduced CitAc Ni@Sil-1 SH. The red circle indicates the presence of nickel nanoparticles outside the zeolite nanoboxes.

TEM measurements indicated that the number of encapsulated nickel nanoparticles was ca. 52 per nanobox for CitAc Ni@Sil-1 SH (counting 20 nanoboxes). It is yet difficult to conclude whether or not some of the Ni located inside the 5%Ni@Sil-1 SH nanoboxes was also leached out during the citric acid treatment. ICP measurements revealed that 75 wt.% of the initial content in Ni was removed during the treatment (Table 3.1). The catalytic hydrogenation study described in section 2.4.1 was performed using two reactants with markedly different sizes to get a better insight at the proportion of external and internal Ni particles that were removed during the citric acid treatment.

Table 3.1 Textural properties of the silicalite-1 samples. Metal surface area, diameter and dispersion are based on the corresponding d_{sw} . The given precision is based on the standard deviation of the distribution.

Catalyst	Support	Metal loading (wt.%)	Metal surface area ($m^2 g_{catalyst}^{-1}$)	Mean metal particle diameter (nm)	Metal dispersion (%)
5%Ni/Sil-1	Sil-1	4.5	0.85 ± 0.5	46 ± 16	2.8 ± 1.4
5%Ni@Sil-1	hollow Sil-1	6.2	6.6 ± 3	7.9 ± 3	16 ± 7
CitAc Ni@Sil-1	hollow Sil-1	1.5	2.6 ± 0.7	4.5 ± 1	26 ± 7

It should be noted that a similar treatment on 5%Ni@Sil-1 SH using acetylacetone instead of citric acid was not efficient in leaching out the external Ni content. However, the presence of external Ni agglomerates in the CitAc Ni@Sil-1 SH stresses that the citric acid treatment should be improved or the nature of the complexing agent changed to completely remove external Ni nanoparticles while leaving those embedded essentially untouched.

2.2. Characterization of the zeolitic samples

2.2.1. Thermogravimetric analyses

The reduction of NiO/Sil-1 (Figure 3.8) and NiO@Sil-1 SH (Figure 3.9) was monitored by temperature programmed reduction (TPR) and thermogravimetric analysis (TGA) under H₂ flow up to 900 °C.

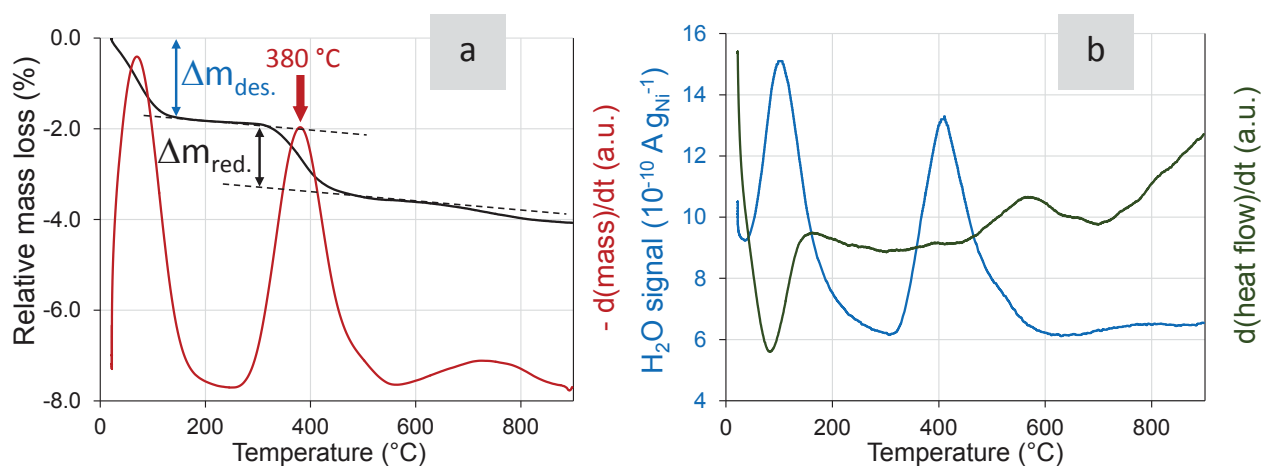


Figure 3.8 Thermal gravimetric profile (a) and related H₂O production (b) of NiO/Sil-1 under H₂.

Both techniques indicate that the reduction of the NiO/Sil-1 catalyst started above 260 °C with a maximum weight loss ($\Delta m_{\text{red.}}$) centered at 380 °C (Figure 3.8). This reduction step decreased the mass of the catalyst by 1.4 wt.%. It is known that Ni/SiO₂ catalyst prepared by impregnation has a major H₂ consumption peak at ca. 350-400 °C.^[177-179] This peak is usually attributed to the reduction of NiO that has a weak interaction with the support. The peak detected below 150 °C arises from the desorption of H₂O rather adsorbed on the zeolite surface ($\Delta m_{\text{des.}}$). Such zeolites are somewhat hydrophobic and water does not easily enter the porosity. A broad peak was also observed above 560 °C. This minor weight loss might be attributed to the high-temperature elimination of H₂O from Si-O-H silanol groups with parallel formation of new Si-O-Si bridges and isolated silanols.^[180,181] Indeed, silicalite-1 prepared in basic media is a well-known example of a zeolite containing large numbers of silanol functions, and is often called defective silicalite-1.^[182] Yet, in the absence of a thermal gravimetric analysis on the parent Ni-free silicalite-1, this assignment is only tentative.

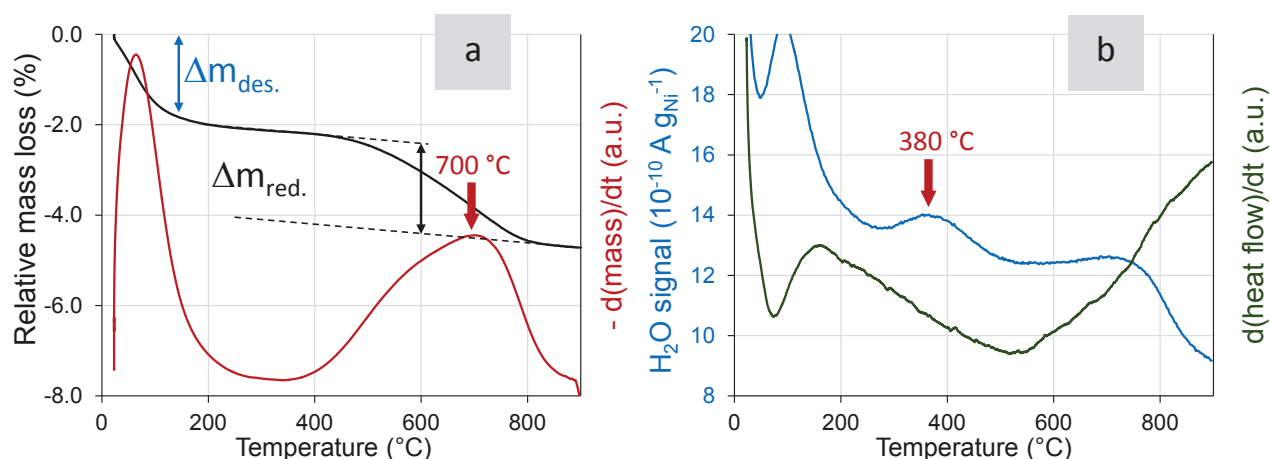


Figure 3.9 Thermal gravimetric profile (a) and related H₂O production (b) of NiO@Sil-1 SH under H₂.

The thermogravimetric profile of the NiO@Sil-1 SH catalyst as a function of temperature is presented in (Figure 3.9a). Two major mass-loss steps ($\Delta m_{\text{des.}}$ and $\Delta m_{\text{red.}}$) were observed upon heating. The initial change in the catalyst mass ($\Delta m_{\text{des.}}$) is attributed to the release of physically adsorbed H₂O. At 150 °C, this step loss has reduced the mass of the catalyst by 1.8 wt.% and was equal to that of the NiO/Sil-1 sample. Above 350 °C, a gradual 2.0 wt.% mass reduction was observed. According to the derivative thermogravimetric profile, the presence of two convoluted peaks with different broadenings is suggested: a large peak with maximum weight loss in the temperature range 550-600 °C and a well-defined one centered at 700 °C. These high reduction temperatures are indicative of Ni²⁺ species that are different from NiO. However, the TPR profile (Figure 3.9b) of this samples shows two distinct peaks: a broad one at temperatures higher than 550 °C and a small one centered at 380 °C. It can thus be concluded that different forms of Ni²⁺ are present, including NiO. Yet, no significant mass loss was observed in the temperature range typical for the reduction of this compound, suggesting that the presence of NiO is negligible (a). XRD scans (Figure 3.9a) did not show any peaks corresponding to cubic NiO (main peak at 37.2°, JCPDS 47-1049), therefore a small amount of NiO below XRD detection limit cannot be ruled out.

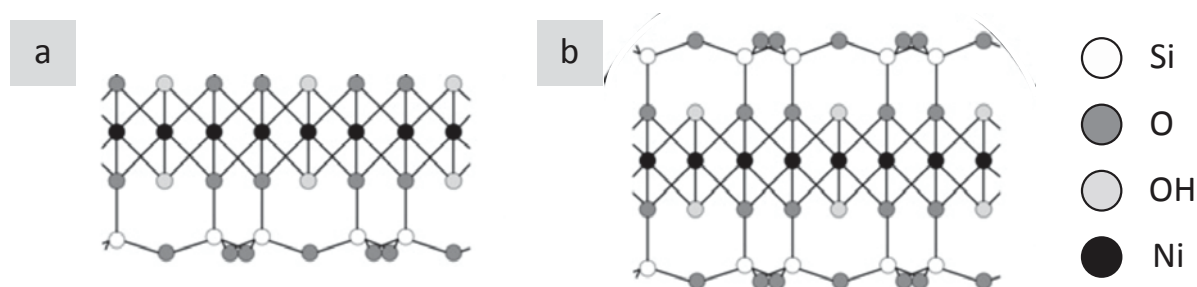


Figure 3.10 Projection of a TO layer of 1:1 (a) and a TOT layer of 2:1 (b) nickel phyllosilicate.

Based on the preparation method of Ni supported on silica, strong Ni-support interactions can be formed resulting in high reduction temperatures. For example, under hydrothermal conditions in basic media, Ni hydroxide formed from Ni salt reacts with silicic acid to form Ni-O-Si silicate bonds.^[84,183,184] Subsequent steps of polymerization lead to the layered structure of Ni phyllosilicate. Depending on the synthesis conditions, two forms of nickel silicates can be derived from nickel hydroxide:^[84] 1:1 phyllosilicate $\text{Ni}_3(\text{Si}_2\text{O}_5)(\text{OH})_4$ and 2:1 phyllosilicate $\text{Ni}_3(\text{Si}_2\text{O}_5)_2(\text{OH})_2$. Each layer of 1:1 phyllosilicate consist of a brucite-type sheet containing Ni^{2+} in octahedral coordination and a sheet containing linked tetrahedral SiO_4 units (TO layer structure). In 2:1 phyllosilicates, the octahedral sheet is sandwiched between two tetrahedral SiO_4 sheets (TOT layer structure)(Figure 3.10). Burattin et al. observed that 1:1 (respectively 2:1) Ni phyllosilicates require high temperatures in the range 450-650 °C (resp. 690-760 °C) on Ni/SiO₂ catalysts for complete reduction.^[84]

Therefore, it can be concluded that both forms of Ni phyllosilicate are likely present in NiO@Sil-1 SH. The mass reduction at 550-600 °C can be attributed to the reduction of 1:1 phyllosilicate. The second peak at 700 °C can be associated with reduction of 2:1 phyllosilicate. However, a definitive assignment of the phyllosilicate form cannot be based on only the reduction temperature, as this parameter also strongly depends on the catalyst preparation procedure.^[184]

2.2.2. Environmental Transmission Electron Microscopy

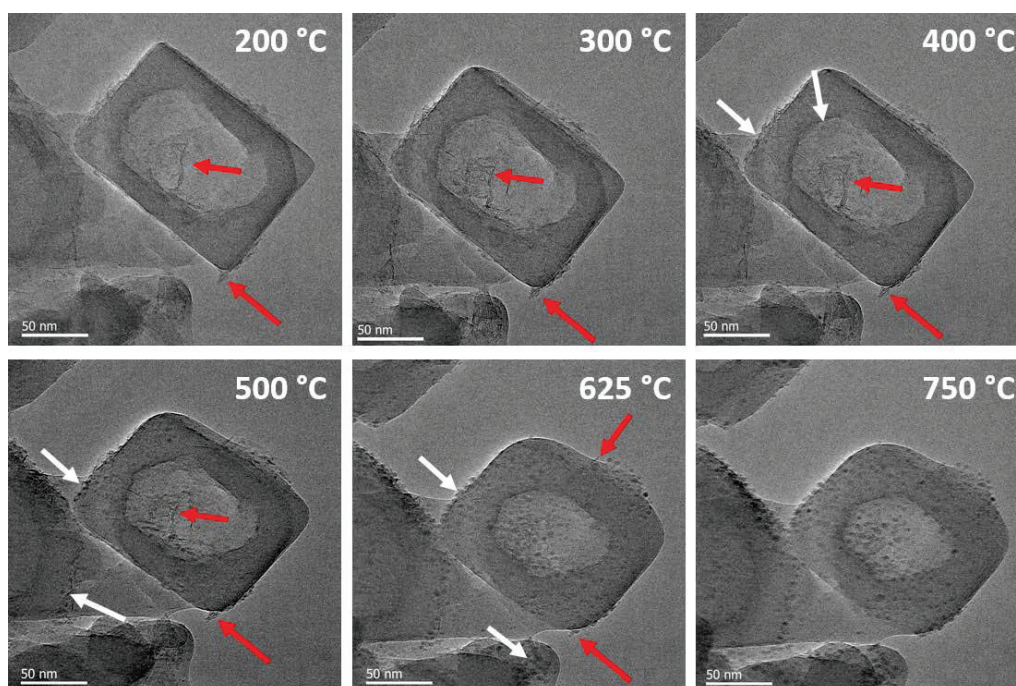


Figure 3.11 TEM images of the NiO@Sil-1 SH under a H₂ pressure of 5.5 mbar from 200 up to 750 °C. Red arrows indicate Ni phyllosilicate species and white arrows indicate Ni particles.

The evolution of the calcined NiO@Sil-1 SH with temperature was followed by Environmental Transmission Electron Microscope (ETEM) under H₂ pressure to study the reduction of phyllosilicate species. Images of a zeolite crystal after heating *in situ* up to 750 °C are shown in Figure 3.11. At 200 °C, Ni phyllosilicates are observed both inside and outside the hollow cavity. Small Ni particles (white arrows) start to be formed upon 300 °C on the external surface of the crystal while the phyllosilicate fibers (red arrows) remain mostly intact. This is in agreement with our observations in TGA and corresponds to the reduction of NiO species that did not form Ni phyllosilicates during the TPAOH treatment (Figure 3.9). Above 500 °C, Ni-based fibers start to be reduced and are no more observed at 750 °C, as expected from TGA results. The accordance between TGA and *in situ* ETEM results should however be further queried, as the sample is prone to reduction under exposure to the electron beam. Additionally, this slow acquisition method (170 min in total), yet similar to the heating rate used in the TGA measurements, did not preserve the integrity of the sample leading to a shrinkage and a loss in crystallinity of the zeolite membrane.

Figure 3.12a shows the phyllosilicate-containing area analyzed by electron energy loss spectroscopy (EELS) at 200 (top picture) and 750 °C (bottom picture). EELS measurements record the change in the kinetic energy of an incident electron after it has passed through and interacted with a sample to provide structural information. Here, EEL spectra (Figure 3.12b) were acquired *in situ* before (blue signal) and after (red signal) reduction of Ni species to determine changes in the shapes of the Ni L₂ (respectively L₃) jump in intensity observed at 872 (resp. 855) eV which is induced by the transition of Ni electrons from 2p_{1/2} (resp. 2p_{3/2}) core states to empty 3d states. The ratio between the L₃ and L₂ peaks depends on the oxidation state of Ni. Reference EEL spectra of NiO and Ni are presented in

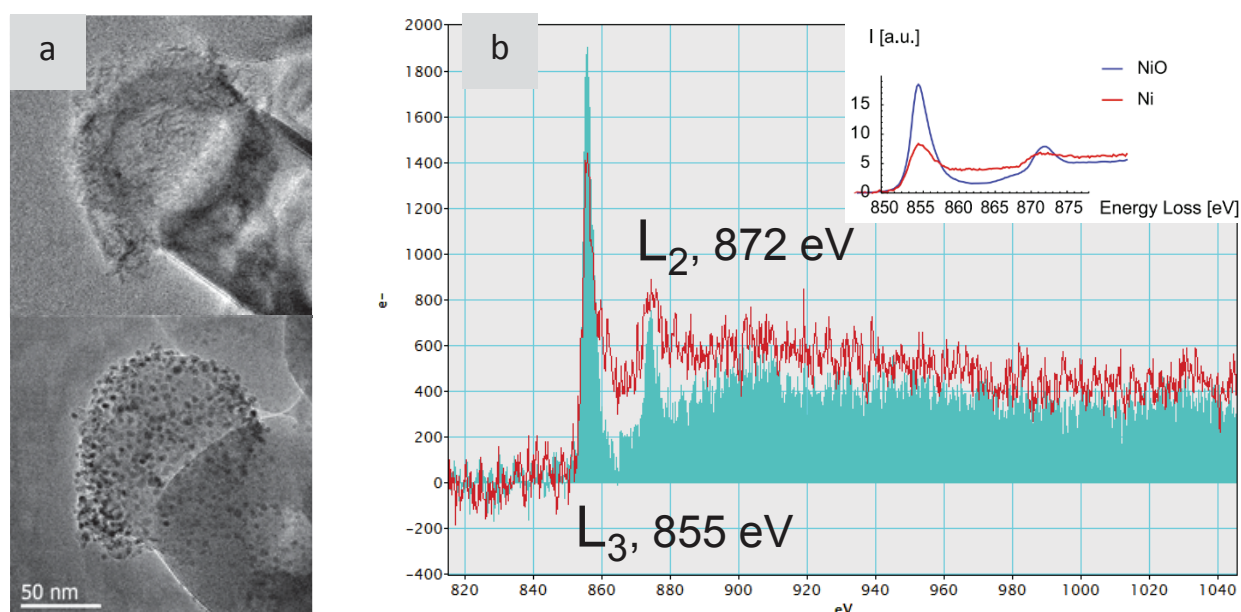


Figure 3.12 (a) TEM images and (b) EELS spectra of the NiO@Sil-1 SH before (blue) and after (red) reduction.

the inset of Figure 3.12b and show that the ratio of the Ni L₃ over L₂ intensities tends to equilibrate upon reduction of NiO into Ni.^[185,186] A decrease from ca. 5.8 to 3.7 in the L₃/L₂ ratio was observed experimentally, stressing the reduction of NiO species in Ni metal.

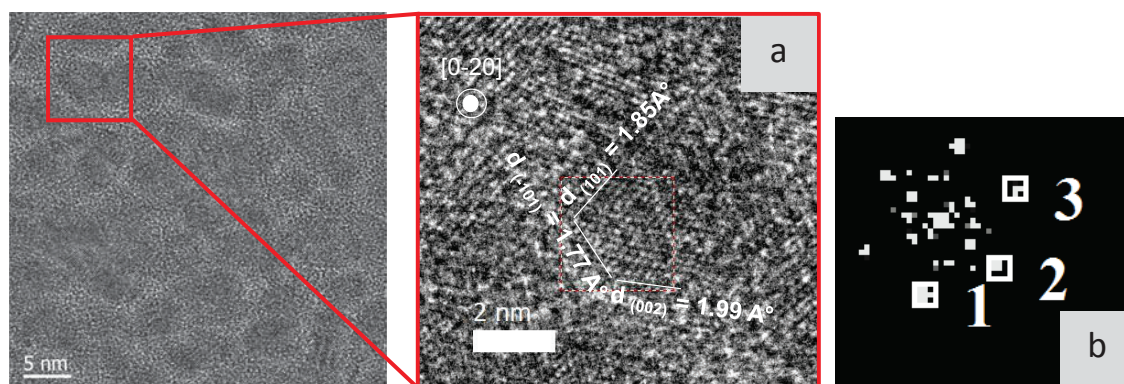


Figure 3.13 (a) HRTEM picture and (b) corresponding Fast Fourier Transform (FFT) diffraction patterns of a Ni particle from NiO@Sil-1 SH after *in situ* reduction at 750 °C in H₂ pressure.

The HRTEM image and the corresponding Fast Fourier Transform (FFT) diffraction patterns of a Ni particle from NiO@Sil-1 SH after *in situ* reduction at 750 °C and located in the area of the EELS analysis are given in Figure 3.13. The interplanar angles along (101), (002) and (-101) planes are measured from the diffraction patterns. The interplanar lattice spacings along a axis are 1.85, 1.99 and 1.77 respectively which is in descent agreement with the unit cell parameter of hexagonal metallic nickel particles (JCPDS 89-7129) along a-axis (Table 3.2). [0-20] is the axis perpendicular to the image planar, which is calculated from the 3 known plans on the image.

Table 3.2 Experimental and theoretical of interplanar spacings and angles of nickel metallic particle

Spot	Observed d-spacing (a) (Å)	Measured angles to spot 1 (°)	Theoretical d-spacing (a) (Å)	Theoretical angle between plans (°)	HKL
1	1.85	0	2.01	0	101
2	1.99	64.14	2.16	62.28	002
3	1.77	125.42	2.01	124.56	-101

2.2.3. X-ray diffraction

The XRD patterns of all samples were consistent with the presence of well-crystallized silicalite-1 (Figure 3.14). Weak peaks attributed to NiO could also be noted in the cases of the calcined 5%Ni/Sil-1 and 5%Ni@Sil-1 SH (Figure 3.14a). However, no XRD pattern associated with Ni phyllosilicate could be observed. The reduction of the samples at 750 °C resulted in the conversion of the NiO into metallic Ni, as shown for instance in the case of the reduced 5%Ni@Sil-1 SH (pattern n°4), better seen in the corresponding difference diffractogram (pattern n°6).

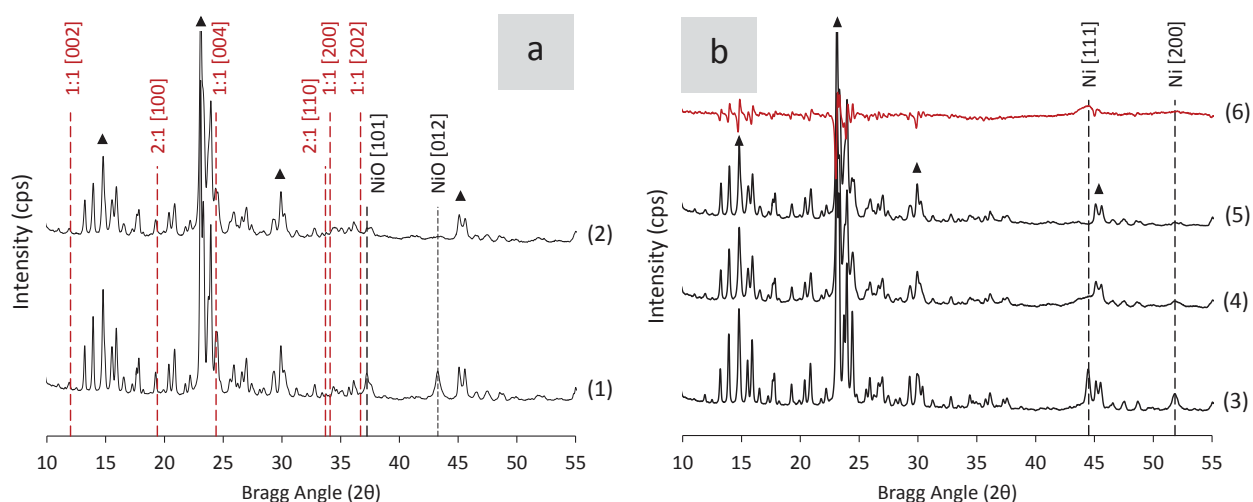


Figure 3.14 XRD patterns of (a) calcined and (b) reduced samples: (1) NiO/Sil-1, (2) NiO@Sil-1, (3) 5%Ni/Sil-1, (4) 5%Ni@Sil-1, (5) CitAc Ni@Sil-1. Pattern (6) was obtained by subtracting (2) from (4). The positions of the main characteristic XRD peaks of NiO (JCPDS: 47-1049), Ni phyllosilicate (1:1 JCPDS: 49-1859, 2:1 JCPDS: 43-0663) and Ni (JCPDS: 04-0850) are represented by dashed lines. (▲): Silicalite-1 (JCPDS: 48-0136).

A main diffraction peak was observed at $2\theta = 44.5^\circ$, characteristic of the [111] facet in the cubic Ni structure (JCPDS 04-0850). The CitAc Ni@Sil-1 SH sample (pattern n°5) only exhibited peaks typical of silicalite-1, the Ni phases were not detected by XRD, due to the low Ni loading of this sample (Table 3.1). Regarding the peaks of the silicalite-1 phase, minor modifications in the patterns of 5%Ni/Sil-1 and 5%Ni@Sil-1 SH could be observed in the region between 23 and 25° . This will be further discussed in chapter 4.

2.2.4. Nitrogen physisorption

The 5%Ni/Sil-1 sample exhibited a type-I isotherm (Figure 3.15a), which is a fingerprint of purely microporous compounds. Note that the isotherm of 5%Ni/Sil-1 was similar to that of the parent silicalite-1 (data not shown), meaning that the sample porosity was not affected by the Ni impregnation and subsequent thermal treatments. The micropore volume ($0.14 \text{ cm}^3 \text{ g}^{-1}$) was defined as the volume of N_2 adsorbed at the point at which the derivative of the adsorption branch (measured from two consecutive points) became lower than $10^3 \text{ cm}^3 \text{ g}^{-1}$. This value is consistent with those generally reported for MFI-type zeolites.^[187,188] The total pore volume was estimated from the nitrogen uptake on the desorption branch at $P/P^\circ = 0.9$.

5%Ni@Sil-1 SH (Figure 3.15b) exhibited a combination of type-I and IV isotherms.^[119] The adsorption branch was similar to that of 5%Ni/Sil-1, indicating that the microporous nature of the sample was preserved following the formation of the hollow core. The minor hysteresis at $P/P^\circ = 0.2$ is usually attributed to a phase transition of adsorbed N_2 in defect-free highly crystalline silicalite-1.^[189,190]

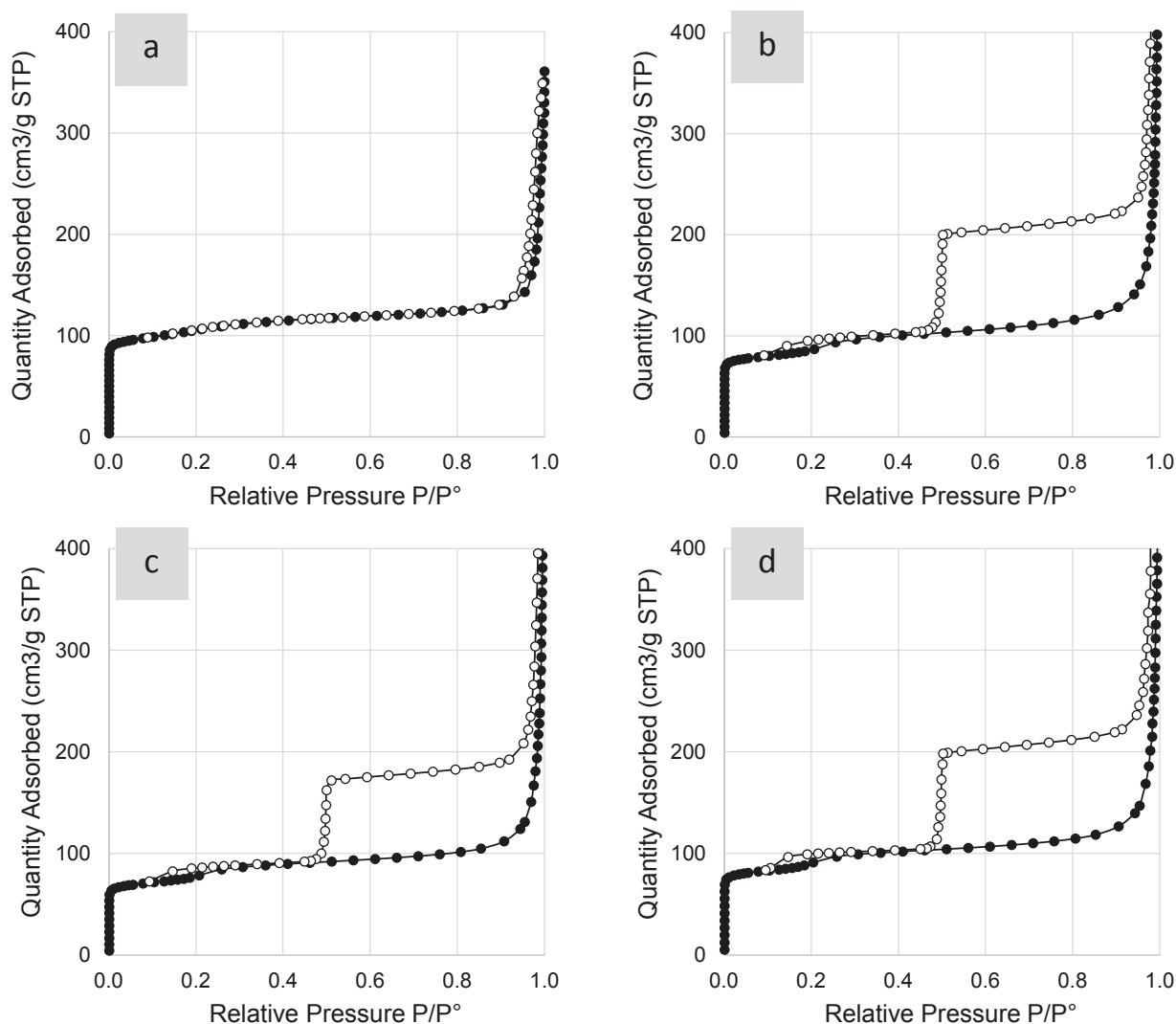


Figure 3.15 N₂ adsorption (full circle) and desorption (empty symbol) isotherms at 77 K for the (a) 5%Ni/Sil-1, (b) 5%Ni@Sil-1 SH, (c) CitAc 5%Ni@Sil-1 SH and (d) calc-CitAc Ni@Sil-1 SH.

The TPAOH-based treatment proceeds through a dissolution/recrystallization during which the defect-rich core of the zeolite crystal is preferentially dissolved and the resulting silica species are recrystallized on the crystal outer surface upon hydrothermal treatment to form a crack-free zeolite shell.^[123] During the TPAOH treatment, nickel cations react with dissolved silica species yielding fibrous nickel phyllosilicates attached to the zeolite. The formation of these fibers partly hinders the recrystallization step, explaining the somewhat lower V_{micro} ($0.12 \text{ cm}^3 \text{ g}^{-1}$) as compared to the case of the 5%Ni/Sil-1 sample ($0.14 \text{ cm}^3 \text{ g}^{-1}$) (Table 3.3). The large H₂-type hysteresis loop with a steep closure at $P/P^\circ = 0.45$, known as “cavitation” phenomenon is characteristic of crack-free zeolite shells with an inner cavity only accessible via pores smaller than 4 nm.^[191,192] The desorption branch was parallel to the adsorption branch, the difference between the two branches corresponding to the amount of N₂ adsorbed in internal cavities. The volume of this entrapped macroporous cavity was $0.15 \text{ cm}^3 \text{ g}^{-1}$.

Table 3.3 Porosity of the zeolitic samples

Catalyst	$S_{\text{BET}}^{\text{a}}$ ($\text{m}^2 \text{g}^{-1}$)	$V_{\text{micro}}^{\text{b}}$ ($\text{cm}^3 \text{g}^{-1}$)	$V_{\text{cavity}}^{\text{c}}$ ($\text{cm}^3 \text{g}^{-1}$)	$V_{\text{total}}^{\text{d}}$ ($\text{cm}^3 \text{g}^{-1}$)
5%Ni/Sil-1	369	0.14	0	0.20
5%Ni@Sil-1	316	0.11	0.15	0.34
CitAc Ni@Sil-1	272	0.10	0.11	0.29
calc-CitAc Ni@Sil-1	328	0.12	0.15	0.34

^a BET method

^b Volume of N_2 adsorbed when the slope of the adsorption branch becomes lower than $10^3 \text{ cm}^3 \text{ g}^{-1}$

^c Difference in N_2 uptake between the adsorption and the desorption branches of the isotherms at $P/P^\circ = 0.5$

^d Volume of N_2 adsorbed at $P/P^\circ = 0.9$ from desorption branch

The textural properties of the citric acid-treated sample (i.e. CitAc Ni@Sil-1 SH) were similar to those of the parent sample 5%Ni@Sil-1 SH (Table 3.3). The lower S_{BET} and pore volumes values obtained were presumably due to carbonaceous deposits created during the treatment with citric acid and the subsequent reduction. Shi et al. have shown that large proportions of carbonaceous deposits can be left on samples prepared with citric acid-based methods.^[193] As a matter of fact, additional calcination of the sample CitAc Ni@Sil-1 SH at 550 °C during 6 h led to increased porosity (Table 3.3, sample calc-CitAc Ni@Sil-1 SH).

2.2.5. Infrared spectroscopy

Figure 3.16 presents the DRIFT spectra obtained for the 5%Ni/Sil-1, 5%Ni@Sil-1 SH and CitAc Ni@Sil-1 SH samples in the region of the OH groups ($4000\text{-}3400 \text{ cm}^{-1}$). Spectra were corrected with the spectrum of pure H_2O (NIST database) and normalized using the area of the silica overtone band at 1875 cm^{-1} . Different OH species are observed at 3740, 3730 and 3520 cm^{-1} that correspond to stretching vibrations of Si–OH on the external surfaces of crystals, free Si-OH in defects and Si-OH in defects bonded by hydrogen bonding to framework oxygen in hydroxyl nests, respectively. We observed that the treatment of silicalite-1 with TPAOH decreases the intensity of both bands at 3520 and 3730 cm^{-1} , which is attributed to the dissolution of the defect-rich core of the parent zeolite and subsequent recrystallization. It should be noted that the band related to isolated surface silanol groups at 3740 cm^{-1} was not impacted, as the recrystallization step leads to a new surface with a similar density of SiOH groups.

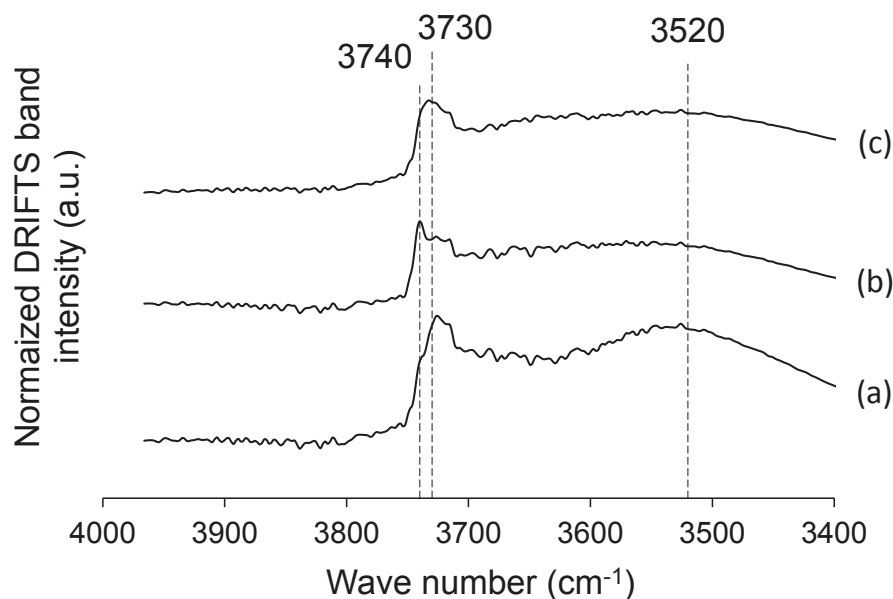


Figure 3.16 IR spectra of (a) 5%Ni/Sil-1, (b) 5%Ni@Sil-1 and (c) CitAc Ni@Sil-1 in the 4000-3400 cm^{-1} region.

Interestingly, we observed that after acid washing the intensity of both bands at 3730 and 3520 cm^{-1} slightly increased (Figure 3.16c), which could be attributed to the formation of internal defects within the zeolite framework. This remark is important as the collapse upon thermal annealing of MFI-type frameworks is nucleated by binary encounter of defect sites and then propagates rapidly throughout the crystal, hindering their use in high-temperature applications.^[194] Additionally, Saczk and co-workers reported that a similar citric acid treatment (0.5-2 M solution, 60-80 °C, 3 h) could lead to the creation of defects and the formation of mesopores in H-ZSM-5 zeolites.^[195]

2.3. Extension of the preparation method to Rh and NiPt

2.3.1. Preparation of Rh particles encapsulated in single hollow silicalite-1

Similarly to nickel, several synthesis methods were attempted to prepare an Rh-based sample made of Rh nanoparticles encapsulated inside hollow silicalite-1 single crystals. Both post impregnation method and impregnation followed by the formation of hollow structures method were considered. Various precursors ($\text{Rh}(\text{NO}_3)_3$, $\text{Rh}(\text{NO}_3)_3 \cdot 2(\text{H}_2\text{O})$, $\text{Rh}_2(\text{OOCCH}_3)_4$, RhCl_3) and impregnation conditions (temperature, pH, duration, nature of the solvent) were investigated but Rh always appeared to be located outside the nanoboxes (Figure 3.17). The origin of this failure is still not clear but may be associated either with the poor solubility and/or diffusional restrictions of the Rh(III) precursors. No attempts were made to further investigate this point.

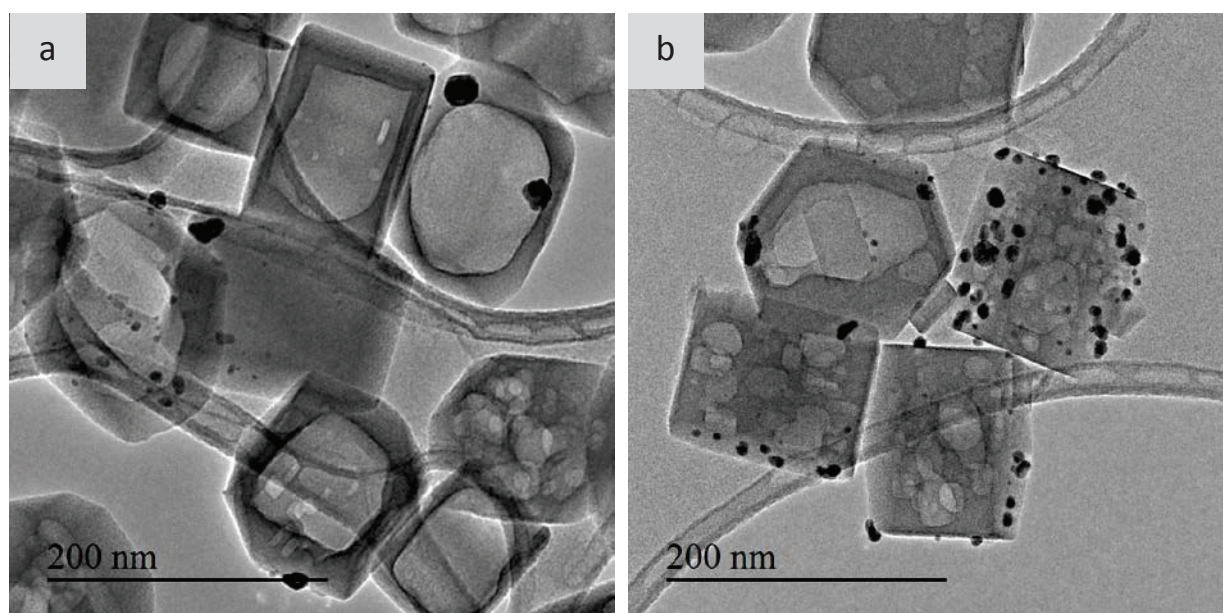


Figure 3.17 TEM pictures of Rh-based hollow silicalite-1 samples prepared by (a) post-impregnation and (b) impregnation followed by the formation of hollow structures using $\text{Rh}(\text{NO}_3)_3 \cdot 2(\text{H}_2\text{O})$ as precursor and H_2O as solvent.

2.3.2. Preparation of NiPt particles encapsulated in single hollow silicalite-1

We attempted to prepare an alloy-based 5%Ni1%Pt@Sil-1 SH sample by the impregnation followed by the formation of hollow structures method. Similarly to the synthesis of 5%Ni@Sil-1 SH, bulk silicalite-1 crystals were co-impregnated with Ni and Pt ($\text{Pt}(\text{NH}_3)_4(\text{NO}_3)_2$) precursors, treated with TPAOH, calcined at 450 °C and reduced at 750 °C. TEM images of the sample are given in Figure 3.18.

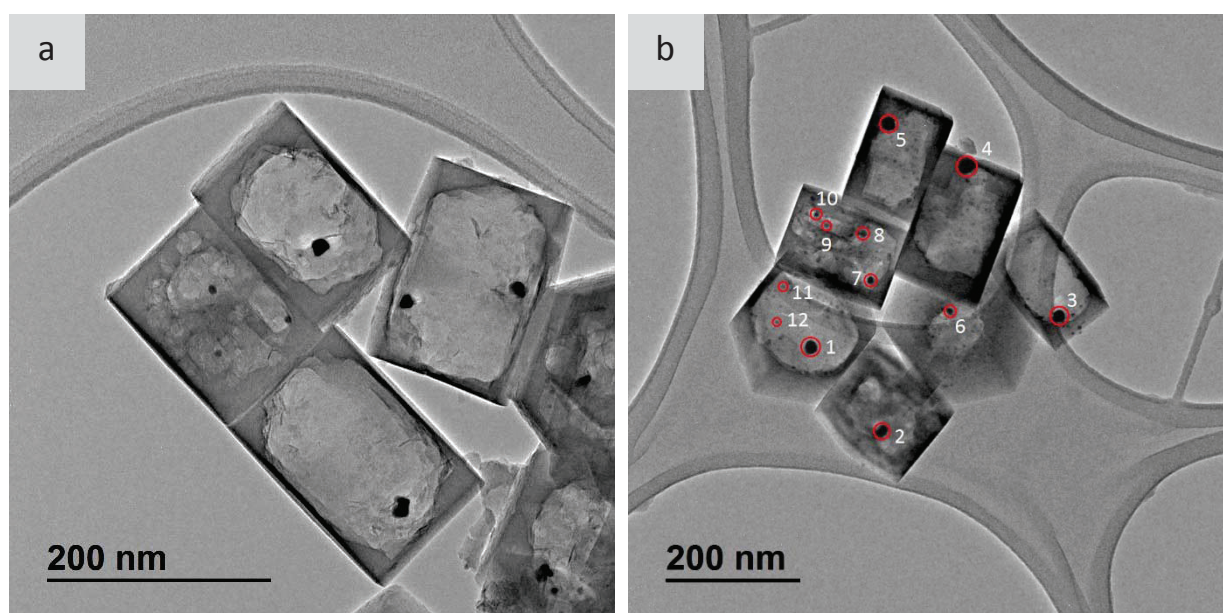


Figure 3.18 TEM pictures of the NiPt-based hollow silicalite-1 (a) calcined at 450 °C and (b) reduced at 750 °C. The zones analyzed by EDX are indicated by a red circle. EDX results are reported in Table 3.4.

Table 3.4 Local composition in Ni and Pt revealed by EDX of the various zones circles in Figure 3.18b.

Zone	1	2	3	4	5	6	7	8	9	10	11	12
Ni (wt.%)	8.8	5.3	11.1	4.7	6.3	7.2	12.2	9.8	11.9	8.9	6.6	7.6
Pt (wt.%)	71.7	27.1	34.5	38.7	25.7	13.7	19.6	15.6	4.2	6.7	0.0	0.0
Ni/Pt	0.1	0.2	0.3	0.1	0.3	0.5	0.6	0.6	2.9	1.3	-	-

Figure 3.18a shows that the sample calcined at 450 °C turned out to lead to segregated Pt particles and Ni phyllosilicates. Pt@Sil-1 materials are known to form a unique Pt-based particle per nanobox upon calcination.^[147] After reduction at 750 °C, several small Ni-rich particles and a unique large Pt-rich particle were present in each single hollow crystal (Table 3.4). The origin of the segregation observed here is due to differences in reduction temperature associated with intermediates phases, in particular the hard-to-reduce phyllosilicate of Ni which hamper the formation of NiPt nanoalloys that are homogeneous in composition (Figure 3.9). It must be noted that the Ni/Pt ratio increased in case of particles included in silicalite-1 crystals presenting several inner cavities (zones 7, 8, 9 and 10), stressing that spatial restriction could limit the segregation of Pt and favor its alloying with Ni. The reduced sample was further treated at 800 °C for 3 h in H₂, yet the formation of unique NiPt particles was not achieved, Ni particles being too strongly bonded to the inner zeolite walls (Figure 3.19a). Post impregnation of the Pt precursor was also attempted on the reduced 5%Ni@Sil-1 SH sample, but the Pt content appeared to be located outside of the nanoboxes (Figure 3.19b). No more attempts were made to improve this method.

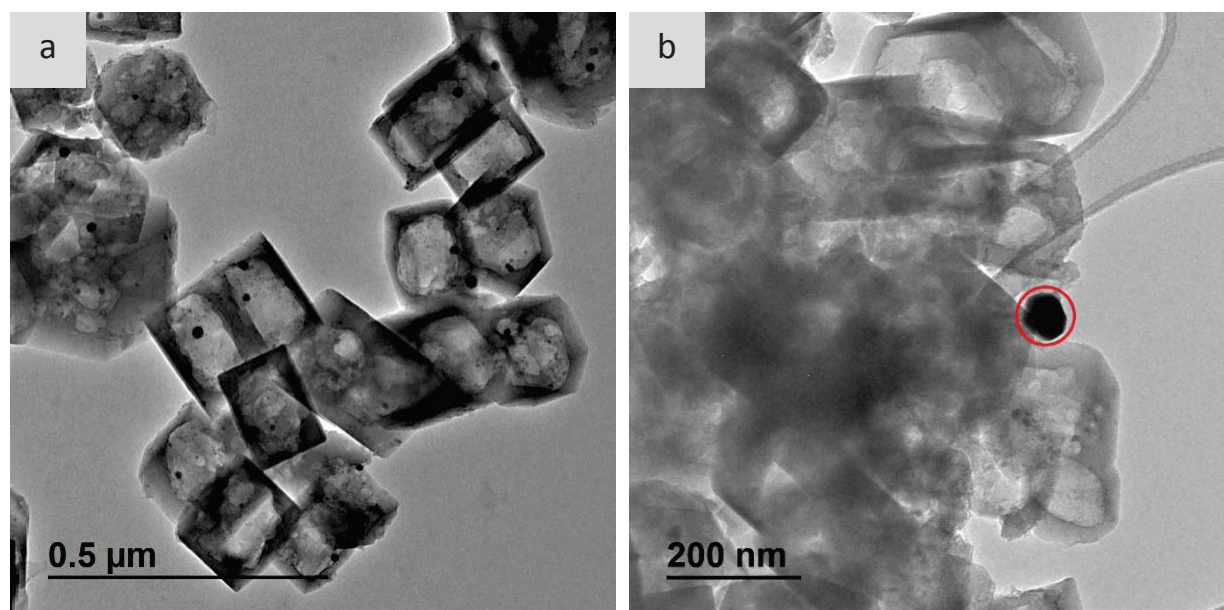


Figure 3.19 TEM pictures of the NiPt-based hollow silicalite-1 (a) further reduced at 800 °C and (b) prepared by post-impregnation of the 5%Ni@Sil-1 with Pt(NH₃)₄(NO₃)₂ precursor. The red circle indicates external Pt.

2.4. Catalytic results

2.4.1. Arene hydrogenation

The catalytic activity of the 5%Ni/Sil-1, 5%Ni@Sil-1 SH and CitAc Ni@Sil-1 SH samples in the hydrogenation of toluene (kinetic diameter: 0.58 nm) and mesitylene (1,3,5-trimethylbenzene, kinetic diameter: 0.87 nm) was measured between 50 and 100 °C (Table 3.5 and Figure 3.20). Note that the silicalite-1 support did not exhibit any catalytic activity. The only product detected in each case was the corresponding cycloalkane. These two model reactants were chosen because the transport of mesitylene through the silicalite-1 pores (0.55 nm pore size) was shown to be totally blocked under these experimental conditions, in contrast to that of toluene, which was unrestricted.^[147] Therefore, any mesitylene hydrogenation activity will be associated with Ni nanoparticles that are not fully coated by a MFI-type membrane.

Table 3.5 Arene hydrogenation activity for the Ni-based samples.

Catalyst	Toluene hydrogenation rate			Mesitylene hydrogenation rate			Toluene / Mesitylene hydrogenation rate ratio at 80°C
	Rate at 80°C	TOF at 80°C ^[a]	E _{app}	Rate at 80°C	TOF at 80°C ^[a]	E _{app}	
	($\mu\text{mol s}^{-1}\text{g}_{\text{Ni}}^{-1}$)	(10^{-3} s^{-1})	(kJ mol^{-1})	($\mu\text{mol s}^{-1}\text{g}_{\text{Ni}}^{-1}$)	(10^{-3} s^{-1})	(kJ mol^{-1})	
5%Ni/Sil-1	0.58	1.2 ± 0.5	54.5 ± 3	0.09	0.19 ± 0.06	60 ± 4	6
5%Ni@Sil-1	7.7	2.8 ± 1	55 ± 3	0.38	0.14 ± 0.05	64 ± 4	20
CitAc Ni@Sil-1	19	4.3 ± 1.5	56 ± 3	0.28	0.06 ± 0.02	69 ± 5	67

^[a] TOF: Turn Over Frequency, expressed as molecules of reactant converted per second per surface Ni atoms.

It should be stressed that the three catalysts exhibited similar apparent activation energies (E_{app}) of ca. 55 kJ mol⁻¹ for toluene hydrogenation (Table 3.5), in line with those reported in the literature for silica-supported Ni under similar conditions.^[196,197] This result indicates that the reaction for 5%Ni@Sil-1 SH and CitAc Ni@Sil-1 SH was not limited by toluene transport in the micropores of the zeolite membrane, as a much lower (possibly halved) E_{app} would otherwise be expected.^[198]

The TOFs for toluene hydrogenation were of the same order of magnitude for the three Ni-based samples (Table 3.5) and appeared to decrease slightly with increasing Ni nanoparticle size (Table 3.1), probably due the mild structure-sensitivity of arene hydrogenation over Ni.^[199] These TOFs were close to those reported in the literature, i.e. a TOF value of $1.2 \times 10^{-3}\text{ s}^{-1}$ was calculated at 80 °C from the toluene hydrogenation work on nickel reported by Keane and Patterson.^[200]

The TOF for the hydrogenation of mesitylene measured over the 5%Ni/Sil-1, in which the Ni nanoparticles are not coated by the silicalite-1, were lower than those of toluene (Table 3.5 and Figure 3.20). The lower TOF of mesitylene was primarily due to the lower reactivity of this bulkier molecule, and also possibly due to the lower partial pressure used.^[201] Interestingly, the decays of the TOFs observed in the case of mesitylene were markedly larger in the cases of the 5%Ni@Sil-1 SH (triangles) and especially in that of the CitAc Ni@Sil-1 SH (circles) catalysts (Figure 3.20). This observation is explained by the fact that a significant fraction of the nickel nanoparticles were embedded in the silicalite-1 nanoboxes for these two materials and were not accessible to mesitylene. Since the CitAc Ni@Sil-1 SH catalyst was still active in mesitylene hydrogenation, one must conclude that the citric acid treatment did not remove all external nickel nanoparticles. In fact, some Ni nanoparticles could still be observed by TEM after citric acid treatment (Figure 3.7b).

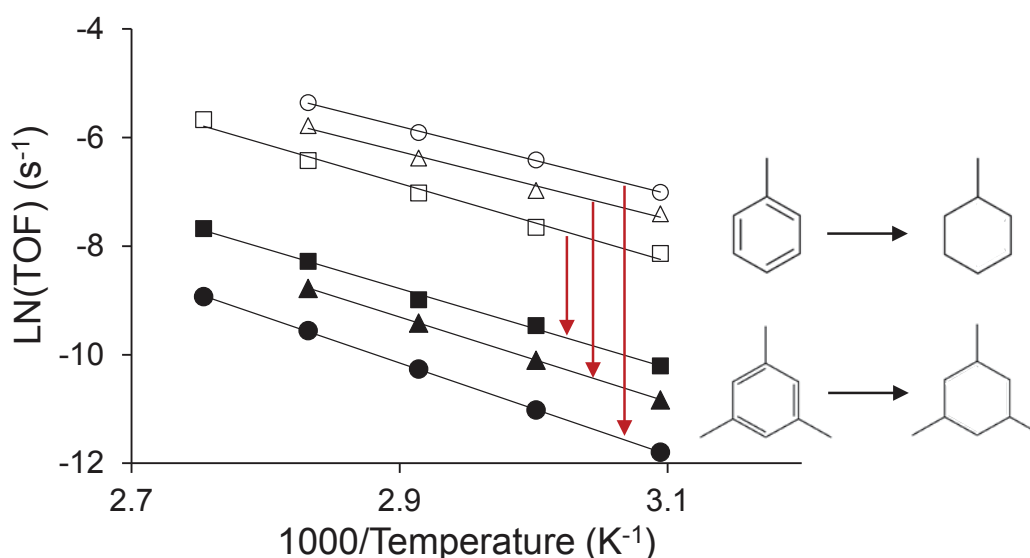


Figure 3.20 Arrhenius plots relating to the TOF of toluene hydrogenation (open symbols) and that of mesitylene (full symbols) over 5%Ni/Sil-1 (square), 5%Ni@Sil-1 (triangle) and CitAc Ni@Sil-1 (circle).

The fraction of nickel surface atoms accessible to mesitylene can be estimated from the ratios between the hydrogenation rate of toluene and mesitylene measured on the various samples (Table 3.5). In the case of the 5%Ni/Sil-1, all the Ni nanoparticles are located outside the zeolite plain crystals and therefore all surface Ni atoms were also accessible to mesitylene. The toluene/mesitylene rate ratio was 6 in this case. The 5%Ni@Sil-1 SH and CitAc Ni@Sil-1 SH would then only contain about 30 % (= 6/20) and 9 % (= 6/67) of Ni sites accessible to mesitylene, respectively. The latter figure thus indicates that the citric acid treatment led to a catalyst in which more than 90% of Ni sites were embedded in silicalite-1.

2.4.2. CO methanation in presence of pyrene

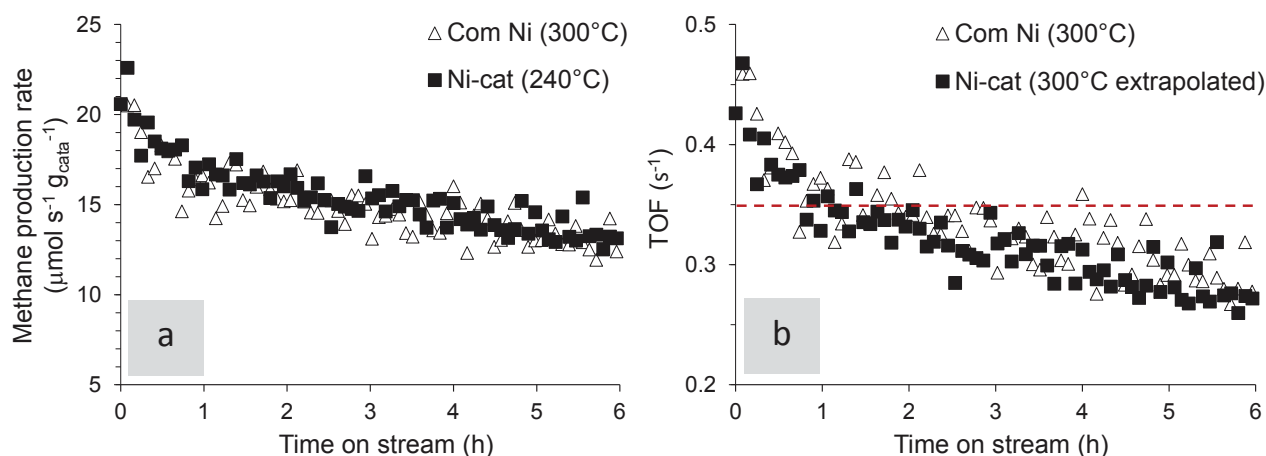


Figure 3.21 (a) CO methanation rate and (b) TOFs at 300 °C for Com Ni (triangles) and at 240 °C for Ni-cat (squares). The TOF of Ni-cat was extrapolated to 300 °C using an activation energy of 97 kJ mol^{-1} .^[163]

The catalytic activity of two supported Ni-based catalysts in the methanation of CO, named Ni-cat (proprietary catalyst) and Com Ni (HiFUEL R110, Alfa Aesar, ref. 45465) was respectively measured at 240 and 300 °C to remain under differential conditions (Figure 3.21). Structural properties of these samples were evaluated by *in situ* H_2 chemisorption measurements after reduction at 700 °C for 2 hours and are reported in Table 3.6. The two catalysts presented significant differences in terms of particle sizes and were selected to assess the structure sensitivity of the methanation reaction. Prior to the reaction, 20 mg of catalyst was reduced *in situ* at 700 °C for 2 hours to reach a Ni surface area equal to that reported in Table 3.6. The reaction temperature and a high H_2/CO ratio (Table 2.5) were selected to avoid the formation of hot spots. The activity at 240 °C of the highly dispersed Ni-cat was similar to that measured at 300 °C on Com Ni (Figure 3.21a). The profile of activity of both samples shows a slow deactivation. After 18 hours on stream (data not shown), the activity of Ni-cat was $12 \mu\text{mol s}^{-1} \text{g}_{\text{cata}}^{-1}$ and similar to that measured after 6 hours, stressing that this deactivation mechanism is only observed during the first few hours on stream. A similar phenomena was observed by Mirodatos and co-workers, the authors reported that CO hydrogenation induces a marked restructuring of the nickel surface with a selective development of dense planes.

Table 3.6 Textural properties of supported Ni samples

Catalyst	Ni loading (wt.%)	Ni surface area ($\text{m}^2 \text{g}^{-1}$)	Ni dispersion (%)	Ni particle size (nm)
Com Ni	11.4	1.75	2.3	43.5
Ni-cat	19.6	24.9	19.0	6.7

The turn over frequency of Ni-cat was extrapolated at 300 °C using an activation energy of 97 kJ mol⁻¹, a value reported by Sehested et al. under similar experimental conditions.^[163] These TOFs were in excellent agreement with those reported in the literature, i.e. a TOF value of 0.35 s⁻¹ was calculated at 300 °C from the CO hydrogenation work on nickel reported by Sehested et al.^[163] Additionally, the TOFs of both samples were identical, stressing that the methanation of CO on nickel is structure insensitive. Hence, the hydrogenation of CO can be used as a model reaction to derive the number of accessible active sites, assuming a TOF of 0.35 s⁻¹ for each active site and an average area of a surface Ni atom of 6.5 × 10⁻²⁰ m².

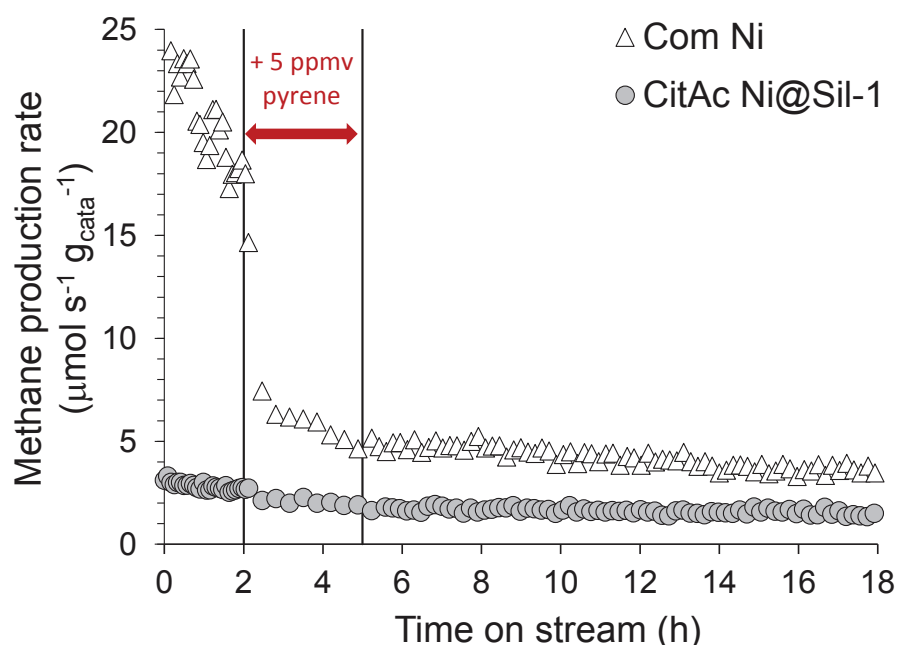


Figure 3.22 CO methanation rate at 300 °C of Com Ni (triangles) and CitAc Ni@Sil-1 (circles). 5 ppmv of pyrene were fed only between 2 h up to 5 h.

The effect of the additions of 5 ppmv of pyrene in the feed stream on the activity in CO methanation was studied on Com Ni and CitAc Ni@Sil-1 SH samples (Figure 3.22). For the Com Ni catalyst, the introduction of pyrene led to a sharp and significant loss of the production of methane at 300 °C. In comparison, the CitAc Ni@Sil-1 SH was almost not impacted by pyrene addition, stressing that the encapsulated Ni nanoparticles were efficiently protected from tar poisoning. Pyrene has a kinetic diameter of 0.75 nm and is hence too large to diffuse through the pores of the MFI-type zeolite at 300 °C. The fraction of accessible nickel surface atoms poisoned by pyrene can be estimated from the drop in activity observed at 2 h. In the case of the Com Ni, for which all surface Ni atoms were accessible to the tar model compound, a marked loss of 66% of active site is measured. The CitAc Ni@Sil-1 SH only contain about 12% of Ni sites accessible to pyrene, strengthening the results of the hydrogenation tests in which approximately 90% of Ni sites embedded in silicalite-1 were estimated.

2.4.3. Sintering test

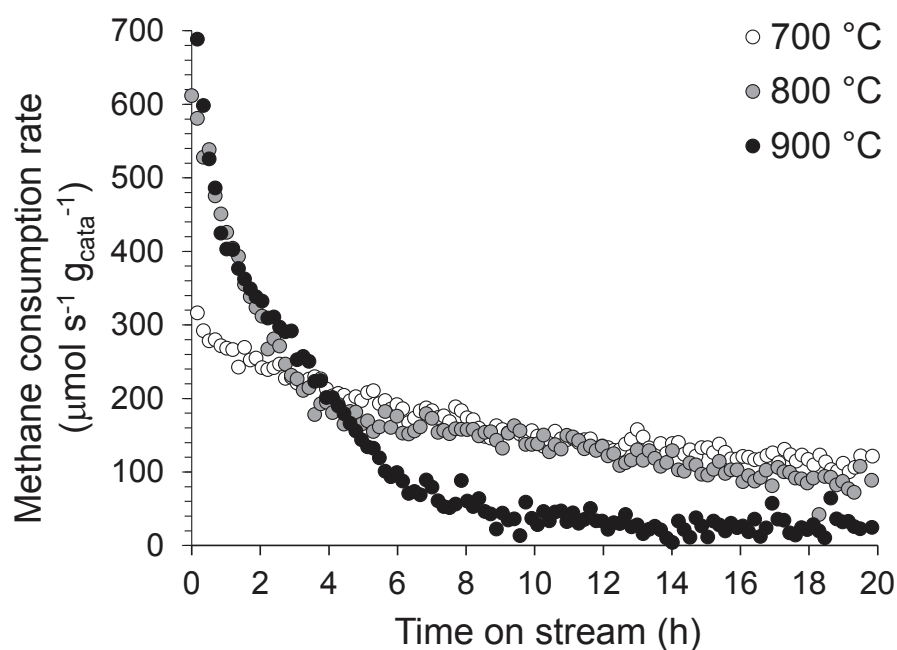


Figure 3.23 Steam methane reforming rate for the CitAc Ni@Sil-1 at 700 (white), 800 (grey) and 900 °C (black). Contaminant-free feed composition is given in Table 2.2.

The thermal stability of Ni particles embedded in silicalite-1 single crystals has been tested in a contaminant-free reforming atmosphere (feed composition given in Table 2.2) at 700, 800 and 900 °C for 18 hours over 10 mg of CitAc Ni@Sil-1 SH material (Figure 3.23). Prior to testing, the sample was reduced *in situ* for 2 hours at 700 °C. TEM images of the samples after sintering and the particle size distributions are shown in Figure 3.24. The activity of the sample at 700 °C decreased significantly with time, before levelling off after ca. 15 hours. TEM pictures of the spent catalyst clearly showed that the average particle size had increased during the catalytic test from $d_{sw} = 4.5 \pm 1.1$ nm to 7.9 ± 2.1 nm (Figure 3.24a), supporting that a gradual loss of dispersion of the catalytic phase was responsible of the loss of reforming activity. Thus, the microporous shell did not prevent metal nanoparticles from sintering at high temperature in a H₂O-rich atmosphere. However, the yolk-shell nanostructure was maintained after the sintering test and the presence of particles outside hollow crystals was not observed. In contrast, the thermal stability of the nanoboxes at 800 and 900 °C was more problematic, shrinkage and complete breakdown of the hollow structure were respectively identified in TEM observations of the used samples (Figure 3.24b and c). The average particle size had markedly increased during the sintering tests at 800 and 900 °C up to $d_{sw} = 12.1 \pm 3.0$ nm and 17.8 ± 6.4 nm, respectively. A sharp sintering-related decrease in catalytic activity was observed during the first 6 hours on stream, the sample being exposed for the first time at these high temperatures. The sample tested at 900 °C was no more active after 10 hours on stream.

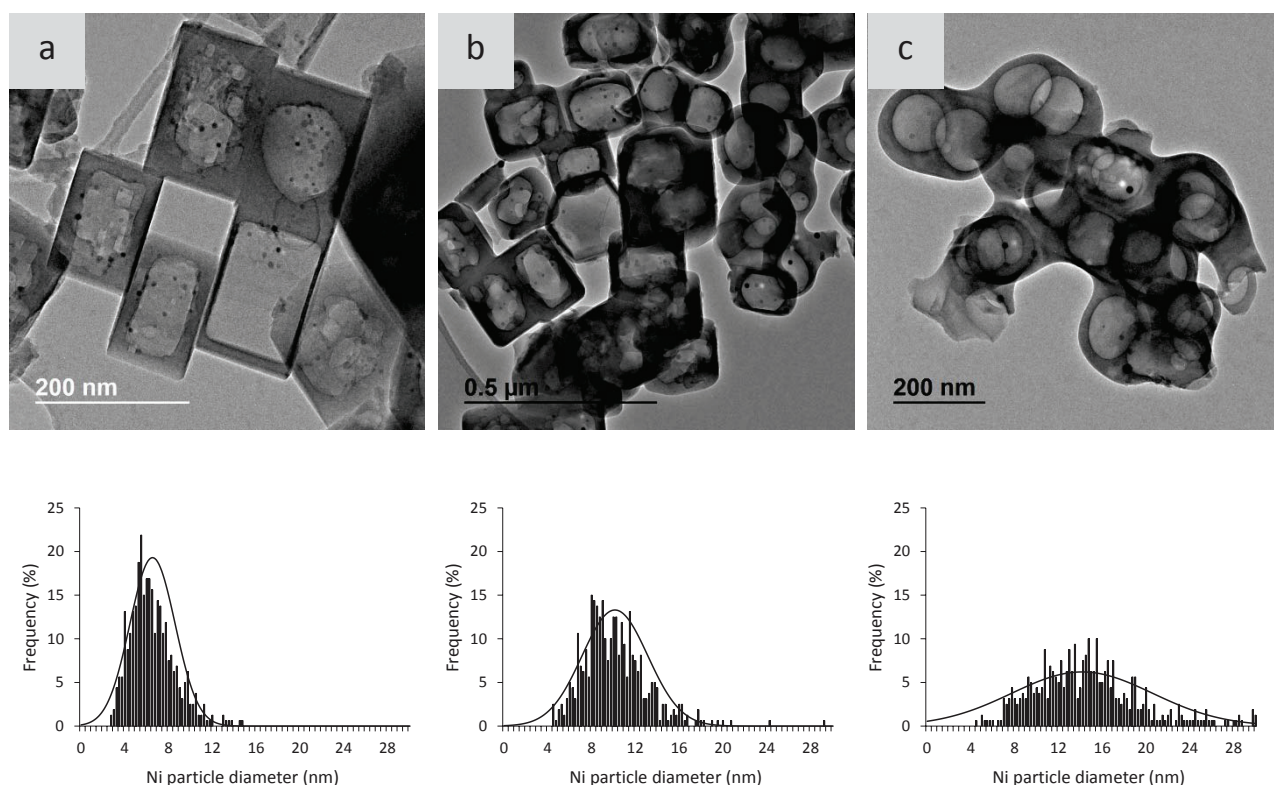


Figure 3.24 TEM images (top) and corresponding particle size distribution (bottom) of used samples at (a) 700, (b) 800 and (c) 900 °C.

3. Conclusions

The original ship-in-a-bottle type synthesis enabled us to prepare encapsulated nickel nanoparticles with size control below 10 nm and narrow particle size distributions. This preparation pathway is straightforward since the hydrothermal conditions required to form the core-shell structure are similar to that needed in the synthesis of the parent zeolite, emphasizing the scalability of this novel method. Each silicalite-1 hollow crystal contained dozens of Ni nanoparticles strongly attached to the inner zeolite wall, resulting from the high-temperature reduction of the intermediate Ni phyllosilicate fibres. The application of this synthesis method to the preparation of Rh@Sil-1 SH and nanoalloy NiPt@Sil-1 SH was not successful because of the poor appropriateness of Rh(III) precursor and the differences in reduction temperature associated with intermediates phases, respectively. The maximum incorporation level of Ni species inside the silicalite-1 was ca. 1.5 wt% and exceeded in the preparation of the 5%Ni@Sil-1 SH catalyst, resulting in the presence of some Ni contents on the external surfaces of the nanoboxes upon the TPAOH treatment. It was possible to use citric acid to selectively leach out most of the external Ni species from 5%NiO@Sil-1 SH material. X-ray diffraction, N₂ physisorption and infrared spectroscopy suggested that the citric acid treatment had only a minor impact on the structural properties of the zeolite membranes. The molecular-sieving

driven selectivity was observed on hollow silicalite-1 samples with a cut-off of ca. 0.7 nm in the arene hydrogenation reactions. The leached sample exhibited a significantly improved selectivity for small arene hydrogenation when compared to the non-treated sample. In the case of CitAc Ni@Sil-1 SH material, we have shown that the single crystal zeolite shell can act as a permselective membrane that prevents the encapsulated metal nanoparticles from tar poisoning in the hydrogenation of CO at 300 °C. Additionally, sintering of the particles encapsulated in each nanobox occurred under reforming atmosphere at 700-900 °C, leading to unstable reforming activities when using the CitAc Ni@Sil-1 SH sample. A poor thermal stability was observed when operating at high (800-900 °C) reforming temperatures. This series of well controlled nanosized transition particles encapsulated in microporous hollow silicalite-1 opens new perspectives in catalysis since they can be applied as shape and/or size selective catalysts in a wide range of catalytic systems at low and moderate temperatures.

Highlights

- Ni@Silicalite-1 SH materials were successfully synthesized using an original preparation method previously developed for noble metal encapsulation.
- The mechanism of Ni metal nanoparticle formation resulted in the high-temperature reduction of Ni phyllosilicate species and was markedly different from that of noble metals.
- The incorporation level of Ni species inside the silicalite-1 was ca. 1.5 wt% and many external Ni particles were observed.
- Citric acid selectively leached out most of the external Ni particles.
- The leached sample exhibited size-selectivity in arene hydrogenation and CO methanation.
- Intra crystal particle sintering and high thermal stability of the membrane were observed in the reforming of producer gas at 700 °C.

Chapter 4 - Highly dispersed Ni nanoparticles via the refinement of the confining hollow structure

1. Introduction

As addressed in chapter 1, many studies have focused on strengthening metal-support interactions (MSI) of Ni catalysts to prevent sintering-related deactivation. Among the different approaches, Burattin et al. studied the reduction of nickel phyllosilicates, prepared by a deposition-precipitation method using urea hydrolysis, that are promising synthesis intermediates showing a strong MSI property.^[84,85] The advantage of this method is that the resulting nickel particles are small, evenly dispersed, highly loaded (> 20 wt.% Ni) and more resistant to sintering than those produced by more conventional syntheses.

More recently, Majewsky et al. used this method to prepare core@shell materials that consist in silica spheres covered with a nickel phyllosilicate layer.^[184,202] The catalyst exhibited noteworthy activity and stability for the low-temperature steam methane reforming. The authors attributed these performances to coke-resistance property due to the strong interaction of nickel with support, confirmed by temperature programmed reduction (TPR) analysis. Yet, no information relating to nickel particle size before and after use was given.

Zhang et al. reported an alternative synthesis of Ni-containing phyllosilicates via the ammonia evaporation method.^[203] The reduced catalyst presented both higher activity and stability in the steam reforming of ethanol at 600 °C when compared to that prepared by incipient wetness impregnation. The authors associated this feature to hindrance against the formation of a nickel carbide phase, and to a strong MSI-related sintering resistance. Yet, the authors did not discuss the discrepancies in nickel surface areas measured from TEM observations and H₂ chemisorption tests, which suggests that nickel surface sites were not all accessible.

In a former study at IRCELYON, the sintering resistance of a Pt@silicalite-1 catalyst under H₂ at 750 °C was reported by assessing the evolution of the mean particle size which remained unchanged along the test. This material consisted of hollow silicalite-1 single crystals, each of them encapsulating a unique Pt nanoparticle of 6-14 nm in diameter.^[147]

In chapter 3, we have seen that Ni nanoparticles encapsulated inside single hollow nanocrystals deactivate under steam reforming conditions. Despite the strong MSI resulting from the high temperature reduction of phyllosilicates fibers, nickel particles sinter during the first few hours on stream within the confined environment to form larger ones. The spatial restriction strategy exerted by the nanoshell is defeated by the fact that each single hollow crystal encapsulate several particles which are able to make contact under reforming operations. Hence, in this case the strong MSI is regarded as a drawback preventing the formation of a unique, isolated and stable Ni particle upon reduction of the nickel phyllosilicates. However, the small particle size of the reduced catalyst originates from these strong interactions.

In this chapter, we report the preparation of Ni-containing multi hollow (MH) zeolitic shells. These monocrystalline microcapsules consist of silicalite-1 nanocrystals containing several inner cavities and were prepared using TBPOH as a mild desilicating agent. This sample will try to combine the best of two worlds:

- A high metallic dispersion deriving from the reduction of nickel phyllosilicates formed during the basic treatment
- An improved sintering resistance of the metallic guest originating from the enhanced spatial restrictive feature of the multi-hollow structure

We will provide here some insights on the influence of the porous architecture on the size-selectivity and on the reforming stability of this advanced encapsulated catalyst.

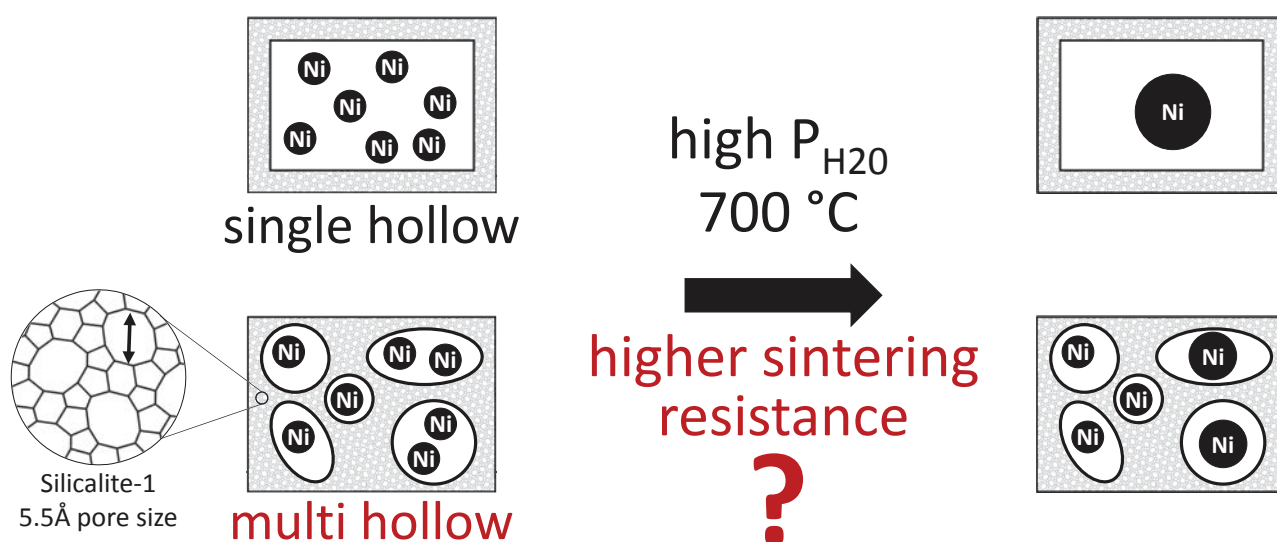


Figure 4.1 Scheme of the potential higher sintering resistance property of multi hollow Ni@Sil-1 catalysts.

2. Characterization of multi hollow catalysts

2.1. Ni-free silicalite-1 hollow crystals

As reported in chapter 2, two different types of Ni-free hollow silicalite-1 were obtained depending on the nature of templating molecules and crystallization temperature. Single-hollow silicalite-1 crystals (Sil-1 SH) were prepared using TPAOH. Typically, single-crystal regular nanoboxes of ca. 200 nm in size with a wall thickness around 20-30 nm were obtained after treatment of the pristine crystals (Figure 4.2a) at 170 °C for 24 hours (Figure 4.2b). Multi-hollow crystals (Sil-1 MH) were synthesized using solutions of TBPOH for 96 hours at a lower temperature, typically 115 °C. In fact, TBPOH is not the best templating molecule for the crystallization of MFI-type zeolites. However, under specific crystallization conditions, TBPOH can direct the crystallization of silicalite-1 and ZSM-5 as well as mixtures of MFI/MEL (ZSM-5/ZSM-11) structures. Tuel et al. have reported the synthesis of titanium silicalite-1 (TS-1) using TBP⁺ ions.^[204] Yet, large crystals of 2-3 μm in size were obtained under their synthesis conditions, resulting in poor catalytic activity. It has also been shown that the combination of TBPOH with relatively low hydrothermal synthesis temperatures could lead to MFI-type zeolites with hierarchical structures, consisting of orthogonally connected thin nanosheets of ca. 2 nm thickness. This house-of-cards arrangement of zeolite nanosheets created intercrystalline mesopores that could be used to improve molecular traffic and catalytic activities in etherification reactions.^[205] When applied to silicalite-1 modification, the strategy effectively led to highly mesoporous nanocrystals with many regular voids of 10-20 nm in diameter size separated by thin zeolite layers inside the crystals (Figure 4.2c).

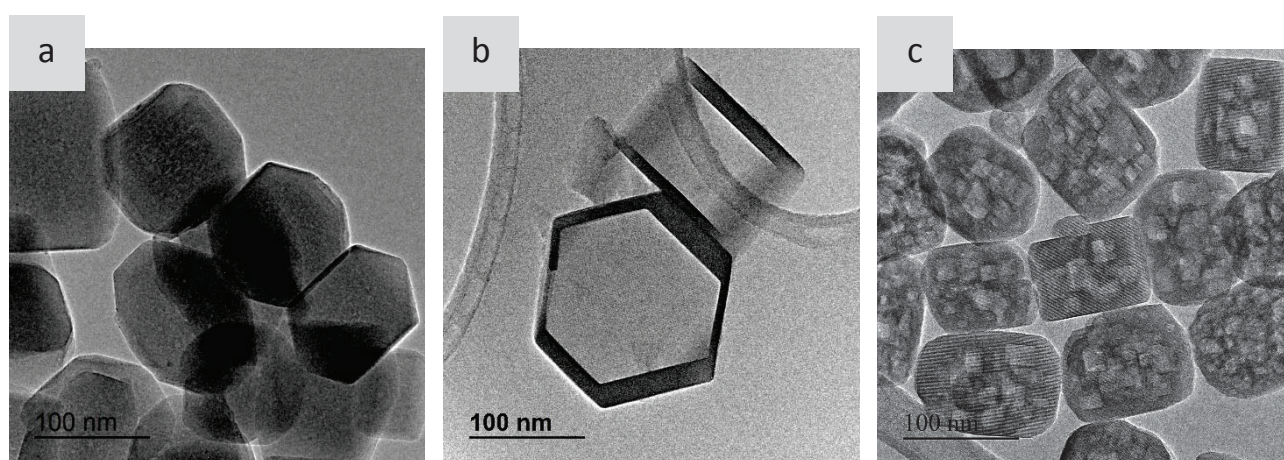
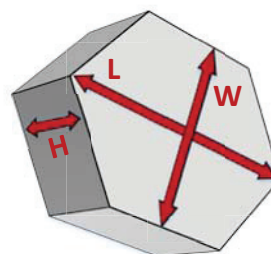


Figure 4.2 TEM images of plain (a), single-hollow (b) and multi-hollow (c) Ni-free silicalite-1 single crystals (magnification x 30000).

In contrast to a direct synthesis of silicalite-1, the preparation of nanoboxes involves first the dissolution of the inner part of the crystals followed by recrystallization of dissolved species. In the case of TPAOH, both the dissolution and recrystallization rates are improved at high temperature and the corresponding single-hollow zeolites possess regular external faces similar to those observed on original bulk crystals. Recrystallization of dissolved species was even confirmed by the slightly larger external dimensions of the crystals, thus supporting our previous model for the formation of hollow structures (Table 4.1). With TBPOH, the relatively low crystallization temperature makes that dissolution and recrystallization were not complete, as evidenced by the irregular shape of hollow crystals and their smaller mean size as compared to the non-treated material (Table 4.1).

Table 4.1 Average size of the plain and hollow single crystals in nm (length x width x height).

Crystals	Average size of the single crystals (L x W x H)
Plain	215 x 175 x 130 nm
Single Hollow	230 x 190 x 145 nm
Multi Hollow	185 x 150 x 115 nm



The textural properties of the single hollow and multi hollow zeolites was also studied by nitrogen physisorption at 77 K (Figure 4.3). Treatment with TPAOH followed by calcination produced type-IV isotherms. A hysteresis loop closing at $P/P^\circ = 0.42$ was observed, this pressure corresponding to the lower limit of N_2 capillary condensation at 77 K. Such hysteresis loops which appear in the multilayer range are generally associated with the filling and emptying of mesoporous structures. For silicalite-1-based materials, this loop is characteristic of internal voids connected to the zeolite surface via apertures smaller than 4 nm; this phenomenon is referred to as the Tensile Strength Effect (TSE).^[189,190,206,207] It reflects the hollow structure of the zeolite and the absence of cracks in the zeolite walls. A small loop was also observed at $P/P^\circ = 0.15$ which is not related to an internal porosity but to a fluid-to-crystalline-like phase transition observed only in monoclinic MFI-type zeolites.^[208] The presence of this small loop is also considered to be an indicator of the high crystallinity degree of the silicalite-1. This loop at $P/P^\circ = 0.15$ was not observed upon treatment with TBPOH and calcination. This absence suggests that the degree of crystallinity of the multi hollow zeolite is lower than that of the single hollow counterpart. This observation is in good agreement with the hypothesis on the recrystallization step which is hampered at low temperature. The multi hollow sample also displays type-IV isotherms with a hysteresis loop closing at $P/P^\circ = 0.42$. A continuous N_2 uptake is observed for P/P° between 0.1 and 0.9, confirming the presence of internal

mesopores with different sizes and a wide pore size distribution. This increase is caused by multilayer adsorption resulting in capillary condensation inside the mesopores below the N_2 condensation pressure. In contrast, the N_2 uptake in this domain was negligible for the single hollow sample, as the unique cavities are too large to allow capillary condensation. The resulting volume of N_2 condensed inside the mesopores (i.e. the difference of quantity adsorbed between desorption and adsorption branches, named V_{cavity}) was smaller in case of the TPAOH-treated crystals (Figure 4.3).

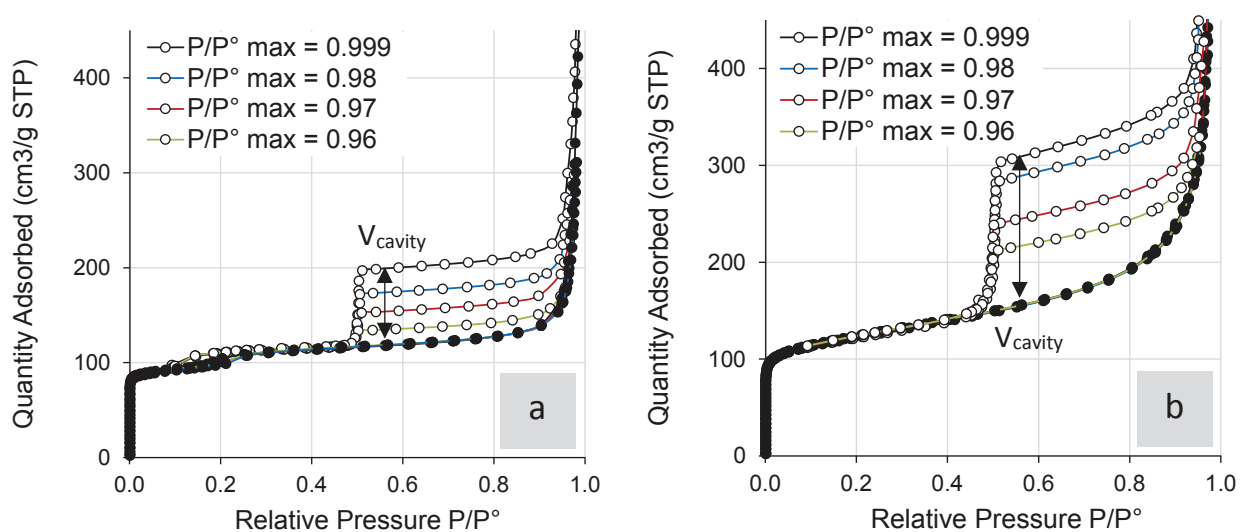


Figure 4.3 Scanning curves of single-hollow (a) and multi-hollow (b) Ni-free silicalite-1 single crystals. Adsorption (full symbols) and desorption (empty symbols) data points are represented with circles. V_{cavity} are represented with black arrows.

Scanning isotherms provide important information about the pore network geometry of hierarchical materials, including its connectivity and pore size distribution.^[191] They are usually produced by reversing the adsorption/desorption process over the $P/P^\circ = 0-1$ pressure range, where the pores are being filled or emptied by condensation or evaporation. In Figure 4.3 are presented the scanning curves of the hollow samples. Four independent measurements were carried out differing in their maximum P/P° set-points, from 0.96 up to 0.999.

After treatment with TPAOH, the hysteresis loops were symmetrical with parallel adsorption and desorption branches (Figure 4.3a). These H1-type loops are considered characteristic of confined systems with an ordered porosity (i.e. pores with a simple and regular shape).^[209] However, the volume of N_2 condensed inside the mesopores (V_{cavity}) increased steadily with the P/P°_{max} set-point, suggesting a discrepancy in the single hollow cavity size. Indeed, the larger the internal cavity, the higher the N_2 pressure requirement to be filled (Figure 4.4). Considering the crystal size reported in

Table 4.1 and an average wall length of 30 nm, V_{cavity} was calculated to be closed to $0.6 \text{ cm}^3 \text{ g}^{-1}$. V_{cavity} measured in the $P/P^\circ_{\text{max}} = 0.999$ experiment was lower ($0.13 \text{ cm}^3 \text{ g}^{-1}$), suggesting that a fraction of single hollow nanoboxes is not filled with N_2 at this high pressure. In addition, each descending scanning curves met the hysteresis loop at the characteristic pressure $P/P^\circ = 0.42$. According to the independent domain theory, such a convergence is characteristic of an assembly of mesopores made of independent domains.^[210] Mesopore emptying occurs independently through cavitation (i.e. the cavity empties while the micropores of the zeolite remains filled by the liquid).

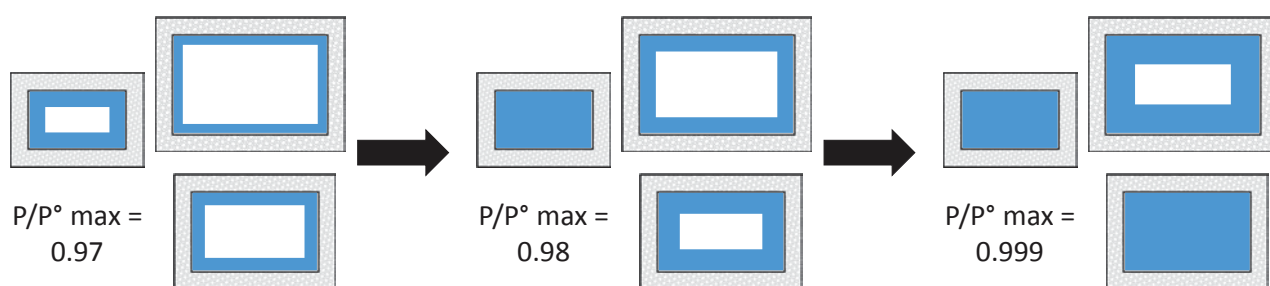


Figure 4.4 Scheme of N_2 filling (blue) inside single hollow nanoboxes for different maximum N_2 pressure.

In contrast, post-TBPOH hystereses are rather asymmetrical with adsorption branches steeper than the desorption branches (Figure 4.3b). Such H2-type hysteresis loops are indicative of porous media with disordered and connected pores.^[209] Furthermore, the presence of mesopores in direct contact with the outside was strongly suggested by the absence of a plateau on the desorption branches. The volume of the internal cavities (V_{cavity}) also increased with the P/P°_{max} set-point. A measurement at $P/P^\circ_{\text{max}} = 0.99$ exhibited no difference with the one at $P/P^\circ_{\text{max}} = 0.999$, suggesting a complete filling of the mesopores from $P/P^\circ_{\text{max}} = 0.99$ (data not shown). In comparison with the post-TPAOH sample, a slightly more gradual desorption was observed on the descending curves from $P/P^\circ = 0.52$ down to 0.42. We suggest a dual mechanism of desorption where neck-connected mesopores empty first through pore blocking and isolated mesopores empty subsequently through cavitation (Figure 4.5). Pore blocking phenomenon occurs when desorption in the cavities is triggered by desorption via constrictions with apertures larger than the micropore size of the zeolite.^[210]

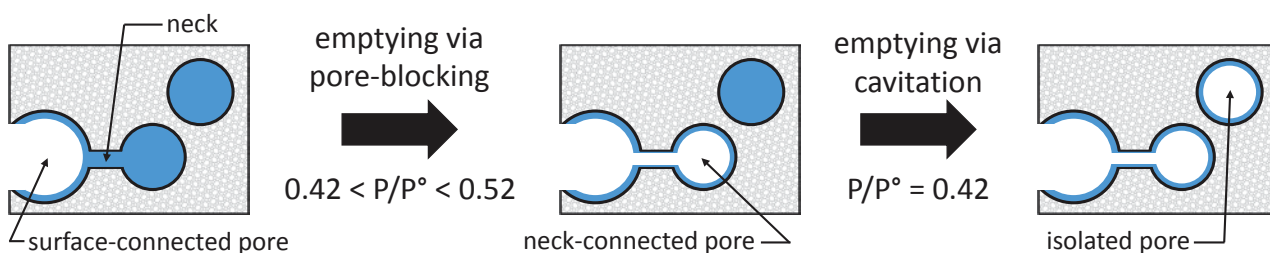


Figure 4.5 Scheme of suggested N_2 desorption (blue) mechanisms for multi hollow nanoboxes.

2.2. Ni-loaded silicalite-1 hollow crystals

Either TPAOH or TBPOH were used to prepare silicalite-1 hollow nanocrystals that had been initially loaded by wet impregnation with nickel nitrate (see chapter 2). In both cases, the presence of Ni in the zeolite (nominal loading = 5 wt.%) had no significant influence on the dissolution and recrystallization processes: the structure of hollow crystals was mostly similar to that obtained in the absence of Ni, i.e. a single regular hole with TPAOH and many cavities with TBPOH (Figure 4.6). However, a significant difference with the Ni-free single hollow silicalite-1 is that a fraction of nanoboxes shows several internal cavities instead of one unique cavity (Figure 4.6a). In addition, upon treatment with TBPOH in presence of Ni, sponge-like nanoporous boxes are obtained with internal voids smaller than in case of the Ni-free counterpart (Figure 4.6b). We can propose that these differences arise from the formation of the phyllosilicates during the basic treatment. When Ni-phyllosilicates crystallize, a chemical bond is formed with silica species and the observed fibres are strongly attached to the silica walls. Hence, the formation of phyllosilicates certainly affects the dissolution process.

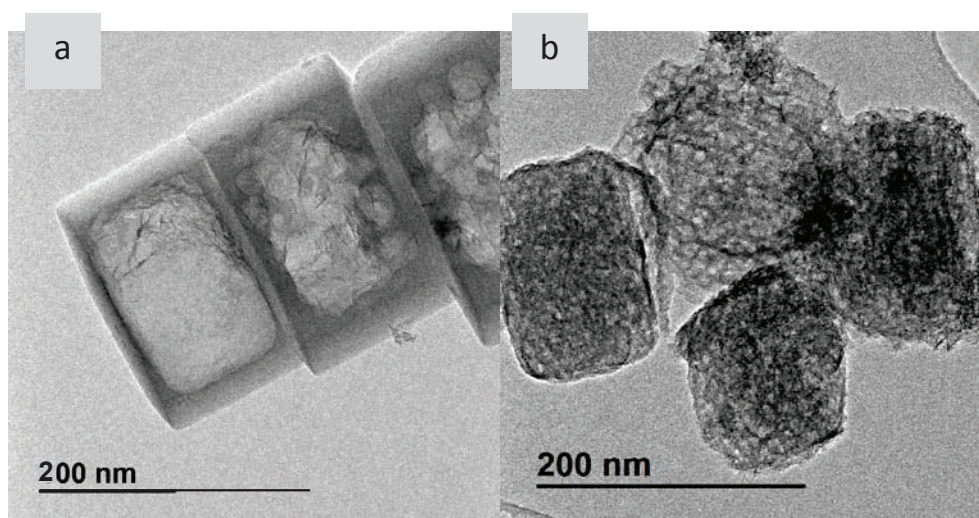


Figure 4.6 TEM images of 5%NiO@Sil-1 single hollow (a) and multi hollow (b).

The samples noted 5%NiO@Sil-1 SH and 5%NiO@Sil-1 MH were obtained by calcination at 450 °C to remove the organic part of the structure directing agents, i.e. TPAOH and TBPOH respectively. Upon reduction for 3 hours under H₂ at 750 °C, the actual Ni loadings obtained were respectively 6.2 wt.% and 5.1 wt.% for the single and multi-hollow crystals (Table 4.2). These metal loadings are close to the expected one (i.e. 5 wt.%).

Table 4.2 Nickel loadings of hollow silicalite-1 catalysts before and after selective removal of external metallic particles with citric acid.

Catalyst	Nickel loading (wt.%)		Nickel removal during the citric acid treatment
	Before citric acid treatment	After citric acid treatment	
Ni/Sil-1	4.5	-	-
Ni@Sil-1 SH	6.2	1.5	76%
Ni@Sil-1 MH	5.1	2.2	57%

It is known that some transition metals (i.e. Co and Cu) do not directly form nanoparticles upon treatment in alkaline solution, as it has been shown for the case of noble metals.^[211] Partial dissolution of silica species of the zeolite leads to the formation of stable nickel phyllosilicates, located both inside the cavities and on the outer surface of the crystals (Figure 4.6). Nickel species also appeared in large isolated domains alongside amorphous silica, probably due to the high Ni loading originally present in bulk crystals. Upon reduction at high temperature, Ni²⁺ species were reduced and metallic nanoparticles were formed. The corresponding samples are denoted Ni@Sil-1 SH and Ni@Sil-1 MH for single and multi-hollow crystals, respectively. In contrast to the cases of noble metals such as Au or Pt, sample reduction did not lead to a single large Ni particle per cavity, but instead to numerous small nanoparticles attached to the zeolite surface (Figure 4.7).^[146,147]

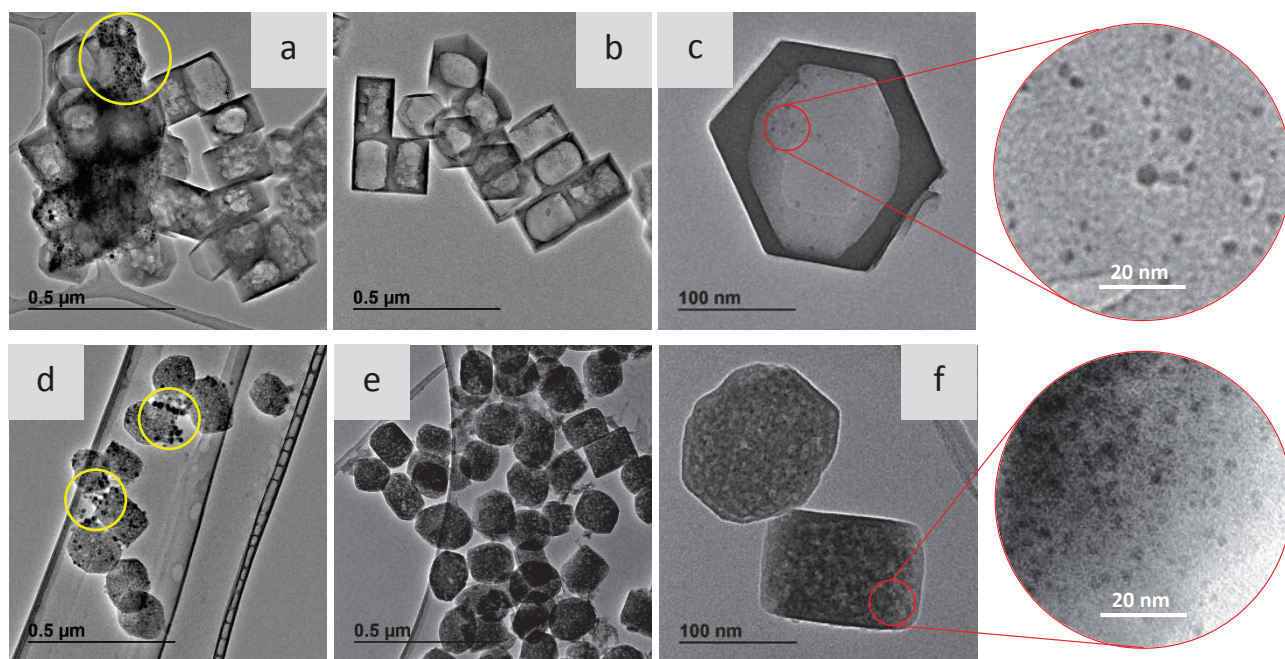


Figure 4.7 TEM images of Ni-loaded single-hollow (a,b,c) and multi-hollow (d,e,f) silicalite-1 treated (b,c,e,f) and not treated (a,d) with citric acid. Yellow circles point out external nickel.

For both single and multi-hollow materials, only a fraction of Ni nanoparticles were located inside the crystals, the rest being part of large amorphous domains as those highlighted by yellow circles in images a and d of Figure 4.7. Most external Ni species could yet be removed by treating the hollow crystals with citric acid. Such treatment is expected to remove almost totally external Ni species, while leaving a significant number of small Ni nanoparticles inside the cavities. After acid leaching, the original Ni content dropped by 76 and 57 % for the single and multi-hollow materials, respectively (Table 4.2). The corresponding catalysts were denoted CitAc Ni@Sil-1 SH and CitAc Ni@Sil-1 MH in which the Ni nanoparticles were essentially only located in zeolite cavities (images b,c,e and f of Figure 4.7). While the Ni contents were of the same order of magnitude for both samples, the average particle size was significantly larger in the case of CitAc Ni@Sil-1 SH ($d_{sw} = 4.5 \pm 1.1$ nm), as compared to that of CitAc Ni@Sil-1 MH ($d_{sw} = 2.7 \pm 0.5$ nm). This difference could be explained by the fact that approximately the same amount of Ni species was dispersed in many cavities in the case of Sil-1 MH crystals and only in one single cavity in the case of Sil-1 SH crystals.

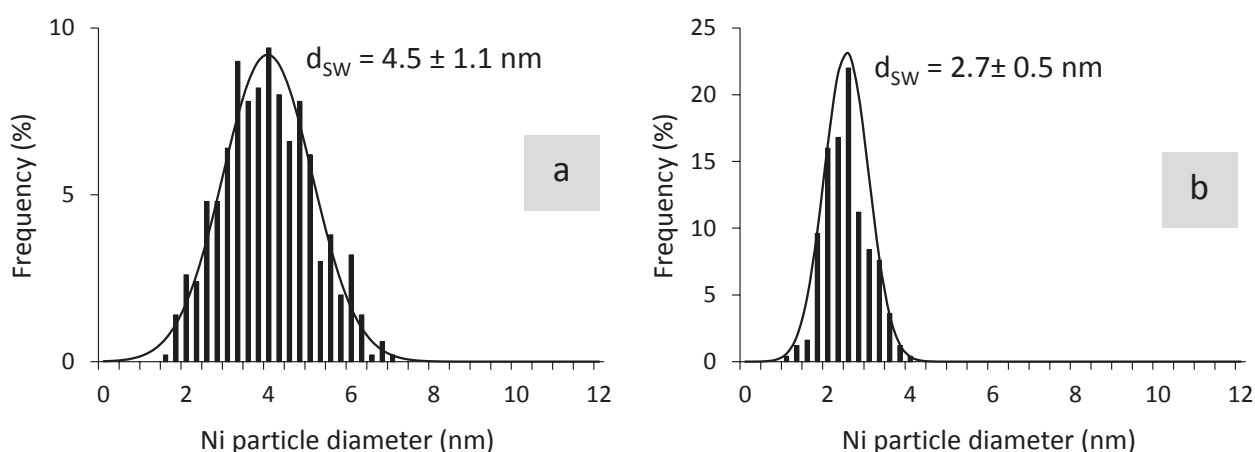


Figure 4.8 Particle size distribution of CitAc Ni@Sil-1 SH (a) and CitAc Ni@Sil-1 MH (b).

2.2.1. X-ray diffraction

X-ray diffraction was used to examine the effect of citric acid treatment on the structural properties of Ni-containing hollow zeolites. Diffractogrammes are presented in Figure 4.9 where, for comparative purposes, intensities were normalized using the area of the silicalite-1 peak centered on $2\theta = 14.8^\circ$. As evidenced by TEM pictures (Figure 4.7), the treatment did not significantly affect the crystal habit and the internal mesoporosity remained intact, particularly in the case of multi-hollow crystals. The preservation of the zeolite structure was confirmed by the similarity of the XRD patterns of the treated and untreated samples (Figure 4.9). Yet, minor modifications could be observed in the region between 23 and 25° . For bulk silicalite-1 crystals, this region contains five

main diffraction peaks with a singlet at 24.48° corresponding to the (1 33) reflection in orthorhombic lattice (see inset in Figure 4.9). Calcined silicalite-1 exhibits a monoclinic symmetry at room temperature; the persistence of the orthorhombic symmetry has been attributed to the presence of internal framework defects, particularly present in nanocrystals with a size below 500 nm.^[212–216] When the zeolite was treated with TPAOH, most of the inner part of the crystals was removed and the symmetry of the lattice changed with the splitting of the line at 24.4° into a doublet.

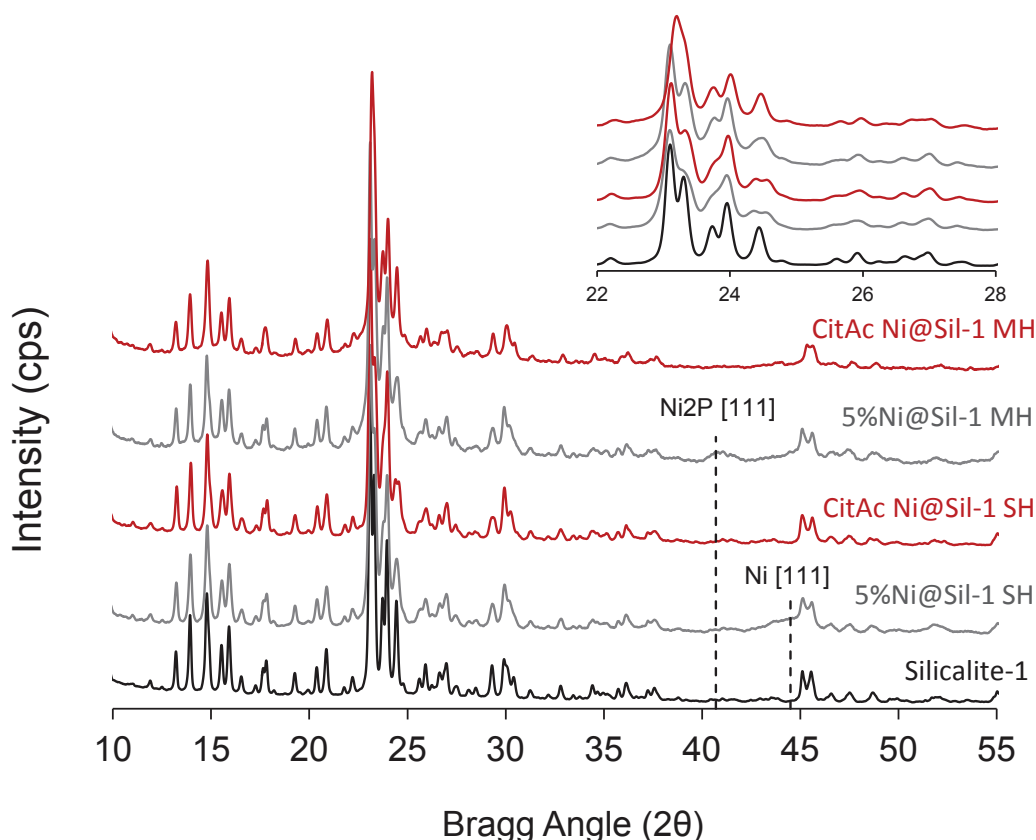


Figure 4.9 XRD patterns of the parent silicalite-1 (black) and the citric acid treated Ni-loaded hollow silicalite-1 catalysts (red). Patterns of the corresponding non-treated samples are presented in grey. A zoom in the region $2\theta = 22\text{--}28^\circ$ is shown at the top right corner of the figure.

This result confirms our previous data suggesting that most of the lattice defects are formed at the early stages of crystal growth and are thus located at the center of the crystals.^[143,144] Using TBPOH at 115°C to form multi-hollow crystals removed only partially the inner part of the crystals and the orthorhombic symmetry of the zeolite lattice was preserved. Moreover, the singlet at 24.4° was even more pronounced after citric acid treatment, suggesting that the acid could create additional defects, which could possibly explain why hollow silicalite-1 appeared less stable after acid treatment in the steam reforming of methane at 900°C .

We also have seen in Figure 3.14 that the diffraction pattern of the 5%Ni@Sil-1 SH sample was in agreement with the presence of a cubic Ni structure, showing a main diffraction peak at $2\theta = 44.5^\circ$

(JCPDS 04-0850). Regarding the 5%Ni@Sil-1 MH sample, no XRD pattern associated with the Ni [111] facet could be observed so prominently. In addition, a broad peak centered at $2\theta = 40.8$ was discernible and could be assigned to the [111] facet of small particles of Ni₂P (JCPDS 72-2514). Ni₂P phosphide is generally prepared by temperature programmed reduction of Ni²⁺ and phosphate species.^[217] The CitAc Ni@Sil-1 MH sample only exhibited peaks typical of silicalite-1, Ni phases were not detected by XRD due to the low Ni loading of this sample.

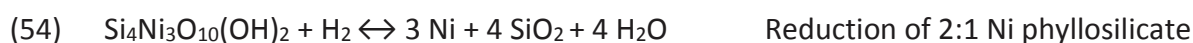
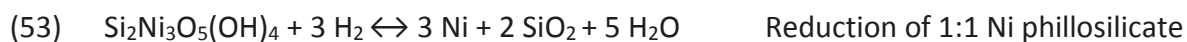
2.2.2. Thermogravimetric analyses

Table 4.3 Experimental and theoretical mass losses of Ni-loaded samples due to H₂O desorption and Ni²⁺ reduction during TPR measurements.

Catalyst	Experimental mass loss (%)		Theoretical mass loss from Ni ²⁺ reduction			Theoretical mass loss from PO ₄ reduction (%)
	$\Delta m_{des.}$	$\Delta m_{red.}^a$	NiO	1:1 Phyllo	2:1 Phyllo	
5%NiO/Sil-1	1.8	1.4	1.3	2.1	1.7	-
5%NiO@Sil-1 SH	1.8	2.0	1.4	2.3	1.8	-
5%NiO@Sil-1 MH	2.8	3.5	1.4	2.4	1.9	2.8
CitAc NiO@Sil-1 MH	4.2	0.8	0.5	0.8	0.6	0.3

^a Calculated on a dry basis

The reduction of Ni phyllosilicates to Ni nanoparticles was monitored by temperature programmed reduction (TPR) and thermogravimetric analysis (TGA) under H₂ flow up to 900 °C. The reduction profiles of 5%NiO/Sil-1 and 5%NiO@Sil-1 SH was already discussed in chapter 3. The reducibility of the Ni-loaded multi hollow sample was measured prior (Figure 4.10) and after (Figure 4.11) the citric acid treatment. Experimental mass loss arising from the low-temperature desorption of H₂O adsorbed on the zeolite surface ($\Delta m_{des.}$) and from the formation of H₂O related to the reduction of Ni²⁺ species ($\Delta m_{red.}$) are reported in Table 4.3. The theoretical mass loss derived from Ni reduction was calculated for the different rational natures of Ni²⁺ (i.e. NiO, 1:1 phyllosilicate and 2:1 phyllosilicate) according to Equations 52, 53 and 54:



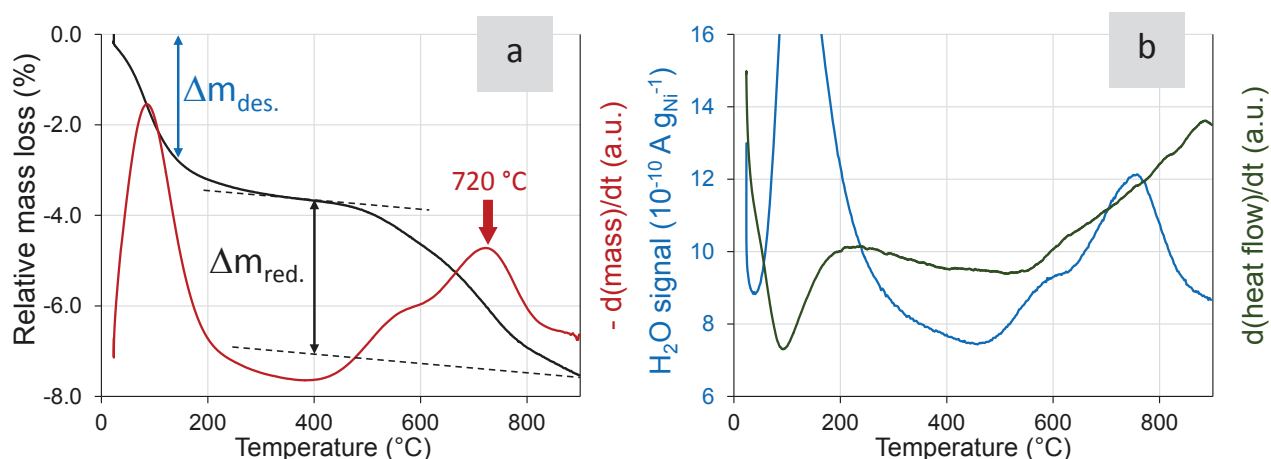


Figure 4.10 Thermal gravimetric profile (a) and related H₂O production (b) of 5%NiO@Sil-1 MH under H₂

The thermogravimetric profile of the NiO@Sil-1 MH catalyst prior to citric acid treatment is shown in Figure 4.10. At 150 °C, the initial change in the catalyst mass due to H₂O desorption had reduced the mass of the catalyst by 2.8 wt.%. This value is higher than that of the NiO@Sil-1 SH and confirms our hypothesis on the high density of defects present in the multi-hollow sample (Figure 4.9). Indeed, Si–O–H silanol groups present at defect sites can retain H₂O via hydrogen bond interactions, causing an increase in the hydrophilicity of the material.^[218] After the citric acid treatment (Figure 4.11), the amount of physisorbed H₂O was even larger (i.e. 4.2 wt.%), confirming that the acidic treatment creates additional defects (Figure 4.9). In Figure 4.10b, no H₂O peak at 380 °C is observed, indicating the absence of NiO species.

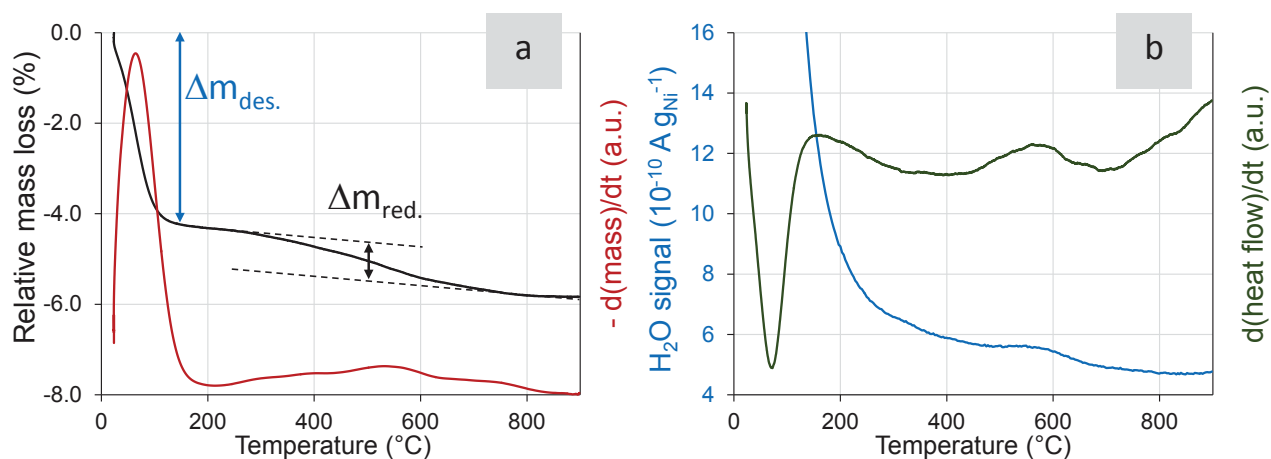


Figure 4.11 Thermal gravimetric profile (a) and related H₂O production (b) of CitAc NiO@Sil-1 MH under H₂

Beyond 400 °C, a gradual 3.5 wt.% mass reduction was observed. Both TGA and TPR techniques indicates the presence of two peaks, one with maximum weight loss in the temperature range 550-600 °C and another one centred at 720 °C. This is in good agreement with our observations on the

NiO@Sil-1 SH sample, where the presence of the two forms of phyllosilicates was suggested (Figure 3.9). Such an assignment must however remain questionable in the case of the multi hollow catalyst. Indeed, as indicated in Table 4.3, the experimental mass reduction Δm_{red} (3.5 wt.%) is not in line with the theoretical one expected from the reduction of a mixture of 1:1 and 2:1 Ni phyllosilicates (ranging between 1.9 and 2.4 wt.%). It must be stressed that in case of the single hollow catalyst, the experimental mass loss (2.0 wt.%) complied with the theoretical silicate-related one (between 1.8 and 2.3 wt.%). Such a compliance was also observed for the CitAc NiO@Sil-1 MH catalyst. Hence, prior to the citric acid treatment, the presence of additional species that are prone to reduction is likely and would range between 1.1 and 1.6 wt.% of the sample mass. This mass may be due to partial reduction of PO_4 species into elementary P or NiP_x species (Table 4.3). This loss was calculated from ICP results considering all the phosphorous content present in the multi hollow samples to be in the form PO_4 (Table 4.9). Sano and co-workers had observed that N-based and P-based templates occluded in zeolitic micropores exhibited different decomposition behaviours when as-synthesized zeolites were calcined. N-containing templates could be completely removed by calcination at 600 °C, whereas monomeric and condensed phosphate compounds were formed in the zeolitic pores by the decomposition/oxidation of P-containing template.^[219] This hypothesis would suggest that phosphate species were mostly removed during the citric acid treatment and subsequent washings.

2.2.3. Nitrogen physisorption

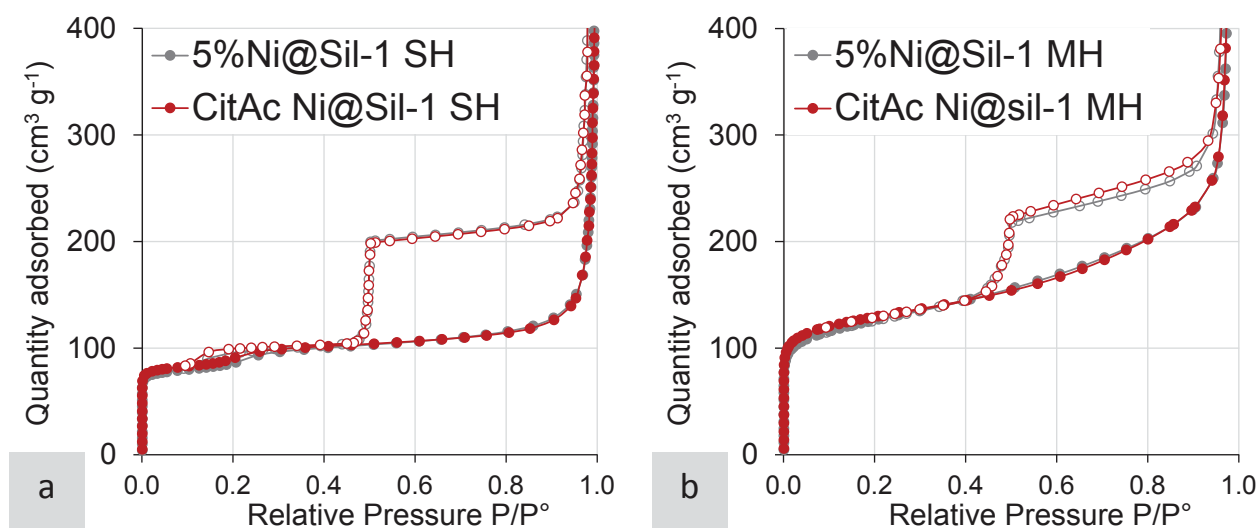


Figure 4.12 N_2 adsorption (full symbols) and desorption (empty symbols) isotherms at 77 K of the reduced Ni-loaded single (a) and (b) multi hollow samples treated (red) and not treated (grey) with citric acid.

The textural properties of Ni-loaded hollow zeolites upon citric acid treatment have also been studied by nitrogen adsorption at 77 K (Figure 4.12). Prior to measurement, these samples were

calcined at 500 °C for 6 h for complete removal of carbon traces due to the thermal decomposition of the residual citrates. Similarly to their Ni-free counterpart (Figure 4.3), both CitAc Ni@Sil-1 SH and MH showed a type-IV isotherms with the characteristic hysteresis loop closing at $P/P^\circ = 0.42$. The large increase at $P/P^\circ > 0.95$ corresponds to intercrystalline mesoporosity, which can be particularly important in the case of small crystals. In case of the single hollow sample, the small loop at $P/P^\circ = 0.15$ nm was still observed, indicating that the formation of phyllosilicates only affects partially the dissolution/recrystallization process.

Table 4.4 Porosity of the different samples.

Catalyst	$S_{\text{BET}}^{\text{a}}$ ($\text{m}^2 \text{g}^{-1}$)	$V_{\text{micro}}^{\text{b}}$ ($\text{cm}^3 \text{g}^{-1}$)	$V_{\text{cavity}}^{\text{c}}$ ($\text{cm}^3 \text{g}^{-1}$)	$V_{\text{total}}^{\text{d}}$ ($\text{cm}^3 \text{g}^{-1}$)
Silicalite-1	390	0.13	0.00	0.20
5%Ni@Sil-1 SH	316	0.11	0.15	0.34
CitAc Ni@Sil-1 SH	328	0.12	0.15	0.34
5%Ni@Sil-1 MH	453	0.14	0.10	0.42
CitAc Ni@Sil-1 MH	472	0.14	0.11	0.43

^a BET method

^b Volume of N_2 adsorbed when the slope of the adsorption branch becomes lower than $10^3 \text{ cm}^3 \text{ g}^{-1}$

^c Difference in N_2 uptake between the adsorption and the desorption branches of the isotherms at $P/P^\circ = 0.5$

^d Volume of N_2 adsorbed at $P/P^\circ = 0.9$ from desorption branch

Both the BET surface area and the micropore volume were consistent with values usually reported for ZSM-5 and silicalite-1 (Table 4.4).^[188] The TPAOH-treated sample present a lower BET surface area than the parent zeolite, which might be attributed to the less defective nature of the single hollow framework. In contrast, the BET surface area of the multi hollow sample increased with respect to the original zeolite due to the contribution of the external surface of the mesopores. However, it has been reported that the measurement of BET surface areas of materials presenting combination of type-I and type-IV isotherms could be problematic, particularly when the plateau of the isotherm is not horizontal.^[220] Under such conditions, the differences observed after treatment cannot be considered as real modifications of accessible surface areas but rather to the difficulty to separate the processes of monolayer-multilayer adsorption and micropore filling. It must be stressed that the citric acid treatment has no observable impact on the porosity of the two samples. The BET surface area of the treated zeolite was similar to that of the not treated crystals, suggesting that the acid treatment do not significantly damage the zeolite structure. However, it should be noted that the formation of internal defects do not necessarily modify the BET surface area.^[221]

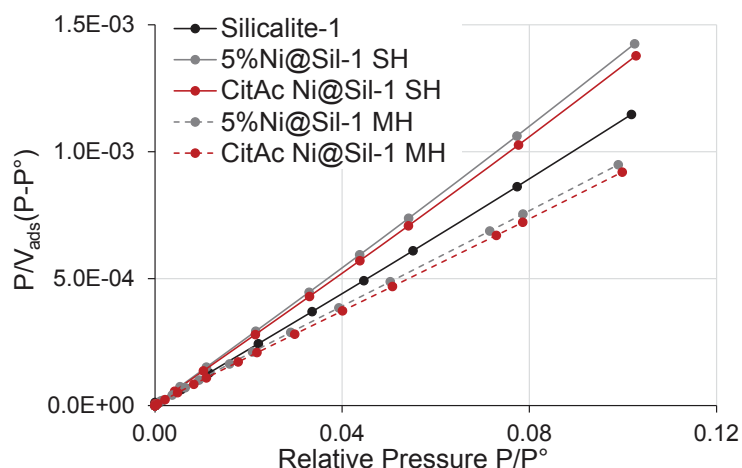


Figure 4.13 BET plots of the different samples.

3. Catalytic properties of multi hollow catalysts

3.1. Selectivity in arene hydrogenation

The confinement of Ni nanoparticles into zeolite cavities was also confirmed by an investigation based on the hydrogenation of substituted arenes. The experimental protocol was fully described in part 3.2 of chapter 2. We have reported in chapter 3 that nickel nanoparticles encapsulated in single-hollow silicalite-1 crystals could discriminate between toluene and mesitylene. Toluene was able to diffuse through the micropores of the zeolite walls and be hydrogenated on embedded metal nanoparticles, in contrast to mesitylene, which was almost fully size-excluded from the silicalite-1 micropores. This led to a high selectivity towards toluene hydrogenation as compared to that of mesitylene, the latter being only hydrogenated over external metal particles. The results regarding toluene and mesitylene hydrogenations on the CitAc Ni@Sil-1 MH sample are reported in Table 4.5. They are compared with those obtained on the supported 5%Ni/Sil-1 and the encapsulated CitAc Ni@Sil-1 SH.

Table 4.5 Catalytic activity for the hydrogenation of arenes.

Catalyst	Toluene hydrogenation rate		Mesitylene hydrogenation rate		Toluene / Mesitylene hydrogenation rate ratio at 100°C
	Rate at 100°C	$E_{app} (\pm 3)$	Rate at 100°C	$E_{app} (\pm 3)$	
	($\mu\text{mol s}^{-1}\text{g}^{-1}\text{Ni}$)	(kJ mol^{-1})	($\mu\text{mol s}^{-1}\text{g}^{-1}\text{Ni}$)	(kJ mol^{-1})	
5%Ni/Sil-1	3.9	54.5 ± 3	0.34	60 ± 4	11
CitAc Ni@Sil-1 SH	67.4	56 ± 3	1.04	69 ± 4	65
CitAc Ni@Sil-1 MH	4.8	51 ± 3	0.10	62 ± 3	48

The toluene/mesitylene hydrogenation rate ratio was equal to 11 on the 5%Ni/Sil-1, for which all nanoparticles were accessible and for which no molecular sieving mechanism is expected. This rate ratio increased to 48 and 65 for CitAc Ni@Sil-1 MH and CitAc Ni@Sil-1 SH catalysts, respectively. This clearly demonstrates a preferential hydrogenation of the smaller molecule on the hollow catalysts and proves that most of Ni nanoparticles were entrapped into zeolite cavities and accessible only via zeolite micropores. The finite value of the ratio indicates that both samples still contained external Ni nanoparticles capable of hydrogenating mesitylene that were not removed during the citric acid treatment. The lower ratio was obtained on multi-hollow crystals for which the extent of Ni removal was only 57 %. This shows that there is room for improving the treatment to leach out external Ni particles. In addition, Ni particles encapsulated inside mesopores in direct contact with the outside participated in hydrogenating mesitylene.

It must be noted that the observed apparent activation energies were similar for the three samples and in line with values reported in the literature.^[196,197,222] This suggests that activity in toluene hydrogenation is not limited by transport phenomena through the hollow zeolite shell and that mesitylene only react on accessible particles for which no molecular sieving mechanism is expected.

3.2. Stability in steam methane reforming at 700 °C

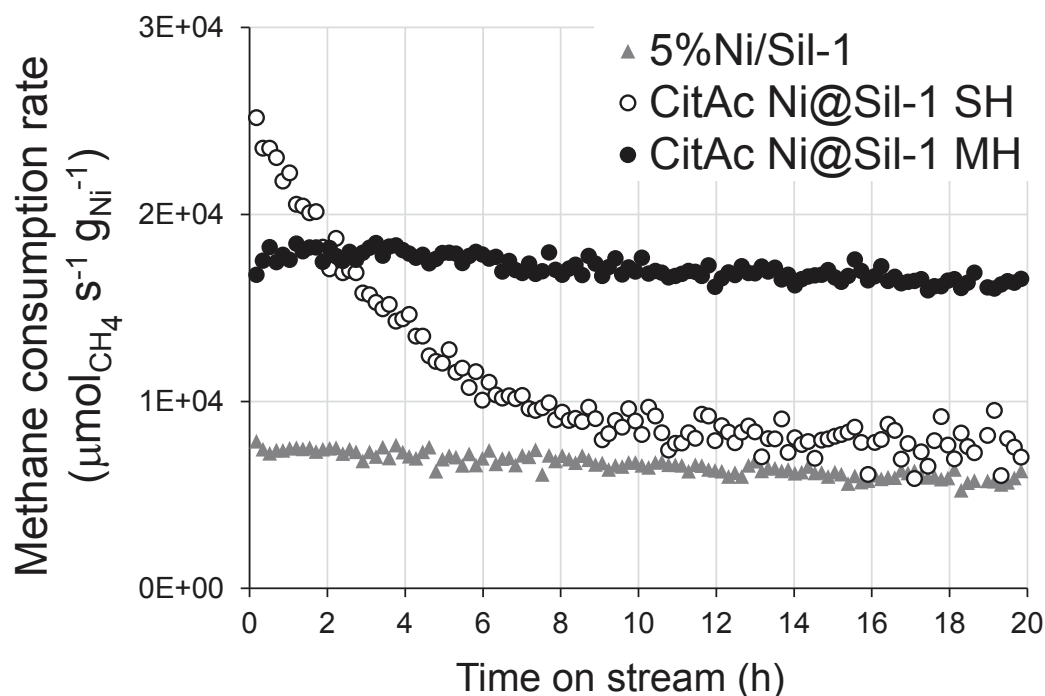


Figure 4.14 Steam methane reforming rate at 700 °C for the 5%Ni/Sil-1 (triangles), CitAc Ni@Sil-1 SH (open circles) and CitAc Ni@sil-1 MH (full circles). Contaminant-free feed composition is given in Table 2.2.

The catalytic activities on 10 mg of sample of the acid-treated Ni-containing hollow zeolites in the steam reforming of CH₄ were monitored at 700 °C over 20 hours (Figure 4.14). These were compared to those obtained on the supported 5%Ni/Sil-1. No contaminant was present in the feed stream: these tests were carried out to evaluate the thermal stability of the entrapped Ni particles at high temperatures under a high steam pressure. Note that initial activities were all measured below 50 % conversion in CH₄. The single hollow-based sample was initially more active than that based on multi-hollow crystal. However, the activity of the former decreased significantly with time, before levelling off after ca. 15 hours. In contrast, the activity of the multi hollow-based catalyst remained essentially stable over the whole period. Thus, the activity measured after 20 hours over CitAc Ni@sil-1 MH was approximately twice that observed on CitAc Ni@sil-1 SH. Many factors could explain deactivation of the catalyst with time, for example coke formation or a gradual loss of dispersion of the catalytic phase. TEM pictures of spent catalysts clearly showed that the average particle size had increased during the catalytic test from $d_{sw} = 4.5 \pm 1.1$ nm to 7.9 ± 2.1 nm for CitAc Ni@Sil-1 SH and $d_{sw} = 2.7 \pm 0.5$ nm to 4.3 ± 0.9 nm for CitAc Ni@Sil-1 MH (Figure 4.15 and Figure 4.16). The respective metal dispersions are given in Table 4.6.

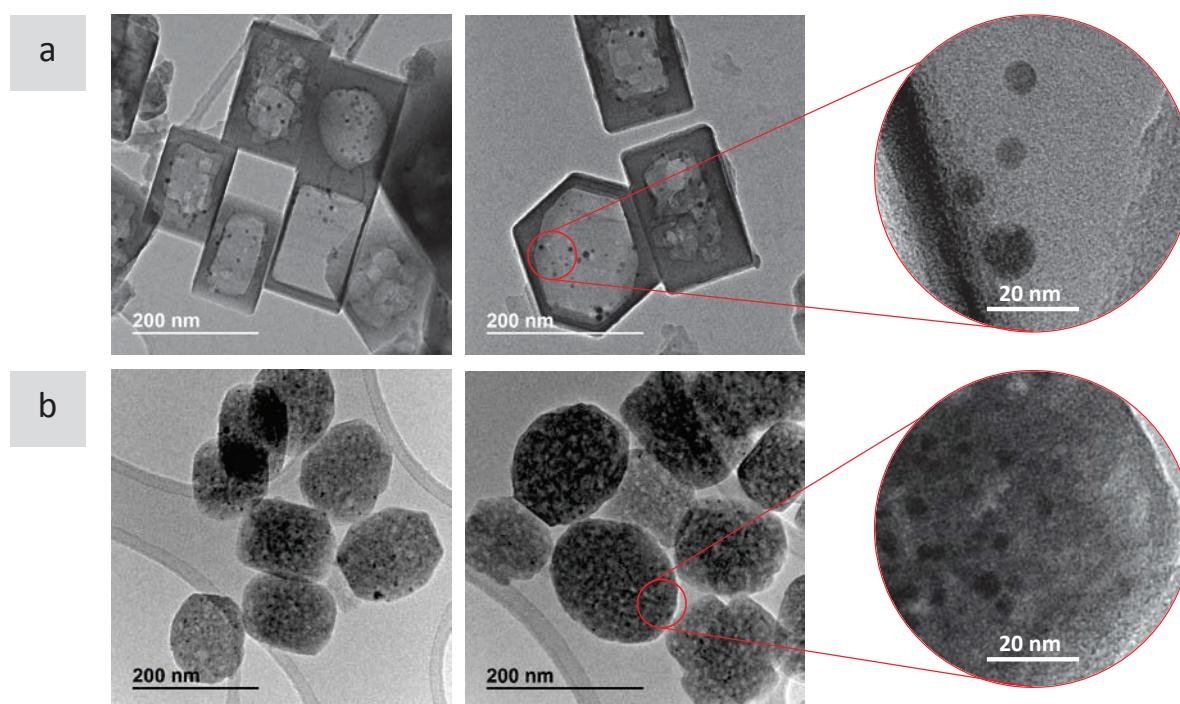


Figure 4.15 TEM images of the post-reforming CitAc Ni@Sil-1 SH (a) and CitAc Ni@Sil-1 MH (b).

The increase in average particle size of CitAc Ni@Sil-1 SH corresponded to a dispersion decreasing from 31 down to 21 %. It has been proposed that the most active sites of metallic nanoparticles for the steam methane reforming were those exhibiting low coordination numbers, e.g. atoms located at steps, edges and corners.^[59,223] Assuming that Ni particles were regular cubooctahedra, it is

possible for each particle size to estimate the proportion of low coordination sites over the total number of surface sites (LCS), typically those on edges and corners.^[153] This proportion decreases from 22 % to 14 % after test (Table 4.6). Therefore, the overall concentration of LCS (= Dispersion x LCS) exhibited a ca. 2.4-fold decrease. The extent of this decay is similar to that of the activity decrease of the CitAc Ni@Sil-1 SH catalyst (Figure 4.14) from the initial value $r_i = 25 \text{ mmol}\cdot\text{s}^{-1}\cdot\text{g}_{\text{Ni}}^{-1}$ to $r_f = 8 \text{ mmol}\cdot\text{s}^{-1}\cdot\text{g}_{\text{Ni}}^{-1}$ after 20 hours ($r_i/r_f = 3.1$). Therefore, the activity loss can be mostly attributed to the sintering of the Ni particles in the case of the CitAc Ni@Sil-1 SH catalyst.

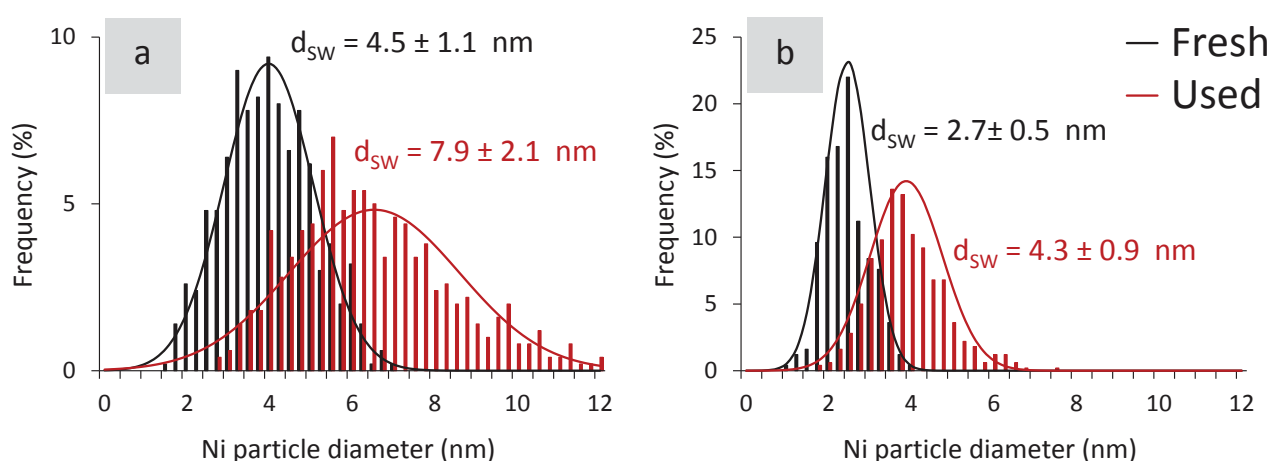


Figure 4.16 Particle size distributions of fresh (black) and post-reforming (red) CitAc Ni@sil-1 SH (a) and CitAc Ni@sil-1 MH (b). Distributions are modelled using a Normal law.

Sintering was also observed on CitAc Ni@Sil-1 MH, although to a lower extent (Figure 4.15 and Figure 4.16). The comparison between the initial and final dispersions and LCS indicates that the catalyst activity should have exhibited a 2.5-fold decrease after 20 hours, similarly to the case of CitAc Ni@Sil-1 SH (Table 4.6). This was clearly not the case (Figure 4.14). The essentially constant value of the activity of the CitAc Ni@sil-1 MH could possibly be explained by the fact that particle sintering could have been compensated by an almost exactly identical gain in specific activity.

Table 4.6 TEM-derived specific metal surface areas, metal dispersions and proportion of Low Coordination Sites (“LCS”, step and corner atoms, calculated from ^[153]) over the total number of surface sites.

Catalyst	Fresh samples			Post-reforming samples			Relative decay of dispersion x LCS after reforming
	Specific Ni surface area ($\text{m}^2 \text{g}^{-1}$)	Dispersion (%)	LCS (%)	Specific Ni surface area ($\text{m}^2 \text{g}^{-1}$)	Dispersion (%)	LCS (%)	
5%Ni/Sil-1	1.4	4.7	3.0	1.0	3.5	2.2	1.8
CitAc Ni@Sil-1 SH	3.1	31	22	2.1	21	14	2.4
CitAc Ni@Sil-1 MH	7.0	48	37	4.5	31	23	2.5

3.3. Activity in CO methanation at 300 °C

Both single and multi-hollow catalysts were tested in a model reaction, i.e. CO methanation at 300 °C, before and after methane reforming to unravel this matter. Experimental conditions are described in section 3.4.2 of chapter 2. As discussed in chapter 3, CO methanation experiments performed at 300 °C using supported catalysts exhibited a constant TOF of ca. 0.35 s^{-1} . Prior to the reforming tests, the methanation activity of the fresh single and multi-hollow catalysts was measured *in situ*. The CO methanation activity was used to derive the initial metal specific surface area assuming a TOF of 0.35 s^{-1} for each active site and an average area of a surface Ni atom of $6.5 \times 10^{-20} \text{ m}^2$ (Table 4.7).^[163]

Table 4.7 Methanation activity of the fresh samples at 300 °C, the corresponding specific metal surface area and the proportion of accessible metal Ni.

Catalyst	Methanation activity at 300°C ($\mu\text{mol}_{\text{CH}_4} \text{ s}^{-1} \text{ g}_{\text{Ni}}^{-1}$)	Specific metal surface area ($\text{m}^2 \text{ g}^{-1}$)	Accessible metallic Ni (%)
CitAc Ni@sil-1 SH	110	0.19	6.1
CitAc Ni@sil-1 MH	23	0.06	0.8

It appears that the specific metal surface areas determined by CO methanation (Table 4.7) were significantly lower than those derived from TEM measurements for both fresh samples (Table 4.6). This observation indicates that most Ni surface sites were actually not available for CO methanation, possibly because a part of those were in an oxidized state (i.e. as in silicate compound) or the Ni metal nanoparticles were covered by a layer of siliceous material. Actually, HRTEM observations of the fresh 5%Ni@Sil-1 SH catalyst revealed the presence of metallic particles located inside the hollow zeolite that are surrounding by a ca. 1 nm thick layer of amorphous mater (Figure 4.17a). Regarding external Ni particles, high resolution images indicates that some facets are not covered and apparently accessible (Figure 4.17b). Yet, these particles remained static under the electron beam of the microscope, pointing out their strong interactions with the support or their partial encapsulation inside siliceous material.

The proportions of “accessible metallic Ni” defined as the fraction of active Ni surface sites participating to the methanation reaction over the total number of Ni surface sites derived by TEM are given in Table 4.7 and were markedly small. The two catalysts were prepared by treating Ni-loaded silicalite-1 crystals under alkaline conditions and the formation of Ni-phyllsilicates was

observed in both cases (Figure 4.6). Zhang et al. reported that Ni-phyllsilicates led to Ni particles partially embedded in an amorphous silica matrix upon reduction at 700 °C under H₂. In their work, the percentage of surface Ni atoms titrated by H₂ chemisorption on 3.3 nm nanoparticles obtained by direct reduction of phyllsilicates was only 6%, whereas this percentage increased to 30% when the catalyst was prepared by reduction of Ni impregnated onto silica.^[203]

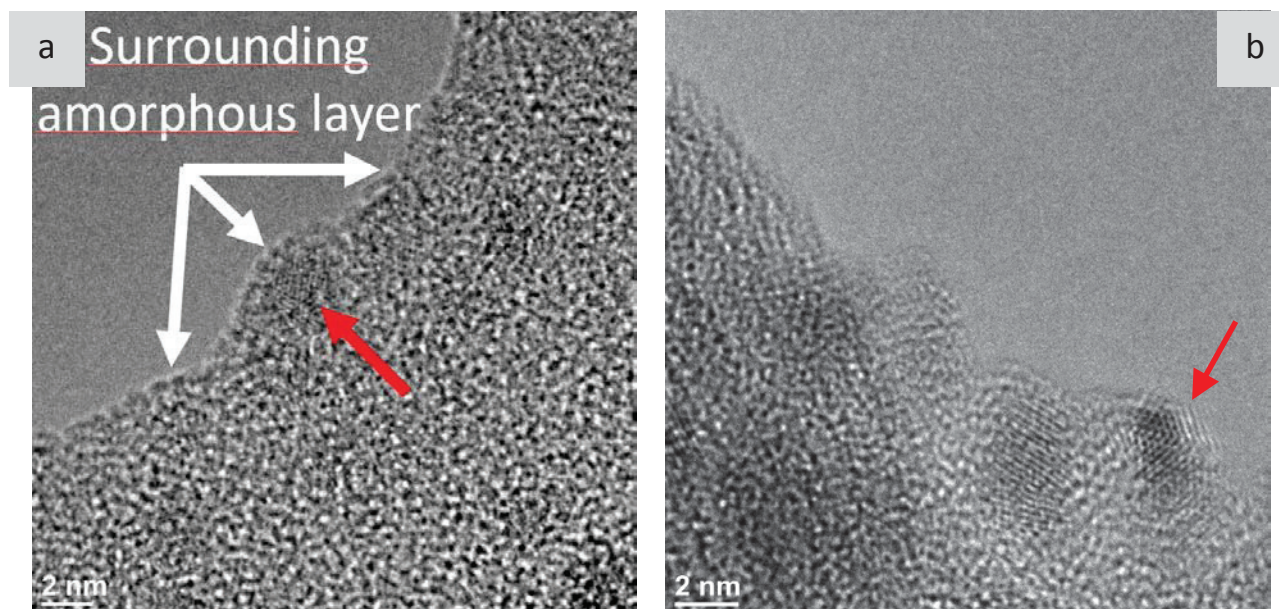


Figure 4.17 HRTEM images of external (a) and internal (b) Ni particles in the fresh 5%Ni@Sil-1 SH.

H₂ chemisorption analysis carried out on the present single and multi-hollow catalysts (Table 4.8) confirmed that the surface sites able to chemisorb H₂ were scarce, i.e. 5.7 and 3.1 % of the total number of surface Ni atoms for CitAc Ni@Sil-1 SH and CitAc Ni@Sil-1 MH, respectively. These values are similar to those based on CO methanation activity that are reported in Table 4.7.

Table 4.8 H₂ chemisorption-derived specific metal surface area and proportion of accessible metal Ni.

Catalyst	Specific metal surface area (m ² g ⁻¹)		Accessible metallic Ni (%)	
	Not treated	CitAc treated	Not treated	CitAc treated
Ni@Sil-1 SH	1.31	0.18	-	5.7
Ni@Sil-1 MH	BDL	0.22	-	3.1

BDL = Below Detection Limit

The encapsulation/poisoning of most Ni nanoparticles by amorphous silica cannot account for the whole difference in performance in methane reforming between the CitAc Ni@Sil-1 SH and CitAc Ni@Sil-1 MH catalysts (Figure 4.14), as well as the very low fraction of surface atoms accessible in

CitAc Ni@Sil-1 MH during CO methanation (Table 4.7). In addition to differences in the size, morphology and number of mesopores inside the crystals, the single hollow and multi hollow catalysts also differ by the nature of mineralizing agent that was used to create the porosity. Multi hollow crystals were obtained in the presence of phosphonium cations, which are known to contaminate zeolites with phosphorus-containing species upon calcination.^[219] Phosphorous-based compounds are also known as poisons for nickel catalysts.^[72] In addition, XRD (Figure 4.9) and TGA (Table 4.3) data suggested the formation of Ni phosphide during the reduction process.

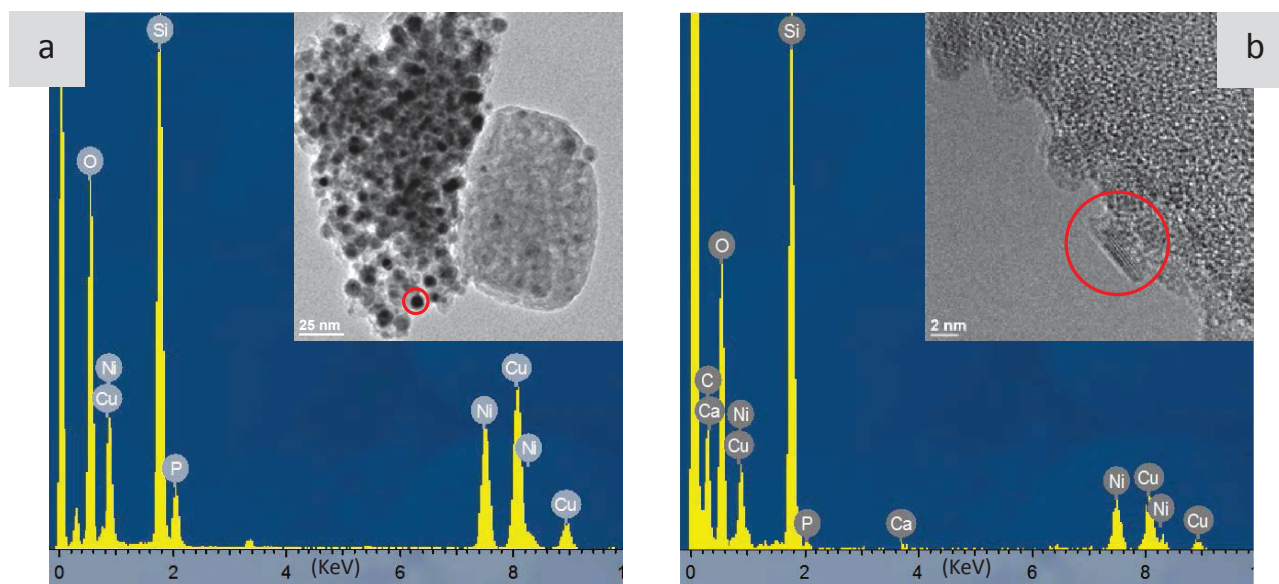


Figure 4.18 EDX spectra of an external particle in 5%Ni@Sil-1 MH (a) and an internal particle in CitAc Ni@Sil-1 MH prepared by ultramicrotomy (b). Analysed areas are indicated by a red circle. Cu peaks in the spectra are from the Cu grid used as the sample holder in TEM measurements.

Chemical analysis by ICP of multi hollow crystals before treatment with citric acid confirmed the presence of phosphorus species in the zeolite with a P/Ni atomic ratio of 0.5 (Table 4.9). For this sample, the amount of adsorbed H₂ was below the detection limit, suggesting that P species had reacted with surface Ni atoms and totally prevented H₂ adsorption. In addition, no activity in methanation was detected at 300 °C over this sample. Furthermore, EDX analysis confirmed the presence of P-based compounds aligned with Ni particles located outside the crystals (Figure 4.18a). After treatment with citric acid, the P/Ni ratio decreased to 0.15 and the proportion of surface sites chemisorbing H₂ became measurable (ca. 3.1 %), thus supporting the poisoning role of P species on the catalyst activity (Table 4.8). Precise EDX analysis on a particle located inside the mesopores was possible by analyzing thin slices of CitAc Ni@Sil-1 MH sample (Figure 4.18b). Thin sections (70-90 nm thick) were cut using an ultramicrotome equipped with a diamond knife (Leica Ultracut UCT) upon embedding inside an epoxy resin medium. EDX spectra confirmed the contamination of encapsulated Ni particles by P species to a lower extent than the ones in 5%Ni@Sil-1 MH.

Table 4.9 Elemental analysis and P/Ni atomic ratio of MH samples obtained by EDX (Figure 4.18) and ICP. EDX wt. % values are based on a composition made of only Si, O, Ni and P elements.

Catalyst	EDX data			ICP data		
	Ni (wt. %)	P (wt. %)	P/Ni	Ni (wt. %)	P (wt. %)	P/Ni
5%Ni@Sil-1 MH	6.8	3.9	0.57	5.1	1.3	0.5
CitAc Ni@Sil-1 MH	3.1	0.2	0.06	2.2	0.2	0.15

A possible explanation for the peculiar behavior of CitAc Ni@sil-1 MH catalyst during steam reforming could be that phosphorous species initially present were gradually removed from Ni nanoparticles with time on stream, leading to a gradual increase of the proportion of accessible metal Ni atoms. This increase could have compensated the loss of activity resulting from particle sintering inside the multi-hollow cavities. This assumption is supported by *in situ* methanation test realized after reforming: the CO methanation activity was three times higher than that of the fresh catalyst and the fraction of accessible metal increased from 0.8 to 4.3% (Table 4.10).

Table 4.10 Methanation activity of the fresh and post-reforming CitAc Ni@sil-1 MH sample at 300 °C.

Catalyst	Methanation activity at 300°C	Specific metal surface area	Accessible metallic Ni
	($\mu\text{mol}_{\text{CH}_4} \text{s}^{-1} \text{g}_{\text{Ni}}^{-1}$)	($\text{m}^2 \text{g}^{-1}$)	(%)
CitAc Ni@sil-1 MH fresh	23	0.06	0.8
CitAc Ni@sil-1 MH used	79	0.20	4.3

4. Multi Hollow catalysts prepared by a P-free desilicating agent

4.1. Synthesis of Ni@silicalite-1 TBA

Ni containing multi hollow catalysts were prepared using TBAOH (tetrabutylammonium hydroxide) as an alternative structure directing agent to TBPOH. Based on the desilication method using TBPOH (section 1.2.3 of chapter 2), the hollow structure was obtained by treating 1 gram of Ni(NO₃)₂/Sil-1 using a solution of TBAOH (5 ml; 1 M; pH = 14.5) with a same ratio mol_{SDA}/g_{Ni(NO₃)₂/Sil-1}. The above mentioned TBAOH solution was prepared by mixing 32.3 g of TBABr (tetrabutylammonium bromide, Sigma-Aldrich, 99%) with 11.6 g of Ag₂O (Alfa Aesar, 99.99%) in 100 mL of H₂O for 5 minutes in absence of light (precipitated AgBr was then removed by filtration). The mixture was then transferred into a Teflon-lined autoclave and heated at 115 °C under rotating conditions for 96 h.

The solution was then cooled down, washed with water until pH = 7 and dried overnight at 90 °C. Finally the powder was successively calcined in air at 450 °C for 6 h to obtain the 5%NiO@Sil-1 TBA and reduced at 750 °C under H₂ for 3 h with a heating rate of 2.5 °C min⁻¹ to yield the 5%Ni@Sil-1 TBA. 0.5 gram of 5%NiO@Sil-1 TBA was added to 50 mL of a 0.5 mol/L aqueous solution of citric acid (≥ 99.0%, Sigma-Aldrich). The mixture was stirred vigorously at 80 °C for 2 h. The solution was then centrifuged and washed with water until pH = 7 and dried overnight at 90 °C. Finally the solid was reduced at 750 °C under H₂ for 3 h to yield the sample referred to as CitAc Ni@Sil-1 TBA.

4.2. Characterization of Ni@silicalite-1 TBA

TBAOH is an appropriate templating molecule for the crystallization of MEL-type zeolites (Silicalite-2 and ZSM-11).^[224] Similarly to the MFI framework, MEL-type zeolites have three dimensional 0.55 nm channels. However, the MFI topology consists of intersecting straight and sinusoidal channels, while the MEL topology has only straight channels. Under specific crystallization conditions, TBAOH can direct the crystallization of a mixtures of MFI/MEL structures.^[205]

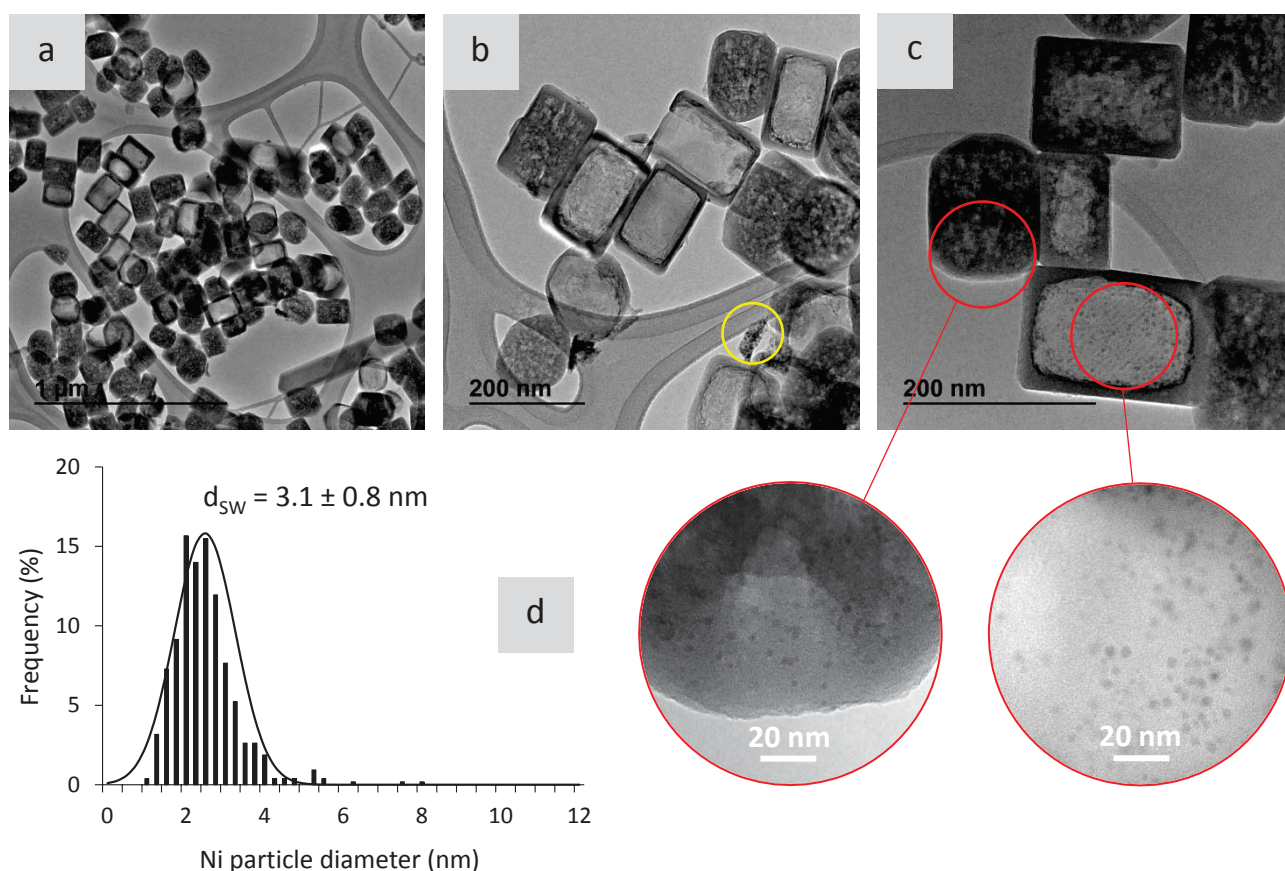


Figure 4.19 TEM images of 5%NiO@Sil-1 TBA (a,b). Yellow circles point out external nickel. TEM images (c) and particle size distribution (d) of CitAc Ni@Sil-1 TBA. The distributions is modelled using a Normal law.

When applied to silicalite-1 nanocrystals loaded with Ni, TBAOH-based desilication led mostly to sponge-like nanoporous boxes, as observed in the TBPOH-treated samples (Figure 4.19a,b,c). However, approximately 20-25 % in number of the boxes present a large and unique internal cavity, indicating that a hybrid-like material made of single and multi hollow nanoboxes was obtained upon the TBAOH treatment. The presence of sharp-edged single hollow crystals suggest that dissolution and recrystallization were possible for some of the crystals, even at the relatively low crystallization temperature. The heterogeneity observed in the shape of the hollow crystals may arise from discrepancies in terms of degree of crystallinity among the original plain silicalite-1 crystals. Van Bokhoven and co-workers had demonstrated that structural properties of MFI zeolites have an effect on creation of porosity upon alkaline treatment. Preferential pore formation occurs in defective materials; in contrast the lack of defect explains the stability of the zeolite crystals.^[221]

Table 4.11 Nickel loadings of hollow silicalite-1 catalysts before and after selective removal of external metallic particles with citric acid.

Catalyst	Nickel loading (wt.%)		Nickel removal during the citric acid treatment
	Before citric acid treatment	After citric acid treatment	
Ni@Sil-1 TBA	4.2	2.3	45%

Similarly to the single and multi hollow samples, partial dissolution of silica species of the zeolite leads to the formation of stable nickel phyllosilicates, located inside and outside the cavities (Figure 4.19a,b). When expose under H₂ for 3 hours at 750 °C, Ni²⁺ species were reduced and numerous metallic nanoparticles were formed both inside single hollow and multi hollow crystals (Figure 4.19c). External Ni species were mostly removed by treating 5%NiO@Sil-1 TBA with citric acid, resulting in a drop in Ni content by 45 % (Table 4.11). The sample obtained upon reduction was denoted CitAc Ni@Sil-1 TBA and presented a narrow particle size distribution (Figure 4.19d). The average particle size ($d_{sw} = 3.1 \pm 0.8$ nm) was comprise between that of CitAc Ni@Sil-1 SH ($d_{sw} = 4.5 \pm 1.1$ nm) and that of CitAc Ni@Sil-1 MH ($d_{sw} = 2.7 \pm 0.5$ nm). This intermediate mean size is due to a partial encapsulation of particles in single hollow boxes, whereas the remainder is entrapped inside multi hollow crystals. Largest Ni particles were observed within single hollow crystals.

Table 4.12 Experimental and theoretical mass losses due to H₂O desorption and Ni²⁺ reduction.

Catalyst	Experimental mass loss (%)		Theoretical mass loss from Ni ²⁺ reduction		
	$\Delta m_{des.}$	Δm_{red}	NiO	1:1 Phyllo	2:1 Phyllo
5%NiO@Sil-1 TBA	2.6	1.6	1.1	1.9	1.5

4.2.1. Thermogravimetric analyses

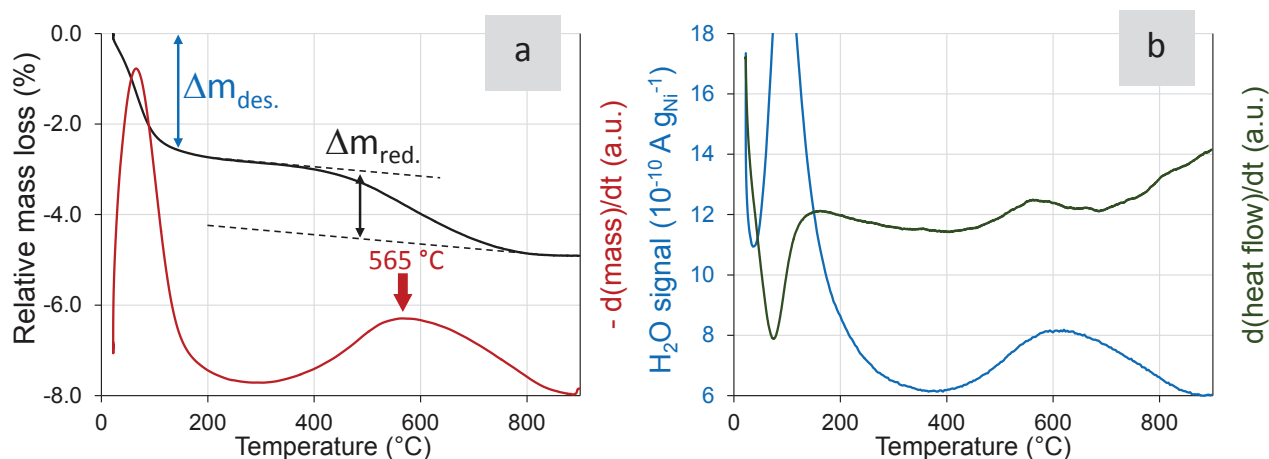


Figure 4.20 Thermal gravimetric profile (a) and related H₂O production (b) of NiO@Sil-1 TBA under H₂.

The thermogravimetric profile of the NiO@Sil-1 TBA catalyst prior to citric acid treatment is shown in Figure 4.20. At 150 °C, the initial change in the catalyst mass due to H₂O desorption had reduced the mass of the catalyst by 2.6 % (Table 4.12). This value was higher than that of NiO@Sil-1 SH (1.8 %) and lower than that of NiO@Sil-1 MH (2.8 %), indicating that the density of defects of the TBA sample was intermediate between the ones of the SH and the MH samples. Beyond 400 °C, a gradual 1.6 wt.% mass reduction associated with an endothermic phenomenon was observed. As indicated in Table 4.12, this experimental mass reduction is in line with the theoretical one expected from the reduction of Ni phyllosilicates. Both TGA and TPR techniques indicates the presence of a single peak, with maximum weight loss centred at 565 °C. We have seen in chapter 3 that this peak can be attributed to the reduction of 1:1 Ni phyllosilicates. Interestingly, no peak was observed in the temperature range 700-750 °C, suggesting the absence of 2:1-type phyllosilicates. In addition, this absence emphasizes the idea that the peculiar TGA profile of the NiO@Sil-1 MH is governed by the presence of P-containing compounds.

4.2.2. X-ray diffraction

X-ray diffraction was used to examine the effect of the TBAOH and subsequent citric acid treatments on the structural properties of the parent silicalite-1 (Figure 4.21). The preservation of the structure of the original zeolite was confirmed by the similarity of the XRD patterns. Minor modifications were observed in the region between 23 and 25°. Upon treatment with TBAOH, a split in the peak at 24.4° into a doublet indicate a lower degree of internal framework defects. This is due to the presence of highly crystalline single hollow nanoboxes in significant proportions (20-25 %). The doublet was less

pronounced after citric acid treatment, supporting that the acid creates additional defects. For both TBAOH-treated samples, Ni phases were not detected by XRD due to the low loading of this sample.

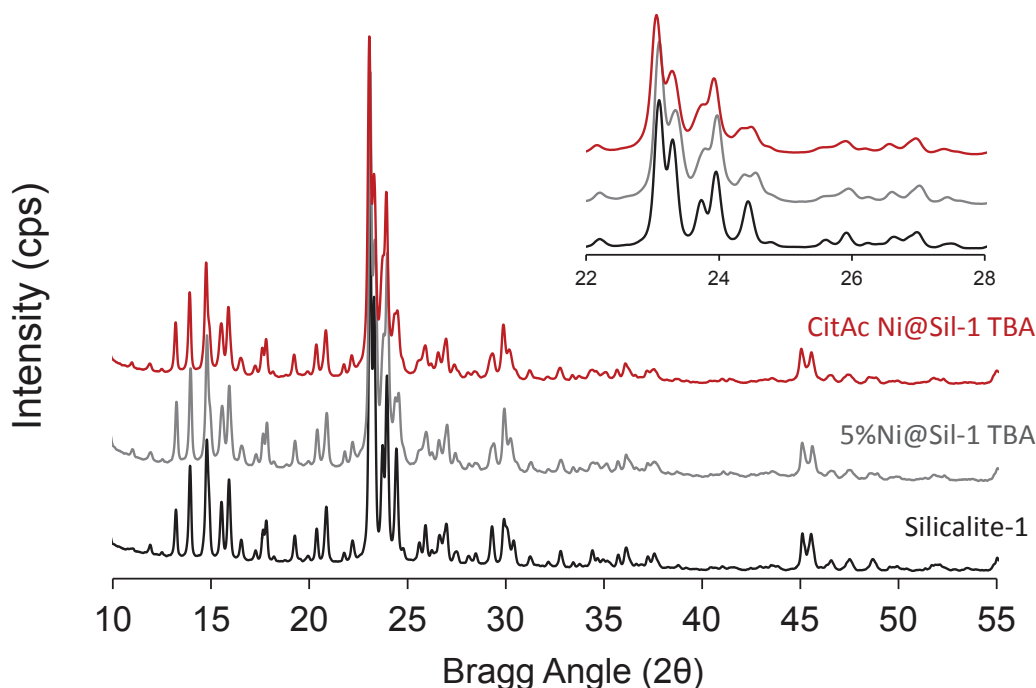


Figure 4.21 XRD patterns of the various samples. A zoom in the region $2\theta = 22-28^\circ$ is shown at the top right corner of the figure.

4.2.3. Nitrogen physisorption

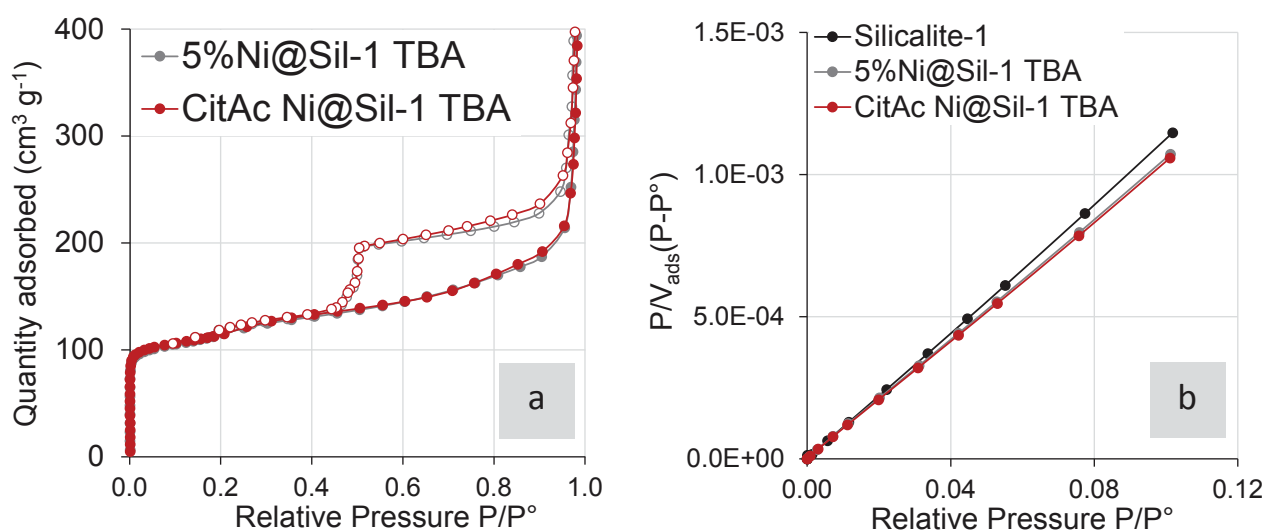


Figure 4.22 N_2 physisorption isotherms at 77 K (a) and BET plots (b) of the TBAOH-treated samples.

Textural properties of the 5%Ni@Sil-1 TBA and CitAc Ni@Sil-1 TBA were studied by N_2 adsorption at 77 K (Figure 4.22a). Both samples showed type-IV isotherms similar to that of the multi hollow samples, with characteristic hysteresis loops closing at 0.42. The peculiar shape of these isotherms

suggest that these materials behave as a linear combination of the porous properties of the purely single and multi hollow materials (Table 4.12). The small loop at $P/P^{\circ} = 0.15$ nm was not clearly observed, but was suggested by the presence of a shoulder on the desorption branches.

The presence of internal mesopores with different sizes and a wide pore size distribution is confirmed by the continuous N_2 uptake between 0.1 and 0.9. Desorption by pore blocking was endorsed by the gradual decrease observed on the descending curves from 0.52 down to 0.42. BET surface areas of the desilicated samples slightly increased with respect to the original silicalite-1, as commonly reported for hierarchical zeolites (Figure 4.22b).^[188] Porous volumes were closed to that reported for the purely single and multi hollow samples (Table 4.4). Finally, it must be noted that the citric acid treatment has no relevant impact on the porosity of the sample.

Table 4.13 Porosity of the TBAOH-treated samples.

Catalyst	S_{BET}^a ($m^2 g^{-1}$)	V_{micro}^b ($cm^3 g^{-1}$)	V_{cavity}^c ($cm^3 g^{-1}$)	V_{total}^d ($cm^3 g^{-1}$)
Silicalite-1	390	0.13	0.00	0.20
5%Ni@sil-1 TBA	411	0.14	0.09	0.35
CitAc Ni@sil-1 TBA	418	0.14	0.09	0.37

^a BET method

^b Volume of N_2 adsorbed when the slope of the adsorption branch becomes lower than $10^3 cm^3 g^{-1}$

^c Difference in N_2 uptake between the adsorption and the desorption branches of the isotherms at $P/P^{\circ} = 0.5$

^d Volume of N_2 adsorbed at $P/P^{\circ} = 0.9$ from desorption branch

4.3. Catalytic properties of Ni@silicalite-1 TBA

This work was not completed at the time of the thesis submission and will hopefully be presented at the viva.

5. Conclusions

Two different strategies were pursued to create hollow silicalite-1 crystals and to use the corresponding cavities to encapsulate Ni nanoparticles. While the use of TPAOH and relatively high temperatures lead to crystals exhibiting a single internal large cavity, the use of TBPOH at 115 °C resulted in multi-hollow architectures. During formation of the porosity, Ni precursors react with

dissolved silica species to form Ni phyllosilicates, further reduced into nanoparticles under hydrogen at 700 °C. Even in the case of a unique cavity, this reduction did not lead a single Ni particle, mainly because of the strong interaction between phyllosilicates and the zeolite surface. Ni nanoparticles displayed sintering with time under steam methane reforming condition at 700 °C, leading to a significant particle growth and catalyst deactivation for both samples. Nonetheless, the dispersion of Ni particles into the numerous cavities of the multi hollow crystals remained higher after reaction than that obtained in the case of the single hollow crystals before reaction. Both catalytic activities and hydrogen adsorption data indicate that the fraction of accessible Ni metal atoms was very low, suggesting that the main part of surface atoms were covered with amorphous silica resulting from the reduction of phyllosilicates. This fraction was even lower in multi-hollow crystals because of the presence of phosphorus containing species that were formed during calcination of the organic templates. The gradual removal of these phosphorous poisoning species probably explained the apparent constant methane steam reforming activity with time on stream, by compensating almost exactly the limited sintering occurring simultaneously.

These results indicate that the presence of multi hollow crystals is effective in keeping highly dispersed Ni nanoparticles, but the catalytic performance of the corresponding encapsulated Ni nanoparticles suffered from the presence of poisoning P-containing species resulting from the calcination of the template in air. Attempts to prepare similar materials using phosphorus-free molecules were successful and should greatly improve the properties of such catalysts under the harsh conditions of steam reforming reactions.

Highlights

- Silicalite-1 crystal can be converted into multi hollow crystals.
- Highly dispersed nickel nanoparticles can be encapsulated within the multi hollow solid.
- The catalytic activity of the multi hollow solid suffered from the presence of P-containing poisoning species.
- Reduction of phyllosilicates leads to nickel surface coverage with amorphous silica and to a low fraction of accessible metallic sites.
- Multi hollow catalysts were also prepared in absence of P-containing poisoning species and are expected to be highly active in methane reforming.

Chapter 5 - Effect of tars on the activity of Ni@Sil-1 SH catalysts in the reforming of producer gas

1. Introduction

As addressed in chapter 1, tars are well known coke precursors that can lead to the deactivation of reforming catalysts. The propensity for coke formation from tars will depend on the catalyst formulation and reaction conditions such as reaction temperature and steam/carbon (S/C) ratio.

Most of former studies on the upgrading of producer gas have focused on the steam reforming of representative tar compounds, as well as toluene or naphthalene. Kiennemann and co-workers reported the high stability and activity of a Ni/olivine catalyst in the steam reforming of toluene for 30 hours over 650 °C.^[105] Sato and Fujimoto also reported stable naphthalene conversions at 825 °C over a WO₃-promoted Ni/MgO-CaO catalyst, even in the presence of H₂S.^[225]

The impact of tars on the reforming of methane is less documented and is necessary for a successful application of the biomass-derived gas. However, Di Carlo et al. reported no deactivation at 800 °C of a Ni/Ca₁₂Al₂₄O₃₃ catalyst used for the steam reforming of methane and tars derived from hazelnut shells gasification.^[226] Dagle et al. recently showed that the presence of benzene and naphthalene led to marked deactivations of methane conversion due to coking over Ni, Rh and Ir-based catalysts.^[227] The coking was alleviated by using higher reaction temperatures and by the presence of a noble metal.

In this chapter, the effect of naphthalene on methane conversion using Rh and Ni-based catalysts was investigated at 700, 800 and 900 °C and, importantly, at high space velocities to limit the full conversion of methane and better assess deactivation. Additional experiments were also performed using toluene and pyrene to unravel the main origin of the deactivation.

Our investigation focused on naphthalene because this model molecule is one of the most difficult tar representatives to steam reform and one of the most abundant among the polyaromatics

formed during low-temperature gasification of woody biomasses (Figure 1.7).^[42,104] Naphthalene is also the smallest polyaromatic available and thus any catalyst that would display a size-selective resistance with respect to this molecule should also do so for the other larger compounds. Indeed, naphthalene has a kinetic diameter of 0.62 nm, which is larger than the pore diameter of MFI zeolites (ca. 0.56 nm). Millini et al. reported that diffusion of naphthalene in the medium pore-size zeolite of the MFI-type was difficult, with energy barriers of around 114 kJ mol^{-1} .^[228] In contrast, the transport of H_2O , CO_2 , CO , H_2 and CH_4 (and many other small hydrocarbons) through the MFI zeolite layer is markedly faster. It is therefore possible that the slow transport of naphthalene through MFI-type pores could protect the metal particles encapsulated therein from coking, through the interplay of coke formation and gasification/reforming. These materials would thus exhibit size selective properties, being able to reform small-size hydrocarbons, while being resistant against coking due to large polyaromatics.

We reported in chapter 3 on the size exclusion at low temperatures of mesitylene (kinetic diameter = 0.87 nm) from Ni-loaded MFI-type silicalite-1 single hollow nanocrystals. Still in chapter 3, we have observed that these nanoboxes act as nanoreactors in which the metallic particles are encapsulated and protected at intermediate temperatures from tar poisoning by molecular sieving. The activity and durability of Ni particles embedded in similar silicalite-1 nanoboxes during methane reforming catalyst will be of particular interest here, since the molecular sieving property at temperatures as high as $900 \text{ }^\circ\text{C}$ has not yet been discussed. The aim of chapter 5 is to investigate into the extension of this particular feature to reforming conditions.

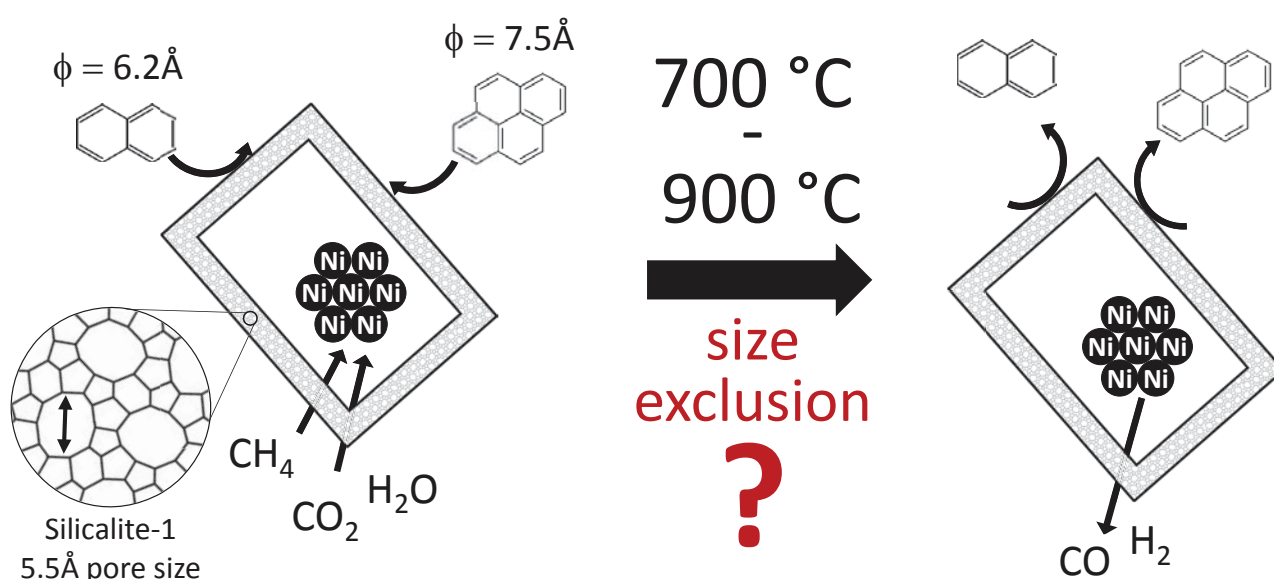


Figure 5.1 Scheme of the potential molecular sieving property of single hollow Ni@Sil-1 catalysts.

2. Experimental procedure

2.1. Choice of catalysts

In the present chapter, the stability of the single hollow 5%Ni@Sil-1 and CitAc Ni@Sil-1 catalysts was evaluated in the reforming of CH₄ in presence of tar model compounds. These two samples were selected because of their promising tar sieving property at lower temperatures, in the hydrogenation of arenes and in CO methanation (see chapter 3). In addition, the high degree of crystallinity of the single hollow samples should endorse a high thermal stability of the material.

Two commercial catalysts based on Rh and Ni, known to be respectively the most active noble and transition metal in SMR (see section 2.2.2.1 of chapter 1), were also studied. The objective was to discriminate between these two classes of metals on their propensity to deactivate when exposed to tar model compounds. The commercial Rh-based catalyst (1%Rh/Al₂O₃, Alfa Aesar, ref. 11769) and the commercial Ni-based catalyst (11%Ni/CaAl₂O₃, HiFUEL R110, Alfa Aesar, ref. 45465) were selected and used as unprotected reference catalysts. These two samples were labeled Com Rh and Com Ni, respectively.

2.2. Properties of commercial catalysts

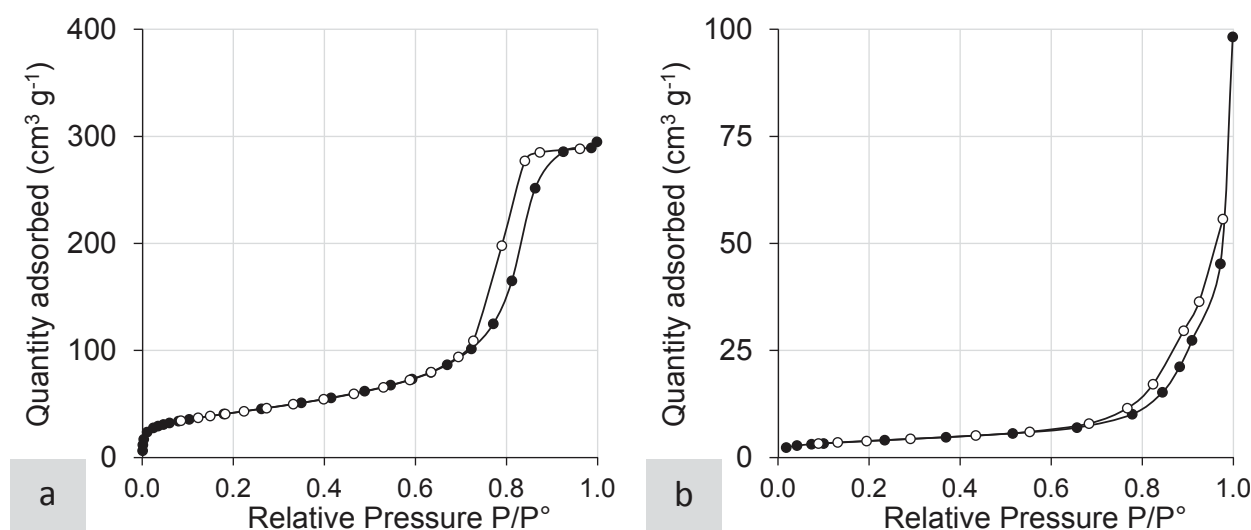


Figure 5.2 Nitrogen adsorption (full symbols) and desorption (open symbols) isotherms of Com Rh (a) and Com Ni (b) at 77 K.

Porosities (Table 3.2), N₂ physisorption isotherms (Figure 3.15) and metal contents (Table 3.1) of the single hollow samples were already reported in chapter 2. The textural properties of the commercial

samples are reported in Table 5.1. Com Rh exhibits a type-IV isotherm, which is characteristic of mesoporous materials (Figure 5.2). Despite the low content in Rh, a high metal surface area was derived from the H₂ chemisorption measurement (Table 5.1). The calcium aluminate support of Com Ni exhibits a type-II nitrogen isotherm which is given by nonporous or macroporous adsorbents.^[220] The resulting BET surface area was low and the Ni content was poorly dispersed.

Table 5.1 Textural properties of commercial samples.

Catalyst	Support ^[a]	S _{BET} ^[b] (m ² g ⁻¹)	V _{micro} ^[c] (cm ³ g ⁻¹)	V _{total} ^[d] (cm ³ g ⁻¹)	Metal loading ^[e] (wt.%)	Metal surface area ^[f] (m ² g ⁻¹)	Metal dispersion ^[f] (%)
Com Rh	γ-Al ₂ O ₃	150	0.12	0.45	0.8 (Rh)	2.25 ± 0.05	63 ± 1
Com Ni	CaAl ₂ O ₃	14	-	0.13	11.4 (Ni)	1.75 ± 0.05	2.3 ± 0.1

^a Based on XRD analyses, ^b BET method, ^c t-plot method

^d Volume of N₂ adsorbed at P/P° = 1, ^e ICP analyses, ^f Based on H₂ chemisorption analyses

2.3. Reforming tests

The reforming experiments were performed on a lab-scale reforming unit described in details in part 3.3 of chapter 2. The fixed-bed continuous-flow reactor consisting of a quartz tube containing the non-diluted catalyst powder. Prior to testing, the sample was reduced *in situ* at 700 °C with a heating rate of 400 °C h⁻¹ for 2 h in a 200 mL min⁻¹ flow rate of 20 vol.% H₂/Ar mixture. The feed gas composition used in these tests is described in Table 2.2 (H₂S was not added to the feed stream). The overall system pressure was controlled and set at P_{total} = 2.2 bar. It must be noted that the impact of various tar model compounds (naphthalene, toluene and pyrere) on the activity in CH₄ reforming was studied individually and discussed in three different sections of this chapter. The desired concentration of tar was fed using a saturator operated as follows:

- Section 3.1 (1400 ppmv naphthalene): T_{saturator} = 107 °C, F_{carrier gas} = 12.5 mL min⁻¹ of CO₂
- Section 3.2 (10000 ppmv toluene): T_{saturator} = 78 °C, F_{carrier gas} = 7.5 mL min⁻¹ of Ar + N₂ mixture
- Section 3.3 (5 ppmv toluene): T_{saturator} = 149 °C, F_{carrier gas} = 20 mL min⁻¹ of CO₂ + Ar + N₂ mixture

In the tests discussed in section 3.1, 10 mg of the catalyst was tested sequentially at 700, 800 and 900°C, dwelling 24 h at each temperature. At each of these temperatures, 1400 ppmv of naphthalene was only introduced in the feed for 6 hours, between t = 2 h and up to t = 8 h (Figure

5.3). The reversibility of the deactivation was then studied by maintaining the catalyst under a naphthalene-free feed for up to 16 h. In section 3.3 are reported the catalytic results over 24 hours at 700 °C operating in presence of 5 ppmv of pyrene. Similarly to naphthalene, pyrene as only introduced in the feed between $t = 2$ h and up to $t = 8$ h. The total gas flow rate of reactants was 125 ml min^{-1} . The corresponding WHSV was 689 h^{-1} (the GHSV was $750\,000 \text{ h}^{-1}$, assuming catalyst density to be unity). This high WHSV value was selected to obtain an accelerated ageing in terms of tar exposure on a reasonable timescale. Furthermore, these conditions prevented total conversion of hydrocarbons, providing insights in terms of activity and stability of the different catalysts.

Catalytic reforming tests using toluene as a tar model compound are described in section 3.2 and were carried out on 25 mg of catalyst in three independent tests, i.e. at 700, 800 and 900 °C. 10000 ppmv of toluene were fed continuously during each of the 24 h-long test. For the sake of clarity, similar tests were also performed in absence of toluene. The corresponding WHSV was 276 h^{-1} (the GHSV was $300\,000 \text{ h}^{-1}$, assuming catalyst density to be unity).

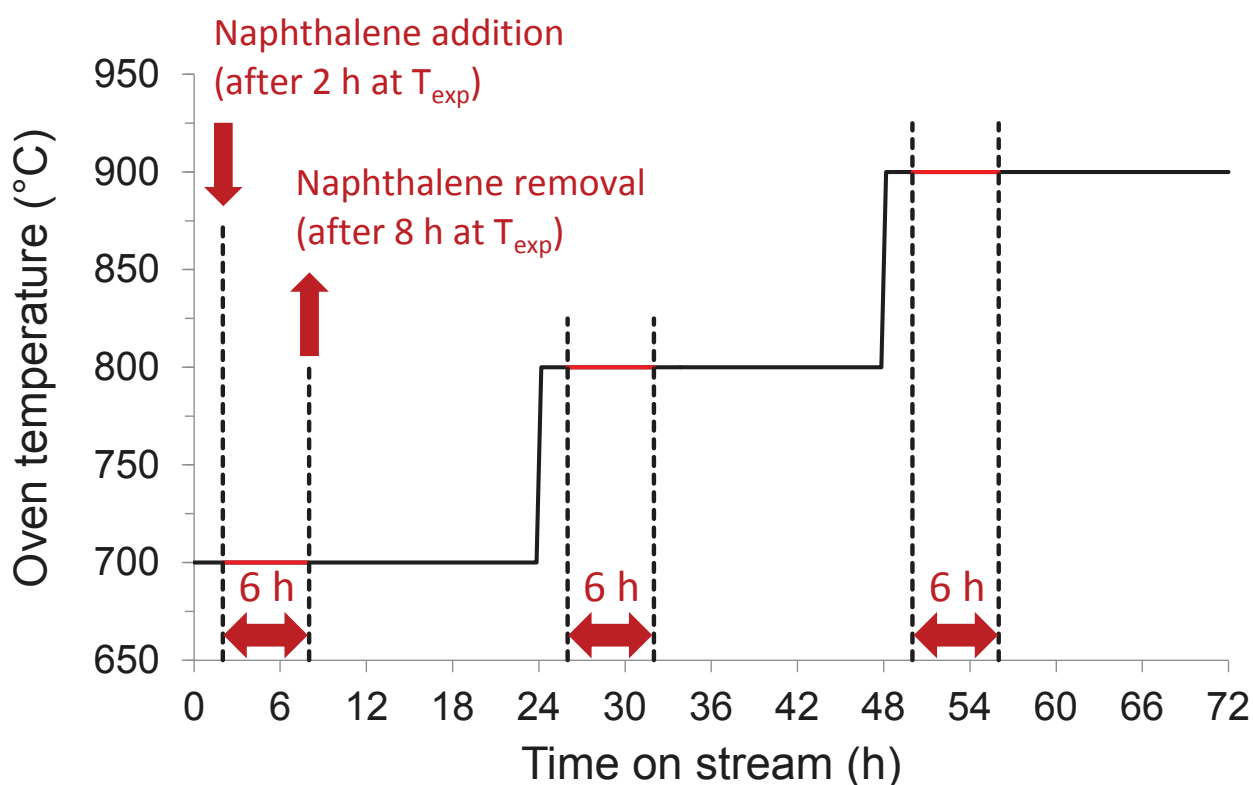


Figure 5.3 Oven temperature set-point as a function of the time on stream for the tests on the effect of naphthalene (section 3.1)

3. Catalytic results

3.1. Reforming activity in presence of a 2-ring aromatic

3.1.1. Catalytic activities and stabilities

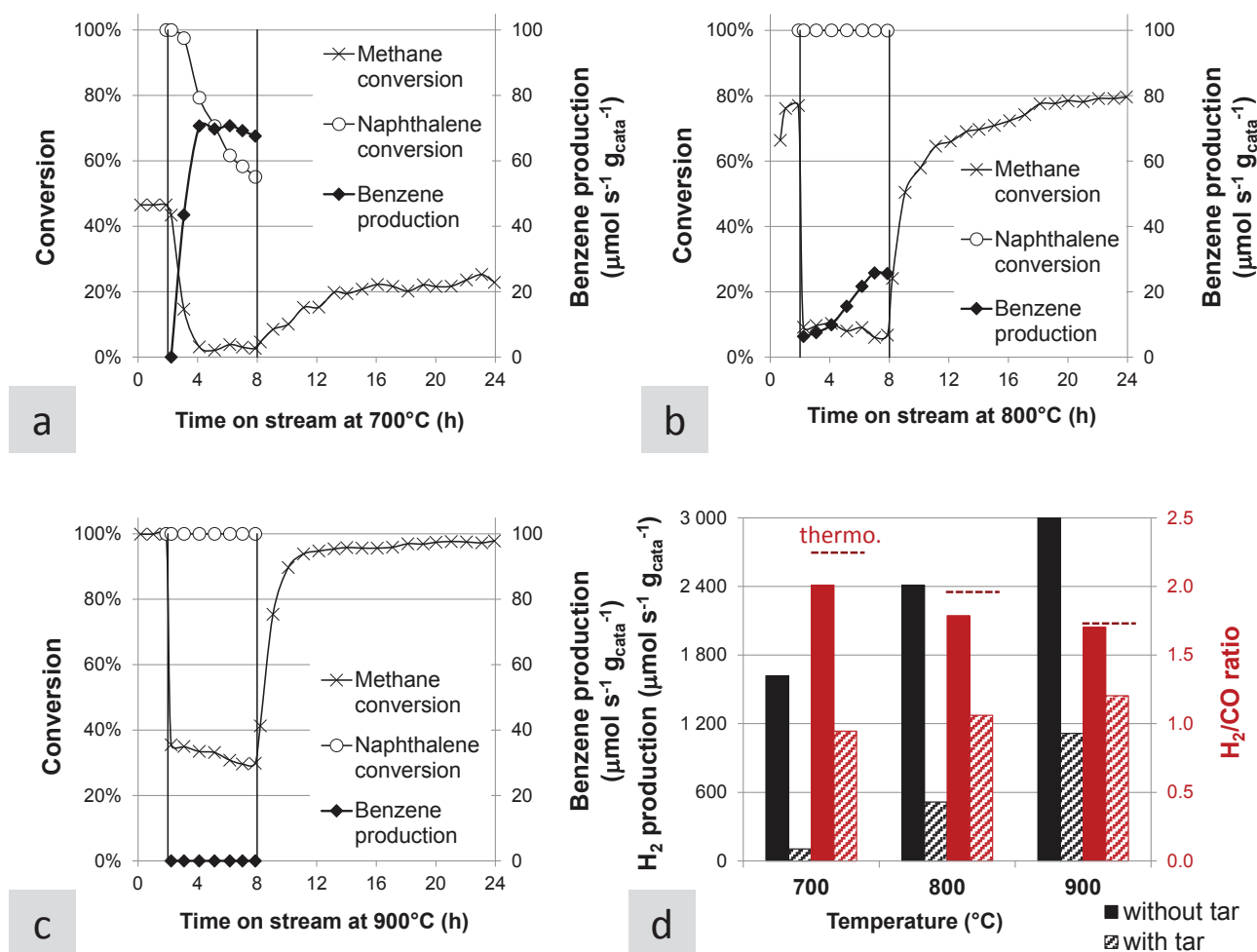


Figure 5.4 Methane and naphthalene conversions and benzene production measured over time on stream at (a) 700 °C, (b) 800 °C and (c) 900 °C over Com Rh catalyst. H₂ production and H₂/CO ratio measured in presence/absence of naphthalene (d). 1400 ppmv of naphthalene were fed only between 2 h up to 8 h.

The effect of the addition of 1400 ppm of naphthalene on the activity of the various catalysts was determined successively at 700, 800 and 900 °C (Figure 5.4 to Figure 5.7). At each temperature and for all the catalysts, the introduction of naphthalene led to a sharp and almost total loss of the conversion of methane. The poisoning effect of this hydrocarbon appeared to be only partly and slowly reversible at 700 °C over the commercial Rh and Ni catalysts (Figure 5.4 and Figure 5.5a). Yet, methane conversion was fully and readily recovered at 800 and 900 °C over these two commercial samples. It should be noted that benzene was formed as a decomposition product of naphthalene.

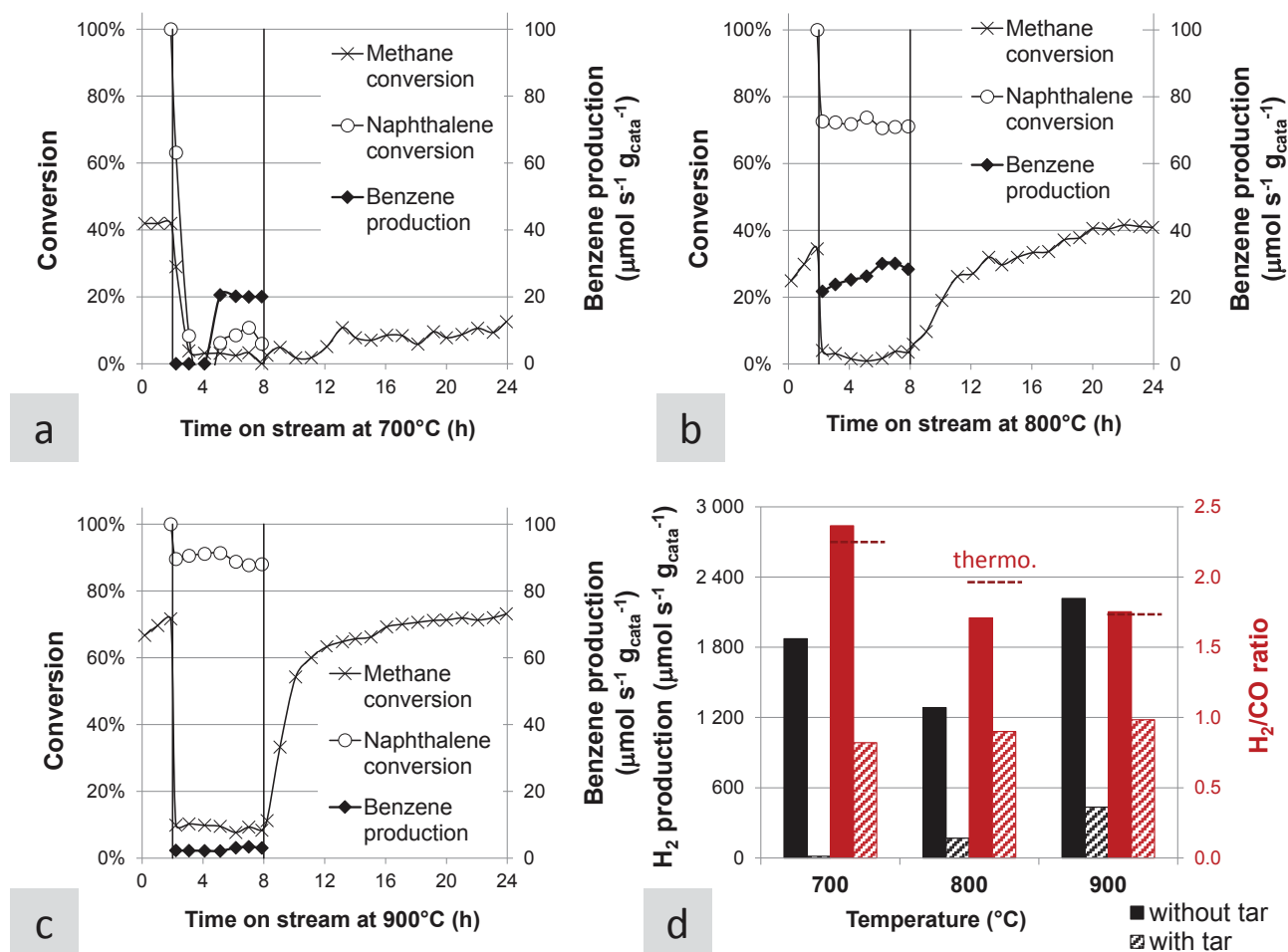


Figure 5.5 Methane and naphthalene conversions and benzene production measured over time on stream at (a) 700 °C, (b) 800 °C and (c) 900 °C over Com Ni catalyst. H₂ production and H₂/CO ratio measured in presence/absence of naphthalene (d). 1400 ppmv of naphthalene were fed only between 2 h up to 8 h.

The composition at the reactor outlet (i.e. hydrogen productions and H₂/CO ratio) at 700, 800 and 900 °C in absence and in presence of the tar model compound were respectively measured at $t = 2$ h prior to naphthalene introduction, and at $t = 8$ h before naphthalene removal (Figure 5.4d and Figure 5.5d). For the two commercial catalysts, at each temperature the addition of naphthalene led to a significant drop in the production of hydrogen, in agreement with the loss of methane conversion. In addition, it is clear that the lower the temperature, the higher the impact of tar poisoning on the hydrogen production. The H₂/CO ratio measured at the reactor outlet in absence of tars was higher than 1.5 and close to that calculated at the thermodynamic equilibrium (dashed lines in Figure 5.4d and Figure 5.5d). Thermodynamics data calculated at the equilibrium were presented in Figure 1.10. Yet, when naphthalene was present in the feed, a drop in this ratio below 1.5 was observed. When methane conversion was fully hampered by naphthalene, the related H₂/CO ratio was close to ca. 0.8, which correspond to that at the reactor inlet. This indicates that tar poisoning do not only prevent methane reforming but also the water-gas shift reaction.

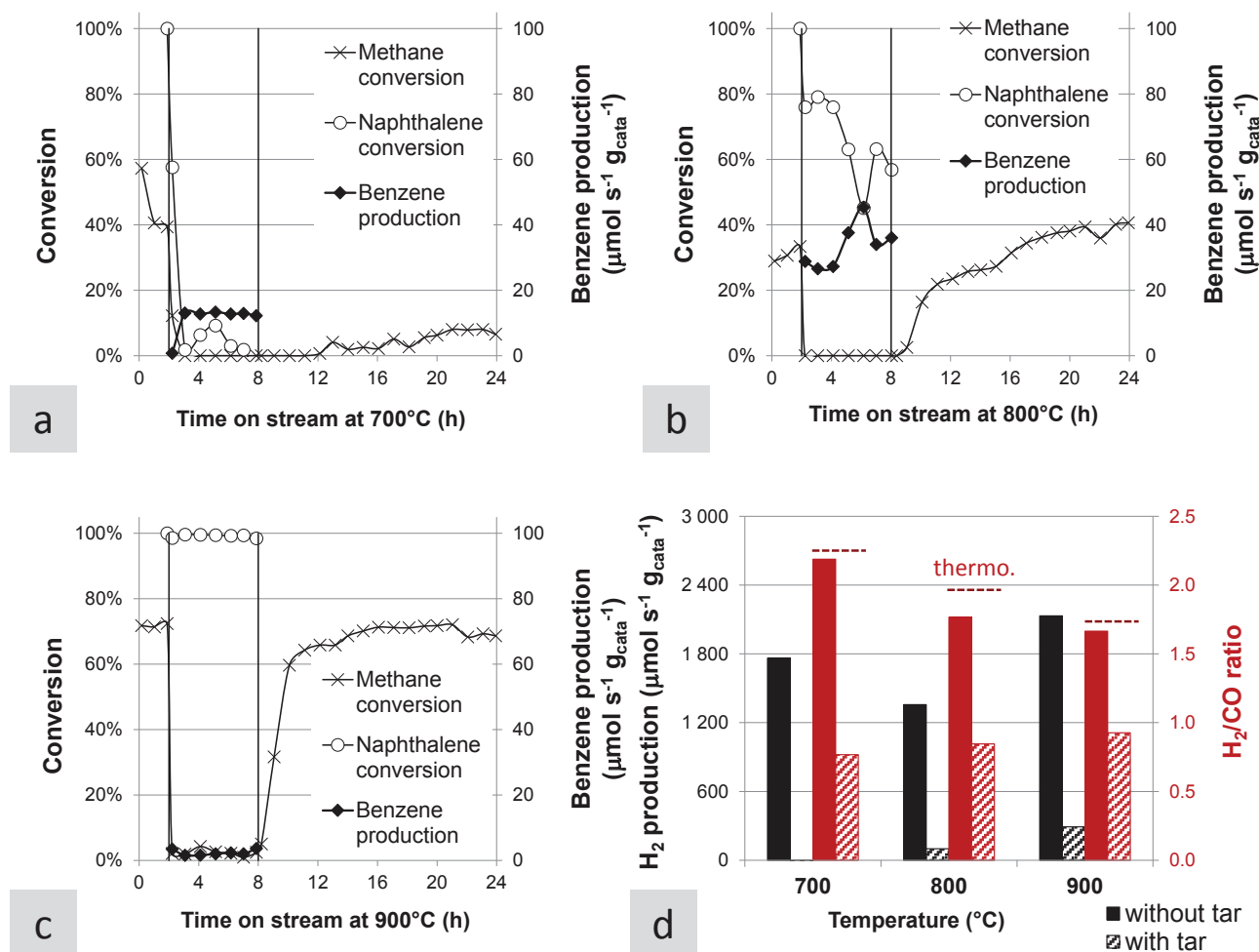


Figure 5.6 Methane and naphthalene conversions and benzene production measured over time on stream at (a) 700 °C, (b) 800 °C and (c) 900 °C over 5%Ni@Sil-1 catalyst. H_2 production and H_2/CO ratio measured in presence/absence of naphthalene (d). 1400 ppmv of naphthalene were fed only between 2 h up to 8 h.

The 5%Ni@Sil-1 catalyst and especially the citric acid-treated CitAc Ni@Sil-1 sample appeared to deactivate even before the introduction of naphthalene (Figure 5.6 and Figure 5.7). As discussed in chapter 3, this initial deactivation was due to Ni nanoparticle sintering, enhanced by the presence of steam and the high reforming temperature. These two hollow zeolite-based catalysts showed a strong deactivation in the presence of naphthalene at all temperatures, from 700 up to 900 °C. This result is disappointing as the zeolite membrane looks ineffective in the molecular sieving of this 2-ring model aromatic. In particular for the CitAc Ni@Sil-1 sample because most of the Ni particles were initially embedded inside the silicalite-1 nanoboxes (Figure 3.6) and were expected to show a better resistance against the bulky naphthalene molecules. However, it should be noted that the 5%Ni@Sil-1 sample shows a catalytic activity very similar to that of the Com Ni while being twice less loaded (Table 5.1) and encapsulating partly inaccessible Ni particles (Figure 4.17). In addition, methane conversion was fully and readily recovered at 800 and 900 °C after tar removal.

The activity at 900 °C of the CitAc Ni@Sil-1 sample showed a peculiar behaviour, with a transient activity spike followed by total deactivation (Figure 5.7c), contrary to the case of the sample not-treated by citric acid (Figure 5.6c). Furthermore, the H₂/CO ratio measured after naphthalene removal was close to that in the reactor inlet, indicating a complete loss of active Ni that prevent the fast water-gas shift equilibrium to be established (Figure 5.7c).

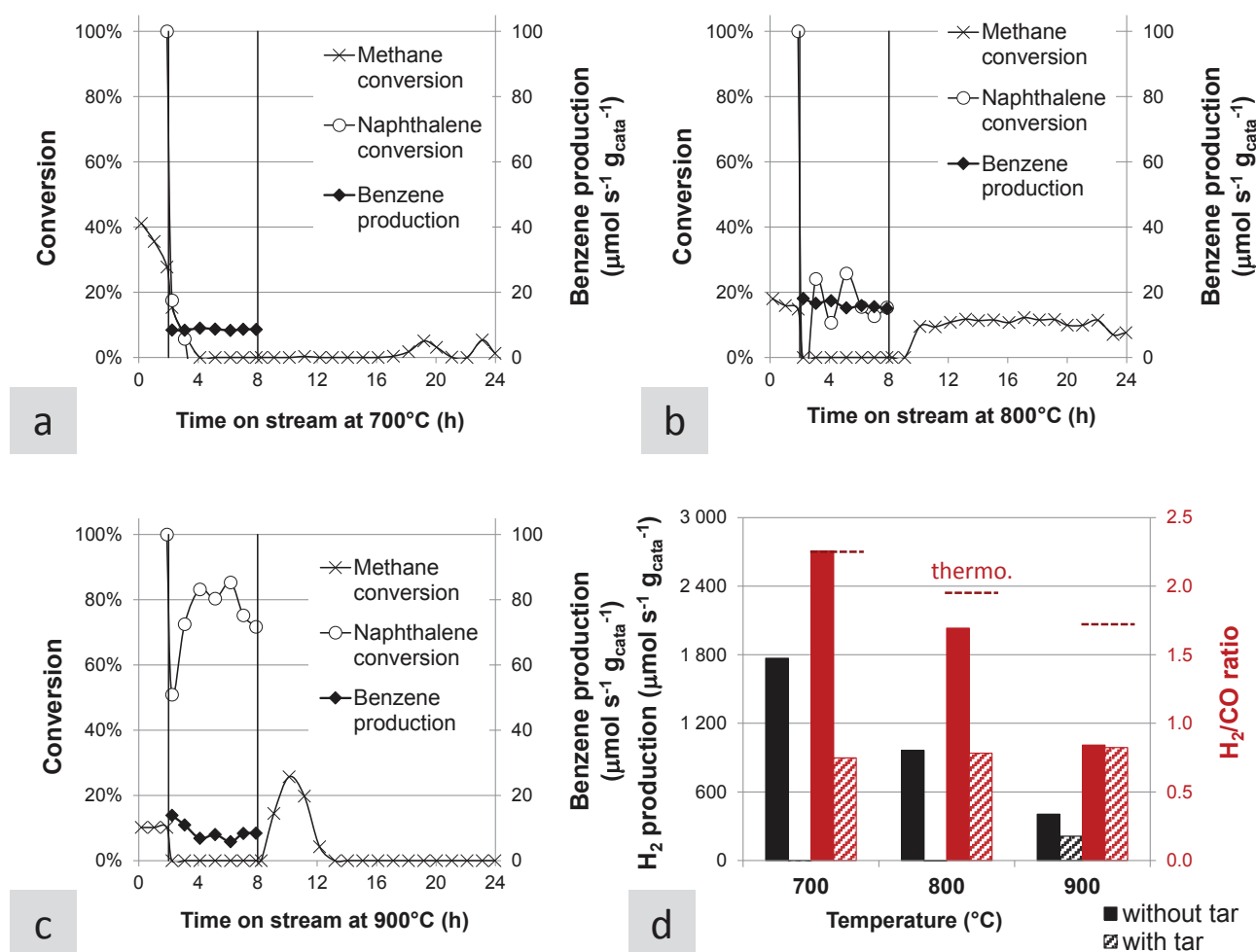


Figure 5.7 Methane and naphthalene conversions and benzene production measured over time on stream at (a) 700 °C, (b) 800 °C and (c) 900 °C over CitAc Ni@Sil-1 catalyst. H₂ production and H₂/CO ratio measured in presence/absence of naphthalene (d). 1400 ppmv of naphthalene were fed only between 2 h up to 8 h.

3.1.2. Characterizations of used samples

A close inspection of these two single hollow catalysts after reaction by TEM indicated that the structure of nanoboxes of the citric acid-treated sample had totally collapsed (Figure 5.8b), contrary to the case of the 5%Ni@Sil-1 sample (Figure 5.8a). The crystalline structure of the nanoboxes was observed by electron diffraction, confirming that the MFI framework was preserved during the reaction, while that of the CitAc Ni@Sil-1 was almost no more observed (Figure 5.8 right).

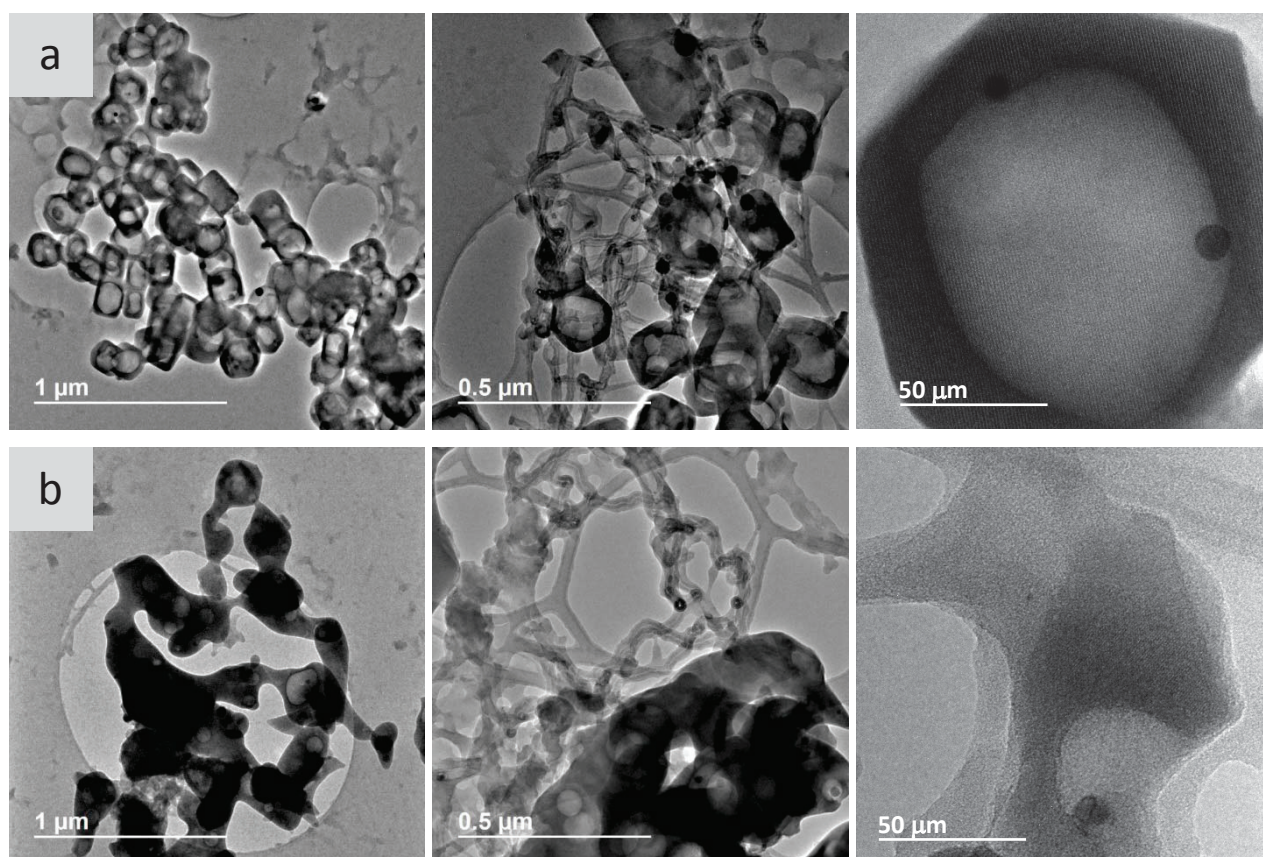


Figure 5.8 TEM images of post-reaction 5%Ni@sil-1 (a) and CitAc Ni@sil-1 (b) using magnification of x5000 (left), x10000 (middle) and x80000 (right).

In addition, the size of the Ni particles in the hollow zeolite samples had increased markedly under the reforming conditions, mostly leading to the formation of a unique particle per nanobox (Figure 5.8). From TEM observations, the average particle diameter grew in size from below 10 nm up to ca. 35 nm (Figure 5.9, Table 5.2). Comparing the average Ni crystallite sizes before and after reaction (Table 5.2), the CitAc 5%Ni@sil-1 sample was even more prone to particle agglomeration (8-fold increase of the average particle diameter) than the non-treated sample (4-fold increase). This observation underlines the ability of the hollow zeolite shell to limit Ni nanoparticles sintering, at least until the complete breakdown of the nanobox structure occurred.

Table 5.2 Calculations of the Ni crystallite size (nm) using both the d_{sw} (TEM) and the Scherrer equation (XRD) and of the loss in silicalite-1 crystallinity (%) for post-reaction 5%Ni@Sil-1 and CitAc Ni@Sil-1.

Catalyst	Ni crystallites pre-reaction		Ni crystallites post-reaction			Loss in silicalite-1 crystallinity (%)
	Average ϕ TEM (nm)	Dispersion (%)	Average ϕ TEM (nm)	XRD (nm)	Dispersion (%)	
5%Ni@Sil-1	7.9	16	35	32	3.7	44
CitAc Ni@Sil-1	4.5	26	37	35	3.5	90

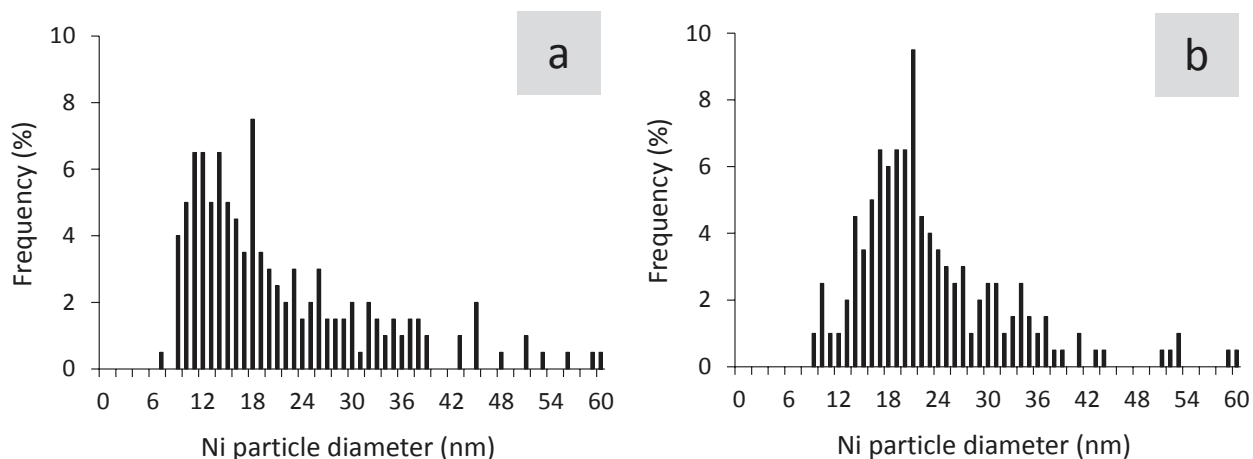


Figure 5.9 Post-reaction particle size distributions of 5%Ni@Sil-1 (a) and CitAc Ni@Sil-1 (b). Based on the measurements of 200 particles.

An XRD analysis (Figure 5.9 and Table 5.2) revealed that both hollow zeolite samples exhibited a loss of crystallinity of the silicalite-1 phase after reaction. Diffractograms of post-reaction samples show an increase of the baseline in the range $2\theta = 12 - 40^\circ$ corresponding to sample amorphisation and the breakthrough of a tight peak at $2\theta = 44.5^\circ$ associated with the Ni [111] facet (JCPDS 04-0850). The formation of cristobalite was also apparent in the case of the CitAc Ni@Sil-1, stressing the lower thermal stability of this sample likely arising from the formation of defects within the MFI framework during the citric acid treatment. Silicalite-1 conversion in cristobalite is known to occur at high temperatures (ca. 1300°C) and to be influenced by the chemical modifications made to the zeolite.^[182,229] Elsewhere, it has been reported that the collapse in air of a monoclinic silicalite-1 into cristobalite started at 750°C and was completed at 850°C .^[230]

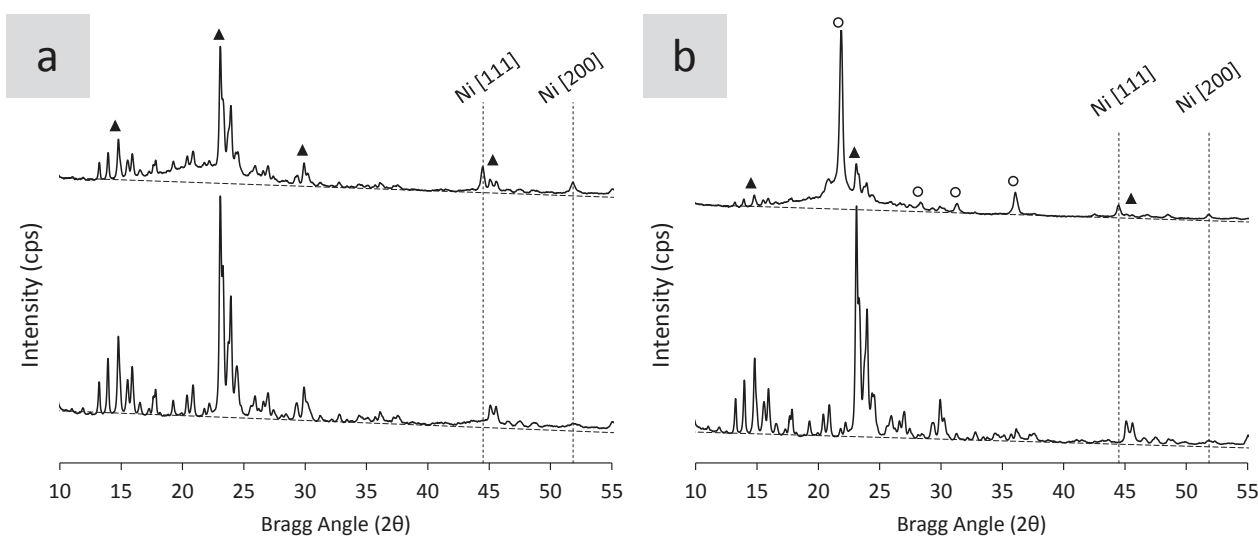


Figure 5.10 XRD analysis of fresh (bottom diffractogram) and post-reaction (top diffractogram) 5%Ni@Sil-1 (a) and CitAc Ni@Sil-1 (b). (\blacktriangle): Silicalite-1 (JCPDS: 48-0136). (\circ): Cristobalite (JCPDS: 39-1425).

It should be noted that the average Ni particle sizes determined by TEM and XRD were fully consistent (Table 5.2). No indication of carbon graphite formation was clearly observed from XRD patterns (characteristic peak at $2\theta = 28^\circ$). The formation of carbonaceous species, mostly present as graphitic whiskers, was also detected from TEM observations on both aged silicalite-1-based samples (Figure 5.8 middle). Some carbon whiskers ending with Ni particles were also visible. The results of thermogravimetric analyses for the quantification of this residual carbon indicate that the propensity of the samples to be coked is in the following order: Com Ni > CitAc Ni@Sil-1 > 5%Ni@Sil-1 > Com Rh (Figure 5.11a). The recorded mass loss in the temperature range 550-650 °C was attributed to the combustion of graphitic carbon only, since identical analyses on the corresponding fresh samples exhibited no mass loss over the same range. These results are consistent with literature data related to whisker gasification on similar catalysts.^[231,232] Furthermore, this order of tendency to form carbon was in excellent agreement with the carbon balance calculated over the 72 hours of the catalytic test: the lower the carbon balance, the higher the mass loss derived from the combustion of deposited carbon (Figure 5.11b).

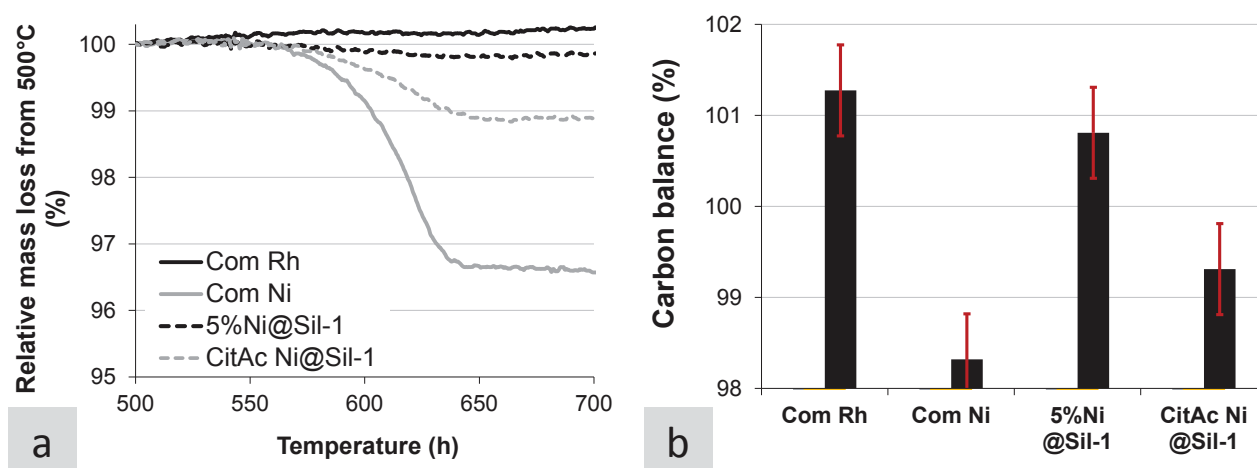


Figure 5.11 Relative mass loss of the post-reaction samples during TGA measurements (a) and carbon balance derived from the 72h-long reforming tests (b).

The observed major sintering of Ni particles could yet not be the cause of the reversible deactivations observed in the presence of naphthalene over the 5%Ni@Sil-1 (Figure 5.6), since Ni redispersion upon removing naphthalene is not expected. Ni sintering over the 5%Ni@Sil-1 is likely to have occurred in the very first instants following exposure to the steam-containing feed at 700 °C, as suggested by the initial decay of methane conversion (Figure 5.6a), and also during the subsequent temperature increases to 800 and 900 °C. The reversible deactivation likely arose from carbon deposition, as suggested by the TEM pictures (Figure 5.8) and TGA analyses (Figure 5.11a).

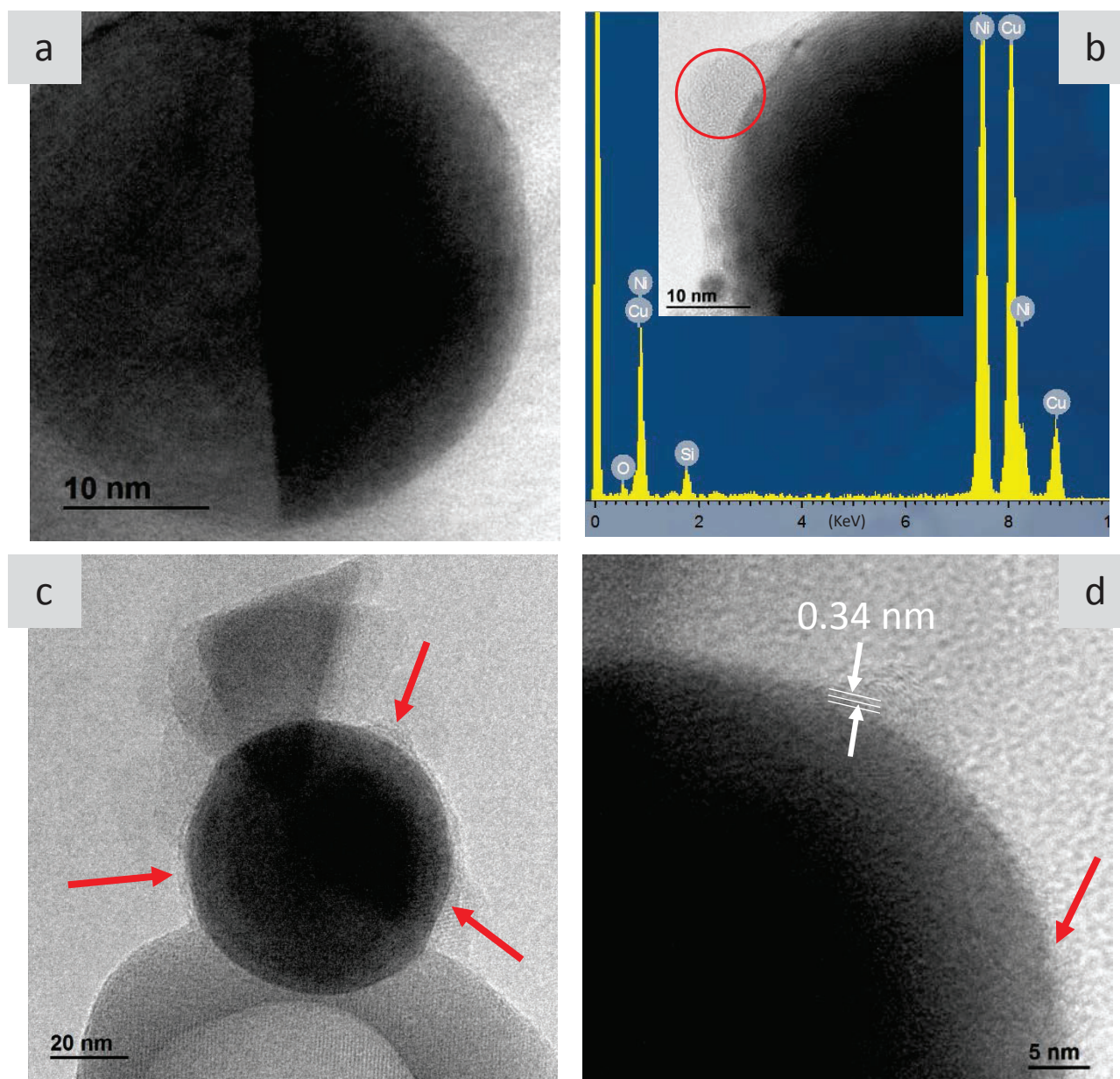


Figure 5.12 HRTEM pictures of encapsulated (a) and external (c,d) particles in the post-reaction 5%Ni@Sil-1. EDX spectra of the area indicated by a red circle (b). Cu peaks in the spectra are from the Cu grid used as the sample holder in TEM measurements. Surrounding amorphous silica is pointed out by red arrows. White arrows indicate carbon graphite fringes.

Further high resolution TEM observations provided some insights in the peculiar deactivation observed at 900 °C for the CitAc Ni@Sil-1 sample (Figure 5.7). In Figure 5.12, we observed in the post-reaction 5%Ni@Sil-1 sample that most of the Ni particles located outside of the nanoboxes were covered with a ca. 2 nm-thick layer of amorphous mater. EDX analysis (Figure 5.12b) in this area revealed the siliceous nature of this poison-like coating which arise from silicalite-1 breakdown while reforming at high temperature and clarify the hampered regeneration of the CitAc Ni@Sil-1 at 900 °C. Yet, it must be noted that encapsulated Ni particles were protected from such a coverage. In addition, graphite fringes with a characteristic interlayer spacing of 0.34 nm were also observed

at the surface of external particles, emphasizing the higher propensity of non-encapsulated particles to deactivate under reforming conditions.

3.2. Reforming activity in presence of a 1-ring aromatic

Complementary methane steam reforming experiments were carried out to unravel the nature, i.e. mono or polyaromatic, of the molecule responsible for the coking taking place in the presence of naphthalene, as benzene was observed in all experiments (Figure 5.4 to Figure 5.7). It must be stressed that benzene was formed from naphthalene even in the absence of any catalyst (and over a Ni-free single hollow silicalite-1 sample) above 650 °C (Figure 5.13). This fact is important because it shows that heavy aromatics will thermally crack into monoaromatics at the typical reaction temperatures needed to steam reform methane. Monoaromatics are expected to readily diffuse throughout silicalite-1 membranes, as depicted in chapter 3 and 4. It was therefore necessary to ascertain the role of monoaromatics on the deactivation under our conditions.

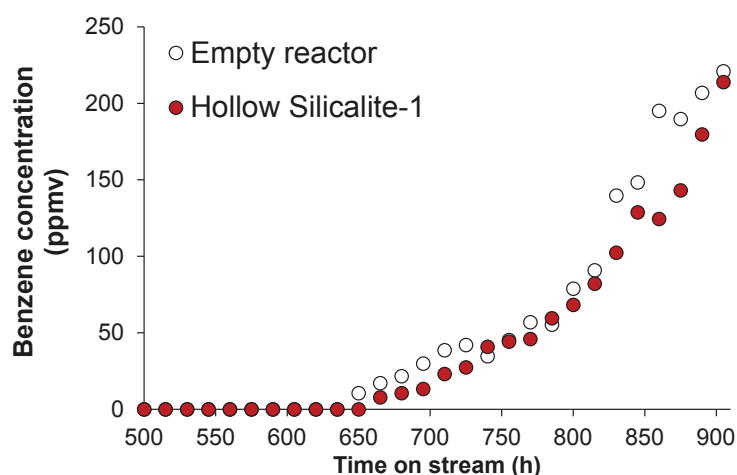


Figure 5.13 Benzene concentration measured in the reactor effluent while reforming methane in presence of naphthalene on an empty reactor (white) and one filled with Ni-free hollow silicalite-1 (red).

The use of toluene was preferred to that of benzene for the sake of safety and convenience, especially since the propensity for coking of these two molecules is expected to be similar. The presence of 1% of toluene induced a significant deactivation of the Rh-based commercial catalyst at 800 and 700 °C (Figure 5.14). Any potential deactivation at 900 °C could not be ascertained because methane conversion was too close to 100%. The deactivation obtained using a large concentration of toluene (1%, i.e. 10000 ppmv) appeared yet more limited than that observed under 1400 ppmv of naphthalene (Figure 5.5) over 10 mg of the same sample. In addition, full conversion of toluene was observed at 700, 800 and 900 °C for both the commercial samples (Figure 5.16).

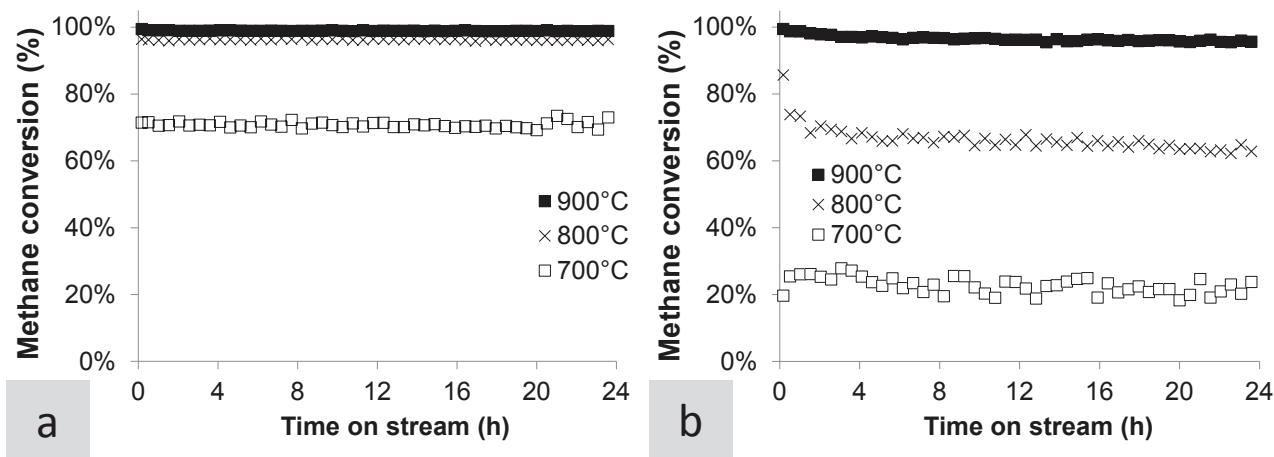


Figure 5.14 Methane conversions measured with time on stream at 700, 800 and 900 °C over Com Rh in absence (a) and in presence (b) of 1% of toluene. Catalyst mass = 25 mg.

Surprisingly, the Ni-based commercial catalyst (Figure 5.15) was somewhat less inhibited by toluene than the Rh-based sample was (Figure 5.14). This may be due to the large difference in dispersion between the two commercial samples (Table 5.1) and the fact that methane steam reforming is a structure-sensitive reaction, thought to be taking place more efficiently on low coordination atoms such as those located on edges and corners.^[56,59] This means that only a minor fraction of surface sites are actual active sites in the case of the poorly dispersed Ni catalyst. Hence, the Ni active sites are “in proportion” less poisoned by toluene (which is expected to be adsorbed on less active high coordination atoms located on dense surfaces) than those of the highly dispersed Rh-based sample. Indeed, Myers et al. predicted that on both the Ni (100) and (111) surfaces benzene adsorbs above the fourfold and threefold hollow sites respectively, i.e. on the high coordination sites.^[233]

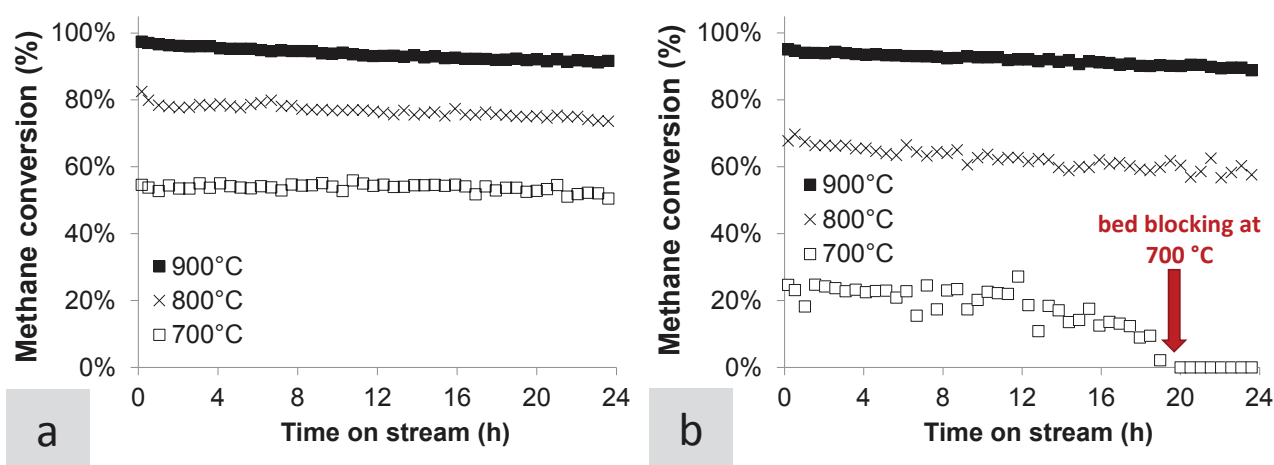


Figure 5.15 Methane conversions measured with time on stream at 700, 800 and 900 °C over Com Ni in absence (a) and in presence (b) of 1% of toluene. Catalyst mass = 25 mg.

A bed blockage was observed in the case of the commercial Ni-based catalysts at 700 °C after ca. 18 h on stream (Figure 5.15b). This is consistent with the extensive formation of carbon whiskers (as observed in Figure 5.8, middle) on Ni particles under reforming conditions, especially at low temperatures. Formation of whiskers, leading to Ni particles being detached from the support, yields hardly any conversion loss until the catalyst bed becomes fully blocked.^[234] This result supports our assumption on the high propensity of the Com Ni sample to be coked, as expected from TGA measurements and carbon balance calculations (Figure 5.11).

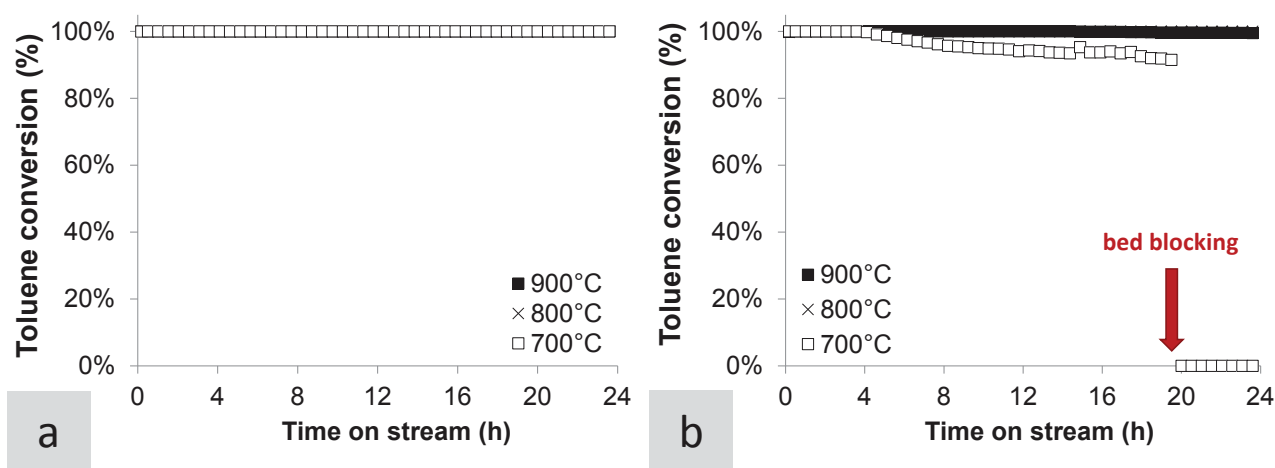


Figure 5.16 Toluene conversions measured with time on stream at 700, 800 and 900 °C over the Com Rh (a) and the Com Ni (b). Catalyst mass = 25 mg.

As we discussed, in the case of Ni the poisoning effect of toluene (Figure 5.15) was almost negligible as compared to that of naphthalene (Figure 5.5). It can be concluded that monoaromatics are unlikely to be responsible for the strong deactivation of Ni-based samples induced by naphthalene. Therefore, we propose that naphthalene itself directly poisoned the Ni particles located inside the silicalite-1 nanoboxes through the formation of coke, a process which appeared reversible over most samples at the higher temperatures (Figure 5.4 to Figure 5.7).^[10,234]

3.3. Reforming activity in presence of a 4-ring aromatic

Since naphthalene appeared to be able to cross the silicalite-1 membrane of the CitAc Ni@Sil-1, an additional experiment was carried out using a much bulkier polyaromatic, i.e. pyrene (kinetic diameter = 7.2 Å calculated using a method described by Jae and co-workers).^[235] In chapter 3, we reported the size selectivity property of single hollow silicalite-1 catalysts using pyrene as a poisoning tar model compound in the methanation of CO. In the reforming of methane at 700 °C, a concentration of 5 ppmv of pyrene appeared to readily deactivate the Com Ni catalyst (Figure

5.17a), but also the CitAc Ni@Sil-1 sample. Since naphthalene was observed in the reactor effluent, it is proposed that naphthalene or some other cracking products of pyrene could have coked the embedded nickel (Figure 5.17b). The deactivation of the CitAc Ni@Sil-1 appeared to be faster than that of the commercial Ni-based catalyst, possibly because of the lower concentration of Ni and a low metal surface area arising from Si covering present on the former.

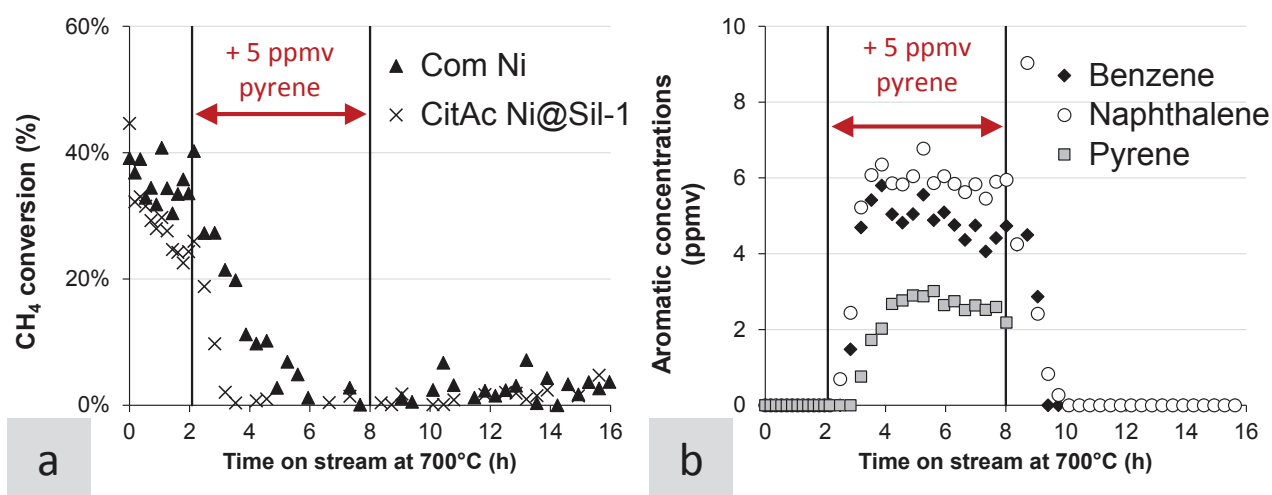


Figure 5.17 Methane conversions measured with time on stream at 700 °C over 10 mg of Com Ni and CitAc Ni@Sil-1 samples (a). Concentrations in benzene, naphthalene and pyrene detected in reactor effluent of CitAc Ni@Sil-1 sample (b). 5 ppm of pyrene were introduced over a period of 6 h.

4. Conclusions

A concentration of 1400 ppmv of naphthalene readily and strongly poisoned the steam reforming of methane over Rh and Ni-based catalysts. The use of encapsulated Ni@Sil-1 samples did not lead to naphthalene-resistant catalysts, most likely because this molecule was able to access the embedded Ni in spite of the silicalite-1 nanobox membrane surrounding the metal particles. The bulkier pyrene, at a concentration of 5 ppmv, lead to similar results, as pyrene was shown to partly crack into naphthalene. In contrast, the effect of a monoaromatic such as toluene was almost negligible on the activity of Ni-based samples, apart from possible bed blocking through carbon whisker formation at low temperature (700 °C). The silicalite-1 single hollow nanobox was inefficient in preventing the sintering of Ni particles. It was also concluded that the citric acid treatment used to remove most of the external Ni particles led to structural modifications of the nanoboxes, making those unstable at high temperatures and a source of Ni poisoning. The results presented in this chapter emphasize the difficulty in obtaining size-selective systems for high temperature applications, since reactant cracking is common and smaller reactants are generated *in situ*.

Highlights

- Naphthalene, toluene and pyrene were used as model tars during steam methane reforming.
- Both Rh and Ni-based catalysts were strongly poisoned by tars, sometimes reversibly.
- The zeolite membrane of the Ni@silicalite-1 samples could not prevent deactivation.
- The highly-selective CitAc Ni@Sil-1 sample showed low thermal stability
- Sintering, coking and silica poisoning were identified as sources of deactivation

Chapter 6 - Effects of tars and H₂S on the reforming of a model producer gas

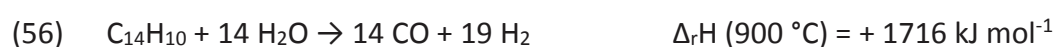
1. Introduction

As discussed in chapter 5, tars can induce a strong deactivation during catalytic reforming. We stressed that polyaromatics such as naphthalene and pyrene are significantly more poisonous than toluene using Ni or Rh-based catalysts. Furthermore, we reported that coking and bed blocking were alleviated by using higher reaction temperatures and by the presence of a noble metal. It is worth mentioning that the promotion of metals, for example by boron, has been reported to decrease coke formation during reforming and pyrolysis.^[92,236,237]

As addressed in chapter 1, H₂S is also present in producer gas derived from biomass gasification at concentration levels typically around 50 to 200 ppmv and induces a marked deactivation of catalysts used for reforming (Table 1.1). The active surface of Ni-based catalysts gets covered with sulfur, reaching a S:Ni stoichiometry of ca. 1:2 in terms of surface atoms at saturation.^[238] S coverage and rate loss expression have been derived depending on the H₂S/H₂ ratio used (Equation 14).^[8] The sulfidation of nickel surface can yet have positive effects, mainly in the suppression of carbon formation during steam reforming.^[239] According to its the surface electronic state, Rh is expected to be more resistant to S poisoning than Ni, in agreement with the data reported by Steele and co-workers, who found that Rh maintained some activity for CH₄ steam reforming in the 800-900 °C temperature range in the presence of ca. 90 ppm of H₂S, while Ni-based catalysts became totally inactive.^[107,113] This report suggests that high temperatures should be preferably used to limit catalyst deactivation in the presence of tars and sulfur and that Rh-based catalysts should be more active and resistant than Ni-based samples. Note that a theoretical study proposed the opposite, possibly because of the choice of crystallographic planes considered.^[108]

In the present chapter, a series of supported Rh and Ni-based catalysts were tested for the reforming of CH₄ and phenanthrene using a feed composition similar in terms of main components to that of the biogas produced from wood gasification in ECN MILENA gasifier (Table 1.1). The objective was to identify formulations that would enable reforming CH₄ and tars without the need

to purify the biogas produced by the gasifier. In the frame of the FASTCARD project, it was decided to perform a screening of these materials using a model feed composition. The most promising formulation would then be selected for production scale-up and subsequent duration tests at the pilot level using ECN Milena gasifier to generate more realistic conditions. Regarding the difficulties in attempting to encapsulate Rh particles inside hollow silicalite-1 crystals (chapter 3), and the inefficiency of the zeolite membrane to prevent tar poisoning under reforming conditions (chapter 5), it was decided to focus on more conventional supported catalysts. In addition to exhibiting a high intrinsic activity in CH₄ reforming, Rh was selected because of its low propensity to form bulk sulfide (Figure 6.1). It should be stressed that the thermodynamic calculations shown in Figure 6.1 regard the formation of the bulk compounds and thus the stability of surface sulfide phases cannot be predicted from these calculations. Phenanthrene was chosen as tar representative because this compound is produced in significant concentrations during low-temperature gasification of woody biomasses (Figure 1.7) and its three-ring structure favors coke formation. It should be reminded that CH₄ and especially phenanthrene reforming are highly endothermic reactions (Equation 55 and 56) and thus difficulties relating to heat transport limitations can be expected:



The concentration of H₂S was set at the higher range of typical values, i.e. 200 ppmv, to make these tests more challenging. The temperatures investigated were set around 900 °C to enable significant methane conversions in the presence of H₂S.

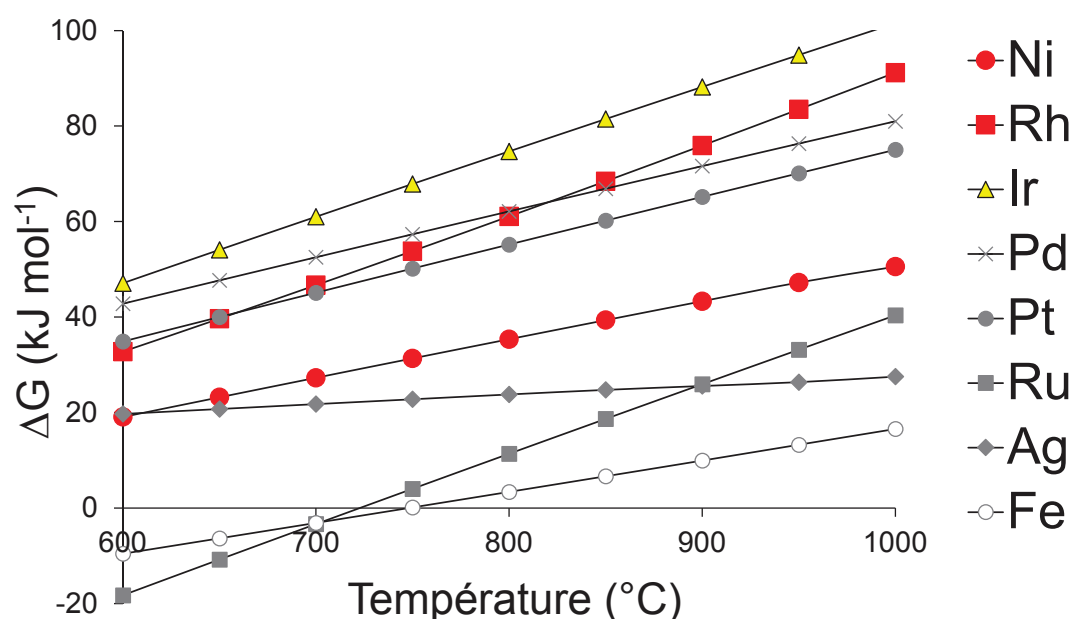


Figure 6.1 Gibbs energy of the formation of various bulk metal sulfide ($\text{M} + \text{H}_2\text{S} = \text{M-S} + \text{H}_2$) as a function of the temperature under the feed gas composition described in Table 2.2. Thermodynamic data were obtained using HSC software.

2. Experimental procedure

2.1. Choice and properties of catalysts

Eight samples containing only one metal (either Ni or Rh) or both metals differing in their metal loading and type of support were investigated (Table 6.1). Samples 1-N, 3-Rh and the magnesium aluminate support (noted “MgAlO_x”) were supplied by Johnson Matthey and were prepared according to proprietary methods.

Table 6.1 Composition, metal dispersion and metal surface areas of the catalysts.

Catalyst code	Support	Specific surface ^[a] (m ² g ⁻¹)	Metal loading (wt %)		Dispersion ^[b] (%)		Metal surface area (m ² g ⁻¹)	
			Ni	Rh	Ni	Rh	Ni	Rh
1-Ni	alumina	60	34.1	-	5.9	-	13.4	-
2-Ni	meso-MgAlO _x	128 ^[c]	16.2	-	3.7	-	4	-
3-Rh	alumina	152	-	1.8	-	38.5	-	3
4-Rh	MgAlO _x	186	-	0.4	-	43	-	0.7
5-Rh	MgAlO _x	186	-	2.2	-	39.6	-	3.8
6-Rh	meso-MgAlO _x	128 ^[c]	-	0.4	-	50.4	-	0.8
7-Rh	meso-MgAlO _x	128 ^[c]	-	2.6	-	41.8	-	4.8
8-NiRh	meso-MgAlO _x	128 ^[c]	18.6	1	4.1	38.5	5.1 ^[d]	1.7 ^[d]

^a BET method

^b based on particle size measurements in TEM of used samples tested in absence of H₂S (200 particles were counted)

^c surface area of support before impregnation

^d assuming that most larger particles were mostly made of Ni and most smaller particles were mostly made of Rh

An ordered mesoporous crystalline magnesium-aluminum oxidic support (noted “meso-MgAlO_x”) was prepared at ECN by a solvent evaporation induced self-assembling method. Pluronic P123 (Sigma-Aldrich, lot MKAA0323) was dissolved in ethanol at room temperature. Nitric acid, aluminum isopropoxide, and magnesium nitrate were then added into the above solution under stirring. The mixture was covered with a polyethylene film, stirred at room temperature for about 5 h, and then put into a 100 °C drying oven to undergo solvent evaporation process. After 40 h of aging, the sample was calcined at 800 °C, leading to the meso-MgAlO_x support. The nitrogen physisorption data at 77 K of the calcined support is presented in Figure 6.2b. MgAl₂O₄ was the main phase observed by XRD present after calcination (Figure 6.2a). Dry impregnation was used to promote the supports with Ni

and Rh, the amount of liquid was chosen to exceed the pore volume by not more than approximately 10 % which resulted in essentially dry impregnation. Solutions of appropriate concentrations of Ni(II) nitrate hexahydrate (99.999%, Sigma-Aldrich) and Rh(III) nitrate (Alfa Aesar, lot GR0037) were used. The 8-NiRh sample was prepared by co-impregnation. The metal loadings, dispersion and metal surface area are given in Table 6.1. Dispersions and metal surface areas were derived from measurements in TEM of the surface weighted mean particle size d_{sw} (Figure 6.10) of used samples tested in absence of H₂S (e.g. $d_{sw} = 35$ nm in case of used 2-Ni) .

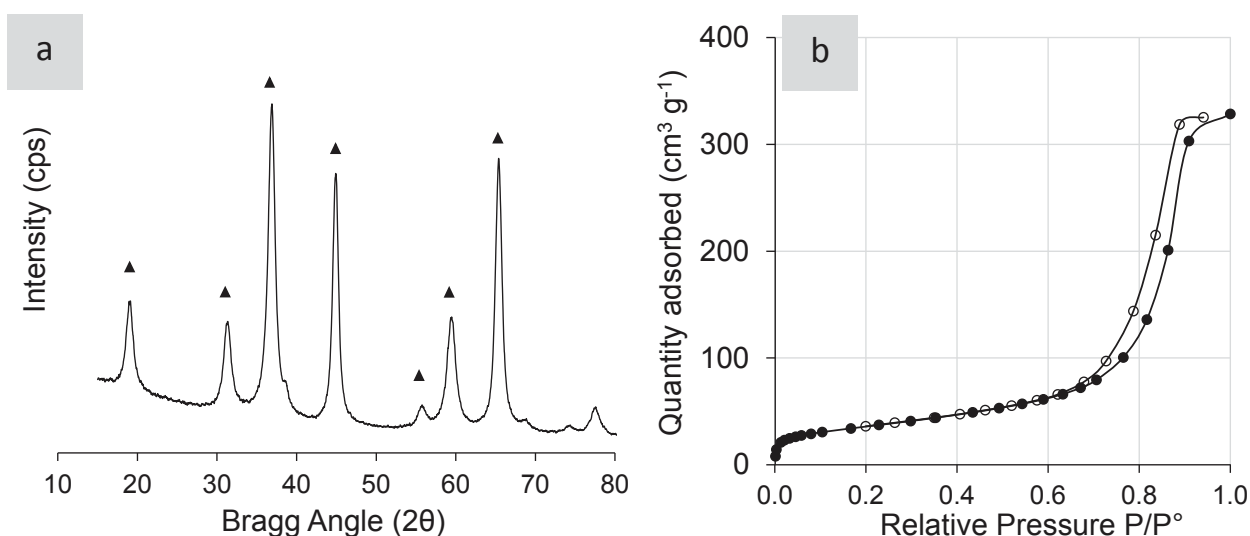


Figure 6.2 (a) XRD analysis and (b) N₂ physisorption (full symbols: adsorption branch, open symbols: desorption branch) isotherm of the meso-MgAlO_x sample. (▲): cubic spinel MgAl₂O₄ (JCPDS: 75-1796).

2.2. Reforming tests

The reforming experiments were performed on a lab-scale reforming unit described in details in part 3.3 of chapter 2. The fixed-bed continuous-flow reactor consisting of a quartz tube containing the non-diluted catalyst powder. The samples were crushed and sieved into a powder retaining particle sizes between 100 and 200 μm (unless otherwise stated). 10 mg of catalyst were tested in the absence of H₂S, while 100 mg of catalyst were used in the case of H₂S-containing feeds. The bed heights varied between 0.5 and 3 mm, meaning that the reactor could not be considered in a plug-flow regime. Prior to testing, the supported sample was reduced *in-situ* at 900 °C with a heating rate of 600 °C h⁻¹ for 2 h in a 200 mL min⁻¹ flow rate of 20 vol.% H₂/Ar mixture. The feed gas composition used in these tests is described in Table 2.2. The desired concentration (200 ppmv) of phenanthrene was fed using a saturator heated at 141 °C and carried by a 12.5 mL min⁻¹ flow rate of CO₂. The overall system pressure was controlled and set at $P_{total} = 2.2$ bar. The catalytic activities were sequentially measured according to the programs described in Figure 6.3.

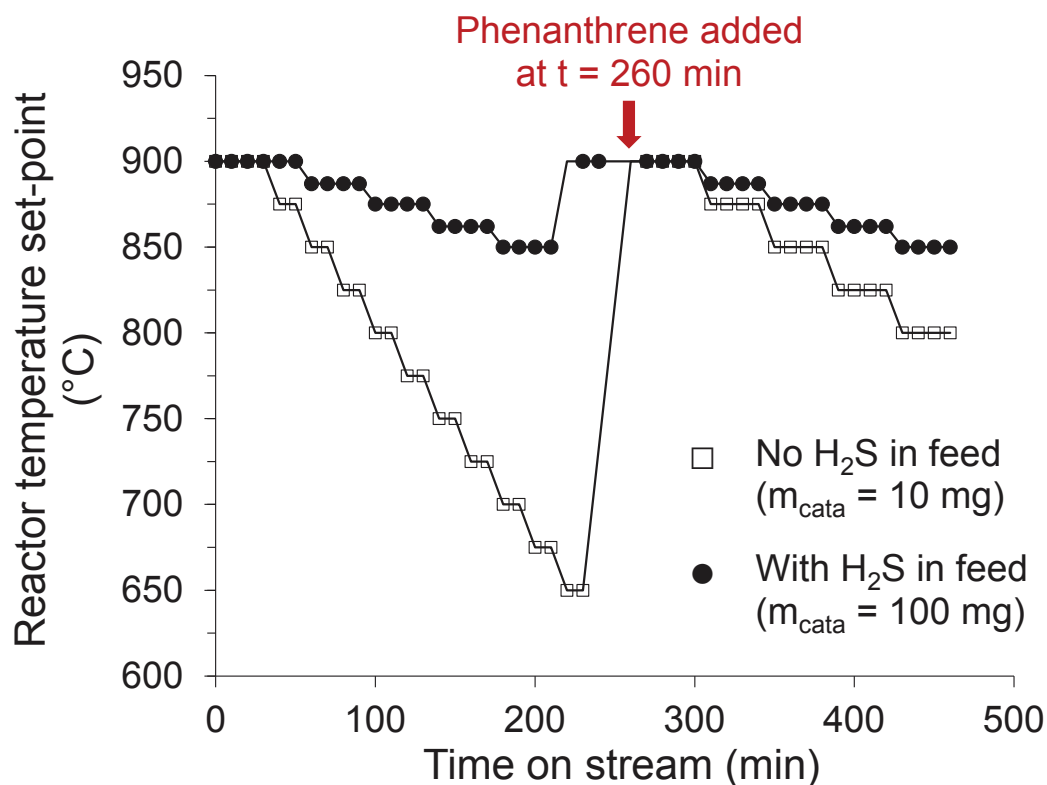


Figure 6.3 Temperature profiles used for the catalytic tests with (full circles) and without (open squares) 200 ppmv H₂S present in the stream. 200 ppmv phenanthrene were added at 260 min. The symbols (squares and circles) represent the time at which the reactor effluent was sampled.

It is worth mentioning that the impact of phenanthrene and H₂S on the activity in CH₄ reforming was studied both individually and simultaneously in two series of tests:

- Series 1 (10 mg of sample): measurement of the activity at 900 down to 650 °C in absence of contaminant, addition of 200 ppmv phenanthrene at 260 min, subsequent activity measurement at 900 down to 800 °C.
- Series 2 (100 mg of sample): measurement of the activity at 900 down to 850 °C in presence of 200 ppmv of H₂S, addition of 200 ppmv phenanthrene at 260 min, subsequent activity evaluation at 900 down to 850 °C.

The total gas flow rate of reactants was 125 ml min⁻¹. The corresponding WHSV was 689 h⁻¹ (respectively 69 h⁻¹) when using 10 mg (resp. 100 mg) of catalyst. Assuming catalyst density to be unity, the GHSV was 750 000 h⁻¹ (resp. 75 000 h⁻¹). These high WHSV values were used to obtain an accelerated ageing in terms of tar and sulfur exposure on a reasonable timescale. Furthermore, these conditions prevented total conversion of hydrocarbons, providing insights in terms of activity and stability of the different catalysts.

3. Catalytic results

3.1. Impact of C₁₄H₁₀ and H₂S on the activity in CH₄ reforming

3.1.1. Measurements of reaction rates at 850, 875 and 900 °C

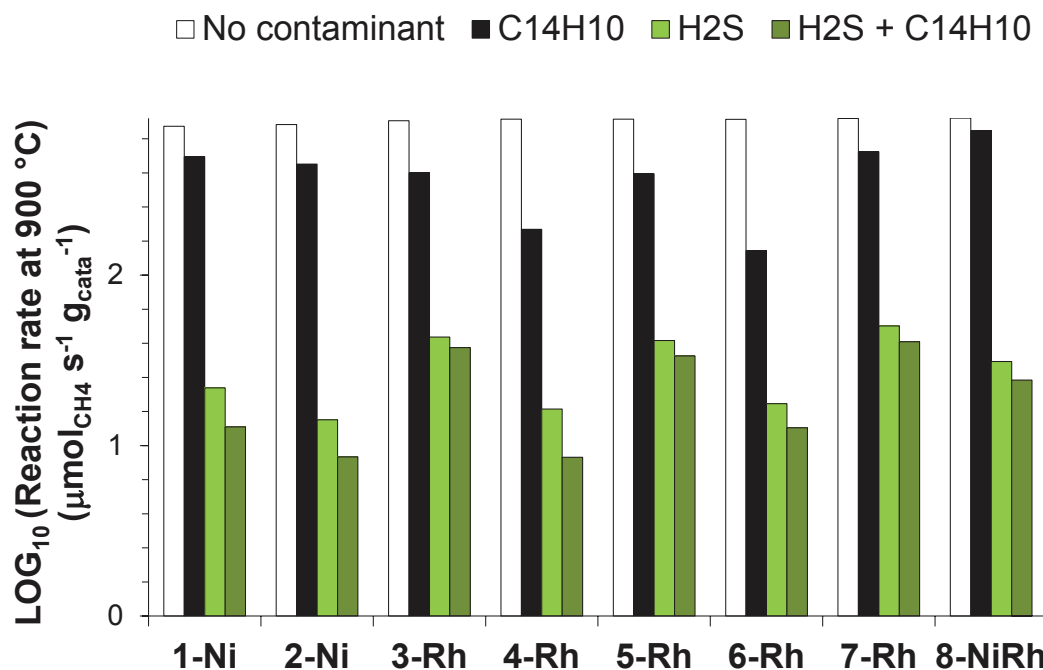


Figure 6.4 Methane consumption rates measured at 900 °C over the various catalysts: (white) poison-free, (black) with 200 ppm phenanthrene, (light green) with 200 ppm H₂S and (dark green) with both 200 ppm phenanthrene and 200 ppm H₂S.

Figure 6.4 gathers the logarithm of the integral rates of methane consumption measured at 900 °C over the various samples after 1h on stream. The rates measured in a feed (Table 2.2) free of poisons are represented by white bars. The rates appeared similar because all catalysts were highly active at this temperature and full conversion of methane was essentially achieved. The rates measured in the presence of phenanthrene (black bars) were significantly lower than those without this compound. These data thus indicate that 200 ppm of phenanthrene had a non-negligible poisoning effect even at 900 °C. The drop of methane consumption rate due to 200 ppm of H₂S (light green bars) was yet more than one order of magnitude larger than that associated with phenanthrene (black bars). The conversion of methane in the presence of H₂S was typically always lower than 60 %. The activity loss obtained when both poisons were present (dark green bars) was marginally lower than those obtained with H₂S only (light green bars). Furthermore, the monometallic Ni-based and low loaded Rh-based formulations were the less active when phenanthrene and/or H₂S were present in the feed stream.

A similar set of data collected at 875 °C is shown in Figure 6.5. The detrimental effects of phenanthrene (black bars) was more obvious than that observed at 900 °C, though the drop of the true intrinsic rate cannot be exactly determined because methane conversions were too high. The loss of rates induced by H₂S was here again more than one order of magnitude larger than that associated with phenanthrene. The combined effect of both poisons was similar to that of only H₂S, although the two formulations only based on Ni showed a significantly worse loss.

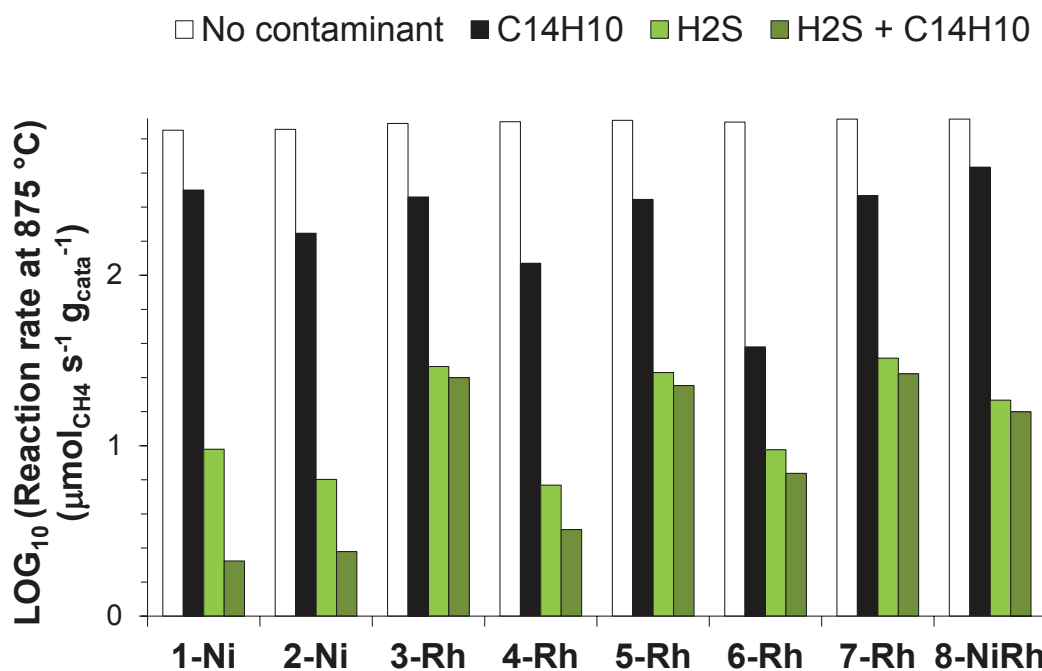


Figure 6.5 Methane consumption rates measured at 875 °C over the various catalysts: (white) poison-free, (black) with 200 ppm phenanthrene, (light green) with 200 ppm H₂S and (dark green) with both 200 ppm phenanthrene and 200 ppm H₂S.

Both sets of data at 900 °C and 875 °C clearly indicate that H₂S was the most potent poison in the present conditions and that the further effect of phenanthrene was minor, except for formulation purely based on Ni (i.e. 1-Ni and 2-Ni). The four most active formulations in the presence of both poisons all contained Rh (i.e. 3-Rh, 5-Rh, 7-Rh and 8-NiRh). While Ni only-based formulation were significantly less active, it should nonetheless be stressed that non-zero rates were measured.

The effect of lowering the temperature down to 850 °C on the value of the integral methane consumption rate when both poisons were present is compared to the cases of 900 and 875 °C in Figure 6.6. Most importantly, the samples purely based on Ni (i.e. 1-Ni and 2-Ni) were essentially inactive. In contrast, the Rh-based samples still exhibited a significant rate, especially the four best formulations highlighted above, i.e. the samples with the higher loading in Rh.

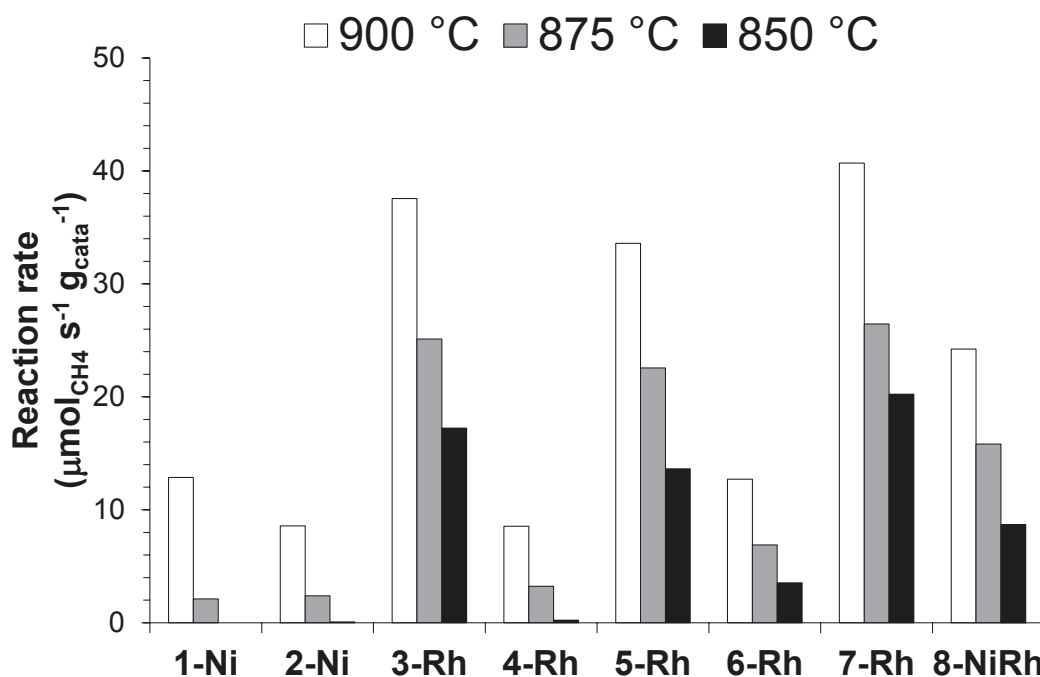


Figure 6.6 Methane consumption rates measured at 900, 875 and 850 °C over the various catalysts with both 200 ppm of phenanthrene and 200 ppm of H₂S. Full methane conversion corresponds to an integral rate of 84 μmol_{CH₄} s⁻¹ g_{cata}⁻¹.

The integral rates of methane reforming in the presence of H₂S and phenanthrene are plotted as a function of the Ni or Rh metal surface areas in Figure 6.7. The metal dispersions were measured on the samples used up to 900 °C in the standard feed in the presence phenanthrene, but in the absence of H₂S. Yet, H₂S is not expected to modify metal particle size and metal dispersion, merely forming sulfur adlayers with S:Ni = 0.5 in the case of nickel-based catalysts.^[238,240] Sample 8-NiRh contained both Ni and Rh and is therefore reported twice in Figure 6.7, with respect to the corresponding Ni and Rh areas, assuming that the smaller (respectively larger) particles observed by TEM were predominantly made of Rh (resp. Ni)(Figure 6.10).

Rate values for metal surface areas of ca. 4 m² g⁻¹ for the samples only containing Ni and only containing Rh indicated that Rh was about five-fold more active than Ni (Figure 6.7). The higher activity of Rh as compared to Ni in the presence of H₂S had been reported by Steele and co-workers.^[113] Note that this is in contrast with the data reported in S-free feeds for which Ni appears to be intrinsically more active than Rh.^[58] The methane consumption rates for Rh-containing samples (circles) appeared to be proportional to the Rh metal surface area (Figure 6.7). This indicates that methane consumption rate was essentially associated with Rh surface atoms under the present conditions for these samples.

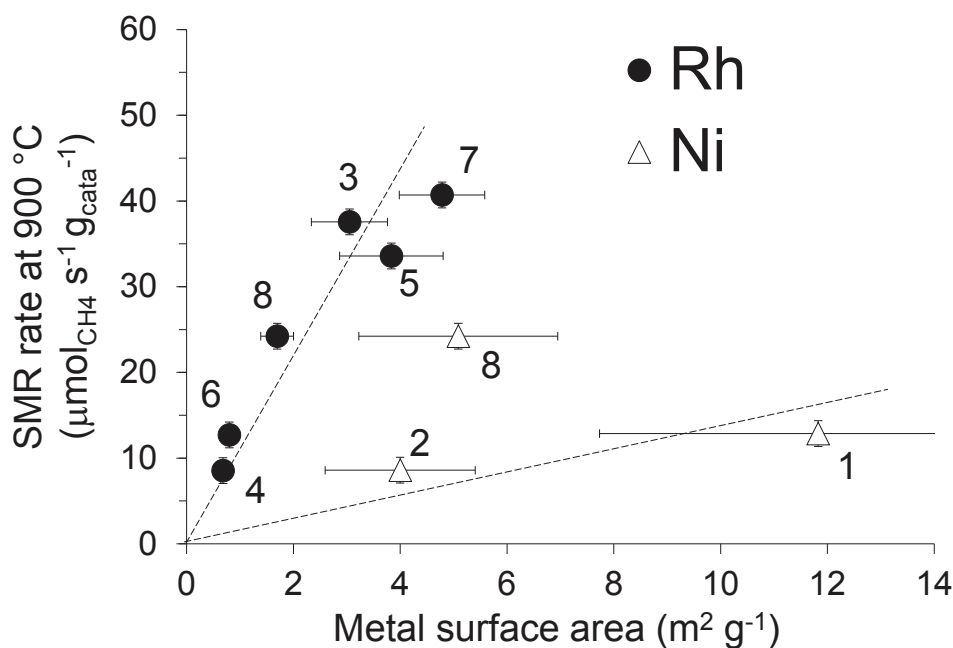
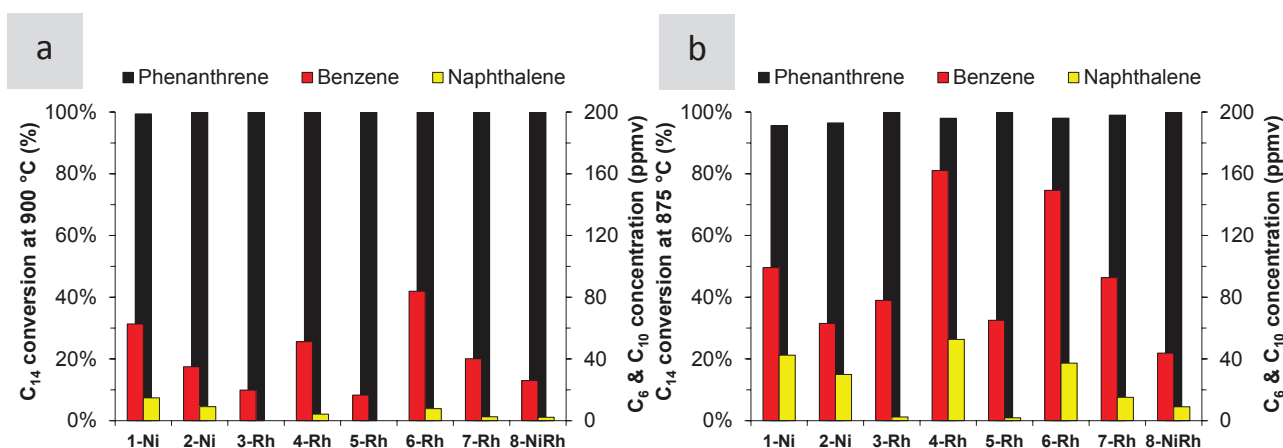


Figure 6.7 Methane consumption rates measured at 900 °C in the presence of H₂S and phenanthrene over the various catalysts as a function of Ni or Rh metal surface area. The triangles refer to Ni, while the circles refer to Rh.

The data regarding methane consumption rates for Ni-containing samples (triangles) are more difficult to interpret because of the fewer samples investigated and the fact that one of those also contained Rh (i.e. 8-NiRh). Since Rh is significantly more active than Ni in the presence of H₂S, sample 8-NiRh cannot be used to evaluate any activity trend with respect to Ni content. Therefore, only samples 1-Ni and 2-Ni can be discussed. The rate measured over these two samples appeared to be very low in comparison with Rh, and were in line with the origin, suggesting a proportionality between Ni metal surface area and rate of methane consumption, as in the case of Rh.

3.1.2. Tar conversion and cracking product production at 850, 875 and 900 °C



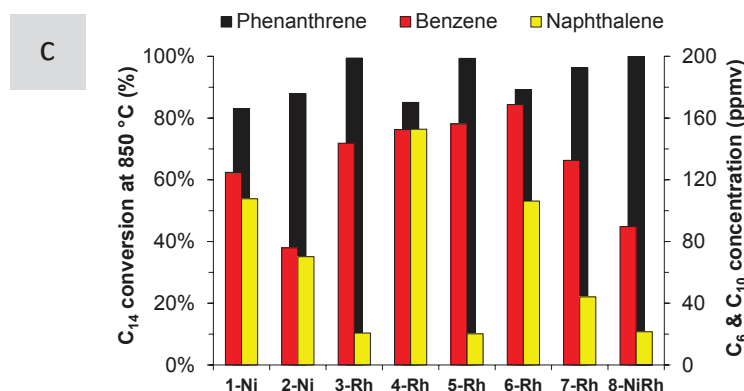


Figure 6.8 Phenanthrene conversion (black) and benzene (red) and naphthalene (yellow) concentrations at (a) 900, (b) 875 °C and (c) 850 °C over the various catalysts in the presence of both 200 ppm phenanthrene and 200 ppm H₂S. Catalyst mass = 100 mg.

Phenanthrene conversions were total for all samples at 850, 875 and 900 °C in the absence of H₂S and neither benzene nor naphthalene could be detected at the reactor exhaust (data not shown). Essentially total conversion of phenanthrene was also obtained in the presence of H₂S at 900 and 875 °C (Figure 6.8a and Figure 6.8b), though in this case benzene and naphthalene were observed at the reactor exit. In contrast, the reaction carried out at 850 °C led to incomplete phenanthrene conversion for several formulations and also led to increased concentrations of naphthalene (Figure 6.8c). The catalysts were therefore less able to reform polyaromatics at 875 °C and especially at 850 °C. This is a major shortcoming, since polyaromatics are most detrimental in terms of coke formation (Figure 5.11).^[52] Therefore, long-term process durability could be compromised if too low reaction temperatures are used, even on the best Rh-based samples.

3.2. Characterization of used samples

The sulfur-content of the Rh-only-based catalysts were measured post-reaction. Experimentally, a known mass of the used catalyst was placed in the combustion chamber of the CHONS analyzer under an O₂ flow and heated up to 1800 °C and the resulting combustion product SO₂ was quantified using a TCD. It appears that the uptake of sulfur was essentially proportional to the surface area of Rh, with a S:Rh molar ratio of about 1:2. It is interesting to note that surface saturation with sulfur occurs at the same ratio for Ni-based catalysts.^[241] This observation is consistent with an earlier report on the adsorption of H₂S onto Rh (100) surface, which pointed to a S:Rh ratio of ca. 0.53 at monolayer saturation.^[242]

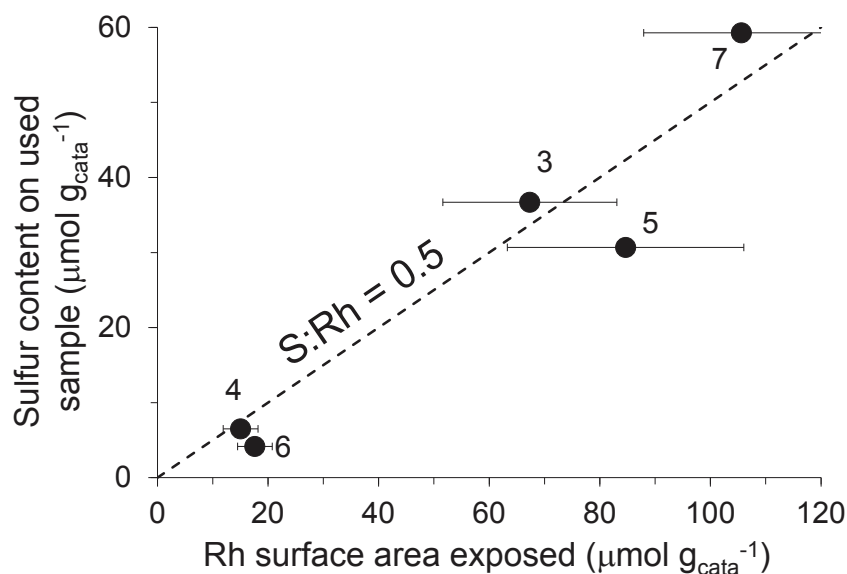


Figure 6.9 Sulfur content present on used samples as a function of the exposed Rh surface area for the various monometallic catalysts. The observed S/Rh ratio is closed to 0.5.

The use of mesoporous supports has been reported to favor the stabilization of metal nanoparticles during catalytic reactions.^[243] Table 6.2 shows the relative loss in metal surface area during (H₂S-free) reforming for some Ni and Rh-based samples. No beneficial effect of the mesoporous support was observed in the case of Ni, since the sample based on a mesoporous support (2-Ni) had lost more metal surface area after use than a non-mesoporous sample (1-Ni) had. In contrast, the rhodium catalysts based on a mesoporous support (6-Rh and 7-Rh) exhibited a more limited loss of metal surface area upon use than one based on a non-mesoporous support (3-Rh). Differences in intrinsic properties such as Tamman temperature of Ni (MP = 1455 °C) and Rh (MP = 1964 °C) or the initial metal particle size could explain these behaviors, but more work would clearly be needed to rationalize these observations.

Table 6.2 Evolution of dispersion and metal surface area during H₂S-free reforming.

Catalyst	Metal dispersion (%)		Metal surface area (m ² g ⁻¹)		Loss in metal surface area after use (%)
	Activated	Used	Activated	Used	
1-Ni	9.4	5.9	21.4	13.4	37
2-Ni	7.4	3.7	8.0	4.0	50
3-Rh	59.5	38.5	4.7	3.0	35
6-Rh	69.3	50.4	1.0	0.8	20
7-Rh	55.0	41.8	5.9	4.8	19

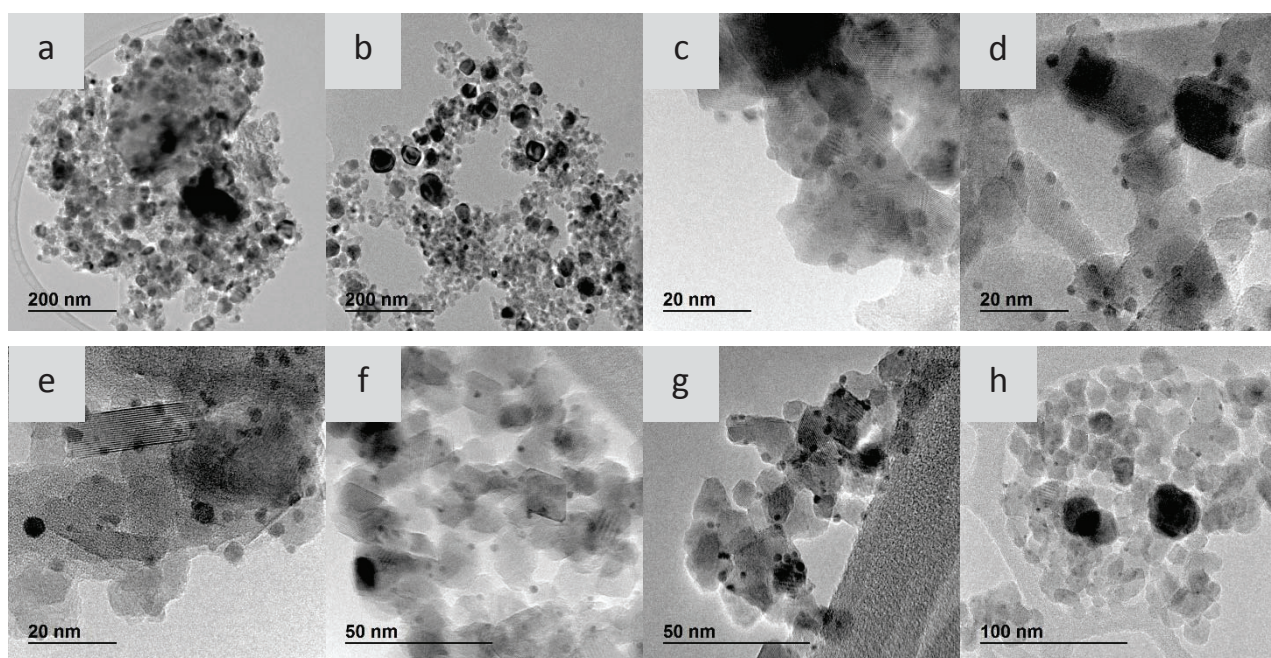


Figure 6.10 TEM images of post-reaction (no H₂S in feed) 1-Ni (a), 2-Ni (b), 3-Rh (c), 4-Rh (d), 5-Rh (e), 6-Rh (f), 7-Rh (g) and 8-NiRh (h). Both large Ni-rich and small Rh-rich particles are observed in 8-NiRh.

It is worth mentioning that the crystallinity of meso-MgAlO_x support remained intact during the 500 min-long reforming test in presence of sulfur, as revealed by XRD spectra of used 2-Ni and 7-Rh samples in which the peaks of the spinel phase were preserved and no deviation of the baselines were observed (Figure 6.11). Metallic Ni particle of ca. 28 nm in size (calculated using the Scherrer formula on Ni [200] and [220] peaks) were formed upon reduction and reforming of the calcined 2-Ni (Figure 6.11a), in good agreement with the mean particle size derived from TEM observations.

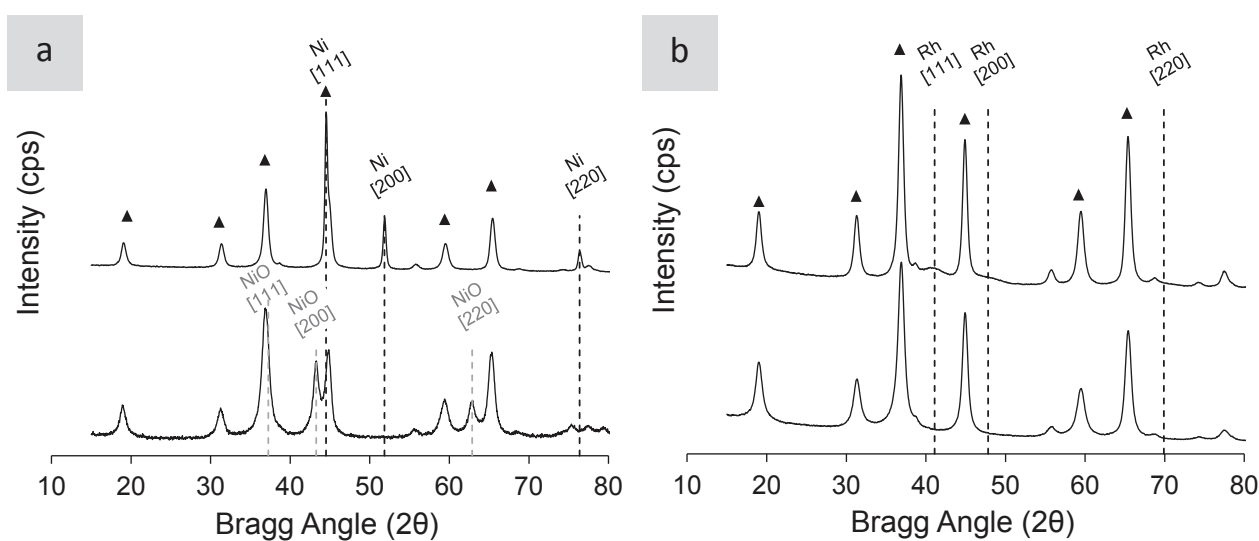


Figure 6.11 XRD analysis of calcined (bottom diffractogram) and post-reaction in the presence of H₂S and phenanthrene (top diffractogram) 2-Ni (a) and 7-Rh (b). (▲): cubic spinel MgAl₂O₄ (JCPDS: 75-1796). Dashed lines represent the main diffraction peak of cubic NiO (JCPDS 47-1049), Ni (JCPDS 04-0850) and Rh (05-0685).

It is interesting to note that bulk nickel sulfide phases was not observed in presence of 200 ppmv of H₂S (i.e. $P_{\text{H}_2\text{S}}/P_{\text{H}_2} = 0.00125$) during reforming. In the steam reforming of natural gas, the concentration of H₂S is generally much lower (ca. few ppmv) after the gas stream has been processed to remove sulfur compounds, leading to a partial coverage of the Ni active sites that depends on the operating temperature.^[106] At typical H₂S concentrations present in a producer gas, it was reported that nickel-based hot gas cleaning catalysts can be prone to bulk sulfide formation, leading to a drop in tar reforming activity.^[40] Furthermore, bulk nickel sulfide is known to form a sticky liquid-like solution at temperatures above 635 °C, resulting in severe metal sintering and bed blocking.^[244]

3.3. Evaluation of the loss in Ni active sites in reforming due to S

The structure sensitivity of S adsorption on Ni catalysts was studied by *in situ* CO methanation and DRIFTS over a commercial Ni-based catalyst, but not on any of the eight catalysts discussed in this chapter. 100 mg of Com Ni was aged at 900 °C for 2 h under reforming conditions in absence of tars and cooled down to methanation temperatures under 160 mL min⁻¹ of Ar (see chapter 5 for some information on Com Ni). When 200 ppmv of H₂S were present in the reforming feed, the activity in subsequent methanation was significantly lower than that of the sample used in absence of H₂S, showing no activity below 500 °C (Figure 6.12a). Extrapolation of the activity of the passivated sample down to 300 °C using the Arrhenius plot (data not shown) was ca. 300 time lower ($1.8\text{E-}02 \mu\text{mol s}^{-1} \text{gcata}^{-1}$) than that measured on the non-poisoned sample ($5.6 \mu\text{mol s}^{-1} \text{gcata}^{-1}$), revealing a S surface coverage close to 1 and an almost complete site poisoning.

Diffuse reflectance FT-IR analysis of the adsorption of CO at 250 °C was carried out over the used Com Ni catalysts to investigate the loss of CO adsorption sites. These data show that a large decrease of CO adsorption capacity occurred after H₂S-exposure (Figure 6.12b). A loss of more than 90% of surface Ni able to chemisorb CO was estimated from these data, assuming that the molar extinction coefficient was similar for all CO_{ads}. In addition, low coordination sites, which are those associated with IR bands of linearly adsorbed CO_{ads} above 2000 cm⁻¹ were most sensitive to S-poisoning than the ones located on bare surface, where multibonded species are preferentially formed on (from 1750 to 2000 cm⁻¹).^[162] This observation is important, because steam methane reforming is a structure-sensitive reaction and low coordination sites are most active and in good agreement with the literature.^[59] The band at 1450 cm⁻¹ was assigned to the stretching vibration of carbonate species.

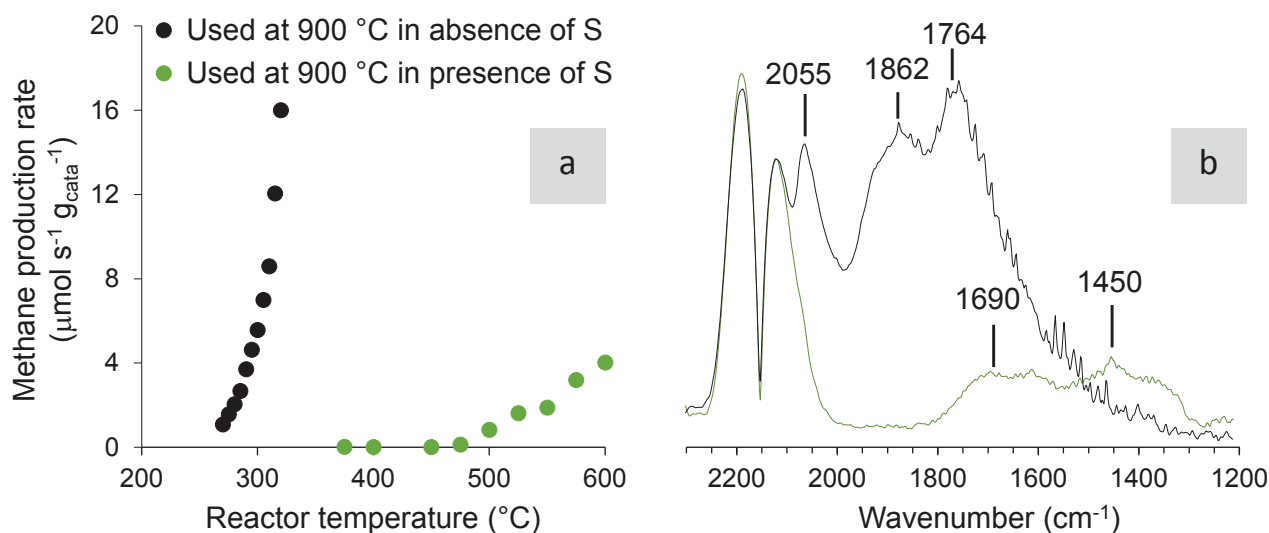


Figure 6.12 (a) Methanation rate and (b) DRIFTS spectra in the presence of CO for the fresh (black) and after S-exposure (green) Com Ni catalyst. H₂S exposure was realized at 900 °C for 2 hours under reforming conditions (Table 2.2). Methanation feed composition is given in Table 2.5. DRIFTS spectra were recorded at 250 °C after 1 min in CO/H₂/He mixture, following reduction at 450 °C in 35 mL min⁻¹ H₂ diluted in 20 mL min⁻¹ He.

These results obtained on this commercial sample reemphasize that it is difficult to estimate turnover frequencies over Ni-based samples in the presence of sulfur, due to near-complete sulfidation of the surface, because the determination of the concentration of S-free surface sites is not precise. In addition, it is possible that S-modified sites could present some intrinsic reforming activity. The activity of our Ni- and Rh-based samples was therefore studied at various temperatures, to evaluate a possible change of the apparent activation energy with temperature, which could possibly indicate a change of the nature of the active site.

3.4. Assessment of transport limitations during reforming

The apparent activation energies (E_{app}) measured for methane consumption for the various samples in the absence of poisons (white bars) appeared to vary from 56 to 104 kJ mol⁻¹ (Figure 6.13). The E_{app} was determined from the activity in methane reforming measured between 650-725 °C. The conversion in methane was typically below 50 %, though differential conditions were not achieved. These values should therefore be taken as gross estimates. The values reported by Wei and Iglesia for methane steam reforming E_{app} are ca. 102 and 109 kJ mol⁻¹ for Ni (full line) and Rh-based (dashed line) catalysts, respectively (represented by red lines in Figure 6.13).^[56,57]

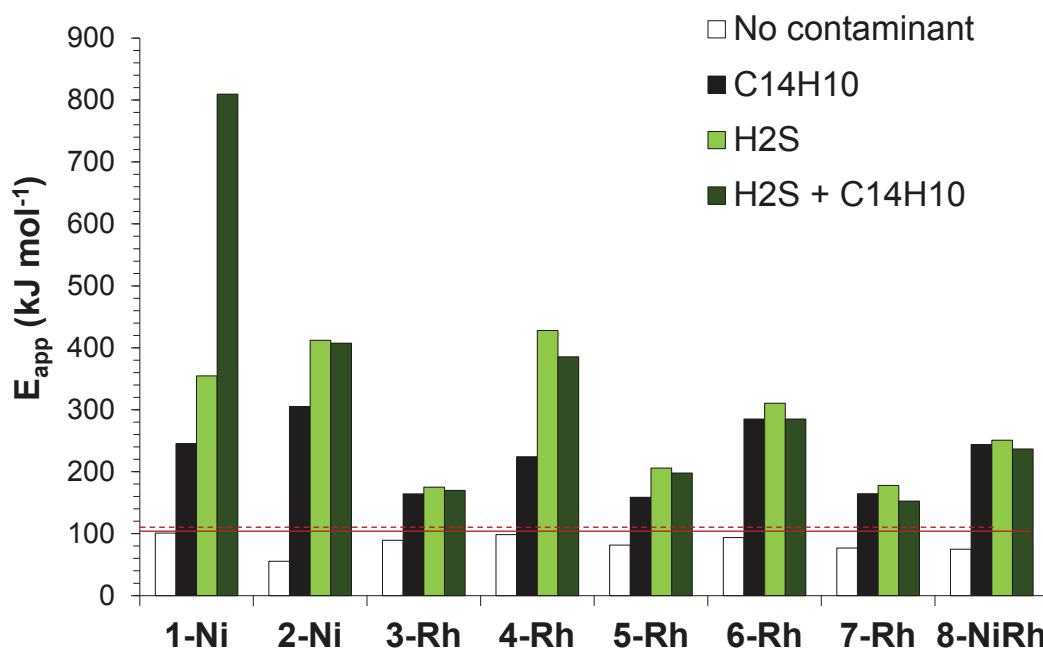


Figure 6.13 Apparent activation energies for methane consumption for the various samples under various feeds: (white) poison-free, (black) with 200 ppm phenanthrene, (light green) with 200 ppm H₂S and (dark green) with both 200 ppm phenanthrene and 200 ppm H₂S.

The occurrence of internal mass transport limitation was checked for the mesopore-based sample 2-Ni that led to the lowest E_{app} . Two different particle size fractions were used and the finest particles yielded higher reaction rates and an E_{app} of 96 ± 9 kJ mol⁻¹, instead of 56 ± 5 kJ mol⁻¹ for the 100-200 μ m fraction (Figure 6.14a). These results support the occurrence of internal mass transport limitations in the case of this particular sample and possibly in the case of the other samples based on the same support. To support this conclusion, the Weisz criterion ($\omega < 0.08$ for a 1st order reaction) was evaluated at 700 °C according to the activities measured at this temperature, an average particle radius of 150 μ m, a density of 3000 kg m⁻³, a temperature of 300 °C, an effective diffusivity of $6.8E-07$ m² s⁻¹, a porosity of 0.4, a tortuosity factor of 3 and a pore radius of 7 nm. Using these values, the ω moulus is calculated to be 0.2 by the Eurokin Gas-Solid fixed bed reactor modeler, which is above the value of 0.08 where pore diffusion is important (Table 6.3).^[164] The calculations therefore support the conclusion made above, that diffusion restrictions in 2-Ni are not negligible under reforming conditions. The distribution of metal nanoparticles within the support pore system was not checked (e.g. by TEM tomography), as this could affect the mass transfer limitation depending on the distribution, e.g. metal nanoparticles near the pore mouth or deeply buried in the particle core.

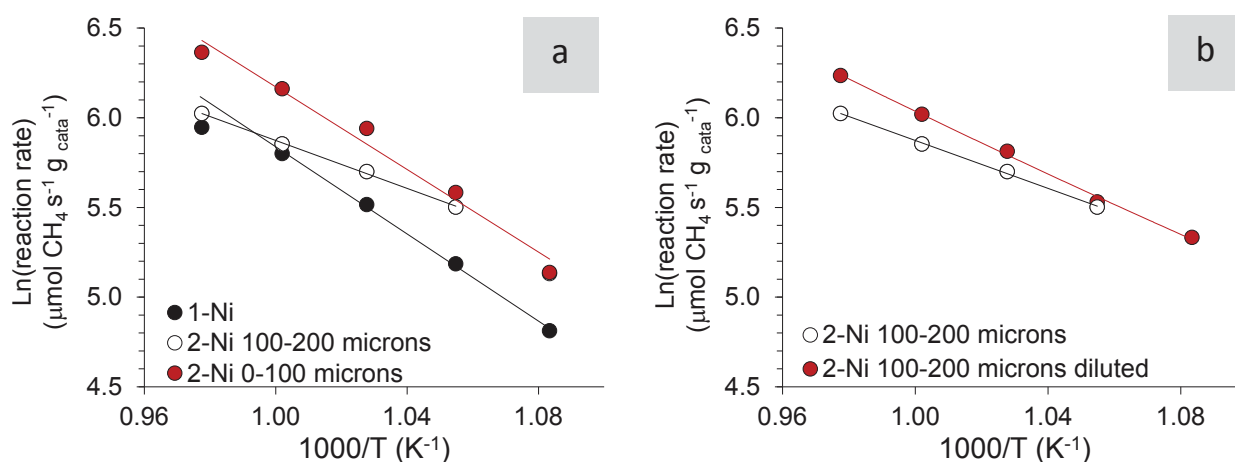


Figure 6.14 Arrhenius-type plots for 1-Ni and 2-Ni samples showing the logarithm of the CH₄ consumption rate versus the reciprocal temperature (range: 650–750 °C) under a poison-free feed. Effect of (a) the grain size and of (b) dilution (10 mg of sample diluted with 28 mg of $\alpha\text{-Al}_2\text{O}_3$) on the activity of the 2-Ni sample.

Similar reactor modeling indicated the presence of a significant radial heat transport limitation resulting in a cold spot of up to 61 °C when the reactor was operated at 900 °C without diluent. An additional experiment was carried out diluting the catalyst in an inert material to facilitate heat exchange with the reactor walls (Figure 6.14b). 10 mg of 2-Ni were diluted in 28 mg of $\alpha\text{-Al}_2\text{O}_3$ (100–200 μm fraction). The observed reaction rate was significantly higher, confirming the occurrence of heat transport limitations. In addition, a higher E_{app} of $72 \pm 5 \text{ kJ mol}^{-1}$ was measured, instead of $56 \pm 5 \text{ kJ mol}^{-1}$ for the non-diluted fraction. The Eurokin modeler was used to support these observations by evaluating the radial heat transfer limitations at 700 °C, considering an average diluent particle radius of 150 μm , a dilution density of 1250 kg m^{-3} and a dilution conductivity of $25 \text{ W m}^{-1} \text{ K}^{-1}$. The model dilution ratio was the same as that used in our experiment (ie. 0.8 in volume). The near wall to the center temperature gradient is calculated to be 3.4 °C, a value low enough to neglect radial heat transfer limitations when the catalyst is diluted (Table 6.3).

Therefore it is clear that the present activity measurements were disguised with heat and mass transport limitations. The TOF obtained under our conditions were compared to those reported by Wei and Iglesia, which were obtained in the absence of mass and heat transport limitations (Figure 6.15).^[58] The data of these authors obtained at 600 °C were extrapolated to 650 °C using an E_{app} of 109 kJ/mol. Differences in reactant concentrations were corrected assuming a reaction first order with respect to CH₄ and zeroth-order with respect to H₂O. The TOF plotted as a function of Rh dispersion (Figure 6.15b) were clearly lower than those measured by Wei and Iglesia, stressing the non-intrinsic nature of the TOF measured under our conditions.^[58] This observation explains why the rate data reported in Figure 6.7 displayed a curve with decreasing slope at higher metal surface area, rather than a straight line.

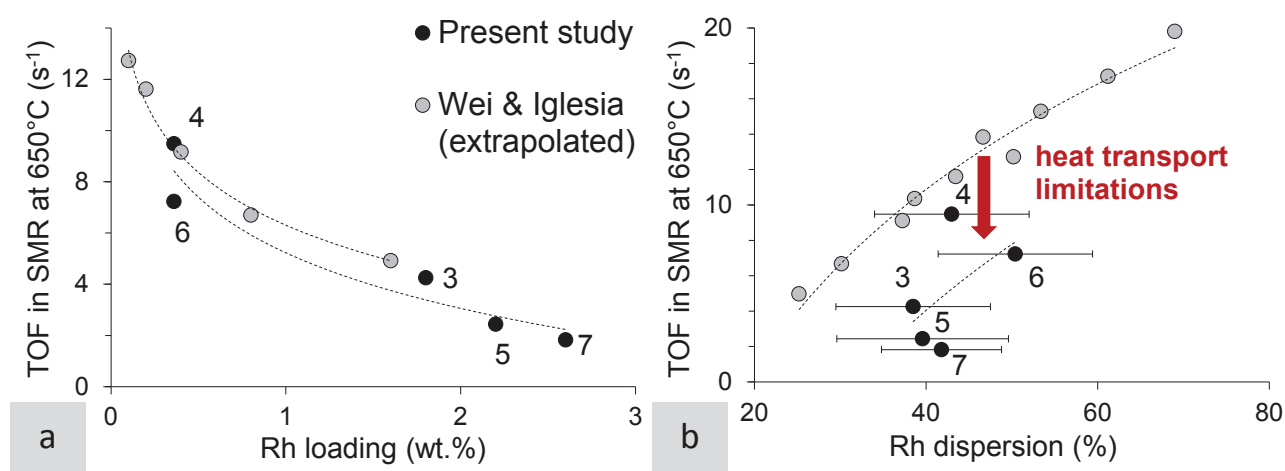


Figure 6.15 CH₄ consumption turnover frequencies measured at 650 °C as a function of the loading in Rh (a) and the Rh dispersion (b) under a poison-free feed. TOFs were calculated using the metal surface areas of the used samples presented in Table 6.2 (no H₂S in feed). Intrinsic kinetic data from Wei & Iglesia were extrapolated in terms of temperature and feed composition to match our experimental conditions.

The apparent activation energies measured in the presence of phenanthrene and H₂S were markedly higher than those observed without these poisons (Figure 6.13). Two and even eight-fold increases were noted. Most E_{app} values were comprised between 150 and 400 kJ mol⁻¹ in the presence of both pollutants, but a value as high as 800 kJ mol⁻¹ was calculated for 1-Ni. E_{app} values in the range 260-290 kJ mol⁻¹ had been reported in the case of Ni-based samples used in the presence of up to 300 ppm of H₂S, consistent with the data reported here.^[240] These exceedingly high values were most likely due a variation of the number of metal sites active for CH₄ reforming with temperature as a result of changes of the surface coverage of sulfur and carbonaceous deposits. It should be yet noted that our best three formulations (i.e. 3-Rh, 5-Rh and 7-Rh) exhibited E_{app} the closest to the values reported by Wei and Iglesia.^[58]

Table 6.3 Transport limitations calculated at 700 °C on 10 mg of 2-Ni sample using Eurokin Gas-Solid fixed bed reactor modeler. Data in green (respectively red) respect (resp. do not respect) the criterion which postulates that the related transport phenomena is not limiting (see section 3.5 in chapter 2).

Particle size (μm)	α-Al ₂ O ₃ dilluent (mg)	Activity in SMR at 700 °C (μmol s ⁻¹ g _{cata} ⁻¹)	Mass transport limitations		Heat transport limitations		
			External (Carberry number)	Internal (Weisz modulus)	External (ΔT _{film})	Internal (ΔT _{int})	Radial (ΔT _{rad})
0-100	0	380	0.001	0.03	0.2	0.01	33.4
100-200	0	299	0.003	0.2	0.9	0.01	26.2
100-200	28	335	0.003	0.22	1.0	0.01	3.4

The observed E_{app} values will therefore encompass terms for the heat of adsorption of both sulfur and carbonaceous surface species, in addition to those due to the adsorption of the reactants, i.e.

CH₄, H₂O and CO₂. Alstrup et al. have reported a heat of adsorption of ca. 289 kJ mol⁻¹ for H₂S on Ni-based catalysts and the heat of sublimation of phenanthrene is ca. 91 kJ mol⁻¹.^[241] It is therefore impossible to extract any direct kinetic (i.e. TOF) or thermodynamic (heat of adsorption) information from temperature-dependent data apart from specific reaction rates, due to the complexity of the system (i.e. high number of reactants and many by-products).

4. Conclusions

200 ppm of H₂S led to a significantly higher loss of activity during the reforming of methane than that induced by 200 ppm of phenanthrene over a series of Ni and Rh-based catalysts used at 900 °C. The surface atomic ratio S/Rh estimated after reaction was close to 0.5, similar to those reported for S-saturated Ni-based samples, suggesting near-to-full monolayer coverage by S under our operating conditions. The rate of methane conversion in the presence of both poisons varied linearly with Rh and Ni metal surface area. The slight deviation observed at higher loadings was in part due to heat and mass transport limitations. The rate of methane consumption per unit of metal surface area was ca. 4-fold higher on Rh as compared to the case of Ni. No information could be derived from the measure of apparent activation energies, due to changes in adsorption coverage of reactants and poisons with temperature. It is therefore impossible to conclude whether the residual activity measured in the presence of sulfur was due solely to a small fraction of sites free of sulfur or also to S-modified sites. The use of lower temperatures (875 °C and especially 850 °C) led to incomplete conversion of polyaromatics, which are well-known coke precursors. Activity tests carried out on much longer time-scale (several days) at high temperatures (ca. 900 °C) in the presence of both phenanthrene and H₂S will be necessary to ascertain the commercial potential of the best formulations investigated here and are in progress.

Highlights

- Supported Ni-based and Rh-based reforming catalysts were studied in the presence of H₂S and phenanthrene.
- 200 ppmv of H₂S was significantly more poisonous than 200 ppmv of phenanthrene.
- Rh exhibits a five-fold higher specific activity than Ni.
- No polycyclic aromatic hydrocarbons (coke precursors) were observed in the effluent of the reactor set at 900 °C on the best Rh-based catalysts.
- Heat transport limitations are of major concern in the reforming process.

References

- [1] M. Stocker, Renewable resources biofuels and BTL fuels in the biorefinery: Catalytic conversion of lignocellulosic biomass using porous materials, *Angew. Chemie Int. Ed.* 47 (2008) 9200–9211.
- [2] E. Vogt, B. Weckhuysen, Fluid Catalytic Cracking : Recent developments on the grand old lady of zeolite catalysis, *Chem. Soc. Rev.* 44 (2015) 7342–7370.
- [3] International Energy Agency, Resources to Reserves: oil, gas and coal technologies for the energy markets of the future, 2013.
- [4] S. Naik, V. Goud, P. Rout, A. Dalai, Production of first and second generation biofuels : A comprehensive review, *Renew. Sustain. Energy Rev.* 14 (2010) 578–597.
- [5] Eurostat, Energy Balance Sheets, 2015.
- [6] 2050 Roadmap, A practical guide to a prosperous low-carbon Europe - Executive Summary Report, 2010.
- [7] European Union Seventh Framework Programme, FASTCARD Description of Work, 2013.
- [8] J. Rostrup-Nielsen, Catalytic Steam Reforming, *Catal. Sci. Technol.* 5 (1984) 1–117.
- [9] C. Murkin, J. Brightling, Eighty years of steam reforming, *Johnson Matthey Technol. Rev.* 60 (2016) 263–269.
- [10] J. Rostrup-Nielsen, J. Sehested, J. Norskov, Hydrogen and synthesis gas by steam and CO₂ reforming, *Adv. Catal.* 47 (2002) 65–139.
- [11] S. Pogutz, A. Russo, P. Migliavacca, Innovation, markets and sustainable energy: The challenge of hydrogen and fuel cells, 2009.
- [12] D. Levin, R. Chahine, Challenges for renewable hydrogen production from biomass, *Int. J. Hydrogen Energy.* 35 (2010) 4962–4969.
- [13] K. Liu, C. Song, V. Subramani, Hydrogen and syngas production and purification technologies, 2009.
- [14] H. Boerrigter, B. Van Der Drift, “Biosyngas” key-intermediate in production of renewable transportation fuels, chemicals, and electricity: Optimum scale and economic prospects of Fischer-Tropsch plants, 2005.
- [15] J. Rostrup-Nielsen, T. Rostrup-Nielsen, Large-scale hydrogen production, *Haldor Topsoe Technol.* (2010).
- [16] J. Armor, The multiple roles for catalysis in the production of H₂, *Appl. Catal. A Gen.* 176 (1999) 159–176.
- [17] S. Panigrahi, A. Dalai, S. Chaudhari, N. Bakhshi, Synthesis gas production from steam gasification of biomass-derived oil, *Energy & Fuels.* 17 (2003) 637–642.
- [18] S. Chaudhari, S. Bej, N. Bakhshi, A. Dalai, Steam gasification of biomass-derived char for the production of carbon monoxide-rich synthesis gas, *Energy & Fuels.* 15 (2001) 736–742.
- [19] T. Wang, J. Chang, P. Lv, Synthesis gas production via biomass catalytic gasification with addition of biogas, *Energy & Fuels.* 19 (2005) 637–644.
- [20] P. Lv, Z. Yuan, C. Wu, L. Ma, Y. Chen, N. Tsubaki, Biosyngas production from biomass catalytic gasification, *Energy Convers. Manag.* 48 (2007) 1132–1139.
- [21] GoBiGas website, (2017). <https://gobigas.goteborgenergi.se/>.
- [22] C. Van Der Meijden, H. Veringa, B. Vreugdenhil, B. Van Der Drift, R. Zwart, R. Smit, Production of bio-methane from woody biomass, 2009.
- [23] C. Van Der Meijden, J.-W. Könemann, W. Sierhuis, B. Van Der Drift, B. Rietveld, Wood to bio-methane demonstration project in the Netherlands, 2013.
- [24] C. Van Der Meijden, Development of the MILENA gasification technology for the production of Bio-SNG, 2010.
- [25] W. Ma, G. Jacobs, D. Sparks, V. Ramana, R. Pendyala, S.G. Hopps, G. Thomas, H. Hamdeh, A. Maclennan, Y. Hu, B. Davis, Fischer-Tropsch synthesis: Effect of ammonia in syngas on the Fischer-Tropsch synthesis performance of a precipitated Iron catalyst, *J. Catal.* 326 (2015) 149–160.
- [26] V. Ramana, R. Pendyala, M.K. Gnanamani, G. Jacobs, W. Ma, W. Shafer, B. Davis, Fischer-Tropsch synthesis: Effect of Ammonia Impurities in Syngas Feed over a Cobalt / Alumina catalyst, *Appl. Catal. A Gen.* 468 (2013) 38–43.
- [27] R. Zwart, S. Van Der Heijden, R. Emmen, J. Bentzen, J. Ahrenfeldt, P. Stoholm, J. Krogh, Tar removal from low-temperature gasifiers, 2010.
- [28] BioSNG website, (2017). <http://www.biosng.com/>.
- [29] Phyllis website, (2017). <https://www.ecn.nl/phyllis2/Browse/Standard/ECN-Phyllis#>.
- [30] C. Li, K. Suzuki, Tar property, analysis, reforming mechanism and model for biomass gasification - An overview, *Renew. Sustain. Energy Rev.* 13 (2009) 594–604.
- [31] Thersites website, (2017). <http://www.thersites.nl/>.
- [32] V. Claude, C. Courson, M. Kohler, S. Lambert, Overview and essentials of biomass gasification technologies and their catalytic cleaning methods, *Energy & Fuels.* 30 (2016) 8791–8814.
- [33] Z. Abu El-Rub, E. Bramer, G. Brem, Review of catalysts for tar elimination in biomass gasification processes, *Ind. Eng. Chem. Res.* 45 (2004) 75–80.

- [34] Y. Shen, K. Yoshikawa, Recent progresses in catalytic tar elimination during biomass gasification or pyrolysis - A review, *Renew. Sustain. Energy Rev.* 21 (2013) 371–392.
- [35] G. Guan, M. Kaewpanha, X. Hao, A. Abudula, Catalytic steam reforming of biomass tar: Prospects and challenges, *Renew. Sustain. Energy Rev.* 58 (2016) 450–461.
- [36] V. Choudhary, A. Rajput, Simultaneous carbon dioxide and steam reforming of methane to syngas over NiO-CaO catalyst, *Ind. Eng. Chem. Res.* 35 (1996) 3934–3939.
- [37] H. Roh, Y. Koo, H. Jeong, T. Seo, J. Seo, Y. Seo, Combined reforming of methane over supported Ni catalysts, *Catal. Letters.* 117 (2007) 85–90.
- [38] G. Olah, A. Goepfert, M. Czaun, S. Prakash, Bi-reforming of methane from any source with steam and carbon dioxide exclusively to metgas for methanol and hydrocarbon synthesis, *J. Am. Chem. Soc.* 135 (2013) 648–650.
- [39] M.M. Danilova, Z. Fedorova, V. Zaikovskii, A. Porsin, V. Kirillov, T. Krieger, Porous Nickel-based catalysts for combined steam and carbon dioxide reforming of methane, *Appl. Catal. B Environ.* 147 (2014) 858–863.
- [40] P. Simell, J. Hepola, O. Krause, Effects of gasification gas components on tar and ammonia decomposition over hot gas cleanup catalysts, *Fuel.* 76 (1997) 1117–1127.
- [41] H. Ronkkonen, P. Simell, M. Reinikainen, O. Krause, M. Veringa, Catalytic clean-up of gasification gas with precious metal catalysts - A novel catalytic reformer development, *Fuel.* 89 (2010) 3272–3277.
- [42] R. Coll, J. Salvado, X. Farriol, D. Montané, Steam reforming model compounds of biomass gasification tars: Conversion at different operating conditions and tendency towards coke formation, *Fuel Process. Technol.* 74 (2001) 19–31.
- [43] H. Jahangiri, J. Bennett, P. Mahjoubi, K. Wilson, S. Gu, A review of advanced catalyst development for Fischer-Tropsch synthesis of hydrocarbons from biomass derived syngas, *Catal. Sci. Technol.* 4 (2014) 2210–2229.
- [44] J. Ginsburg, J. Pin, T. El Solh, H. De Lasa, Coke formation over a Nickel catalyst under methane dry reforming conditions : Thermodynamic and kinetic models, *Ind. Eng. Chem. Res.* 44 (2005) 4846–4854.
- [45] J. Hagen, *Industrial Catalysis - A Practical Approach*, 2006.
- [46] M. Davis, R. Davis, *Fundamentals of Chemical Reaction Engineering*, 2003.
- [47] G. Jones, J. Jakobsen, S. Shim, J. Kleis, M. Andersson, J. Rossmeisl, F. Abild-Pedersen, T. Bligaard, S. Helveg, B. Hinnemann, J. Rostrup-Nielsen, I. Chorkendorff, J. Sehested, J. Norskov, First principles calculations and experimental insight into methane steam reforming over transition metal catalysts, *J. Catal.* 259 (2008) 147–160.
- [48] D. Qin, J. Lapszewicz, Study of mixed steam and CO₂ reforming of CH₄ to syngas on MgO-supported metals, *Catal. Today.* 21 (1994) 551–560.
- [49] J. Rostrup-Nielsen, J.-H. Bak Hansen, CO₂-reforming of methane over transition metals, *J. Catal.* 144 (1993) 38–49.
- [50] J. Wei, E. Iglesia, Mechanism and site requirements for activation and chemical conversion of methane on supported Pt clusters and turnover rate comparisons among noble metals, *J. Phys. Chem. B.* 108 (2004) 4094–4103.
- [51] P. Ferreira-Aparicio, A. Guerrero-Ruiz, I. Rodríguez-Ramos, Comparative study at low and medium reaction temperatures of syngas production by methane reforming with carbon dioxide over silica and alumina supported catalysts, *Appl. Catal. A Gen.* 170 (1998) 177–187.
- [52] J. Sehested, Four challenges for nickel steam-reforming catalysts, *Catal. Today.* 111 (2006) 103.
- [53] F. Schouten, E. Kaleveld, G. Bootsma, AES-LEED ellipsometry study of the kinetics of the interaction of methane with Ni(110), *Surf. Sci.* 63 (1977) 460–474.
- [54] F. Schouten, O. Gijzeman, G. Bootsma, Interaction of methane with Ni(111) and Ni(100): Diffusion of carbon into nickel through the (100) surface (ann AES-LEED study), *Surf. Sci.* 87 (1979) 1–12.
- [55] M. Toebe, J. Bitter, J. Van Dillen, K. de Jong, Impact of the structure and reactivity of nickel particles on the catalytic growth of carbon nanofibers, *Catal. Today.* 76 (2002) 33–42.
- [56] J. Wei, E. Iglesia, Isotopic and kinetic assessment of the mechanism of reactions of CH₄ with CO₂ or H₂O to form synthesis gas and carbon on Nickel catalysts, *J. Catal.* 224 (2004) 370–383.
- [57] J. Wei, E. Iglesia, Structural requirements and reaction pathways in methane Activation and Chemical conversion catalyzed by Rhodium, *J. Catal.* 225 (2004) 116–127.
- [58] A. Yamaguchi, E. Iglesia, Catalytic activation and reforming of methane on supported Palladium clusters, *J. Catal.* 274 (2010) 52.
- [59] H.S. Bengaard, J. Norskov, J. Sehested, B. Clausen, E.H. Nielsen, A. Molenbroek, J. Rostrup-Nielsen, Steam reforming and graphite formation on Ni catalysts, *J. Catal.* 209 (2002) 365–384.
- [60] V. Dal Santo, A. Gallo, A. Naldoni, M. Guidotti, R. Psaro, Bimetallic heterogeneous catalysts for hydrogen production, *Catal. Today.* 197 (2012) 190–205.
- [61] D. Li, Y. Nakagawa, K. Tomishige, Methane reforming to synthesis gas over Ni catalysts modified with noble metals, *Appl. Catal. A Gen.* 408 (2011) 1–24.

- [62] K. Tomishige, T. Miyazawa, M. Asadullah, S. Ito, Catalyst performance in reforming of tar derived from biomass over noble metal catalysts, *Green Chem.* 5 (2003) 399–403.
- [63] M. Yung, W. Jablonski, K. Magrini-bair, Review of catalytic conditioning of biomass-derived syngas, *Energy & Fuels.* 23 (2009) 1874–1887.
- [64] P. Van Beurden, On the catalytic aspects of steam methane reforming - A literature survey, 2004.
- [65] X. Verykios, Catalytic dry reforming of natural gas for the production of chemicals and hydrogen, *Int. J. Hydrogen Energy.* 28 (2003) 1045–1063.
- [66] W.-S. Dong, H.-S. Roh, K.-W. Jun, S.-E. Park, Y.-S. Oh, Methane reforming over Ni/Ce-ZrO₂ catalysts: effect of nickel content, *Appl. Catal. A Gen.* 226 (2002) 63–72.
- [67] S. Yokota, K. Okumura, M. Niwa, Support effect of metal oxide on Rh catalysts in the CH₄-CO₂ reforming reaction, *Catal. Letters.* 84 (2002) 131–133.
- [68] T. Miyazawa, T. Kimura, J. Nishikawa, S. Kado, K. Kunimori, K. Tomishige, Catalytic performance of supported Ni catalysts in partial oxidation and steam reforming of tar derived from the pyrolysis of wood biomass, *Catal. Today.* 115 (2006) 254–262.
- [69] J. Xu, G. Froment, Methane steam reforming, methanation and water-gas shift, *AIChE J.* 35 (1989) 88–96.
- [70] A. Jess, Catalytic upgrading of tarry fuel gases: A kinetic study with model components, *Chem. Eng. Process. Process Intensif.* 35 (1996) 487–494.
- [71] N. Kaisalo, P. Simell, J. Lehtonen, Benzene steam reforming kinetics in biomass gasification gas cleaning, *Fuel.* 182 (2016) 696–703.
- [72] C. Bartholomew, Mechanisms of catalyst deactivation, *Appl. Catal. A Gen.* 212 (2001) 17–60.
- [73] K. Aasberg-Petersen, I. Dybkjaer, C.V. Ovesen, N.C. Schjodt, J. Sehested, S.G. Thomsen, Natural gas to synthesis gas: Catalysts and catalytic processes, *J. Nat. Gas Sci. Eng.* 3 (2011) 423–459.
- [74] J. Sehested, Sintering of nickel steam-reforming catalysts, *J. Catal.* 217 (2003) 417–426.
- [75] J. Sehested, J. Gelten, I. Remediakis, H. Bengaard, J. Norskov, Sintering of nickel steam-reforming catalysts: Effects of temperature and steam and hydrogen pressures, *J. Catal.* 223 (2004) 432–443.
- [76] J. Sehested, J.A.P. Gelten, S. Helveg, Sintering of nickel catalysts: Effects of time, atmosphere, temperature, nickel-carrier interactions, and dopants, *Appl. Catal. A Gen.* 309 (2006) 237–246.
- [77] J. Sehested, Carlsson, Janssens, Hanen, Datye, Sintering of nickel steam-reforming catalysts on MgAl₂O₄ spinel supports, *J. Catal.* 197 (2001) 200–209.
- [78] K. Christensen, D. Chen, R. Lodeng, A. Holmen, Effect of supports and Ni crystal size on carbon formation and sintering during steam methane reforming, *Appl. Catal. A Gen.* 314 (2006) 9–22.
- [79] Y. Matsumura, T. Nakamori, Steam reforming of methane over nickel catalysts at low reaction temperature, *Appl. Catal. A Gen.* 258 (2004) 107–114.
- [80] A. Gadalla, B. Bower, The role of catalyst support on the activity for reforming methane with CO₂, *Chem. Eng. Sci.* 43 (1988) 3049–3062.
- [81] G.S. Gallego, F. Mondragón, J. Barrault, J.M. Tatibouët, C. Batiot-Dupeyrat, CO₂ reforming of CH₄ over La-Ni based perovskite precursors, *Appl. Catal. A Gen.* 311 (2006) 164–171.
- [82] K. Urasaki, Y. Sekine, S. Kawabe, E. Kikuchi, M. Matsukata, Catalytic activities and coking resistance of Ni/perovskites in steam reforming of methane, *Appl. Catal. A Gen.* 286 (2005) 23–29.
- [83] O. Clause, M. Kermarec, L. Bonneviot, F. Villain, M. Che, Nickel(II) ion-support interactions as a function of preparation method of silica-supported nickel materials, *J. Am. Chem. Soc.* 114 (1992) 4709–4717.
- [84] P. Burattin, M. Che, C. Louis, Characterization of the Ni(II) phase formed on silica upon deposition-precipitation, *J. Phys. Chem. B.* 101 (1997) 7060–7074.
- [85] P. Burattin, M. Che, C. Louis, Molecular approach to the mechanism of deposition-precipitation of the Ni(II) phase on silica, *J. Phys. Chem. B.* 102 (1998) 2722–2732.
- [86] P. Turlier, H. Praliaud, P. Moral, G. Martin, J. Dalmon, Influence of the nature of the support on the reducibility and catalytic properties of nickel: Evidence for a new type of metal support interaction, *Appl. Catal.* 19 (1985) 287–300.
- [87] L. Alzamora, J. Ross, E. Kruissink, L. Van Reijen, Coprecipitated nickel-alumina catalysts for methanation at high temperature, *J. Chem. Soc. Faraday Trans.* 77 (1980) 665–681.
- [88] B. Mile, D. Stirling, M. Zammitt, A. Lovell, M. Webb, The location of nickel oxide and nickel in silica-supported catalysts: Two forms of “NiO” and the assignment of temperature-programmed reduction profiles, *J. Catal.* 114 (1988) 217–229.
- [89] C. Courson, E. Makaga, C. Petit, A. Kiennemann, Development of Ni catalysts for gas production from biomass gasification. Reactivity in steam- and dry-reforming, *Catal. Today.* 63 (2000) 427–437.
- [90] F. Morales-Cano, L.F. Lundegaard, R. Tiruvalam, H. Falsig, M.S. Skjoth-Rasmussen, Improving the sintering resistance of Ni/Al₂O₃ steam-reforming catalysts by promotion with noble metals, *Appl. Catal. A Gen.* 498 (2015) 117–125.

- [91] H. Wu, V. La Parola, G. Pantaleo, F. Puleo, A. Venezia, L. Liotta, Ni-based catalysts for low temperature methane steam reforming: Recent results on Ni-Au and comparison with other bi-metallic systems, *Catalysts*. 3 (2013) 563–583.
- [92] M. Ligthart, J. Pieterse, E. Hensen, The role of promoters for Ni catalysts in low temperature (membrane) steam methane reforming, *Appl. Catal. A Gen.* 405 (2011) 108–119.
- [93] A. Fouskas, M. Kollia, A. Kambolis, C. Papadopoulou, H. Matralis, Boron-modified Ni/Al₂O₃ catalysts for reduced carbon deposition during dry reforming of methane, *Appl. Catal. A Gen.* 474 (2014) 125–134.
- [94] S. Li, J. Gong, Strategies for improving the performance and stability of Ni-based catalysts for reforming reactions, *Chem. Soc. Rev.* 43 (2014) 7245.
- [95] H. Tian, X. Li, L. Zeng, J. Gong, Recent advances on the design of group VIII base-metal catalysts with encapsulated structures, *ACS Catal.* 5 (2015) 4959–4977.
- [96] C. Zhang, W. Zhu, S. Li, G. Wu, X. Ma, X. Wang, J. Gong, Sintering-resistant Ni-based reforming catalysts obtained via the nanoconfinement effect, *Chem. Commun.* 49 (2013) 9383–9385.
- [97] F. Wang, L. Xu, W. Shi, Syngas production from CO₂ reforming with methane over core-shell Ni@SiO₂ catalysts, *J. CO₂ Util.* 16 (2016) 318–327.
- [98] J.C. Park, J.U. Bang, J. Lee, C.H. Ko, H. Song, Ni@SiO₂ yolk-shell nanoreactor catalysts: High temperature stability and recyclability, *J. Mater. Chem.* 20 (2010) 1239–1246.
- [99] J. Zhang, F. Li, Coke-resistant Ni@SiO₂ catalyst for dry reforming of methane, *Appl. Catal. B Environ.* 176 (2015) 513–521.
- [100] T. Wu, W. Cai, P. Zhang, X. Song, L. Gao, Cu–Ni@SiO₂ alloy nanocomposites for methane dry reforming catalysis, *RSC Adv.* 3 (2013) 23976.
- [101] Z. Li, L. Mo, Y. Kathiraser, S. Kawi, Yolk-Satellite-Shell structured Ni-Yolk@Ni@SiO₂ nanocomposite : Superb catalyst toward methane CO₂ reforming reaction, *ACS Catal.* 4 (2014) 1526–1536.
- [102] J. Guo, C. Xie, K. Lee, N. Guo, J. Miller, M. Janik, C. Song, Improving the carbon resistance of Ni-Based steam reforming catalyst by alloying with Rh: A computational study coupled with reforming experiments and EXAFS characterization, *ACS Catal.* 1 (2011) 574–582.
- [103] S. Albertazzi, F. Basile, D. Barbera, P. Benito, J. Brandin, J. Einvall, G. Fornasari, F. Trifirò, A. Vaccari, Deactivation of a Ni-based reforming catalyst during the upgrading of the producer gas, from simulated to real conditions, *Top. Catal.* 54 (2011) 746–754.
- [104] F.M. Josuinkas, C.P.B. Quitete, N.F.P. Ribeiro, M.M.V.M. Souza, Steam reforming of model gasification tar compounds over nickel catalysts prepared from hydrotalcite precursors, *Fuel Process. Technol.* 121 (2014) 76–82.
- [105] D. Swierczynski, S. Libs, C. Courson, A. Kiennemann, Steam reforming of tar from a biomass gasification process over Ni/olivine catalyst using toluene as a model compound, *Appl. Catal. B Environ.* 74 (2007) 211–222.
- [106] M. Argyle, C. Bartholomew, Heterogeneous catalyst deactivation and regeneration: A review, *Catalysts*. 5 (2015) 145–269.
- [107] A. Arcoya, A. Cortes, J. Fierro, X. Seoane, Comparative study of the deactivation of group VIII metal catalysts by thiophene, *Catal. Deactiv.* (1991) 557–564.
- [108] K. Lee, C. Song, M. Janik, Ab initio thermodynamics examination of Sulfur species present on Rh, Ni, and binary Rh-Ni surfaces under steam reforming reaction conditions, *Langmuir*. 28 (2012) 5660–5668.
- [109] S.L. Lakhapatri, M.A. Abraham, Deactivation due to sulfur poisoning and carbon deposition on Rh-Ni/Al₂O₃ catalyst during steam reforming of sulfur-doped n-hexadecane, *Appl. Catal. A Gen.* 364 (2009) 113–121.
- [110] S. Lakhapatri, M. Abraham, Sulfur poisoning of Rh–Ni catalysts during steam reforming of sulfur-containing liquid fuels, *Catal. Sci. Technol.* 3 (2013) 2755–2760.
- [111] K. Tomishige, T. Miyazawa, T. Kimura, K. Kunimori, N. Koizumi, M. Yamada, Resistance to sulfur poisoning of hot gas cleaning catalysts for the removal of tar from the pyrolysis of cedar wood, *Appl. Catal. B Environ.* 60 (2005) 299–307.
- [112] C. Xie, Y. Chen, Y. Li, X. Wang, C. Song, Sulfur poisoning of CeO₂-Al₂O₃-supported mono- and bi-metallic Ni and Rh catalysts in steam reforming of liquid hydrocarbons at low and high temperatures, *Appl. Catal. A Gen.* 390 (2010) 210–218.
- [113] A. Steele, S. Poulston, K. Magrini-Bair, W. Jablonski, Catalytic syngas purification from model biomass gasification streams, *Catal. Today*. 214 (2013) 74–81.
- [114] A. Navrotsky, O. Trofymuk, A. Levchenko, Thermochemistry of microporous and mesoporous materials, *Chem. Rev.* 109 (2009) 3885–3902.
- [115] A. Corma, From microporous to mesoporous molecular sieve materials and their use in catalysis, *Chem. Rev.* 97 (1997) 2373–2419.
- [116] J. Weitkamp, Zeolites and catalysis, *Solid State Ionics*. 131 (2000) 175–188.
- [117] IZA website, (2017). <http://www.iza-structure.org/databases/>.

- [118] R. Baur, R. Krishna, Effectiveness factor for zeolite catalysed isomerization reactions, *Chem. Eng. J.* 99 (2004) 105–116.
- [119] J. Perez-Ramirez, C. Christensen, K. Egeblad, C. Christensen, J. Groen, Hierarchical zeolites: Enhanced utilisation of microporous crystals in catalysis by advances in materials design, *Chem. Soc. Rev.* 37 (2008) 2530–2542.
- [120] S. Larsen, Nanocrystalline zeolites and zeolite structures: synthesis, characterization and applications, *J. Phys. Chem. C.* 111 (2007) 18464–18474.
- [121] H. Awala, J.-P. Gilson, R. Retoux, P. Boullay, J.-M. Goupil, V. Valtchev, S. Mintova, Template-free nanosized faujasite-type zeolites, *Nat. Mater.* 14 (2015) 447–51.
- [122] W. Schwieger, A.G. Machoke, T. Weissenberger, A. Inayat, T. Selvam, M. Klumpp, A. Inayat, Hierarchy concepts: Classification and preparation strategies for zeolite containing materials with hierarchical porosity, *Chem. Soc. Rev.* (2015).
- [123] D. Farrusseng, A. Tuel, Perspectives on zeolite-encapsulated metal nanoparticles and their applications in catalysis, *New J. Chem.* 40 (2016) 3933.
- [124] C. Pagis, A.R. Morgado Prates, D. Farrusseng, N. Bats, A. Tuel, Hollow zeolite structures: An overview of synthesis methods, *Chem. Mater.* 28 (2016) 5205.
- [125] Y. Tao, H. Kanoh, L. Abrams, K. Kaneko, Mesopore-modified zeolites: Preparation, characterization, and applications, *Chem. Rev.* 106 (2006) 896–910.
- [126] R.M. Dessau, E.W. Valyocsik, N.H. Goeke, Aluminum zoning in ZSM-5 as revealed by selective silica removal, *Zeolites.* 12 (1992) 776–779.
- [127] J. Groen, L. Peffer, J. Moulijn, J. Perez-Ramirez, Mesoporosity development in ZSM-5 zeolite upon optimized desilication conditions in alkaline medium, *Colloids Surfaces A Physicochem. Eng. Asp.* 241 (2004) 53–58.
- [128] J. Groen, J. Jansen, J. Moulijn, J. Perez-Ramirez, Optimal aluminum-assisted mesoporosity development in MFI zeolites by desilication, *J. Phys. Chem. B.* 108 (2004) 13062–13065.
- [129] J. Groen, L. Peffer, J. Moulijn, J. Perez-Ramirez, Mechanism of hierarchical porosity development in MFI zeolites by desilication: The role of aluminium as a pore-directing agent, *Chem. Eur. J.* 11 (2005) 4983–4994.
- [130] J. Groen, T. Bach, U. Ziese, A. Paulaime-Van Donk, K. de Jong, J. Moulijn, J. Perez-Ramirez, Creation of hollow zeolite architectures by controlled desilication of Al-zoned ZSM-5 crystals, *J. Am. Chem. Soc.* 127 (2005) 10792–10793.
- [131] J. Mielby, J.O. Abildstrom, F. Wang, T. Kasama, C. Weidenthaler, S. Kegnaes, Oxidation of bioethanol using zeolite-encapsulated gold nanoparticles, *Angew. Chemie - Int. Ed.* 53 (2014) 12513–12516.
- [132] S. Goel, Z. Wu, S. Zones, E. Iglesia, Synthesis and catalytic properties of metal clusters encapsulated, *J. Am. Chem. Soc.* 134 (2012) 17688–17695.
- [133] Z. Wu, S. Goel, M. Choi, E. Iglesia, Hydrothermal synthesis of LTA-encapsulated metal clusters and consequences for catalyst stability, reactivity and selectivity, *J. Catal.* 311 (2014) 458–468.
- [134] A. Laursen, K. Hojholt, L. Lundegaard, S. Simonsen, S. Helveg, F. Schuth, M. Paul, J.D. Grunwaldt, S. Kegnoes, C.H. Christensen, K. Egeblad, Substrate size-selective catalysis with zeolite-encapsulated gold nanoparticles, *Angew. Chemie Int. Ed.* 49 (2010) 3504–3507.
- [135] J. a. Schwarz, C. Contescu, A. Contescu, Methods for preparation of catalytic materials, *Chem. Rev.* 95 (1995) 477–510.
- [136] J. Cai, H. Ma, J. Zhang, Q. Song, Z. Du, Y. Huang, J. Xu, Gold nanoclusters confined in a supercage of Y zeolite for aerobic oxidation of HMF under mild conditions, *Chemistry.* 19 (2013) 14215–14223.
- [137] J. Van Den Bergh, N. Nishiyama, F. Kapteijn, Zeolite membranes in catalysis: What is new and how bright is the future?, 2010.
- [138] N. Nishiyama, K. Ichioka, D. Park, Y. Egashira, L. Gora, W. Zhu, F. Kapteijn, J.A. Moulijn, K. Ueyama, Reactant-selective hydrogenation over composite silicalite-1 coated Pt/TiO₂ particles, *Ind. Eng. Chem. Res.* 43 (2004) 1211–1215.
- [139] X. Wang, W. Yang, Y. Tang, Y. Wang, S. Fu, Z. Gao, Fabrication of hollow zeolite spheres, *Chem. Commun.* (2000) 2161–2162.
- [140] A. Dong, Y. Wang, D. Wang, W. Yang, Y. Zhang, N. Ren, Z. Gao, Y. Tang, Fabrication of hollow zeolite microcapsules with tailored shapes and functionalized interiors, *Microporous Mesoporous Mater.* 64 (2003) 69–81.
- [141] A. Dong, N. Ren, W. Yang, Y. Wang, Y. Zhang, D. Wang, J. Hu, Z. Gao, Y. Tang, Preparation of Hollow Zeolite Spheres and Three-Dimensionally Ordered Macroporous Zeolite Monoliths with Functionalized Interiors, *Adv. Funct. Mater.* 13 (2003) 943–948.
- [142] N. Ren, Y.H. Yang, J. Shen, Y.H. Zhang, H.L. Xu, Z. Gao, Y. Tang, Novel, efficient hollow zeolitically microcapsulized noble metal catalysts, *J. Catal.* 251 (2007) 182–188.
- [143] Y. Wang, M. Lin, A. Tuel, Hollow TS-1 crystals formed via a dissolution-recrystallization process, *Microporous Mesoporous Mater.* 102 (2007) 80–85.

- [144] Y. Wang, A. Tuel, Nanoporous zeolite single crystals: ZSM-5 nanoboxes with uniform intracrystalline hollow structures, *Microporous Mesoporous Mater.* 113 (2008) 286–295.
- [145] L. Burel, A. Tuel, Nanozeolites: New strategies for designing ultra small silicalite crystals with very few framework defects, *Microporous Mesoporous Mater.* 174 (2013) 90–99.
- [146] S. Li, L. Burel, C. Aquino, A. Tuel, F. Morfin, J.-L. Rousset, D. Farrusseng, Ultimate size-control of encapsulated gold nanoparticles, *Chem. Commun.* 49 (2013) 8507–8509.
- [147] S. Li, T. Boucheron, A. Tuel, D. Farrusseng, F. Meunier, Size-selective hydrogenation at the subnanometer scale over Platinum nanoparticles encapsulated in silicalite-1 single crystal hollow shells, *Chem. Commun.* 50 (2014) 1824–1826.
- [148] S. Li, C. Aquino, L. Gueudre, A. Tuel, Y. Schuurman, D. Farrusseng, Diffusion-driven selectivity in oxidation of CO in the presence of propylene using zeolite nano shell as membrane, *ACS Catal.* 4 (2014) 4299–4303.
- [149] S. Li, A. Tuel, J.-L. Rousset, F. Morfin, M. Aouine, L. Burel, F. Meunier, D. Farrusseng, Hollow zeolite single-crystals encapsulated alloy nanoparticles with controlled size and composition, *ChemNanoMat.* 2 (2016) 534–540.
- [150] ASTM International, Standard test method for determination of relative crystallinity of zeolite ZSM-5 by x-ray diffraction, 2011.
- [151] A. Galarneau, F. Villemot, J. Rodriguez, F. Fajula, B. Coasne, Validity of the t-plot method to assess microporosity in hierarchical micro/mesoporous materials, *Langmuir.* 30 (2014) 13266–13274.
- [152] H. Merkus, Particle size measurements: fundamentals, practice, quality, 2009.
- [153] R. Van Hardeveld, F. Hartog, The statistics of surface atoms and surface sites on metal crystals, *Surf. Sci.* 15 (1969) 189–230.
- [154] C. Bartholomew, R. Pannell, The stoichiometry of hydrogen and carbon monoxide chemisorption on alumina and silica supported nickel, *J. Catal.* 65 (1980) 390–401.
- [155] J.-P. Candy, A. El Mansour, O. Ferretti, G. Mabilon, J.-P. Bournonville, J.-M. Basset, G. Martino, Organometallic chemistry on metals - Hydrogen and oxygen interaction with silica-supported and with alumina-Supported rhodium, *J. Catal.* 112 (1988) 210–220.
- [156] J. Sanders, Chemisorption and reactions on metallic films, 1971.
- [157] A. Taimoor, I. Pitault, F. Meunier, Correlation between deactivation and Pt-carbonyl formation during toluene hydrogenation using a H₂/CO₂ mixture, *J. Catal.* 278 (2011) 153–161.
- [158] J. Scalbert, C. Daniel, Y. Schuurman, C. Thomas, F. Meunier, Rational design of a CO₂-resistant toluene hydrogenation catalyst based on FT-IR spectroscopy studies, *J. Catal.* 318 (2014) 61–66.
- [159] NIST website, (2017). <http://webbook.nist.gov/chemistry/>.
- [160] D. Goodman, R. Kelley, T. Madey, J. Yates, Kinetics of the hydrogenation of CO over a single-crystal nickel-catalyst, *J. Catal.* 63 (1980) 226–234.
- [161] K. Coulter, X. Xu, W. Goodman, Structural and catalytic properties of model supported nickel catalysts, *J. Phys. Chem.* 98 (1994) 1245–1249.
- [162] M. Agnelli, H. Swaan, C. Marquez-Alvarez, G. Martin, C. Mirodatos, CO hydrogenation on a nickel catalyst - A mechanistic study by transient kinetics and infrared spectroscopy, *J. Catal.* 175 (1998) 117–128.
- [163] J. Sehested, S. Dahl, J. Jacobsen, J. Rostrup-Nielsen, Methanation of CO over Nickel: mechanism and kinetics at high H₂/CO ratios, *J. Phys. Chem. B.* 109 (2005) 2432–2438.
- [164] Eurokin website, (2017). <http://eurokin.org/>.
- [165] D. Mears, Diagnostic criteria for heat transport limitations in fixed bed reactors, *J. Catal.* 20 (1971) 127–131.
- [166] G. Froment, K. Bischoff, J. De Wilde, Chemical reactor analysis and design, 2011.
- [167] I. Nakamura, Y. Yamanoi, T. Imaoka, K. Yamamoto, H. Nishihara, A uniform bimetallic rhodium/iron nanoparticle catalyst for the hydrogenation of olefins and nitroarenes, *Angew. Chemie - Int. Ed.* 50 (2011) 5830–5833.
- [168] M. Takahashi, T. Imaoka, Y. Hongo, K. Yamamoto, Formation of a Pt₁₂ cluster by single-atom control that leads to enhanced reactivity: Hydrogenation of unreactive olefins, *Angew. Chemie - Int. Ed.* 52 (2013) 7419–7421.
- [169] G. Vile, B. Bridier, J. Wichert, J. Perez-Ramirez, Ceria in hydrogenation catalysis: High selectivity in the conversion of alkynes to olefins, *Angew. Chemie - Int. Ed.* 51 (2012) 8620–8623.
- [170] M. Shokouhimehr, Magnetically separable and sustainable nanostructured catalysts for heterogeneous reduction of nitroaromatics, *Catalysts.* 5 (2015) 534–560.
- [171] S. Li, A. Tuel, F. Meunier, M. Aouine, D. Farrusseng, Platinum nanoparticles entrapped in zeolite nanoshells as active and sintering-resistant arene hydrogenation catalysts, *J. Catal.* 332 (2015) 25–30.
- [172] M. Sivaiah, S. Petit, J. Barrault, C. Batiot-Dupeyrat, S. Valange, CO₂ reforming of CH₄ over Ni-containing phyllosilicates as catalyst precursors, *Catal. Today.* 157 (2010) 397–403.
- [173] M. V. Sivaiah, S. Petit, M.F. Beaufort, D. Eyidi, J. Barrault, C. Batiot-Dupeyrat, S. Valange, Nickel based catalysts derived from hydrothermally synthesized 1:1 and 2:1 phyllosilicates as precursors for carbon dioxide reforming of methane, *Microporous Mesoporous Mater.* 140 (2011) 69–80.
- [174] H. Strunz, E. Nickel, *Mineralogical Tables: Chemical–Structural Mineral Classification System*, 9th ed.,

Schweizerbart ed., 2001.

- [175] C. Knapp, A. Obuchi, J.O. Uchisawa, S. Kushiya, P. Avila, Method for selective removal of supported platinum particles from external zeolite surfaces: characterisation of and application to a catalyst for the selective reduction of nitrogen oxide by hydrocarbons, *Microporous Mesoporous Mater.* 31 (1999) 23–31.
- [176] L. Shi, C. Zeng, Q. Lin, P. Lu, W. Niu, N. Tsubaki, Citric acid assisted one-step synthesis of highly dispersed metallic Co/SiO₂ without further reduction: as-prepared Co/SiO₂ catalysts for Fischer-Tropsch synthesis, *Catal. Today.* 228 (2014) 206–211.
- [177] A. Loaiza-Gil, M. Villarroel, J.F. Balbuena, M.A. Lacruz, S. Gonzalez-Cortés, Thermal decomposition study of silica-supported nickel catalyst synthesized by the ammonia method, *J. Mol. Catal. A Chem.* 281 (2008) 207–213.
- [178] T. Lehmann, T. Wolff, C. Hamel, P. Veit, B. Garke, A. Seidel-Morgenstern, Physico-chemical characterization of Ni/MCM-41 synthesized by a template ion exchange approach, *Microporous Mesoporous Mater.* 151 (2012) 113–125.
- [179] C. Dai, S. Zhang, A. Zhang, C. Song, C. Shi, X. Guo, Hollow zeolite encapsulated Ni-Pt bimetal for sintering and coking resistant dry reforming of methane, *J. Mater. Chem. A.* 3 (2015) 16461–16468.
- [180] S. Bordiga, P. Ugliengo, A. Damin, C. Lamberti, G. Spoto, A. Zecchina, G. Spano, R. Buzzoni, L. Dalloro, F. Rivetti, Hydroxyls nests in defective silicalites and strained structures derived upon dehydroxylation: vibrational properties and theoretical modelling, *Top. Catal.* 15 (2001) 43–52.
- [181] D.W. Fickel, A.M. Shough, D. Doren, R. Lobo, High-temperature dehydrogenation of defective silicalites, *Microporous Mesoporous Mater.* 129 (2010) 156–163.
- [182] E. Flanigen, J. Bennett, R. Grose, J. Cohen, R. Patton, R. Kirchner, J. Smith, Silicalite, a new hydrophobic crystalline silica molecular sieve, *Nature.* 271 (1978) 512–516.
- [183] J.C. Park, J. Lee, U. Bang, H. Park, H. Song, Chemical transformation and morphology change of Nickel-silica hybrid nanostructures via Nickel phyllosilicates, *Chem. Commun.* 47 (2009) 7345–7347.
- [184] A. Majewski, J. Wood, W. Bujalski, Nickel-silica core@shell catalyst for methane reforming, *Int. J. Hydrogen Energy.* 38 (2013) 14531–14541.
- [185] O. Krivanek, J. Paterson, ELNES of 3d transition-metal oxides I. Variation across the periodic table, *Ultramicroscopy.* 32 (1990) 313–318.
- [186] Q. Jeangros, T. Hansen, J. Wagner, C. Damsgaard, R. Dunin-Borkowski, C. Hebert, J. Van Herle, A. Hessler-Wyser, Reduction of nickel oxide particles by hydrogen studied in an environmental TEM, *J. Mater. Sci.* 48 (2013) 2893–2907.
- [187] N. Novruzova, A. Tuel, D. Farrusseng, F. Meunier, Influence of crystal size on the uptake rate of isooctane in plain and hollow silicalite-1 crystals, *Microporous Mesoporous Mater.* 228 (2016) 147–152.
- [188] F. Meunier, D. Verboekend, J.P. Gilson, J. Groen, J. Perez-Ramirez, Influence of crystal size and probe molecule on diffusion in hierarchical ZSM-5 zeolites prepared by desilication, *Microporous Mesoporous Mater.* 148 (2012) 115.
- [189] P. Llewellyn, Y. Grillet, F. Schüth, H. Reichert, K. Unger, Effect of pore size on adsorbate condensation and hysteresis within a potential model adsorbent: M41S, *Microporous Mater.* 3 (1994) 345–349.
- [190] H. Li, Y. Sakamoto, Z. Liu, T. Ohsuna, O. Terasaki, M. Thommes, S. Che, Mesoporous silicalite-1 zeolite crystals with unique pore shapes analogous to the morphology, *Microporous Mesoporous Mater.* 106 (2007) 174–179.
- [191] R. Cimino, K. Cychosz, M. Thommes, A. Neimark, Experimental and theoretical studies of scanning adsorption-desorption isotherms, *Colloids Surfaces A Physicochem. Eng. Asp.* 437 (2013) 76–89.
- [192] M. Thommes, B. Smarsly, M. Groenewolt, P. Ravikovitch, A. Neimark, Adsorption hysteresis of nitrogen and argon in pore networks and characterization of novel micro- and mesoporous silicas, *Langmuir.* 22 (2006) 756–764.
- [193] L. Shi, K. Tao, T. Kawabata, Z.X. Jun, T. Shimamura, Surface impregnation combustion method to prepare nanostructured metallic catalysts without further reduction: as-burnt Co/SiO₂ catalysts for Fischer-Tropsch synthesis, *ASC Catal.* 1 (2011) 1225–1233. <http://pubs.acs.org/doi/abs/10.1021/cs200294d>.
- [194] J. Tallon, R. Buckley, Thermal decomposition of the zeolite catalyst ZSM-5, *J. Phys. Chem.* 91 (1987) 1469–1475.
- [195] S. Vieira, Z. Magriotis, M.F. Ribeiro, I. Graca, A. Fernandes, J.M. Lopes, S. Coelho, N. Santos, A. Saczk, Use of HZSM-5 modified with citric acid as acid heterogeneous catalyst for biodiesel production via esterification of oleic acid, *Microporous Mesoporous Mater.* 201 (2015) 160–168.
- [196] J. Volter, A Pi-complex mechanism for catalytic hydrogenation of the benzene ring, *J. Catal.* 3 (1964) 297–298.
- [197] R. Ross, G. Martin, W. Cook, Hydrogenation of olefins over nickel/silica catalysts, *Ind. Eng. Chem. Res.* 14 (1975) 151–154. <http://pubs.acs.org/doi/abs/10.1021/i360055a004>.
- [198] H.S. Foglerer, *Elements of chemical reaction engineering*, 2009.
- [199] G. Martin, J. Dalmon, Benzene hydrogenation over nickel catalysts at low and high temperatures: Structure-sensitivity and copper alloying effects, *J. Catal.* 75 (1982) 233–242.
- [200] M.A. Keane, P.M. Patterson, The role of hydrogen partial pressure in the gas-phase hydrogenation of aromatics

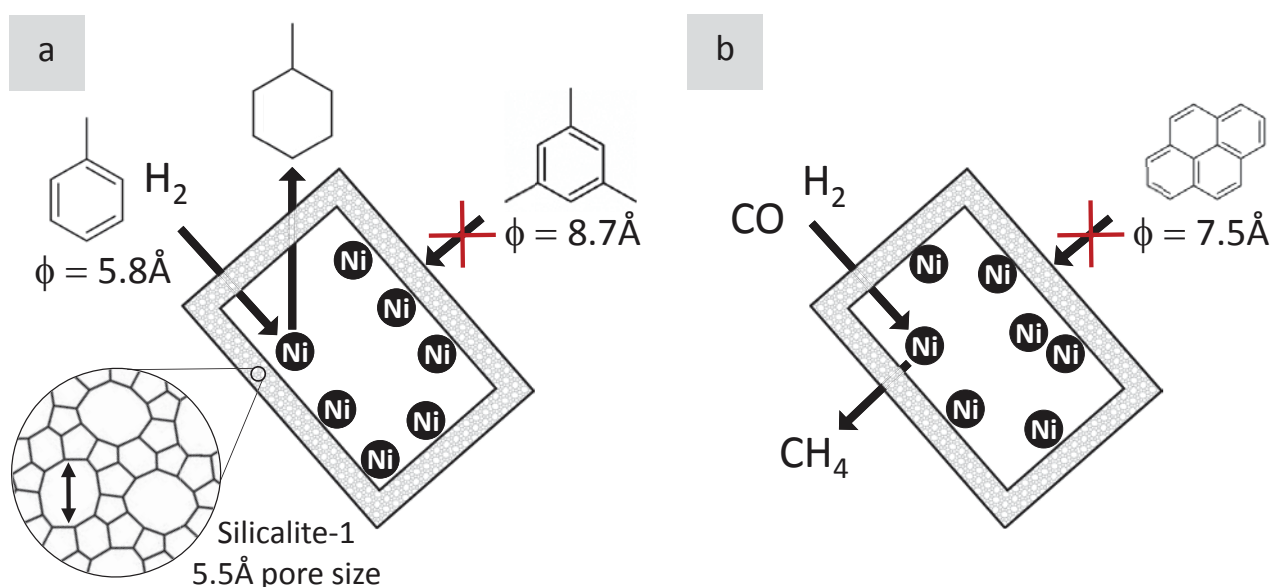
over supported nickel, *Ind. Eng. Chem. Res.* 38 (1999) 1295–1305.

- [201] M. Keane, P. Patterson, Compensation behaviour in the hydrogenation of benzene, toluene and o-xylene over Ni/SiO₂. Determination of true activation energies, *J. Chem. Soc. Faraday Trans.* 92 (1996) 1413–1421.
- [202] A. Majewski, J. Wood, Tri-reforming of methane over Ni@SiO₂ catalyst, *Int. J. Hydrogen Energy.* 39 (2014) 12578–12585.
- [203] C. Zhang, H. Yue, Z. Huang, S. Li, G. Wu, X. Ma, J. Gong, Hydrogen production via steam reforming of ethanol on phyllosilicate-derived Ni/SiO₂: Enhanced metal-support interaction and catalytic stability, *ACS Sustain. Chem. Eng.* 1 (2012) 161–173.
- [204] A. Tuel, Y. Ben Taarit, Synthesis and characterization of titanium silicalite TS-1 prepared using phosphonium ions, *Zeolites.* 14 (1994) 272–281.
- [205] X. Zhang, D. Liu, D. Xu, S. Asahina, K.A. Cychosz, K.V. Agrawal, Y. Al Wahedi, A. Bhan, S. Al Hashimi, O. Terasaki, M. Thommes, M. Tsapatsis, Synthesis of self-pillared zeolite nanosheets by repetitive branching, *Science.* 336 (2012) 1684–1687.
- [206] J. Groen, L. Peffer, J. Perez-Ramirez, Pore size determination in modified micro- and mesoporous materials: Pitfalls and limitations in gas adsorption data analysis, *Microporous Mesoporous Mater.* 60 (2003) 1–17.
- [207] M. Ogura, M. Matsukata, *Mesoporous Zeolites: Preparation, Characterization and Applications*, 2015.
- [208] P. Llewellyn, J. Coulomb, Y. Grillet, J. Patarin, H. Lauter, H. Reichert, J. Rouquerol, Adsorption by MFI-type zeolites examined by isothermal microcalorimetry and neutron diffraction: argon, krypton and methane, *Langmuir.* 9 (1993) 1846–1851.
- [209] K. Sing, D. Everett, R. Haul, L. Moscou, R. Pierotti, J. Rouquerol, T. Siemieniowska, Reporting physisorption data for gas/solid systems with special reference to the determination of surface area and porosity, *Pure Appl. Chem.* 57 (1985) 603–619.
- [210] B. Coasas, Multiscale adsorption and transport in hierarchical porous materials, *New J. Chem.* 40 (2016) 4078–4094.
- [211] S. Li, A. Tuel, D. Laprune, F. Meunier, D. Farrusseng, Transition-metal nanoparticles in hollow zeolite single crystals as bifunctional and size-selective hydrogenation catalysts, *Chem. Mater.* 27 (2015) 276–282.
- [212] G. Marraa, G. Tozzolab, G. Leofantib, M. Padovanb, G. Petrini, F. Genonib, B. Venturellib, Orthorhombic and monoclinic silicalites: structure, morphology, vibrational properties and crystal defects, *Stud. Surf. Sci. Catal.* 84 (1994) 559–566.
- [213] A. Zecchina, S. Bordiga, G. Spoto, L. Marchese, G. Petrini, G. Leofanti, M. Padovan, Silicalite characterization. 1. Structure, adsorptive capacity, and IR spectroscopy of the framework and hydroxyl modes, *J. Phys. Chem.* 96 (1992) 4985–4990.
- [214] A. Zecchina, S. Bordiga, G. Spoto, L. Marchese, G. Petrini, G. Leofanti, M. Padovan, Silicalite characterization. 2. IR spectroscopy of the interaction of carbon monoxide with internal and external hydroxyl groups, *J. Phys. Chem.* 96 (1992) 4991–4997.
- [215] C.H. Cheng, T.H. Bae, B. McCool, R. Chance, S. Nair, C. Jones, Functionalization of the internal surface of pure-silica MFI zeolite with aliphatic alcohols, *J. Phys. Chem. C.* 112 (2008) 3543–3551.
- [216] E. Mallon, M.Y. Jeon, M. Navarro, A. Bhan, M. Tsapatsis, Probing the relationship between silicalite-1 defects and polyol adsorption properties, *Langmuir.* 29 (2013) 6546–6555.
- [217] S. Oyama, X. Wang, Y. Lee, K. Bando, F. Requejo, Effect of phosphorus content in nickel phosphide catalysts studied by XAFS and other techniques, *J. Catal.* 210 (2002) 207–217.
- [218] H. Zhou, J. Mouzon, A. Farzaneh, O. Antzutkin, M. Grahn, J. Hedlund, Colloidal defect-free silicalite-1 single crystals: preparation, structure characterization, adsorption, and separation properties for alcohol/water mixtures, *Langmuir.* 31 (2015) 8488–8494.
- [219] T. Sonoda, T. Maruo, Y. Yamasaki, N. Tsunoji, Y. Takamitsu, M. Sadakane, T. Sano, Synthesis of high-silica AEI zeolites with enhanced thermal stability by hydrothermal conversion of FAU zeolites, and their activity in the selective catalytic reduction of NO_x with NH₃, *J. Mater. Chem. A.* 3 (2015) 857–865.
- [220] M. Thommes, K. Kaneko, A. Neimark, J. Olivier, F. Rodriguez-Reinoso, J. Rouquerol, K. Sing, Physisorption of gases, with special reference to the evaluation of surface area and pore size distribution, *Pure Appl. Chem.* 87 (2015) 1051–1069.
- [221] D. Fodor, A. Beloqui Redondo, F. Krumeich, J. Van Bokhoven, Role of defects in pore formation in MFI zeolites, *J. Phys. Chem. C.* 119 (2015) 5447–5453.
- [222] T. Takahashi, K. Yamashita, T. Kai, I. Fujiyoshi, Hydrogenation of benzene, mono-, di- and trimethylbenzenes over nickel catalysts supported on porous glass, *Can. J. Chem. Eng.* 64 (1986) 3–8.
- [223] F. Abild-Pedersen, O. Lytken, J. Engbæk, G. Nielsen, I. Chorkendorff, J. Norskov, Methane activation on Ni(111): Effects of poisons and step defects, *Surf. Sci.* 590 (2005) 127–137.
- [224] G. Kokotailo, P. Chu, S. Lawton, W. Meier, Synthesis and structure of synthetic zeolite ZSM-11, *Nature.* 275 (1978) 119–120.

- [225] K. Sato, K. Fujimoto, Development of new Nickel based catalyst for tar reforming with superior resistance to sulfur poisoning and coking in biomass gasification, *Catal. Commun.* 8 (2007) 1697–1701.
- [226] A. Di Carlo, D. Borello, M. Sisinni, E. Savuto, P. Venturini, E. Bocci, K. Kuramoto, Reforming of tar contained in a raw fuel gas from biomass gasification using Nickel-mayenite catalyst, *Int. J. Hydrogen Energy.* 40 (2015) 9088–9095.
- [227] V.L. Dagle, R. Dagle, L. Kovarik, A. Genc, Y.G. Wang, M. Bowden, H. Wan, M. Flake, V.A. Glezakou, D. King, R. Rousseau, Steam reforming of hydrocarbons from biomass-derived syngas over MgAl₂O₄-supported transition metals and bimetallic IrNi catalysts, *Appl. Catal. B Environ.* 184 (2016) 142–152.
- [228] R. Millini, F. Frigerio, G. Bellussi, G. Pazzuconi, C. Perego, P. Pollesel, U. Romano, A priori selection of shape-selective zeolite catalysts for the synthesis of 2,6-dimethylnaphthalene, *J. Catal.* 217 (2003) 298–309.
- [229] S. Zhdanov, N. Feoktistova, N. Kozlova, M. Piryutko, Silicalites and their thermal stability, *Bull. Acad. Sci. USSR, Div. Chem. Sci.* 34 (1986) 2467–2472.
- [230] D. Bhange, V. Ramaswamy, Negative thermal expansion in silicalite-1 and zirconium silicalite-1 having MFI structure, *Mater. Res. Bull.* 41 (2006) 1392–1402.
- [231] H. Swaan, V. Kroll, G. Martin, C. Mirodatos, Deactivation of supported nickel catalysts during the reforming of methane by carbon dioxide, *Catal. Today.* 21 (1994) 571–578.
- [232] M. Bradford, A. Vannice, Catalytic reforming of methane with carbon dioxide over nickel catalysts I. Catalyst characterization and activity, *Appl. Catal. A Gen.* 142 (1996) 73–96.
- [233] A. Myers, G. Schoofs, J. Benziger, Comparison of benzene adsorption on Ni (111) and Ni(100), *J. Phys. Chem.* 91 (1987) 2230–2232.
- [234] D. Trimm, Catalysts for the control of coking during steam reforming, *Catal. Today.* 49 (1999) 3–10.
- [235] J. Jae, G. Tompsett, A. Foster, K. Hammond, S. Auerbach, R. Lobo, G. Huber, Investigation into the shape selectivity of zeolite catalysts for biomass conversion, *J. Catal.* 279 (2011) 257–268.
- [236] Q. Trinh, A. Nguyen, D. Huynh, T. Pham, S. Mushrif, Mechanistic insights into the catalytic elimination of tar and the promotional effect of boron on it: first-principles study using toluene as a model compound, *Catal. Sci. Technol.* 6 (2016) 5871–5883.
- [237] D. Reid, D. Fields, Use of boron containing compounds and dihydroxybenzenes to reduce coking in coker furnaces, 1991.
- [238] M. Perdereau, J. Oudar, Structure, mecanisme de formation et stabilite de la couche d'adsorption du soufre sur le nickel, *Surf. Sci.* 20 (1970) 80–98.
- [239] J. Rostrup-Nielsen, Sulfur-passivated nickel catalysts for carbon-free steam reforming of methane, *J. Catal.* 85 (1984) 31–43.
- [240] J. Koningen, K. Sjoström, Sulfur-deactivated steam reforming of gasified biomass, *Ind. Eng. Chem. Res.* 37 (1998) 341. <http://pubs.acs.org/doi/abs/10.1021/ie970452t>.
- [241] I. Alstrup, J. Rostrup-Nielsen, S. Roen, High temperature hydrogen sulfide chemisorption on nickel catalysts, *Appl. Catal.* 1 (1981) 303–314.
- [242] R. Hegde, J. White, Chemisorption and decomposition of H₂S on Rh (100), *J. Phys. Chem.* 90 (1986) 296–300. <http://www.scopus.com/inward/record.url?eid=2-s2.0-0345026643&partnerID=40&md5=8a20ad8b839e22a580be0a5969e578e7>.
- [243] K. Chao, M. Cheng, Y. Ho, P. Liu, Preparation and characterization of highly dispersed gold nanoparticles within channels of mesoporous silica, *Catal. Today.* 97 (2004) 49–53.
- [244] J. Hepola, J. McCarty, G. Krishnan, V. Wong, Elucidation of behavior of sulfur on nickel-based hot gas cleaning catalysts, *Appl. Catal. B Environ.* 20 (1999) 191–203.

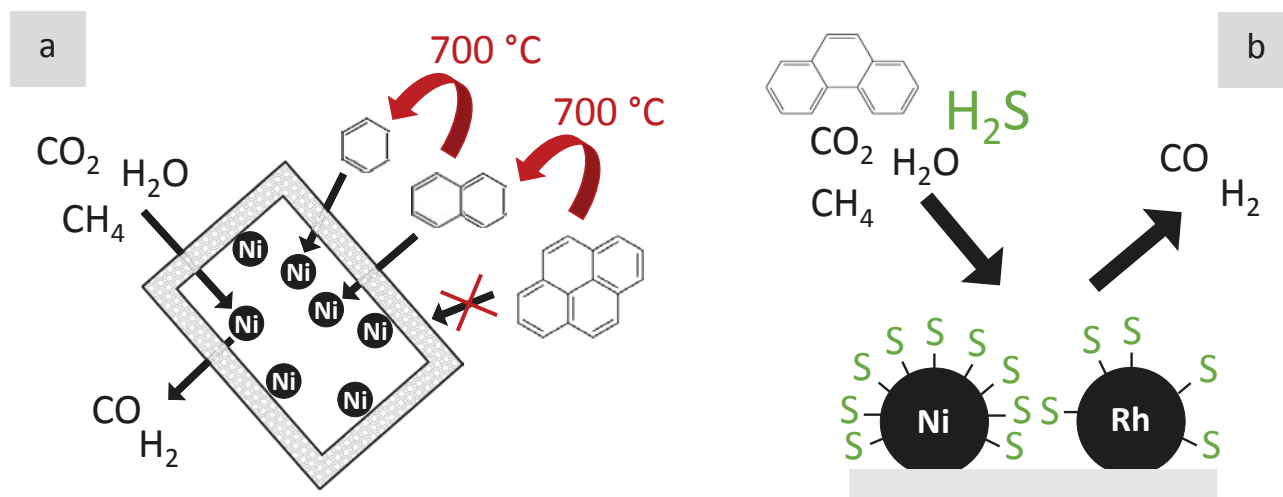
Conclusions

We have developed an original and scalable synthesis pathway that enables the preparation of nickel nanoparticles encapsulated in single hollow single crystals of MFI-type zeolites (silicalite-1, pore size \approx 0.55 nm) with a wall thickness of approximately 20 nm. It is a one-pot synthesis method in which Ni-impregnated crystals are treated by TPAOH solutions to form simultaneously a single cavity at the center of the crystal and encapsulated Ni phyllosilicates fibers by a dissolution-recrystallization process. Ni nanoparticles are obtained only after reduction at high temperature of the Ni silicate species. Each hollow shell obtained contains several Ni particles strongly bonded to the inner zeolite wall, the particle size distribution of which is narrow and centered on ca. 4 nm. The maximum incorporation level of Ni species inside the silicalite-1 is exceeded in the preparation of a 5wt.%Ni@Sil-1 material and results in the presence of Ni phyllosilicates on the external surfaces of the nanoboxes upon the TPAOH treatment. The use of citric acid under specific conditions can selectively leach out most of these external Ni species with no apparent impact on the structural properties of the zeolite membranes. The molecular-sieving property of hollow silicalite-1 samples was demonstrated using arene hydrogenation reactions with a cut-off of ca. 0.7 nm, the transport of mesitylene (kinetic diameter: 0.87 nm) through the silicalite-1 pores being totally blocked while that of toluene (kinetic diameter: 0.58 nm) is unrestricted. The leached sample exhibits a significantly improved selectivity in the arene hydrogenation when compared to the non-treated sample. The single crystal zeolite shell act also as a permselective membrane that prevents the encapsulated metal nanoparticles from pyrene (kinetic diameter = 0.74 nm) poisoning in the hydrogenation of CO at 300 °C. However, sintering of the particles encapsulated in each nanobox occurs under reforming atmosphere at 700-900 °C, leading to unstable reforming activities using the leached sample. A poor thermal stability was also observed when operating at high (800-900 °C) reforming temperatures.



Schemes of the size-selectivity property of the Ni@Silicalite-1 catalyst in the low-temperature (a) hydrogenation of arene and (b) methanation of arene.

To alleviate the intra crystal particle sintering, multi hollow silicalite-1 single crystals were prepared for the first time by an original synthesis pathway using TBPOH as a mild desilicating agent. This new generation of hierarchical zeolite allows the encapsulation of Ni nanoparticles featuring an enhanced confinement of the metallic guest and a thin wall thickness. The multi hollow catalyst exhibited a better stability for methane reforming at 700 °C than a single hollow counterpart, the Ni average particle size being kept lower than 4 nm after 20 h on stream. However, a detailed analysis of kinetic data of the structure-insensitive CO methanation used as a model reaction reveals that the sample activity is adversely affected by two main factors deriving from the preparation steps. First, a siliceous over-layer derived from the decomposition of intermediate Ni phyllosilicates, which partly covers the resulting Ni nanoparticles. Second, phosphorus species from the template remain in the samples, probably forming a Ni-P compound upon reduction. The overall catalytic reforming activities is therefore a complex interplay of improved dispersion and poisonous effects. The gradual removal of these phosphorous poisoning species probably explains the apparent constant methane steam reforming activity with time on stream, by compensating almost exactly the limited sintering occurring simultaneously. However, these results indicate that the presence of multi hollow crystals is effective in keeping highly dispersed Ni nanoparticles. Attempts to prepare similar materials using phosphorus-free molecules were successful and should greatly improve the properties of such catalysts under the harsh conditions of steam-rich reforming reactions.



Schemes of (a) the tar-poisoning mechanism using Ni@Silicalite-1 catalyst in the reforming of methane and (b) the higher activity/S-resistance of Rh in the reforming of a simulated producer gas.

The reforming of methane was then studied over Rh and Ni-based catalysts exposed to naphthalene, which was used as a representative of polyaromatic tars found in biomass-derived producer gas. According to their highly efficient size-selective property in low temperature applications, promising 5wt.%Ni@Sil-1 and CitAc Ni@Sil-1 catalysts were tested. A strong decrease of methane conversion was observed at 700, 800 and 900 °C in the presence of 1400 ppmv of naphthalene, stressing the marked

deleterious effect of this molecule in the present conditions. The effect of naphthalene was partly reversible, especially at higher temperatures. The Rh-based catalyst showed a higher activity in the reforming of hydrocarbons and a higher resistance to coke formation than the Ni-based formulations. The silicalite-1 membrane could not prevent the deactivation of embedded nickel particles, probably because naphthalene (kinetic diameter = 0.62 nm) could diffuse throughout the MFI-type porous layer at the high reaction temperatures used. The effect of 5 ppm of the bulkier pyrene was investigated at 700 °C and also led to a rapid deactivation of the Ni@silicalite-1, because pyrene was cracked into naphthalene, which could then enter the silicalite-1 nanoboxes. The poisoning effect of toluene on the Ni-based catalysts was minor in comparison to that induced by the polyaromatics. A marked sintering of the embedded Ni was also observed. It was also concluded that the citric acid treatment led to structural modifications of the nanoboxes, making those unstable at high temperatures and a poison-like source of siliceous coating. These conclusions emphasize the difficulty in obtaining size-selective systems for high temperature applications, since reactant cracking is common and a range of smaller molecules are generated *in situ*.

A series of Rh and Ni-based catalysts developed in the frame of the FASTCARD project were then tested in the reforming of methane and phenanthrene using a feed composition similar in terms of main components to that of the producer gas released from wood gasification. Regarding the inefficiency of the zeolite membrane to prevent tar poisoning under reforming conditions, it was decided to focus on more conventional supported catalysts. The objective was to identify formulations that would enable reforming methane and tars without the need to purify the producer gas released by the gasifier. The most promising formulation would then be selected for production scale-up and subsequent duration tests at the pilot level using ECN Milena gasifier to generate more realistic conditions. At 900 °C, 200 ppmv of H₂S induced a significantly higher activity loss for methane reforming than that induced by 200 ppmv of phenanthrene. The rate of methane consumption in the presence of both poisons varied linearly with the initial Rh metal surface area. The slight deviation observed at higher Rh loading was in part due to heat and mass transport limitations. The rate of methane consumption per unit of metal surface area was about 5-fold higher on Rh than that on Ni. The surface atomic ratio S/Rh estimated after reaction was close to 0.5, similar to those reported for S-saturated Ni-based samples, suggesting near-to-full monolayer coverage by S under our operating conditions. No information could be derived from the measure of apparent activation energies, due to changes in adsorption coverages of reactants and poisons with temperature. The use of lower temperatures led to incomplete conversion of polycyclic aromatic hydrocarbons, which are well-known coke precursors. These results emphasize the necessity of operating the reforming unit at high temperatures in presence of a low concentrated metal density to avoid a local temperature decrease due to the strong endothermicity of the reforming reactions and heat transport limitations.

Perspectives

The synthesis routes presented in this work seems to be a very elegant way to isolate nanoparticles inside microporous shells. This series of well controlled nanosized nickel particles encapsulated in microporous hollow silicalite-1 opens new perspectives in catalysis since they can be applied as shape and/or size selective catalysts in a wide range of catalytic systems. For practical applications, the number of nanoparticles per volume unit should be increased to avoid oversizing the catalytic unit. We showed that an alternative desilicating treatment using TPAOH lead to multi hollow crystals, which could be loaded by dozens of metal nanoparticles, exhibiting a higher metal density and an improved spatial restriction of the metallic guest. Attempts to prepare similar materials using phosphorus-free molecules were successful and should greatly enhance the properties of such catalysts under the harsh conditions of steam reforming reactions. Improved post-impregnation methods may also be an alternative solution to incorporate nanoparticles in highly porous materials in order to optimize the catalyst volume and increase the metal loading in the zeolite. Additionally, this method would prevent the formation of Ni phyllosilicate species and provide encapsulated particles in which all nickel surface sites are accessible. Further work will also be required in which the experimental conditions of the citric acid treatment or the nature of the complexing agent is varied with a view at determining improved methods for selectively removing external Ni nanoparticles and preserving the high thermal stability of the parent Ni@Silicalite-1 sample. An aspect that should be further investigated is the discrepancies in our conclusions drawn from the measurement of the turn-over frequencies in arene hydrogenation and CO methanation using Ni@Silicalite-1 materials. TOFs measured in the hydrogenation of toluene are in line with those reported in the literature while the low intrinsic activity in methanation suggests that nickel surface sites are only partly accessible.

Unfortunately, applications are limited at high temperatures by the pore size of the zeolite since tar cracking occurs and generated smaller molecules can poison the nanoparticles. In the case of silicalite-1, the pore diameter is relatively large, typically 0.55 nm and does not prevent naphthalene to diffuse throughout the MFI-type porous layer. Therefore, an effort has to be made to prepare similar materials but using zeolites with smaller pores. For example, particles in hollow chabazite zeolites with high Si/Al ratio would be of particular interest but their preparation might be more difficult. Indeed, the creation of hollow structures requires inhomogeneous crystals in terms of density defects, which cannot always be obtained by direct synthesis. To a lesser extent, it would also be interesting to see if the slightly smaller pore size of the silicalite-2 zeolite could prevent naphthalene poisoning at 700 °C.

Biomass is perceived to be a major energy source in the future. The objectives of this Ph.D. work were associated with those of the European project FASTCARD and were to develop advanced catalysts that would enable reforming CH_4 and tars without the need to purify the producer gas. Regarding the choice of catalyst formulation, nickel is usually preferred for industrial steam reforming process because of its low price compared to noble metals. However, we have seen that the deactivation of Ni-based catalysts in terms of coking and sulfur poisoning are critical parameters. High reforming temperatures, high metal surface areas and low metal concentration must be reached for sufficient hydrocarbon conversions. This should be taken into account during the design of the process and more especially for the choice of high-temperature resistant materials. Rhodium is more expensive but much more active, more resistant to poisons and would enable a more efficient reforming of producer gas. This would be beneficial to the process design and operation at higher scale. Improvements of the catalytic bed configuration and material development could be achieved if the strong temperature gradients could be evaluated thoroughly.

The dual bed configuration, composed by a pre-reforming catalyst and a metal-based reforming catalyst, appears to be a good alternative according to preliminary tests performed by FASTCARD partners. The cheap pre-catalyst is aimed to reform the tars and to preserve the stability of the downstream reforming catalyst. Following the screening depicted in chapter 6, the 3-Rh sample was selected within WP1 for its high potential in terms of reforming efficiency and catalyst scale-up. Durations tests are planned at IRCELYON using the dual bed configuration with 1.5 mm diameter alumina beads coated with 3-Rh prepared by Johnson Matthey as reforming catalyst. The pre-catalyst consists of 3 mm diameter “ice-templated” mesoporous beads prepared by Saint-Gobain. A Ni-impregnated version of this pre-catalyst will also be tested. The aim of this campaign will be to study the impact of the presence and of the nature of the pre-reforming catalyst on the overall reforming performances. The most promising configuration should then be tested at the pilot-scale at ECN in the Netherlands under realistic conditions using the MILENA gasifier to generate the producer gas.

Publications

[1] Transition-metal nanoparticles in hollow zeolite single crystals as bifunctional and size-selective hydrogenation catalysts

S.Li, A. Tuel, D. Laprune, F. Meunier, D. Farrusseng

Chemistry of Materials, 2015, 27, 276-282

<https://doi.org/10.1021/cm503921f>

[2] Effect of polyaromatic tars on the activity for methane steam reforming of nickel particles embedded in silicalite-1

D. Laprune, C. Theodoridj, A. Tuel, D. Farrusseng, F. Meunier

Applied Catalysis B: Environmental, 2017, 204, 515-524

<http://dx.doi.org/10.1016/j.apcatb.2016.12.004>

[3] Selective removal of external Ni nanoparticles on Ni@silicalite-1 single crystal nanoboxes: Application to size-selective arene hydrogenation

D. Laprune, A. Tuel, D. Farrusseng, F. Meunier

Applied Catalysis A: General, 2017, 535, 69-76.

<http://dx.doi.org/10.1016/j.apcata.2017.02.011>

[4] Highly Dispersed nickel particles encapsulated in multi-hollow silicalite-1 single crystal nanoboxes: effects of siliceous deposits and phosphorous species on the catalytic performances

D. Laprune, A.Tuel, D. Farrusseng, F. Meunier

ChemCatChem, 2017, 9, 2297-2307

<https://doi.org/10.1002/cctc.201700233>

[5] Effects of H₂S and phenanthrene on the activity of Ni and Rh-based catalysts for the reforming of a simulated biomass-derived producer gas

D. Laprune, D. Farrusseng, Y. Schuurman, F. Meunier, J. Pieterse, A. Steele, S. Thorpe

In preparation

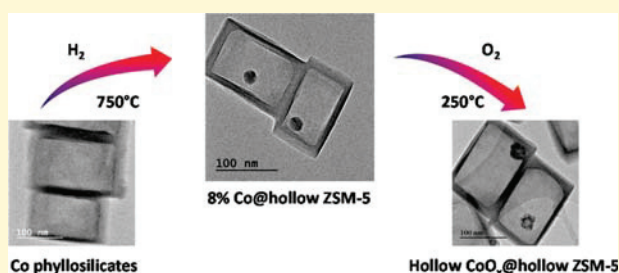
Transition-Metal Nanoparticles in Hollow Zeolite Single Crystals as Bifunctional and Size-Selective Hydrogenation Catalysts

Shiwen Li, Alain Tuel,* David Laprune, Frédéric Meunier, and David Farrusseng

Institut de Recherches sur la Catalyse et l'Environnement de Lyon, IRCELYON, UMR 5256 CNRS-Université de Lyon 1, 2 Avenue Albert Einstein, 69626 Villeurbanne Cedex, France

S Supporting Information

ABSTRACT: Transition-metal nanoparticles (Co, Ni, and Cu) encapsulated in hollow zeolite single crystals were prepared by recrystallization of impregnated bulk MFI crystals in the presence of tetrapropylammonium (TPAOH) solutions. The size and number of particles in hollow MFI depended mainly on the aluminum content. The encapsulation of the nanoparticles prevented them from growing, thus enabling the control of particle size even after high temperature treatments. For low metal loadings (<3 wt %), the mean particle sizes for Co, Ni, and Cu in hollow silicalite-1 were 3.5 ± 0.3 , 3.1 ± 0.5 , and 1.5 ± 0.2 nm, respectively. In the case of hollow ZSM-5, higher loadings (~8 wt %) could be obtained with mean particle sizes of 17 ± 2 nm, 13 ± 2 nm, and 15 ± 2 nm for Co, Ni, and Cu systems. The mechanism of transition metal nanoparticle formation was markedly different from that of noble metals. At high pH values, transition-metal cations first reacted with dissolved silica species yielding fibrous metal phyllosilicates that were located inside the crystal cavities. The metal phyllosilicates were then converted into nanoparticles upon reduction under H_2 at high temperature (500–750 °C). Silicalite-1 encapsulated Ni particles were used in the catalytic hydrogenation of substituted benzenes and showed an outstanding size-selectivity effect. Ni particles were accessible to toluene but not to mesitylene, confirming that the activity is directly related to the diffusion properties of molecules through the zeolite membrane.



INTRODUCTION

Bifunctional heterogeneous catalysts that combine acid and hydrogenation/dehydrogenation functions form an important class of materials in the chemical industry, especially for fluid catalytic cracking (FCC) and hydro-isomerization processes.^{1,2} A simple mechanical mixture of components does not necessarily ensure appropriate proximity between the acid and hydrogenating sites. Catalyst design at the nanoscale level with a hierarchical porosity is essential for obtaining the best operating performances.^{3–5} As an example on Fischer–Tropsch synthesis, the introduction of mesoporosity in Co/ZSM-5 increases the activity and selectivity to the gasoline fraction (C5–C11) leading to an enhanced octane number due to the isomerization reactions.^{6–8} When the metal particles are embedded into porous matrices, such as core–shell structures, the reactants must diffuse first through the porous layer before reaching the metal center, leading to high selectivity by molecular sieving mechanisms.^{9–14} In core–shell systems, the zeolite shell can also determine the product selectivity by favoring the diffusion of less bulky molecules.^{15–17} Yet, an excessive thickness of the zeolite shell may lead to undesirable mass transport limitations affecting the productivity of the desired reaction products.¹⁶

A yolk–shell structure is an alternative catalyst design that consists of metal particles encapsulated inside a hollow shell. The shell is usually made of a very thin layer of porous material

that should limit mass transport limitation. Particles are generally monodispersed in size, isolated from each other, and prevented from sintering by Ostwald ripening mechanisms by the porous shell. Examples of such catalyst designs include metal or oxide particles encapsulated in mesoporous spheres made of carbon, SiO_2 , and ZrO_2 .^{18–24}

We have pioneered the synthesis of yolk–shell materials for which the shell is a zeolite single crystal conferring unique catalytic properties. It consists of single noble metal nanoparticles encapsulated in hollow silicalite-1 single crystals (Au@silicalite-1 and Pt@silicalite-1; Figure S1, Supporting Information).^{25,26} Some of us have already reported the preparation of hollow silicalite-1 by dissolution/recrystallization of bulk crystals with tetrapropylammonium (TPAOH) solutions.^{27–29} The noble metal yolk–shell materials are prepared in a similar manner by treating metal impregnated zeolites in TPAOH solutions.

In this article, we have extended the synthesis of such nanodesigned catalysts to the case of transition metals (Co, Ni, and Cu), which significantly differs from that of noble metal systems. To the best of our knowledge, this is the first report on the encapsulation of transition metal nanoparticles in hollow

Received: October 24, 2014

Revised: December 1, 2014

Published: December 11, 2014

silicalite-1 single crystals. In addition, we report, also for the first time, bifunctional yolk–shell materials displaying outstanding metal nanoparticle dispersion inside ZSM-5 hollow crystals.

EXPERIMENTAL SECTION

Zeolite Synthesis. Silicalite-1 was prepared using tetraethyl orthosilicate (TEOS, Aldrich, 98%) and homemade 1 M TPAOH solutions obtained by reaction of the bromide solution with Ag_2O and water. The gel, with the composition $\text{SiO}_2 \cdot 0.4\text{TPAOH} \cdot 35\text{H}_2\text{O}$ was heated at 170 °C under static conditions for 3 days. The resulting solid was calcined for 12 h at 525 °C in air yielding silicalite-1 crystals of approximately 200 nm \times 150 nm \times 140 nm in size.

ZSM-5 was synthesized following a published recipe.³⁰ The gel containing tetraethyl orthosilicate (TEOS, Aldrich, 98%), 1 M TPAOH solutions, and NaAlO_2 (Strem Chemicals, 99.9%) with composition $140\text{SiO}_2 \cdot \text{Al}_2\text{O}_3 \cdot 30\text{TPAOH} \cdot 1240\text{H}_2\text{O}$ was stirred at room temperature for 7 h, transferred into a Teflon-lined autoclave, and heated under static conditions at 180 °C for 7 days. After crystallization, the autoclaves were cooled, and the solids were recovered by centrifugation, washed with water, and dried overnight at 110 °C. The resulting ZSM-5 was then washed with a 5 M HCl solution at 90 °C for 5 h for the removal of the nonreacted aluminum species, and then centrifuged, washed until pH 7 was achieved, and finally dried at 110 °C in air. The resulting solid was calcined for 12 h at 525 °C in air yielding ZSM-5 microporous crystals that were characterized by an Al gradient (discussed below). Chemical analysis of the calcined zeolite gave a molar ratio Si/Al = 100.

Impregnation Methods. Zeolites were impregnated with aqueous solutions of cobalt, nickel, and copper nitrates ($\text{Co}(\text{NO}_3)_2 \cdot 6\text{H}_2\text{O}$, $\text{Ni}(\text{NO}_3)_2 \cdot 6\text{H}_2\text{O}$, and $\text{Cu}(\text{NO}_3)_2 \cdot 3\text{H}_2\text{O}$), which were all purchased from Sigma-Aldrich. The metal loading was achieved by the impregnation of the starting zeolites (silicalite-1 and ZSM-5) by aqueous solutions of metal precursors (2 mL of aqueous solution/g zeolite). The mixture was then stirred at 50 °C until the complete evaporation of water. A series of samples with different metal loadings was obtained by using metal nitrate solutions of various concentrations, typically from 0.16 to 1.23 mol/L.

Formation of Hollow Structures. Hollow structures were obtained by treating the metal impregnated zeolites in TPAOH solutions at 170 °C.^{25,26} Typically, 1 g of zeolite was suspended in 4.15 mL of 1 M TPAOH solution and 3.35 mL of H_2O , and then the mixture was heated at 170 °C under static conditions for 24 h.

Thermal Treatments. All hollow zeolites were calcined in air at 450 °C for 6 h. The materials were then reduced under hydrogen at 750 °C (standard reduction temperature unless otherwise stated) for 3 h. The reduced samples are referred to as $\text{Me@Sil-1}(x)$ or $\text{Me@ZSM-5}(x)$, depending on the nature of the zeolite (Sil-1: silicalite-1) with Me = Co, Ni, or Cu and x = metal loading obtained by ICP. For selected samples, the reoxidation process was performed under static conditions in an oven at 250 °C for 2 h.

Characterization Techniques. TEM pictures were obtained on a Jeol 2010 LaB6 microscope operating at 200 kV. EDX measurements were performed using an EDX Link ISIS analyzer from Oxford Instruments.

X-ray diffraction (XRD) patterns of the zeolites were recorded on a Bruker (Siemens) D5000 diffractometer using $\text{CuK}\alpha$ radiation. Diffractograms were collected between 4 and 70° (2 θ) with steps of 0.02° and 1 s per step.

N_2 adsorption isotherms and BET surface areas were acquired on an ASAP 2010 (Micromeritics) apparatus on calcined samples preliminarily desorbed at 300 °C for 4 h. Chemical analyses were performed at the IRCELYON-CNRS Analytical Core facilities; metal contents were determined by inductively coupled plasma optical emission spectroscopy (HORIBA Jobin Yvon Activa ICP-OES).

Magnetic measurements were carried out at room temperature in an electromagnet (fields up to 21 kOe) using the Weiss extraction method. The degree of reduction of the sample was determined from the amount of metallic cobalt given by the saturation magnetization of

the samples, obtained by extrapolating to zero the plot of the magnetization against $1/H$ (H = magnetic field). Temperature-programmed reduction of Co-containing hollow zeolite was performed on a BELCAT-B catalyst analyzer. The zeolite was pretreated at 200 °C/Ar and then treated under 5% H_2 /Ar up to to 1000 °C using a rate of 10 °C/min.

NMR spectra were obtained on a Bruker DSX 400 spectrometer equipped with a double-bearing probe-head. Samples are spun at 10 kHz in 4 mm zirconia rotors. ^{27}Al NMR spectra were recorded with a pulse length of 0.6 s ($\pi/12$) and a recycle delay of 250 ms. Thermal analysis data were collected on a SETSYS Evolution-1200 apparatus from SETARAM. Approximately 20 mg of sample was heated from room temperature to 900 °C in 5% H_2 /Ar at a heating rate of 10 °C/min.

Catalytic Reactions. The toluene and mesitylene hydrogenations were carried out using a diffuse reflectance FT-IR reaction cell similar to that described in detail elsewhere.³¹ The reaction bed of the DRIFTS cell was made of a ceramic crucible. A mass of sample precisely weighing 10 mg was deposited on top of a SiC layer filling up the crucible. The system was always operated at ambient pressure, and the samples were reduced at 450 °C in pure H_2 for 90 min before the catalytic tests. Aromatic reactants were fed individually using a saturator kept at 0 °C, leading to partial pressures of 910 and 59 Pa for toluene and mesitylene, respectively. A flow of 50 mL/min of pure hydrogen was used as reactant carrier gas and fed through one saturator at a time. The reactor effluent was then analyzed using a 10 cm path-length gas cell fitted in a Thermo FT-IR spectrophotometer. The proportion of the reactant and the corresponding saturated product were determined through integration of two spectral regions corresponding to the C–H stretching vibration modes. In the case of toluene, methyl-cyclohexane was the only product observed, while trimethyl-cyclohexane was the only product obtained from mesitylene.

RESULTS AND DISCUSSION

Cobalt Encapsulated in Hollow Silicalite-1. The direct application of the synthesis procedure previously developed for noble metal nanoparticles encapsulated in silicalite-1 to transition metals did not yield the oxide nanoparticles, as was expected.^{25,26} In the following, we thoroughly describe the synthesis and characterization of a $\text{Co@Sil-1}(2.5)$ sample (Table 1), which is representative of the cases of other transition metals (summarized hereafter). As reported in our previous publications, silicalite-1 crystals are not stable at high temperature under highly alkaline pH conditions.^{27–29} Zeolite crystals are partially dissolved, preferentially in the middle, which is the region where the density of framework defects sites

Table 1. Average Metal Particle Size and Aluminum Content in the Various Samples

sample	Si/Al ratio	average particle size (nm)
$\text{Co@Sil-1}(2.5)$	n.a. ^c	3.2
$\text{Co@Sil-1}(3.1)$	n.a.	3.7
$\text{Co@Sil-1}(8.0)$	n.a.	4.3
$\text{Co@ZSM-5}(2.2)$	102	15.1
$\text{Co@ZSM-5}(7.4)$	104	18.8
$\text{Ni@Sil-1}(1.0)$	n.a.	2.7
$\text{Ni@Sil-1}(2.5)$	n.a.	3.5
$\text{Ni@ZSM-5}(2.6)$	101	11.2
$\text{Ni@ZSM-5}(7.7)$	105	14.5
$\text{Cu@Sil-1}(2.8)$	n.a.	9.8(1.5) ^a
$\text{Cu@ZSM-5}(3.0)$	102	15–100(2.5) ^b

^aValues in parentheses correspond to the average particle size for a second population of particles. ^bThe population of large particles was very inhomogeneous. ^cn.a.: not applicable.

is maximum. However, when dissolution is performed with TPAOH under appropriate conditions, dissolved species can recrystallize on the surface, leading to regular hollow crystals with well-defined cavities and walls. After the TPAOH treatment, hollow crystals did not contain particles, contrary to the case of noble metals (Figure S1, Supporting Information). The color of the sample was gray, which indicated the presence of some Co species, and TEM pictures surprisingly revealed the presence of dark long fibers covering the internal surface of the boxes (arrows in Figure 1a,b).

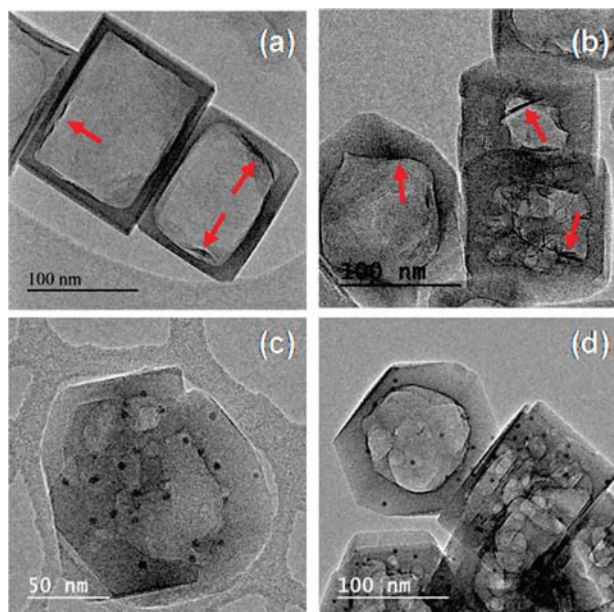


Figure 1. TEM pictures of Co@Sil-1(2.5) before (a,b) and after reduction (c,d) in hydrogen at 750 °C. Arrows in a and b indicate Co-silicate fibers.

This type of fibrous structure is often found in Co/SiO₂ catalysts and corresponds to cobalt phyllosilicates^{32–34} In order to characterize the observed fibers, EDX and high resolution TEM measurements were carried out in the higher Co loading sample (Co@Sil-1(8.0), Figure 2d). EDX analysis on the fibers (red circle in Figure 2d) indicated 26 wt % Co, 24.5 wt % Si, and 49.5 wt % O (Figure S3, Supporting Information) corresponding to the formula CoSi₂O₅·2H₂O, the Si₂O₅²⁻ stoichiometry being characteristic of phyllosilicates according to the Nickel–Strunz classification.³⁵ The cobalt phyllosilicate structure was confirmed by the interlayer distance to ca. 0.9–0.95 nm, which corresponds to the value generally observed in these structures (Figure S2, Supporting Information).³⁶ In addition, we did not observe Co in the zeolite wall by EDX analysis (blue circle in Figure 2d and Figure S3, Supporting Information), which suggests that all Co atoms were in the form of Co-silicate fibers.

As fibers were not observed in the absence of Co, we assumed that they were formed during the TPAOH treatment when partial dissolution of the zeolite occurred. The reduction of Co silicate fibers to Co nanoparticles was monitored by temperature program reduction (TPR) and thermal gravimetric analysis (TGA) under hydrogen flow (Figures S4 and S5, Supporting Information). Both techniques indicated that phyllosilicates started to be reduced at 630 °C in agreement

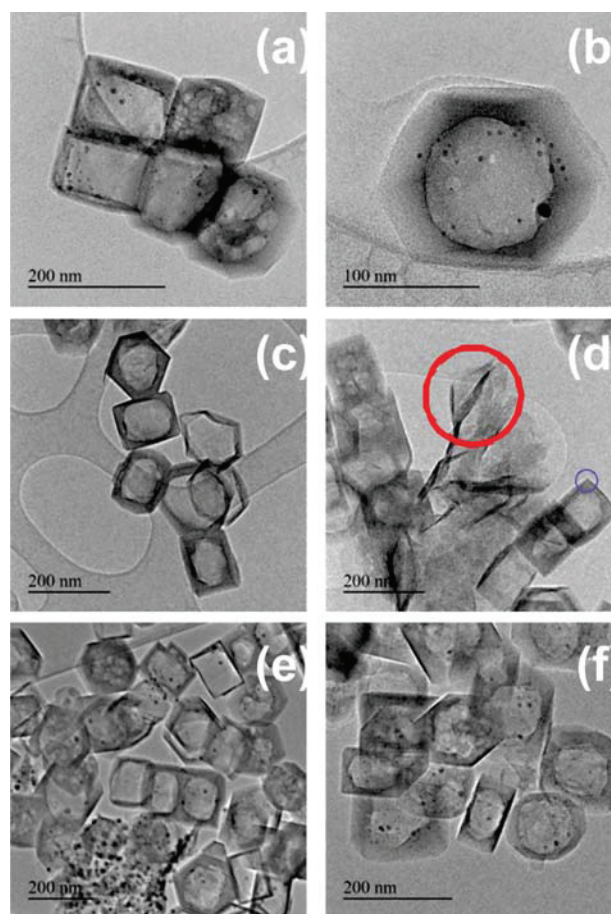


Figure 2. TEM pictures of Co@Sil-1(3.1) after reduction (a,b) and Co@Sil-1(8.0) before (c,d) and after reduction (e,f) in hydrogen at 750 °C. Red and blue circles in panel d indicate, respectively, Co phyllosilicate layers and zeolite walls on which EDX measurements have been performed (the EDX spectra of regions inside the two circles are given in Figure S3, Supporting Information).

with literature data for similar compounds.³⁷ The mass loss observed after 600 °C in the TGA curve was 0.57%, which could correspond to a reduction of approximately 82% of Co²⁺ to Co⁰ (see Figure S5, Supporting Information). The Co silicate sample was then set to 750 °C for 10 h in 10% H₂ atmosphere to ensure sample reduction before magnetic measurements. The degree of reduction of Co@Sil-1(2.5) was estimated to be 85%, in excellent agreement with TGA results.³⁷ TEM pictures of a solid reduced at only 500 °C/H₂ were very similar to those of freshly prepared compounds, thus confirming that Co silicates had not been reduced at this lower temperature (not shown). Increasing reduction temperature to 750 °C led to the formation of particles inside hollow crystals, supporting the transformation of phyllosilicates into metallic cobalt (Figure 1c,d). TEM pictures of Co@Sil-1 (2.5) also revealed the presence of minor amounts of fibrous species (not shown), in agreement with the incomplete reduction of Co²⁺ species measured by magnetic measurement. In the case of noble metal encapsulation in hollow silicalite-1 and with comparable metal loading, Au and Pt@Sil-1 materials showed a single particle inside the big unique cavity of the crystal (Figure S1, Supporting Information).^{25,26} In contrast, for Co containing hollow zeolite samples, many particles are observed in the

internal cavities (Figure 1c,d). The particle size distribution is quite narrow with a mean size of 3.2 nm (Figure 1c,d and Figure S6a, Supporting Information). Another significant difference with noble metal containing hollow silicalite-1 is that a fraction of the Co particles was occluded in the zeolite walls (Figure 1c). We can propose that these differences with respect to noble metal based systems arose from the formation of the phyllosilicates at the TPAOH treatment step. The Co phyllosilicates formed both at the center of the crystals, where the defect concentration was highest, and near the edges of the crystals. The Co particles subsequently grew from the Co phyllosilicates during the reduction process. Since Co phyllosilicates are hardly mobile as they are attached to the zeolite, the reduction process led to dispersed Co nanoparticles strongly bound to the zeolite walls. In addition, phyllosilicates located at the center of the crystal could somewhat limit the dissolution process resulting in the formation of several cavities instead of one single large cavity as observed in the case of noble metal-based materials (Figure 1d).

With a somewhat higher Co loading of 3.1 wt %, Co@Sil-1(3.1) was similar to the previous solid except that Co particles were less regular in size, with large particles (5–11 nm) coexisting with a population of smaller particles (3.7 nm) (Figure 2a,b, Figure S6b, Supporting Information, and Table 1). For a much larger Co content of 8 wt % (Co@Sil-1(8.0)), a significant proportion of Co phyllosilicates was found outside zeolite crystals (Figure 2c and d), which eventually led to external particles after reduction (Figure 2e and f and Figure S6c, Supporting Information).

The presence of many particles outside hollow crystals for samples with high Co loadings suggested that the maximum incorporation level of Co species inside the silicalite-1 had been exceeded. Increasing Co loading mainly affected the mean particle size but not the average number of particles per cavity. Indeed, we have estimated that there were between 9 to 10 particles per hollow zeolite at three different Co loadings (2.5%, 3.1%, and 8.0%). When loading increased by a factor of 1.2 from 2.5 wt % to 3.1 wt %, the particle volume increased by a factor of 1.5 (the mean particle size changed from 3.2 to 3.7 nm) (Table 1 and Figure S6a,b, Supporting Information). It should be noted that the slight difference between the two factors obviously resulted from the presence of bigger particles at higher loading, with about 13% of particle having a diameter above 5 nm. Even at higher Co loading (8%), the correlation between loading and particle volume was confirmed, despite the presence of particles outside crystals in Co@Sil-1(8.0).

Cobalt Encapsulated in Hollow ZSM-5. The synthesis of Co-containing yolk–shell materials was extended to ZSM-5 as the zeolite shell. The desilication process was different when Al^{3+} was present in the structure. For silicalite-1, the creation of hollow structures in the presence of TPAOH solution was attributed to the preferential dissolution of the core of the crystals, a region with a high density of defects compared to that of the surface layers. If aluminum is homogeneously distributed in ZSM-5 crystals, treatment with TPAOH does not form regular hollow structures, and partial dissolution occurs throughout the crystals.^{27,29} In fact, suitable ZSM-5 crystals must show a gradient of composition, exhibiting a Si-rich core and an Al-rich periphery. Hollow structures can thus be formed by the preferential dissolution of Si-rich domains of the crystals.³⁸ Desilication is generally performed using inorganic bases such as NaOH ^{39,40} or Na_2CO_3 ,^{41,42} which leads to a significant loss of matter and nonuniform hollow structures in

the crystals. We have followed the synthesis from Mei et al., which is known to provide an Al gradient in $[\text{Na}]$ ZSM-5 nanocrystals, and we have shown for the first time that very regular ZSM-5 hollow crystals could be obtained upon TPAOH hydrothermal treatment.³⁰ In contrast to inorganic bases, dissolved species recrystallized in the presence of TPAOH and the overall Si/Al ratio remained equal to the ratio of the starting ZSM-5 (Table 1). X-ray diffraction and nitrogen physisorption measurements showed that the characteristics of synthesized hollow ZSM-5 were similar to those previously reported for hollow silicalite-1 (Figure S7,8, Supporting Information). In particular, the presence of a hysteresis loop in the isotherm confirmed the presence of the inner cavity. TEM images showed that zeolites were completely recrystallized with regular cavities, with a wall thickness similar to that observed on silicalite-1 (Figure 3a). Moreover, the ^{27}Al NMR

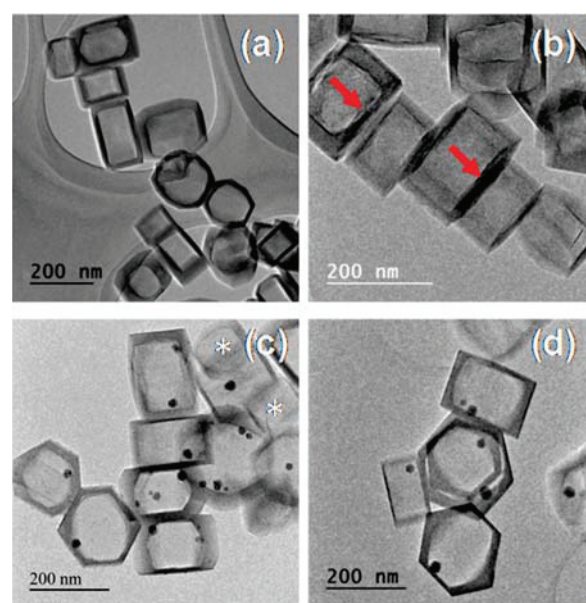


Figure 3. TEM pictures of hollow ZSM-5 (a), Co@ZSM-5(2.2) before (b) and after (c) reduction at 750 °C, and Co@ZSM-5(7.4) (d) after reduction at 750 °C. Arrows in panel b point out phyllosilicate layers on the internal surface of zeolite nanoboxes. Asterisks in panel c indicate empty nanoboxes.

spectrum confirmed that most of the Al species remained at framework positions during the formation of hollow structures, thus providing acidic sites (Figure S9, Supporting Information).

On the basis of these observations, treatments were performed on ZSM-5 impregnated with $\text{Co}(\text{NO}_3)_2$ solution. The presence of Co species did not alter the dissolution/recrystallization process as the morphology of hollow Co@ZSM-5 samples was similar to that of Co-free materials (Figure 3c,d).

After the TPAOH hydrothermal treatment, fibrous phyllosilicates were also observed. In contrast to the case of silicalite-1, phyllosilicates were scarce and generally formed a thin layer on the internal surface of the cavities (Figure 3b). After reduction under H_2 at 750 °C, Co particles were located only inside the cavity of hollow ZSM-5 crystals (Figure 3c,d), in contrast with Co@Sil-1 materials for which particles were also present in the walls. Another difference with the Co@silicalite-1 system was that the number of particles was generally limited to

2 or 3 per hollow ZSM-5 for a comparable loading of 2.2 wt %. As a result, Co particles in Co@ZSM-5 (2.2) were 15 nm large in diameter, which is approximately 5 times larger than those found in Co@Sil-1(2.5) (Table 1).

The origin of such differences is not clear. We hypothesize that the presence of Al^{3+} limited the formation of Co phyllosilicates in the zeolite matrix. Since Co particles were not entrapped inside the zeolite walls, they were free to move into the cavities during reduction and thus grew by Ostwald ripening. By contrast to Co@silicalite-1 systems, larger Co loading of 7.4 wt % in ZSM-5 (Co@ZSM-5(7.4)) did not yield particles outside the hollow crystals. More than 95% of hollow zeolites contained at least one Co particle as shown in Figure 3d. We can note that increasing the loading by a factor of 3.4 from 2.2 to 7.4 wt % led to an increase of mean particle size from 15 to 19 nm, which corresponded to a 2-fold increase in volume (Figure S10-a,b, Supporting Information). This difference can be explained by the fact that ca. 16% of hollow zeolites in Co@ZSM-5(2.2) did not contain Co particles (see Figure 3c for evidence of empty shells).

The stability and the evolution of the morphology of the particles during oxidation/reduction cycles were followed by TEM (Figure 4). After Co@ZSM-5(7.4) was calcined at 250 °C in air for 2 h, a major modification of the shape of Co particles was noted, characterized by a hollow morphology with

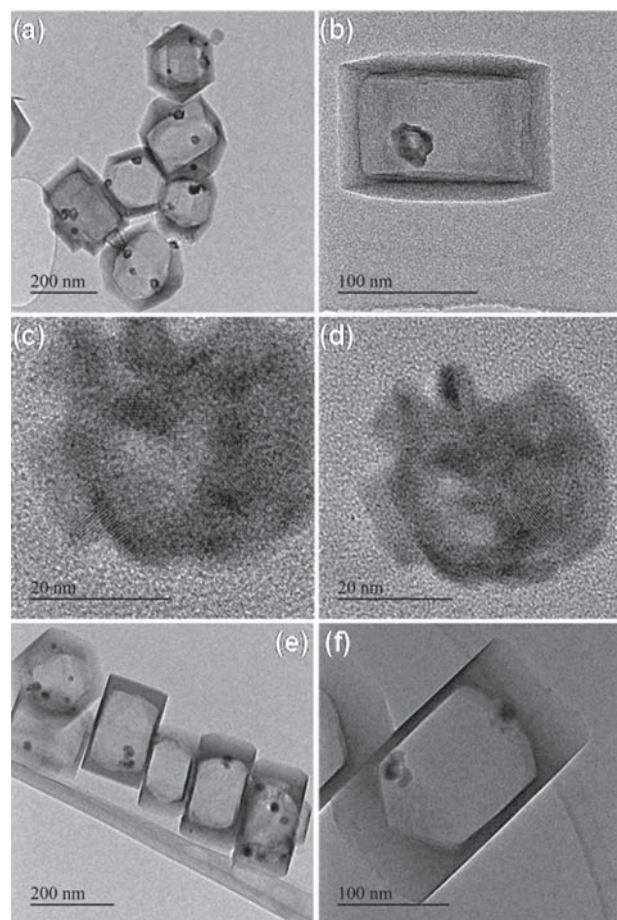


Figure 4. TEM pictures of Co@ZSM-5(7.4) after reoxidation at 250 °C (a,b) and subsequent reduction at 500 °C (e,f). Polycrystalline nature of Co-oxide hollow particles (c,d).

an irregular shape (Figure 4a,b). The formation of these structures has already been reported for many nanoparticle systems and has been attributed to a nanoscale Kirkendall effect, arising from a difference in diffusion rates between anions and cations.⁴³ TEM pictures at high magnification clearly revealed the polycrystalline nature of the cobalt oxide shells, with individual particle size of ca. 3–5 nm (Figure 4c,d). Then, the oxidized Co@ZSM-5(7.4) was reduced under H_2 leading to two populations of Co particles: large particles with a size similar to that observed on freshly reduced solids and very small ones (Figure 4e,f), which were formed by fragmentation and redispersion as already reported in many studies.⁴⁴

Nickel and Copper Encapsulated in Hollow Zeolites.

Nickel- and copper-containing hollow zeolites were prepared following the same procedure (Table 1). For both metals, the mechanisms of formation were similar to that described above for cobalt. Ni and Cu phyllosilicates were formed during the dissolution/recrystallization step in the presence of TPAOH and were then converted to metal nanoparticles upon reduction at high temperature, yielding yolk–shell type materials. The main differences were the size and shape of the particle, as can be expected from the intrinsic properties of metals. In the case of Ni@Sil-1, the mean size of Ni particles varied proportionally to the Ni content as in the case of Co@Sil-1 (Figure S6d,e, Supporting Information, and Table 1). For example, when the loading increased from 1 to 2.5 wt %, the mean particle volume increased by a factor of 2.4.

Nickel particles were much larger in hollow ZSM-5 than in silicalite-1 for a similar Ni content, which is consistent with previously observed trends for Co-based systems (Table 1 and Figure S10c, Supporting Information). The mean particle size for Ni-ZSM-5 (2.6) was 11.2 nm against 3.5 nm for Ni-Sil-1 (2.5). In sample Ni-ZSM-5 (7.7) with a higher Ni loading, much larger particles were formed with well-defined crystallographic shapes, likely due to ripening processes (Figure S11, Supporting Information).

Though similar to Co and Ni-containing zeolites, copper-containing silicalite-1 materials were somewhat different in terms of particle size distribution. Indeed, most of the hollow silicalite-1 crystals contained a bimodal population of Cu particles, as one or two large particles coexisted with very small particles inside the same cavity (Table 1 and Figures S6f and S12, Supporting Information). Increasing the reduction temperature from 500 to 750 °C led to larger particles being formed by aggregation of the small ones (data not shown). However, even at 750 °C, the aggregation mechanism was not complete, and many nanoparticles of 1–2 nm were still present. As for the case of silicalite-1, ZSM-5 crystals containing Cu particles clearly exhibited two distinct populations in the same box: one big aggregate with a size up to 40 nm surrounded by many nanoparticles of ca. 1–2 nm (Figure S13, Supporting Information). In contrast to the case of Cu@Sil-1, only half of the hollow zeolite crystals contained a large particle despite reduction at 750 °C under H_2 . However, these crystals were not Cu-free, and TEM pictures revealed that they contained fibrous matter similar to phyllosilicates observed before reduction.

The presence of Cu phyllosilicates in samples reduced at 750 °C suggests that they were much more difficult to reduce than Ni and Co phyllosilicates. The reduction was more effective in silicalite-1, in which Cu-silicates were only detected at trace levels after treatment at 750 °C.

Catalytic Evaluation of Ni@Sil-1(1.0). Ni@Sil-1(1.0) was evaluated in the catalytic hydrogenation of substituted

aromatics, and its catalytic performance was compared to that of a traditional supported Ni-based catalyst. The conversion of toluene and mesitylene (i.e., 1,3,5-trimethylbenzene) were both significant over the supported Ni catalyst (Figure 5).

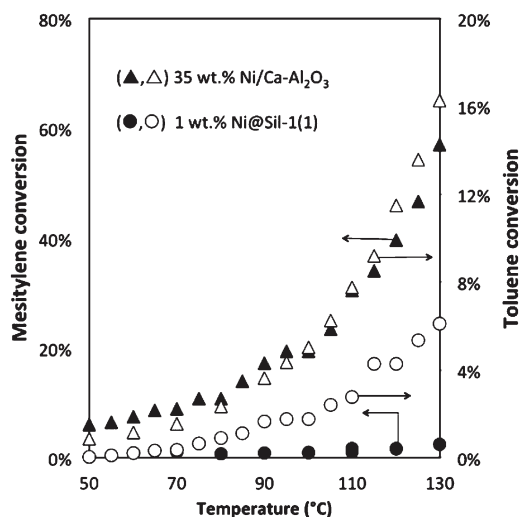


Figure 5. Conversion of toluene (open symbols) and mesitylene (closed symbols) at various temperatures over 9.4 mg of 1 wt % Ni@Sil-1(1.0) (●,○) and 14.2 mg of 35 wt % Ni/Ca–Al₂O₃ commercial catalyst (▲,△).

In contrast, the conversion of mesitylene was essentially negligible over the Ni@Sil-1(1.0), while this sample was still able to convert toluene. Similar to the case of Pt@silicalite-1,²⁶ these data clearly indicate that the transport of the bulkier mesitylene was suppressed through the zeolite layer. The kinetic diameter of mesitylene is significantly larger than the pore size of silicalite-1, while toluene can readily diffuse into this microporous solid. These data can therefore be rationalized by proposing that the zeolite shell surrounding the Ni particles was essentially free of mesoporous defects and was acting as a near-ideal membrane permeable to toluene but not mesitylene. Moreover, it also supports the absence of particles on the outside part of the nanoboxes, in agreement with the TEM analysis presented above. The molecular sieving properties of these transition metal-based catalysts are mirrored by that obtained over Pt nanoparticles inside hollow silicalite-1 single crystals.²⁶

CONCLUSIONS

We have reported for the first time the synthesis and characterization of a hollow ZSM-5 single crystal by dissolution–recrystallization of bulk crystals. The starting bulk crystals must exhibit a gradient of composition with a Si-rich core and an Al-rich periphery. In the presence of TPAOH, hollow structures were formed, similar to those obtained with silicalite-1, with regular walls of ca. 20 nm thick. The presence of trivalent acid sites in hollow ZSM-5 was confirmed by ²⁷Al NMR.

Hollow silicalite-1 and ZSM-5 single crystals containing uniform transition metal particles were prepared for the first time. The synthesis involves the dissolution–recrystallization of bulk crystals previously impregnated with the corresponding nitrate solutions. In contrast to Au and Pt @ silicalite-1, all solids were obtained by reduction of fibrous phyllosilicates

formed inside the cavities by reaction between silicate and metal species at high pH values and temperature. For hollow silicalite-1 systems at low loading, the mean particle sizes were 3.5 ± 0.3 and 3.1 ± 0.5 nm for Co and Ni, respectively. Larger loading could be obtained in ZSM-5, with mean particle sizes of 17 ± 2 nm for Co and 13 ± 2 nm for Ni. Upon oxidation, Co particles adopted a polycrystalline hollow morphology, resulting from a nanoscale Kirkendall effect.

The molecular sieving of the zeolite shell was demonstrated by the difference in hydrogenation conversions between toluene and mesitylene, the latter being too bulky to pass through the zeolite membrane and reach the nanoparticles. We believe that this new family of bifunctional catalysts showing well-controlled particle size and location opens new exciting perspectives in size-selective and bifunctional catalysis.

ASSOCIATED CONTENT

Supporting Information

Particle size distributions of Co-, Ni-, and Cu-containing hollow zeolites (silicalite-1 and ZSM-5) and their characterization by TPR, TEM, N₂ adsorption, XRD, TGA, EDX, and NMR. This material is available free of charge via the Internet at <http://pubs.acs.org>.

AUTHOR INFORMATION

Corresponding Author

*E-mail: alain.tuel@ircelyon.univ-lyon1.fr.

Notes

The authors declare no competing financial interest.

ACKNOWLEDGMENTS

We thank scientific services of IRCELYON. This study has been supported by the European Union Seventh Framework Programme FP7-NMP-2013, under Grant Agreement number 604277 (acronym FASTCARD).

REFERENCES

- (1) Marcilly, C. *Acido-Basic Catalysis: Application to Refining and Petrochemistry*; TECHNIP Ophrys Editions: Paris, France, 2006; Vol. 2.
- (2) Corma, A.; García, H. *Chem. Rev.* **2003**, *103*, 4307.
- (3) Verheyen, E.; Jo, C.; Kurttepel, M.; Vanbutsele, G.; Gobechiya, E.; Korányi, T. I.; Bals, S.; Van Tendeloo, G.; Ryoo, R.; Kirschhock, C. E. A.; Martens, J. A. *J. Catal.* **2013**, *300*, 70.
- (4) Koekkoek, A. J. J.; Kim, W.; Degirmenci, V.; Xin, H.; Ryoo, R.; Hensen, E. J. M. *J. Catal.* **2013**, *299*, 81.
- (5) Na, K.; Jo, C.; Kim, J.; Cho, K.; Jung, J.; Seo, Y.; Messinger, R. J.; Chmelka, B. F.; Ryoo, R. *Science* **2011**, *333*, 328.
- (6) Sartipi, S.; Parashar, K.; Valero-Romero, M. J.; Santos, V. P.; van der Linden, B.; Makkee, M.; Kapteijn, F.; Gascon, J. *J. Catal.* **2013**, *305*, 179.
- (7) Sartipi, S.; Parashar, K.; Makkee, M.; Gascon, J.; Kapteijn, F. *Catal. Sci. Technol.* **2013**, *3*, 572.
- (8) Sartipi, S.; Alberts, M.; Santos, V. P.; Nasalevich, M.; Gascon, J.; Kapteijn, F. *ChemCatChem* **2014**, *6*, 142.
- (9) Cai, J.; Ma, H.; Zhang, J.; Song, Q.; Du, Z.; Huang, Y.; Xu, J. *Chem.—Eur. J.* **2013**, *19*, 14215.
- (10) Højholt, K. T.; Laursen, A. B.; Kegnaes, S.; Christensen, C. H. *Top. Catal.* **2011**, *54*, 1026.
- (11) Laursen, A. B.; Højholt, K. T.; Lundegaard, L. F.; Simonsen, S. B.; Helveg, S.; Schüth, F.; Paul, M.; Grunwaldt, J.-D.; Kegnaes, S.; Christensen, C. H.; Egeblad, K. *Angew. Chem., Int. Ed.* **2010**, *49*, 3504.
- (12) Wu, Z.; Goel, S.; Choi, M.; Iglesia, E. *J. Catal.* **2014**, *311*, 458.
- (13) Tang, Q.; Zhang, Q.; Wang, P.; Wang, Y.; Wan, H. *Chem. Mater.* **2004**, *16*, 1967.

- (14) Goel, S.; Wu, Z.; Zones, S. I.; Iglesia, E. *J. Am. Chem. Soc.* **2012**, *134*, 17688.
- (15) Collier, P.; Golunski, S.; Malde, C.; Breen, J.; Burch, R. *J. Am. Chem. Soc.* **2003**, *125*, 12414.
- (16) Miyamoto, M.; Kamei, T.; Nishiyama, N.; Egashira, Y.; Ueyama, K. *Adv. Mater.* **2005**, *17*, 1985.
- (17) Nishiyama, N.; Ichioka, K.; Park, D.-H.; Egashira, Y.; Ueyama, K.; Gora, L.; Zhu, W.; Kapteijn, F.; Moulijn, J. A. *Ind. Eng. Chem. Res.* **2004**, *43*, 1211.
- (18) Galeano, C.; Güttel, R.; Paul, M.; Arnal, P.; Lu, A. H.; Schüth, F. *Chem.—Eur. J.* **2011**, *17*, 8434.
- (19) Arnal, P. M.; Comotti, M.; Schüth, F. *Angew. Chem., Int. Ed.* **2006**, *45*, 8224.
- (20) Lin, C.-H.; Liu, X.; Wu, S.-H.; Liu, K.-H.; Mou, C.-Y. *J. Phys. Chem. Lett.* **2011**, *2*, 2984.
- (21) Joo, S. H.; Park, J. Y.; Tsung, C.-K.; Yamada, Y.; Yang, P.; Somorjai, G. A. *Nat. Mater.* **2009**, *8*, 126.
- (22) Park, J. C.; Lee, H. J.; Kim, J. Y.; Park, K. H.; Song, H. *J. Phys. Chem. C* **2010**, *114*, 6381.
- (23) Yin, Y.; Chen, M.; Zhou, S.; Wu, L. *J. Mater. Chem.* **2012**, *22*, 11245.
- (24) Chen, Z.; Cui, Z.-M.; Niu, F.; Jiang, L.; Song, W.-G. *Chem. Commun.* **2010**, *46*, 6524.
- (25) Li, S.; Burel, L.; Aquino, C.; Tuel, A.; Morfin, F.; Rousset, J.-L.; Farrusseng, D. *Chem. Commun.* **2013**, *49*, 8507.
- (26) Li, S.; Boucheron, T.; Tuel, A.; Farrusseng, D.; Meunier, F. *Chem. Commun.* **2014**, *50*, 1824.
- (27) Wang, Y.; Tuel, A. *Microporous Mesoporous Mater.* **2008**, *113*, 286.
- (28) Wang, Y.; Lin, M.; Tuel, A. *Microporous Mesoporous Mater.* **2007**, *102*, 80.
- (29) Burel, L.; Tuel, A. *Microporous Mesoporous Mater.* **2013**, *174*, 90.
- (30) Mei, C.; Liu, Z.; Wen, P.; Xie, Z.; Hua, W.; Gao, Z. *J. Mater. Chem.* **2008**, *18*, 3496.
- (31) Meunier, F. C.; Goguet, A.; Shekhtman, S.; Rooney, D.; Daly, H. *Appl. Catal., A* **2008**, *340*, 196.
- (32) Kababji, A. H.; Joseph, B.; Wolan, J. T. *Catal. Lett.* **2009**, *130*, 72.
- (33) Puskas, I.; Fleisch, T. H.; Full, P. R.; Kaduk, J. A.; Marshall, C. L.; Meyers, B. L. *Appl. Catal., A* **2006**, *311*, 146.
- (34) Grams, J.; Ura, A.; Kwapiński, W. *Fuel* **2014**, *122*, 301.
- (35) Strunz, H. N.; Strunz, E. H. *Mineralogical Tables: Chemical-Structural Mineral Classification System*, 9th ed.; Schweizerbart: Stuttgart, Germany, 2001.
- (36) Jabłoński, J. M.; Wolczyk, M.; Krajczyk, L. *J. Catal.* **1998**, *173*, 530.
- (37) Lim, S.; Ciuparu, D.; Chen, Y.; Pfefferle, L.; Haller, G. L. *J. Phys. Chem. B* **2004**, *108*, 20095.
- (38) Fodor, D.; Pacosova, L.; Krumeich, F.; van Bokhoven, J. A. *Chem. Commun.* **2014**, *50*, 76.
- (39) Groen, J. C.; Peffer, L. A. A.; Moulijn, J. A.; Pérez-Ramirez, J. *Microporous Mesoporous Mater.* **2004**, *69*, 29.
- (40) Li, J.; Li, X.; Zhou, G.; Wang, W.; Wang, C.; Komarneni, S.; Wang, Y. *Appl. Catal., A* **2014**, *470*, 115.
- (41) Kim, Y. H.; Lee, K. H.; Nam, C.-M.; Lee, J. S. *ChemCatChem* **2012**, *4*, 1143.
- (42) Fathi, S.; Sohrabi, M.; Falamaki, C. *Fuel* **2014**, *116*, 529.
- (43) Yang, Z.; Yang, J.; Bergstrom, J.; Khazen, K.; Pileni, M.-P. *Phys. Chem. Chem. Phys.* **2014**, *16*, 9791.
- (44) Sadasivan, S.; Bellabarba, R. M.; Tooze, R. P. *Nanoscale* **2013**, *5*, 11139.



Effect of polyaromatic tars on the activity for methane steam reforming of nickel particles embedded in silicalite-1



D. Laprune, C. Theodoridi, A. Tuel, D. Farrusseng, F.C. Meunier*

Institut de Recherches sur la Catalyse et l'Environnement de Lyon, IRCELYON, Université Lyon 1, CNRS, 2, Av. Albert Einstein, F-69626 Villeurbanne, France

ARTICLE INFO

Article history:

Received 17 October 2016

Received in revised form

24 November 2016

Accepted 1 December 2016

Available online 5 December 2016

Keywords:

Methane steam reforming

Nickel

Rhodium

Tar

ABSTRACT

The steam reforming of methane was studied over Rh and Ni-based catalysts exposed to naphthalene, which was used as a representative of polyaromatic tars found in biomass-derived biogas. In particular, two Ni-based samples in which part of the metal was encapsulated within silicalite-1 nanoboxes were tested. The reforming reaction was carried at 700, 800 and 900 °C using a model feed and high space velocities to limit methane full conversion and better evidence any deactivation. A strong decrease of methane conversion was observed in the presence of 1400 ppm of naphthalene, stressing the marked deleterious effect of this molecule in the present conditions. The effect of naphthalene was partly reversible, especially at higher temperatures. The silicalite-1 membrane could not prevent the deactivation of embedded nickel particles, probably because naphthalene (kinetic diameter = 0.62 nm) could diffuse throughout the MFI-type (pore diameter ca. 0.56 nm) porous layer at the high reaction temperatures used. The effect of 5 ppm of the bulkier pyrene (kinetic diameter = 0.74 nm) was investigated at 700 °C and also led to a rapid deactivation of the Ni@silicalite-1, likely because pyrene was cracked into naphthalene, which could then enter the silicalite-1 nanoboxes. The poisoning effect of toluene on the Ni-based catalysts was minor in comparison to that induced by the polyaromatics. A marked sintering of the embedded Ni was also observed.

© 2016 Elsevier B.V. All rights reserved.

1. Introduction

Syngas, a mixture of carbon oxides and dihydrogen, can be obtained from the steam reforming of fossil fuels [1–5] and the gasification of biomasses or carbon-containing wastes [6,7]. The gas obtained from biomass gasification contains significant concentrations of light hydrocarbons and tars that should be preferably reformed to increase syngas yield [8,9].

Tars, a mixture of condensable organic compounds such as mono- and polyaromatics, are well known coke precursors that can lead to the deactivation of reforming catalysts. The propensity for coke formation from tars will depend on the catalyst formulation and reaction conditions such as reaction temperature and steam/carbon (S/C) ratio. Di Carlo et al. reported no deactivation at 800 °C of Ni/Ca₁₂Al₂₄O₃₃ used for the steam reforming of tars derived from hazelnut shells gasification [10]. Sato and Fujimoto also reported stable naphthalene conversions at 825 °C over a WO₃-promoted Ni/MgO–CaO catalyst, even in the presence of H₂S [11].

The impact of tars on the reforming of methane is less documented. Dagle et al. recently showed that the presence of benzene and naphthalene led to marked deactivations of methane conversion due to coking over Ni, Rh and Ir-based catalysts [12]. The coking was alleviated by using higher reaction temperatures and by the presence of a noble metal.

The support has no direct role on the methane reforming, except for the dispersion and stabilization of metal particles [13]. High metal dispersion is important to achieve high specific activities. The reaction is thought to be structure-sensitive, low coordination metal sites exhibiting somewhat higher turn-over frequencies [14–16]. Ni is intrinsically less active than noble metals [13,16], but has a lower cost. The use of MgAl₂O₄ spinel as a support is often favored over that of alumina, especially because Ni can form a spinel phase with the latter that is difficult to reduce to metallic Ni [17].

Extensive carbon deposition can yet occur on Ni-based catalysts that can be of several types, i.e. pyrolytic, encapsulating and whiskers [18,19]. Encapsulating carbon (also referred to as “gum”) is formed during reforming of feeds containing aromatic compounds. The formation of whiskers, which have high mechanical strength, can lead to catalyst particle breaking up and a large pressure drop increase in the reactor. The deposition of carbon is overall

* Corresponding author.

E-mail address: fcm@ircelyon.univ-lyon1.fr (F.C. Meunier).

a complex interplay between methane/hydrocarbon decomposition and carbon gasification [20].

In the present work, two commercial catalysts based on Rh and Ni were studied, as well as two Ni-based samples in which part of the metal was encapsulated in silicalite-1 (MFI structure) nanoboxes. The effect of naphthalene on methane conversion was investigated at 700, 800 and 900 °C and, importantly, high space velocities to limit the full conversion of methane and better assess deactivation. Additional experiments were also performed using toluene and pyrene to unravel the main origin of the deactivation.

Our investigation focused on naphthalene because this molecule is one of the most difficult tar representatives to steam reform [21,22] and one of the most abundant among the polyaromatics formed during low-temperature gasification [23] and fast-pyrolysis [24] of woody biomasses. Naphthalene is also the smallest polyaromatic available and thus any catalyst that would display a size-selective resistance with respect to this molecule should also do so for the other larger compounds.

Naphthalene has a kinetic diameter of 0.62 nm, which is larger than the pore diameter of MFI zeolites (ca. 0.56 nm). Millini et al. reported that diffusion of naphthalene in the medium pore-size zeolite of the MFI-type was difficult, with energy barriers of around 114 kJ/mol [25]. In contrast, the transport of H₂O, CO₂, CO, H₂ and CH₄ (and many other small hydrocarbons) through the MFI zeolite layer is markedly faster. It is therefore possible that the slow transport of naphthalene through MFI-type pores could protect the metal particles encapsulated therein from coking, through the interplay of coke formation and gasification/reforming. These materials would thus exhibit size selective properties, being able to steam reform small hydrocarbons, while being resistant against coking due to large polyaromatics.

We reported earlier on the total size exclusion of mesitylene (kinetic diameter = 0.87 nm) from MFI-type silicalite-1 hollow nanocrystals [26,27]. In addition, we also have reported that these nanoboxes act as nanoreactors [28,29] in which the nanoparticles are encapsulated and protected from sintering by coalescence [30]. The activity and durability of Ni particles embedded in similar silicalite-1 nanoboxes during steam methane reforming catalyst will be of particular interest here, since the effect of operating at temperatures as high as 900 °C has not yet been reported. The synthesis and characterization of the Ni@silicalite-1 samples used here are described in details elsewhere [31] and are only briefly recalled here.

2. Experimental section

2.1. Catalyst synthesis

Silicalite-1 was prepared using tetraethylorthosilicate (TEOS, Aldrich, 98%) and 1 M TPAOH solutions obtained from aqueous TPABr by exchange with Ag₂O. The gel of composition SiO₂-0.4TPAOH-35H₂O was stirred at room temperature overnight to fully hydrolyze the TEOS, then transferred into a Teflon-lined autoclave and heated at 170 °C under static conditions for 3 days. The autoclave was then cooled to room temperature and the solid was centrifuged, washed with water until pH = 7 and dried overnight at 90 °C. Finally, the resulting solid was calcined for 12 h at 525 °C in air yielding silicalite-1 crystals of approximately 200 × 150 × 140 nm in size.

Ni@silicalite-1 materials were synthesized following the previously described generic method for the encapsulation of transition metal nanoparticles in hollow silicalite-1 single crystals [26,27,30,32,33–35]. In brief, 5 wt.%Ni@silicalite-1 catalyst was prepared by incipient wetness impregnation: 2 mL of Ni(NO₃)₂-6(H₂O) (99.99%, Sigma-Aldrich) aqueous solution with a

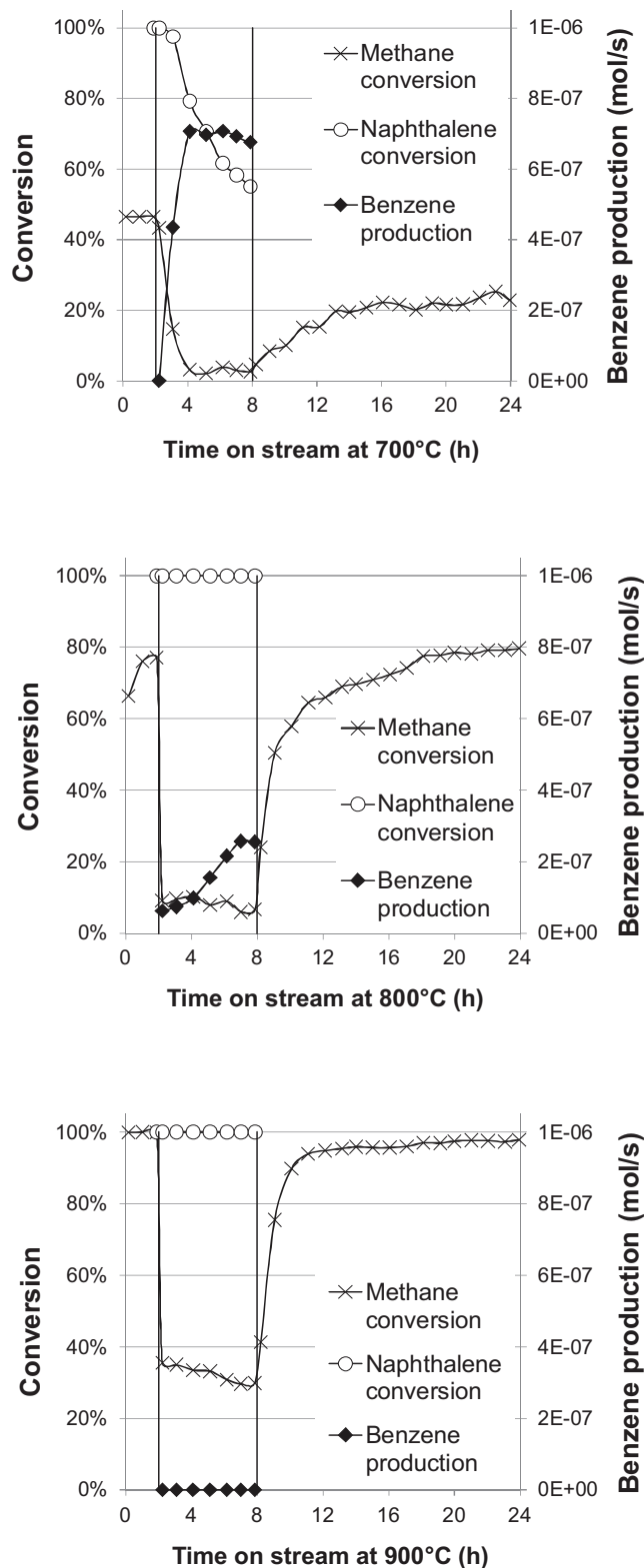


Fig. 1. Methane and naphthalene conversions and benzene production measured over time on stream at 700, 800 and 900 °C over the Rh-based commercial catalyst. 1400 ppm of naphthalene were introduced in the feed between 2 h and up to 8 h.

Table 1

Composition and textural properties of the catalysts reduced at 750 °C. Textural data are based on the calculations of the corresponding d_{SW}^b (respectively H_2 chemisorption measurements) in case of the zeolite-based samples (resp. commercial samples).

Catalyst	Support	S_{BET} ($m^2 g^{-1}$)	Metal loading (wt.%)	Mean metal particle diameter (nm)	Metal dispersion (%)
Commercial Rh	$\gamma-Al_2O_3^a$	150	0.8	1.7 ± 0.2	63 ± 1
Commercial Ni	$CaAl_2O_3^a$	14	11.4	44 ± 1	2.3 ± 0.1
5%Ni@sil-1	hollow silicalite-1	338	6.2	$8 \pm 3^{[b]}$	16 ± 7
CitAc Ni@sil-1	hollow silicalite-1	272	1.5	$4.6 \pm 1^{[b]}$	26 ± 7

^a Based on XRD analyses.

^b Surface-weighted mean diameter (incertitude based on distribution standard deviation – 500 particles counted).

concentration of 426 mmol/L was added to 1 g of silicalite-1, which had been outgassed at 300 °C overnight. The mixture was stirred at 50 °C until complete evaporation of water to obtain the $Ni(NO_3)_2$ -silicalite-1. The hollow structure was obtained by treating 1 g of this material in a TPAOH aqueous solution (7.5 mL; 0.55 M) in a Teflon-lined autoclave at 170 °C under rotating conditions for 24 h. The solution was then cooled down, washed with water until pH = 7, dried overnight at 90 °C and calcined at 450 °C for 6 h to obtain the NiO@silicalite-1. Finally the solid was reduced at 750 °C under H_2 for 3 h with a heating rate of 2.5 °C/min to yield the nominal loading 5%Ni@sil-1. The actual metal loading was 6.2 wt.% (Table 1). A Ni-free hollow silicalite-1 sample was prepared according to the same procedure without any Ni impregnation.

A citric acid post-treatment was used to remove external Ni particles [31]. 500 mg of NiO@silicalite-1 was added to 50 mL of citric acid ($\geq 99.0\%$, Sigma-Aldrich) aqueous solution with a concentration of 0.5 mol/L and the mixture was stirred vigorously at 80 °C for 2 h. The solution was then centrifuged and washed with water until pH = 7 and dried overnight at 90 °C. Finally the solid was also reduced at 750 °C under H_2 for 3 h to yield a sample referred to as CitAc Ni@sil-1.

In addition to the silicalite-1-based materials, a commercial Rh-based catalyst (1%Rh/ Al_2O_3 , Alfa Aesar, ref. 11769) and a commercial Ni-based catalyst (HiFUEL R110, Alfa Aesar, ref. 45465) were used as reference catalysts.

2.2. Catalyst characterization

Powder X-ray diffraction patterns (XRD) were recorded to assess the crystallinity of the samples. Diffractogrammes were collected between 4 and 90° (2θ) with steps of 0.02° and 1 s per step with a Bruker D5005 diffractometer using $CuK\alpha$ radiation at $\lambda = 1.5418 \text{ \AA}$. Relative crystallinity of silicalite-1-based catalysts was calculated following a standard method [36] described as follow:

$$\text{Loss in crystallinity} = (\% \text{Crystallinity}_{\text{fresh}} - \% \text{Crystallinity}_{\text{post-mortem}}) / \% \text{Crystallinity}_{\text{fresh}}$$

$$\text{where } \% \text{Crystallinity} = \frac{\text{Area}_{2\theta = 22.5-25^\circ}}{\text{Area}_{\text{reference } 2\theta = 22.5-25^\circ}} \times 100$$

and where $\text{Area}_{\text{reference } 2\theta = 22.5-25^\circ}$ was measured on a fully crystalline plain silicalite-1 sample used as a reference. The size of the crystalline domains of Ni particles was calculated using the Scherrer formula based on peak broadening of the two most intense peaks of metal Ni (44° and 51°, JCPDS: 04-0850).

Elemental analysis of the fresh catalysts was performed using an ICP-OES ACTIVA from HORIBA Jobin Yvon equipped with a CCD detector for the determination of metallic loadings. Nitrogen adsorption isotherms were measured at 77 K on a Belsorp-mini from BEL-Japan and a Micromeritics 3Flex. Samples were outgassed under vacuum at 150 °C for 4 h.

TEM pictures were obtained using a Jeol 2010 LaB6 microscope operating at 200 kV. Particle size distributions (PSDs) of zeolite-based materials were obtained by counting 500 particles using Image J software [37]. Surface-weighted mean diameters $d_{SW} = \sum n_i d_i^2 / \sum n_i d_i^3$ were calculated from the PSDs, where n_i is the number of particles counted with a diameter d_i . Metal dispersions were

deduced from the corresponding d_{SW} considering a cuboctahedral model and a calculation method described by Van Hardeveld and Hartog [38]. EDX measurements were performed using an EDX Link ISIS analyzer from Oxford Instruments to identify the elements present in the samples.

Metal surface areas were also measured by hydrogen chemisorption at 35 °C using a Micromeritics ASAP 2010. The sample holder was loaded with 0.5 g of catalyst and prior to the measurement the catalyst sample was reduced in situ in flowing hydrogen at 700 °C for 2 h. After reduction, the sample was evacuated for 2 h at 350 °C before cooling down to 35 °C. Two successive adsorption isotherms, separated by a second evacuation of 1 h at 35 °C, were then measured, according to the method described by Iglesia and co-workers [39]. The amount of hydrogen chemisorbed was obtained by correcting the total hydrogen uptake (1st isotherm) with that of weakly adsorbed H_2 (2nd isotherm). Nickel (respectively rhodium) surface areas were calculated assuming a $H/Ni_{\text{surface}} = 1$ (resp. $H/Rh_{\text{surface}} = 2$) ratio [40,41] and a Ni (resp. Rh) atom area of $6.51 \times 10^{-20} \text{ m}^2$ (resp. $7.58 \times 10^{-20} \text{ m}^2$) [42]. Specific surfaces (S_M) were converted to mean particle diameters (d_M) assuming a spherical particle shape, resulting in:

$$d_M(\text{\AA}) = 60000 / (\rho(\text{g cm}^{-3}) \times S_M(\text{m}^2 \text{g}^{-1}))$$

where ρ is the metal mass density. Metal dispersion (D_M) values were deduced considering:

$$D_M(\%) = 6 \times ((v_M(\text{\AA}^3) / a_M(\text{\AA}^2)) / d_M(\text{\AA})) \times 100$$

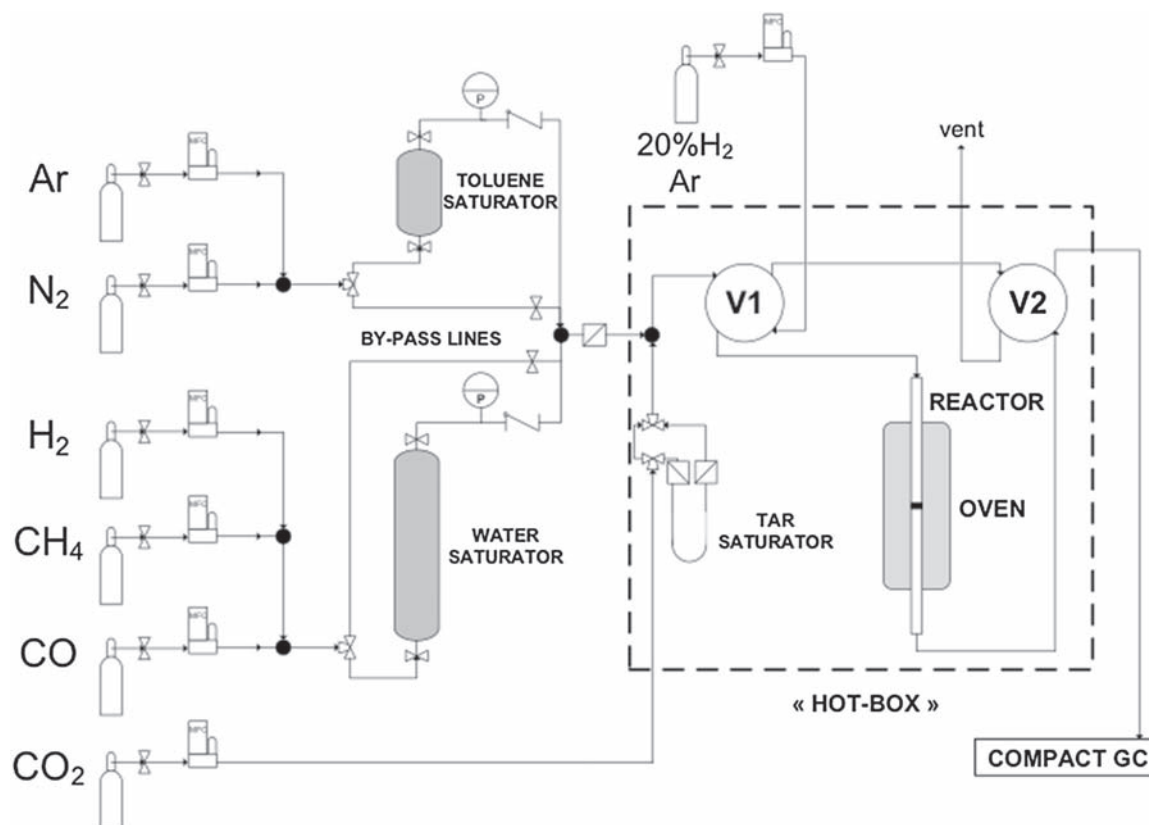
where a_M and v_M are respectively the area occupied by a surface atom and the volume occupied by a bulk atom.

The amount of carbon deposited on spent catalysts was measured by thermogravimetric analysis (TGA) on a Mettler Toledo TGA/DSC1 thermal analyzer. About 4 mg of spent catalyst was used in each TGA experiment during which the sample was heated in air flow at 50 mL/min up to 900 °C at a heating rate of 5 °C/min.

2.3. Steam reforming tests

The steam reforming experiments were performed on a lab-scale system (Scheme 1). The tests were carried out in a fixed-bed continuous-flow reactor consisting of a quartz tube (length 300 mm, 4 mm ID, 6 mm OD) containing 10 mg (unless otherwise stated) of non-diluted catalyst held between plugs of quartz wool. The commercial Rh-based catalyst powder was tested without any pre-shaping. The commercial Ni-based pellets and “ship-in-a-bottle” materials (5%Ni@sil-1 and CitAc Ni@sil-1) were crushed and sieved to obtain particle sizes ranging from 100 to 200 μm . Prior to testing, catalysts were reduced in situ at 700 °C (heating rate of 400 °C/h) for 2 h under a flow of 200 mL/min of 20 vol.% H_2 /Ar mixture. The typical bed height varied between 0.5 and 3 mm, meaning that the reactor could not be considered in a plug-flow regime.

A model gas composition was used (Table 2) that was similar to that of typical reformat compositions [43]. Brooks Instrument mass flow controllers (MFC) were used to control gas flow rates of H_2 , CH_4 , CO , CO_2 , N_2 and Ar. The overall system pressure was set



Scheme 1. Schematic layout of the experimental setup.

Table 2
Feed gas composition for catalytic reforming tests.

Compound	CO	H ₂	CO ₂	H ₂ O	CH ₄	N ₂	Ar	Tar model compound, if any
(vol.%)	20	16	10	39	9	2	4	Naphthalene: 1400 ppm Pyrene: 5 ppm Toluene: 1%

at $P_{\text{total}} = 2.2$ bar using a needle valve located downstream the on-line analyzer. A pressure sensor was placed upstream of the reactor to check for a possible pressure increase due to bed blocking. Solid naphthalene (or pyrene) was placed in a U-shaped $\frac{1}{4}$ " stainless steel tube saturator in the hotbox set at 107°C and water was placed in a 500 mL cylindrical saturator set at 99°C . Toluene was placed in a 150 mL cylindrical saturator set at 82°C . Carrier gas flow rates were set to obtain the desired flow rates of steam and the tar model used (i.e. toluene, naphthalene or pyrene). The catalytic bed was located in the isothermal region of a tube furnace and the temperature was monitored by a thermocouple placed inside the furnace. The catalyst was tested sequentially at 700, 800 and 900°C , dwelling 24 h at each temperature. At each temperature, naphthalene (or pyrene) was only introduced in the feed between $t = 2$ h and up to $t = 8$ h. The reversibility of the deactivation was then studied by maintaining the catalyst under a naphthalene-free feed for up to 16 h.

Online analysis of the reactor effluent was performed with a Compact GC (CGC) from Global Analyzer Solutions. The analyzer was equipped with two columns coupled with TCD and FID analyzers enabling the quantification of permanent gases (N₂, H₂, CO, CO₂ and CH₄) and hydrocarbons (CH₄ and heavier), respectively. The N₂ signal was used as an internal standard for the TCD channel to convert the other surface areas into molar flows. Similarly, the CH₄

signal was used as an internal standard for the FID channel (the CH₄ molar flow rate being itself determined from the TCD channel). H₂O quantification was not performed. Quantitative analyses of permanent gases were performed by calibrating the CGC using different partial pressures of compounds diluted in N₂. On the FID channel, hydrocarbons of interest were quantified by determining their response factor relative to CH₄.

The total gas flow rate of reactants was 125 mL min^{-1} . The corresponding WHSV was 689 h^{-1} (the GHSV was $750\,000\text{ h}^{-1}$, assuming catalyst density to be unity). This high WHSV value was selected to obtain an accelerated ageing in terms of tar exposure on a reasonable timescale. Furthermore, these conditions prevented total conversion of hydrocarbons, providing insights in terms of activity and stability of the different catalysts. Reactor modeling using the Eurokin Gas-Solid fixed bed reactor modeler [44] indicated the presence of a significant radial heat transport limitation resulting in a cold spot of up to 45°C when the reactor was operated at 900°C .

3. Results and discussion

3.1. Sample characterizations

Sample characterizations before catalytic tests are detailed elsewhere [31]. The Ni loading measured by ICP on the 5%Ni@sil-1 was

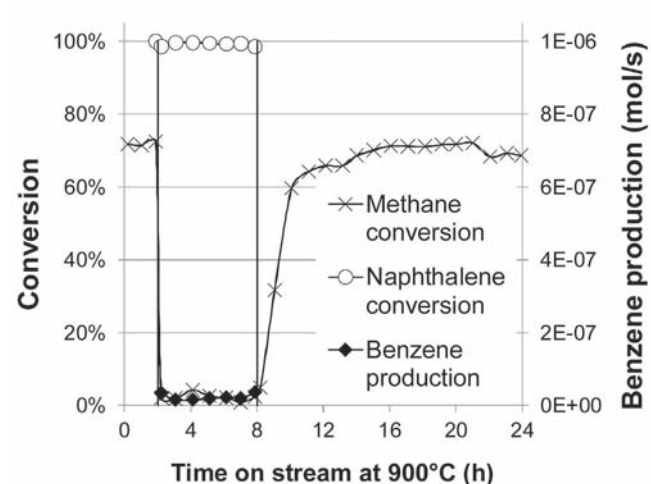
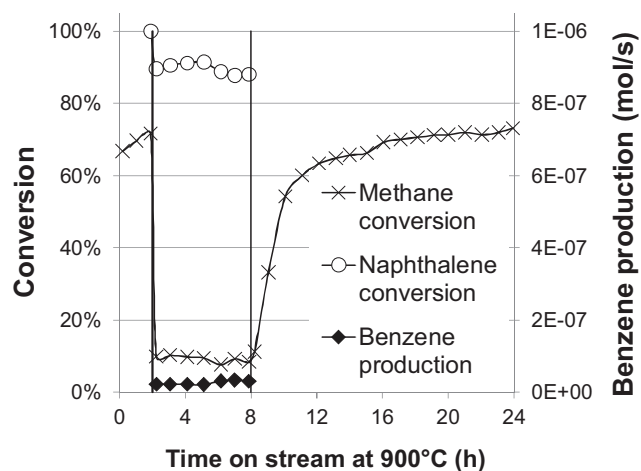
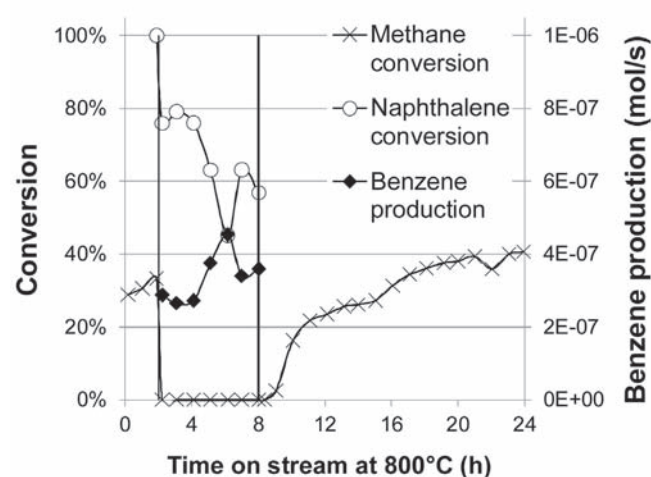
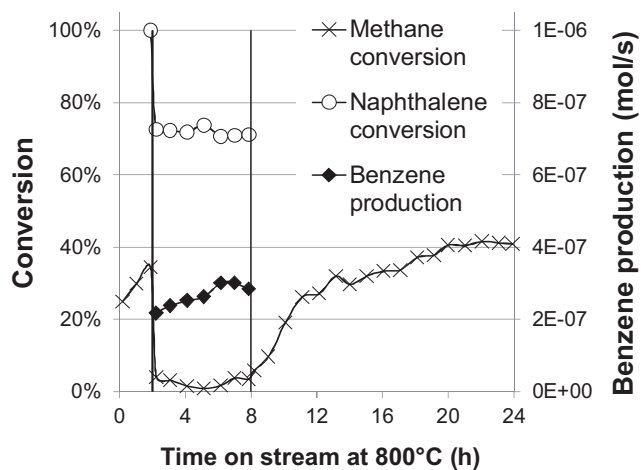
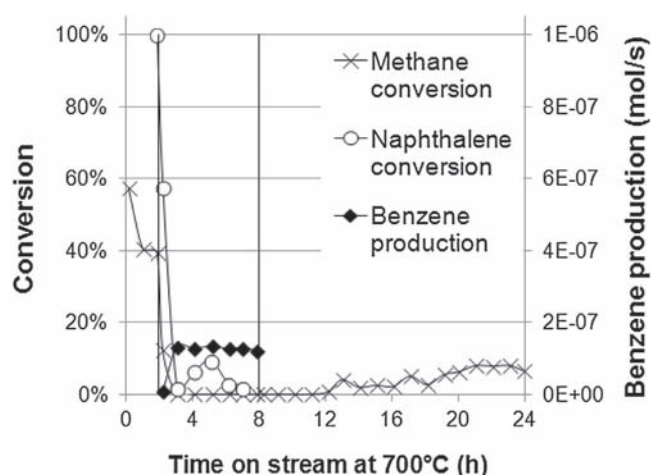
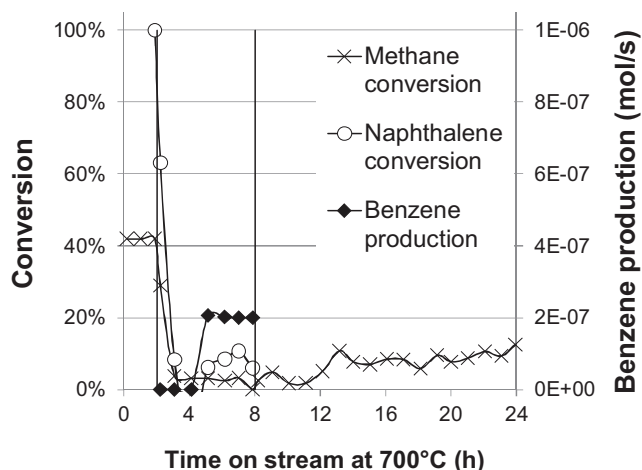


Fig. 2. Methane and naphthalene conversions and benzene production measured over time on stream at 700, 800 and 900 °C over a Ni-based commercial catalyst. 1400 ppm of naphthalene were introduced in the feed between 2 h and up to 8 h.

Fig. 3. Methane and naphthalene conversions and benzene production measured over time on stream at 700, 800 and 900 °C over 5 wt.% Ni@sil-1 catalyst. 1400 ppm of naphthalene were introduced in the feed between 2 h and up to 8 h.

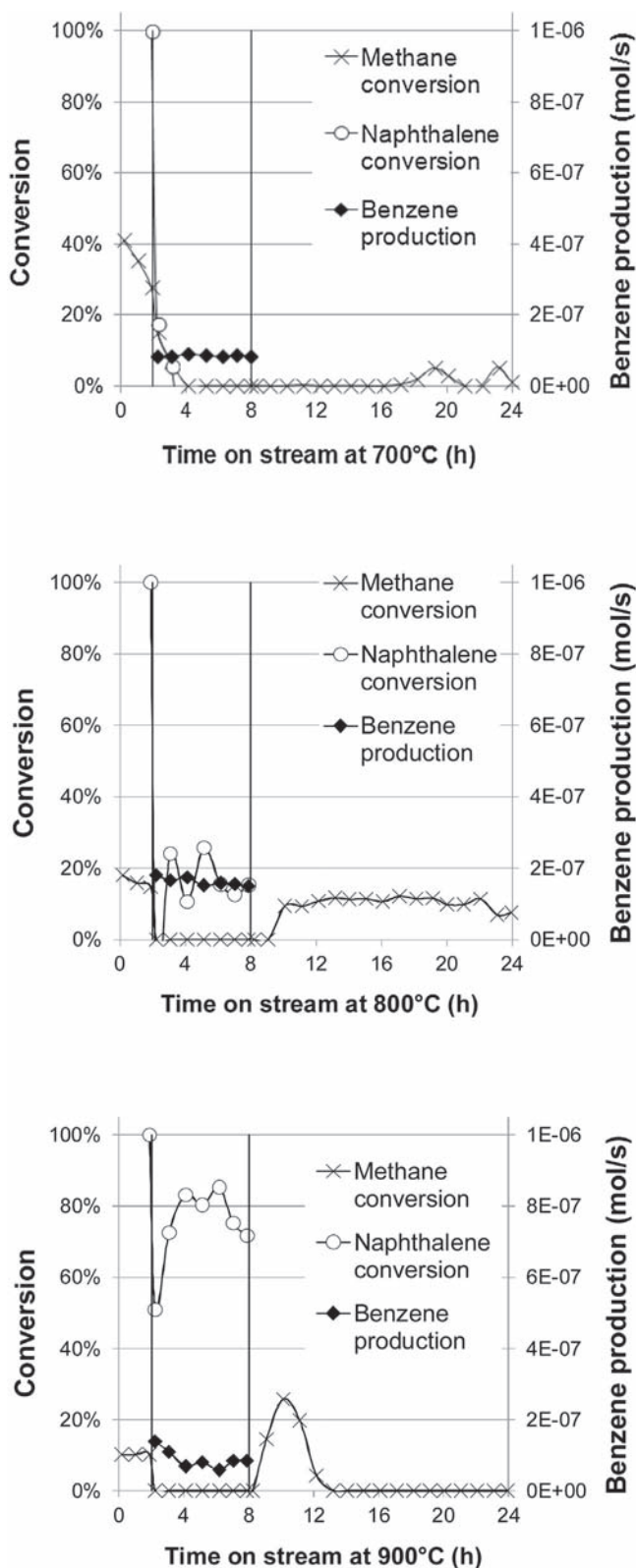


Fig. 4. Methane and naphthalene conversions and benzene production measured over time on stream at 700, 800 and 900 °C over CitAc Ni@sil-1. 1400 ppm of naphthalene were introduced in the feed between 2 h and up to 8 h.

6.2 wt.%, close to the nominal value (Table 1). The loss of Ni due to the citric acid treatment was extensive, resulting in the Ni loading dropping from 6.2 down to ca. 1.5 wt.%. The average particle sizes were below 10 nm for both nanobox-based samples. The citric acid treatment also led to a decreased average particle size, which was due to the removal of more than 90% of larger Ni particles located outside the nanoboxes [31].

3.2. Steam reforming activity

The effect of the addition of 1400 ppm of naphthalene on the activity of the various catalysts was determined at 700, 800 and 900 °C in succession during the same experiment using the same batch (Figs. 1–4). This implies that the catalyst may have partly deactivated at the lower temperatures before being used at the higher ones. At each temperature and for all the catalysts, the introduction of naphthalene led to a sharp and almost total loss of the conversion of methane. The poisoning effect of this hydrocarbon appeared to be only partly and slowly reversible at 700 °C over the commercial Ni and Rh catalysts (Figs. 1 and 2). Yet, methane conversion was fully and readily recovered at 800 and 900 °C over these two commercial samples (Figs. 1 and 2) and the 5 wt.% Ni@silicalite-1 (Fig. 3). It should be noted that benzene was formed as a decomposition product of naphthalene.

The 5 wt.% Ni@sil-1 catalyst and especially the citric acid-treated CitAc 5%Ni@sil-1 sample appeared to deactivate even before the introduction of naphthalene (Fig. 4). This initial deactivation could be due to both Ni sintering (enhanced by the presence of steam [18] and the poor anchoring properties of silicalite-1) and coke formation. These nanobox-based catalysts showed a strong deactivation in the presence of naphthalene at all temperatures (Fig. 4). This was a disappointing result particularly for the CitAc 5%Ni@sil-1 because most of the Ni particles were initially embedded inside the silicalite-1 nanoboxes in this sample [31] and were expected to show a better resistance against the bulky naphthalene molecules.

The activity at 900 °C showed a peculiar behavior, with a transient activity spike followed by total deactivation (Fig. 4), contrary to the case of the sample not-treated by citric acid (Fig. 3). A close inspection of these two samples post-reaction by TEM indicated that the structure of nanoboxes of the citric acid-treated sample had totally collapsed (Fig. 5, bottom), contrary to the case of the 5%Ni@sil-1 sample (Fig. 5, top). In addition, the size of the Ni particles had increased markedly for both samples, from below 10 nm (Table 1) up to ca. 35 nm (Fig. 6, Table 3).

Comparing the average Ni crystallite sizes before and after reaction (Table 1 and Fig. 6), the CitAc 5%Ni@sil-1 sample was even more prone to particle agglomeration (8-fold increase of the average particle diameter) than the non-treated sample (4-fold increase). This observation underlines the ability of the hollow zeolite shell to limit Ni nanoparticles sintering, at least until the complete breakup of the nanobox structure occurred.

An XRD analysis (Fig. 7, Table 3) revealed that both samples exhibited a loss of crystallinity of the silicalite-1 phase after reaction. The formation of cristobalite was also apparent in the case of the CitAc Ni@sil-1, stressing the lower thermal stability of the citric-acid-treated sample [45]. The Ni crystallite sizes (determined through the Scherrer equation) dramatically increased to about 36 nm following reaction (Table 3), while those were lower than 10 nm before reaction. It should be noted that the Ni particle sizes determined by TEM and XRD are fully consistent (Table 3).

The formation of carbonaceous species, mostly present as graphitic whiskers, was also detected from TEM observations on both aged silicalite-1-based samples (Fig. 5, right). Some carbon whiskers ending with Ni particles were also visible. The results of thermogravimetric analyses for the quantification of this residual coke are presented in Table 3. The recorded mass loss in the tem-

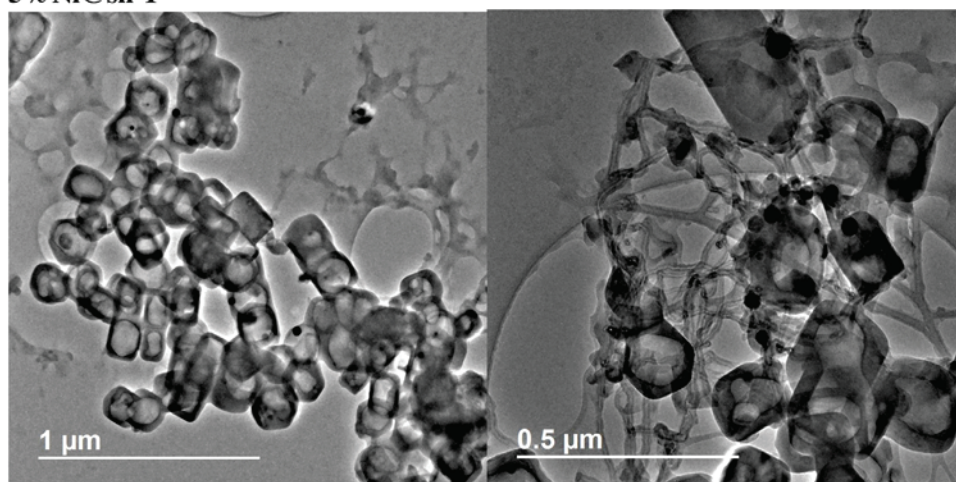
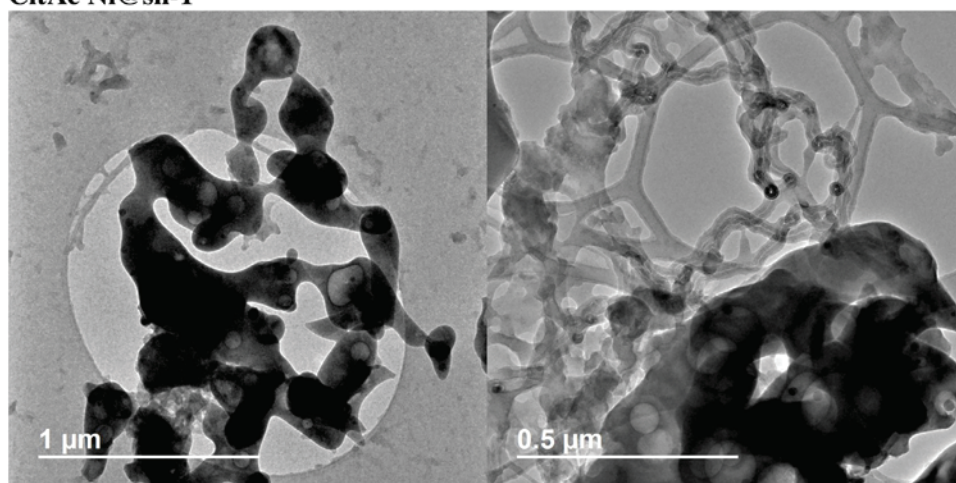
5% Ni@sil-1**CitAc Ni@sil-1**

Fig. 5. TEM images of post-reaction 5%Ni@sil-1 (top) and CitAc Ni@sil-1 (bottom) using magnification of $\times 5000$ (left) and $\times 10000$ (right).

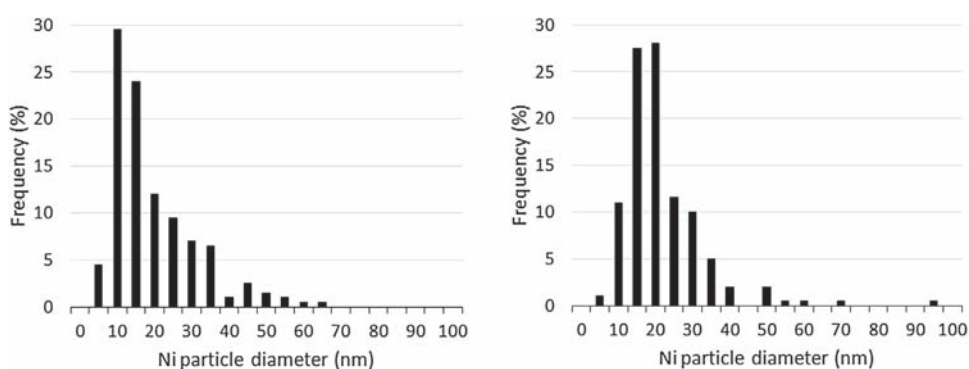


Fig. 6. Post-reaction particle size distributions of 5%Ni@sil-1 (left) and CitAc Ni@sil-1 (right). Measurements based on 200 particles.

Table 3

Calculation of the loss in silicalite-1 crystallinity (%) and of the Ni crystallite size (nm) using both the Scherrer equation (XRD) and the surface-weighted mean diameters (TEM) for post-mortem analysis of the 5%Ni@sil-1 and CitAc Ni@sil-1. The mass loss obtained by thermogravimetric analyses is also given.

	% Loss in silicalite-1 crystallinity	Initial Ni crystallite size (nm)	Ni crystallite size post-reaction		Dispersion Post-reaction	TGA mass loss ($\text{g g}^{-1} \text{cat}$)
			XRD (nm)	TEM (nm)		
5%Ni@sil-1	44	8	32	35	3.7%	1.7×10^{-3}
CitAc Ni@sil-1	90	4.6	35	37	3.5%	1.1×10^{-2}

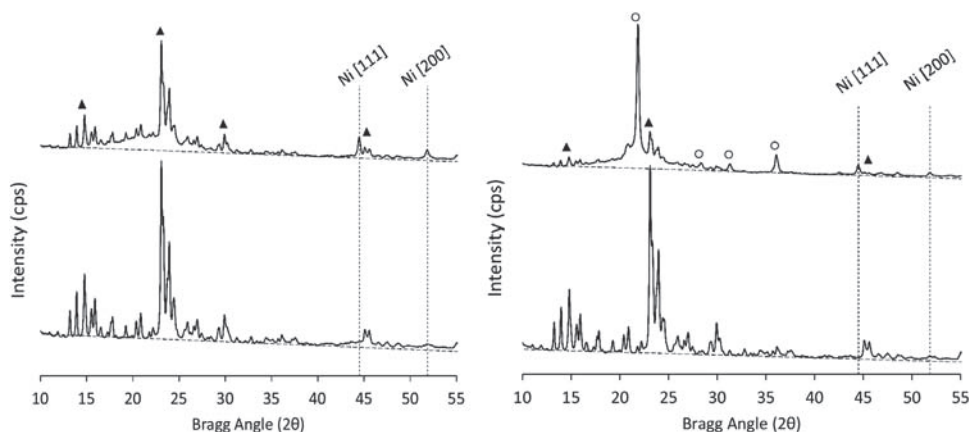


Fig. 7. XRD analysis of fresh (bottom diffractogram) and post-reaction (top diffractogram) 5%Ni@sil-1 (left) and CitAc Ni@sil-1 (right). Post-reaction diffractograms indicate an increase of the baseline in the range $2\theta = 12\text{--}40^\circ$ corresponding to sample amorphisation. (▲): silicalite-1 (JCPDS: 48-0136). (O): Cristobalite (JCPDS: 39-1425). No indication of carbon graphite formation is observed (characteristic peak at $2\theta = 28^\circ$).

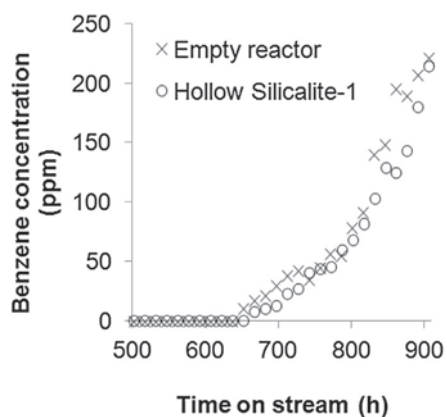


Fig. 8. Benzene concentration measured in the reactor effluent while reforming methane in presence of naphthalene on an empty reactor (x) and one filled with Ni-free hollow silicalite-1 (o).

perature range $550\text{--}650^\circ\text{C}$ was attributed to the combustion of graphitic carbon only, since identical analyses on the corresponding fresh samples exhibited no mass loss over the same range. These results are consistent with literature data related to whisker gasification on similar catalysts [46,47].

The observed major sintering of Ni particles could yet not be the cause of the reversible deactivations observed in the presence of naphthalene over the 5%Ni@sil-1 (Fig. 3), since Ni redistribution upon removing naphthalene is not expected. Ni sintering over the 5%Ni@sil-1 is likely to have occurred in the very first instants following exposure to the steam-containing feed at 700°C , as suggested by the initial decay of methane conversion observed at 700°C (Fig. 3), and also during the subsequent temperature increases to 800 and 900°C . The reversible deactivation likely arose from carbon deposition, as suggested by the TGA analyses (Table 3) and TEM pictures (Fig. 5, right).

Complementary methane steam reforming experiments were carried out to unravel the nature, i.e. mono or polyaromatic, of the molecule responsible for the coking taking place in the presence of naphthalene, as benzene was observed in all experiments (Figs. 1–4). It must be stressed that benzene was formed from naphthalene even in the absence of any catalyst (and over a Ni-free silicalite-1 sample) above 650°C (Fig. 8). This fact is important because it shows that heavy aromatics will thermally crack into monoaromatics at the typical reaction temperatures needed to steam reform methane. Monoaromatics are expected to readily dif-

fuse throughout silicalite-1 membranes [26,27,30]. It was therefore necessary to ascertain the role of monoaromatics on the deactivation under our conditions.

The use of toluene was preferred to that of benzene for the sake of convenience, especially since the propensity for coking of these two molecules is expected to be similar. The presence of 1% of toluene induced a significant deactivation of the Rh-based commercial catalyst at 800 and 700°C (Fig. 9). Any potential deactivation at 900°C could not be ascertained because methane conversion was too close to 100%. The deactivation obtained using a large concentration of toluene (1%) appeared yet more limited than that observed under 1400 ppm of naphthalene (Fig. 3) over (10 mg) of the same sample.

A bed blockage was observed in the case of the commercial Ni-based catalysts at 700°C after ca. 18 h on stream (Fig. 10). This is consistent with the extensive formation of carbon whiskers (as observed in Fig. 5, right) on Ni particles under reforming conditions, especially at low temperatures. Formation of whiskers, leading to Ni particles being detached from the support, yields hardly any conversion loss until the catalyst bed becomes fully blocked [48].

In the case of Ni, the poisoning effect of toluene (Fig. 10) was almost negligible as compared to that of naphthalene (Fig. 2). It can be concluded that monoaromatics are unlikely to be responsible for the strong deactivation of Ni-based samples induced by naphthalene. Therefore, we propose that naphthalene itself directly poisoned the Ni particles located inside the silicalite-1 nanoboxes through the formation of encapsulating coke and whiskers [19,48] process which appeared slowly reversible over most samples at the higher temperatures (Figs. 1–4).

The CitAc Ni@sil-1 sample was the most deactivated by naphthalene (Fig. 4) and its nanobox structure eventually almost totally collapsed (Fig. 5 and Table 3). This is in contrast to the case of the 5%Ni@sil-1, for which the shape of the nanoboxes was preserved (Fig. 5) as well as a much higher degree of crystallinity (Table 3). One possible explanation for this difference is that most of the nickel was embedded within the CitAc Ni@sil-1 sample and this is thus where most of the coke formation would have occurred. Since carbon whiskers were also formed (observed by TEM, Fig. 5) and possess high mechanical strength¹⁹ those probably broke up the nanoboxes. In the case of the 5%Ni@sil-1, it is likely that most of the coke formation took place on the Ni that was in most part located outside the nanoboxes. This probably resulted in the blocking of the silicalite-1 pores by encapsulating coke (easily formed from polyaromatics [18]) and thereby limited access to the Ni contained in the hollow core of the nanoboxes and coke formation in there.

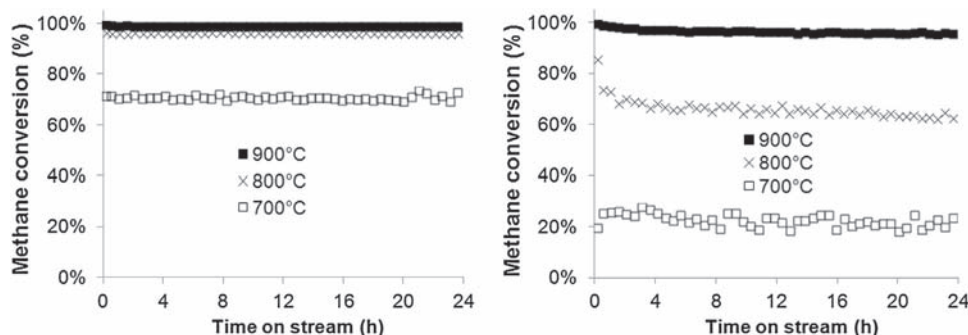


Fig. 9. Methane conversions measured with time on stream at 700, 800 and 900 °C over the Rh-based commercial catalyst in absence (left) and in presence (right) of 1% of toluene. Catalyst mass = 25 mg.

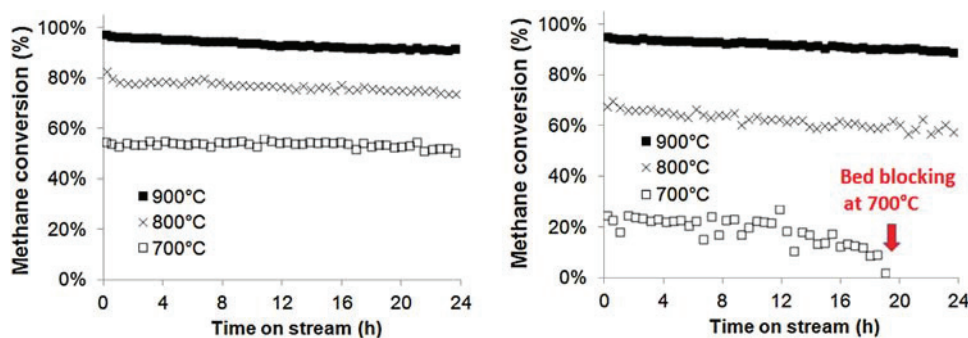


Fig. 10. Methane conversions measured with time on stream at 700, 800 and 900 °C over the Ni-based commercial catalyst in the absence (left) and in presence (right) of 1% of toluene. Catalyst mass = 25 mg.

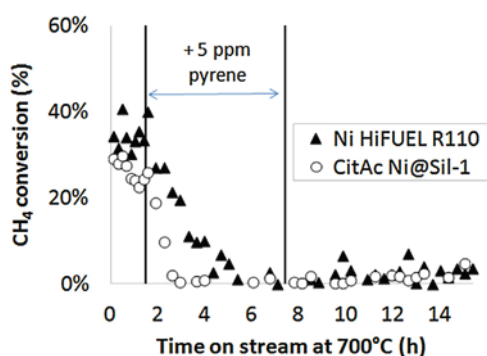


Fig. 11. Methane conversions measured with time on stream at 700 °C over 25 mg of the Ni-based commercial catalyst (Ni HiFUEL 110) and the CitAc Ni@sil-1 sample. 5 ppm of pyrene were introduced over a period of 6 h.

Since naphthalene appeared to be able to cross the silicalite-1 membrane of the CitAc Ni@sil-1, an additional experiment was carried out using a much bulkier polyaromatic, i.e. pyrene (kinetic diameter = 7.24) [49]. A concentration of 5 ppm of pyrene appeared to readily deactivate the commercial Ni-based catalyst (Fig. 11), but also the CitAc Ni@sil-1 sample. Since naphthalene was observed in the reactor effluent, it is proposed that naphthalene or some other cracking product of pyrene could have coked the embedded nickel. The deactivation of the CitAc Ni@sil-1 appeared to be faster than that of the commercial Ni-based catalysts, possibly because of the lower concentration of Ni present on the former.

4. Conclusions

A concentration of 1400 ppm of naphthalene readily and strongly poisoned the steam reforming of methane over Rh and Ni-based catalysts. The use of encapsulated Ni@silicalite-1 sam-

ples did not lead to naphthalene-resistant catalysts, most likely because this molecule was able to access the embedded Ni in spite of the silicalite-1 nanobox membrane surrounding the metal particles. The bulkier pyrene, at a concentration of 5 ppm, lead to similar results, as pyrene was shown to partly crack into naphthalene. In contrast, the effect of a monoaromatic such as toluene was almost negligible on the activity of Ni-based samples, apart from possible bed blocking through carbon whisker formation at low temperature (700 °C). The silicalite-1 single hollow nanobox was inefficient in preventing the sintering of Ni particles. This work emphasize the difficulty in obtaining size-selective systems for high temperature applications, since reactant cracking is common and a range of smaller molecules are generated in situ.

Acknowledgments

This work was partly supported by the European Union Seventh Framework Programme FP7-NMP-2013, under Grant Agreement number 604277 (acronym FASTCARD). Prof X. Verykios from Patras University is acknowledged for organizing the exchange of C.T.

References

- [1] G. Jones, J. Jakobsen, S. Shim, J. Kleis, M. Andersson, J. Rossmeisl, F. Abildpedersen, T. Bligaard, S. Helveg, B. Hinnemann, *J. Catal.* 259 (2008) 147.
- [2] P. Ferreira-Aparicio, A. Guerrero-Ruiz, I. Rodríguez-Ramos, *Appl. Catal. A: Gen.* 170 (1998) 177.
- [3] C. Rioche, S. Kulkarni, F.C. Meunier, J.P. Breen, R. Burch, *Appl. Catal. B* 61 (2005) 130.
- [4] A.M. O'Connor, F.C. Meunier, J.R.H. Ross, *Stud. Surf. Sci. Catal.* 119 (1998) 819.
- [5] J. Xu, C.M.Y. Yeung, J. Ni, F. Meunier, N. Acerbi, M. Fowles, S.C. Tsang, *Appl. Catal. A* 345 (2008) 119.
- [6] D. Sutton, B. Kelleher, J.R.H. Ross, *Fuel Proc. Technol.* 73 (2001) 155.
- [7] U. Arena, *Waste Manage.* 32 (2012) 625.
- [8] R. Bain, D. Dayton, D. Carpenter, S. Czernik, C. Feik, R. French, K. Magrini-Bair, S. Phillips, *Ind. Eng. Chem. Res.* 44 (2005) 7945.

- [9] Ø. Borg, N. Hammer, B.C. Enger, R. Myrstad, O.A. Lindvåg, S. Eri, T.H. Skagseth, E. Rytter, *J. Catal.* 279 (2011) 163.
- [10] A. Di Carlo, D. Borello, M. Sisinni, E. Savuto, P. Venturini, E. Bocci, K. Kuramoto, *Int. J. Hydrogen Energy* 40 (2015) 9088.
- [11] K. Sato, K. Fujimoto, *Catal. Commun.* 8 (2007) 1697.
- [12] V.L. Dagle, R. Dagle, L. Kovarik, A. Genc, Y.-G. Wang, M. Bowden, H. Wan, M. Flake, V.-A. Glezakou, D.L. King, R. Rousseau, *Appl. Catal. B: Environ.* 184 (2016) 142.
- [13] D. Mei, V.-A. Glezakou, V. Lebarbier, L. Kovarik, H. Wan, K.O. Albrecht, M. Gerber, R. Rousseau, R.A. Dagle, *J. Catal.* 316 (2014) 11.
- [14] H.S. Bengaard, J.K. Nørskov, J. Sehested, B.S. Clausen, L.P. Nielsen, A.M. Molenbroek, J.R. Rostrup-Nielsen, *J. Catal.* 209 (2002) 365.
- [15] Y. Wang, Y.H. Chin, R.T. Rozmiarek, B.R. Johnson, Y. Gao, J. Watson, A.Y.L. Tonkovich, D.P. Vander Wiel, *Catal. Today* 98 (2004) 575.
- [16] A. Yamaguchi, E. Iglesia, *J. Catal.* 274 (2010) 52.
- [17] M. Luneau, E. Gianotti, F.C. Meunier, C. Mirodatos, E. Puzenat, Y. Schuurman, N. Guilhaume, *Appl. Catal. B: Environmental* 203 (2017) 289.
- [18] J. Sehested, *Catal. Today* 111 (2006) 103.
- [19] J.R. Rostrup-Nielsen, J. Sehested, J.K. Nørskov, *Adv. Catal.* 47 (2002) 65.
- [20] C.A. Bernardo, I. Alstrup, J.R. Rostrup-Nielsen, *J. Catal.* 96 (1985) 517.
- [21] F. Josuinkas, C. Quitete, N. Ribeiro, M. Souza, *Fuel Process. Technol.* 121 (2014) 76.
- [22] R. Coll, J. Salvado, X. Farriol, D. Montane, *Fuel Process. Technol.* 74 (2001) 19.
- [23] U. Wolfesberger, I. Aigner, H. Hofbauer, *Environ. Prog. Sustain. Energy* 28 (2009) 372.
- [24] T. Carlson, G. Tompsett, W. Conner, G. Huber, *Top. Catal.* 52 (2009) 241.
- [25] R. Millini, F. Frigerio, G. Bellussi, G. Pazzuconi, C. Perego, P. Pollesel, U. Romano, *J. Catal.* 217 (2003) 298.
- [26] S. Li, T. Boucheron, A. Tuel, D. Farrusseng, F. Meunier, *Chem. Commun.* 50 (2014) 1824.
- [27] S. Li, A. Tuel, D. Laprune, F. Meunier, D. Farrusseng, *Chem. Mater.* 27 (2015) 276.
- [28] D. Farrusseng, A. Tuel, *New J. Chem.* 40 (2016) 3933.
- [29] C. Pagis, A. Morgado Prates, D. Farrusseng, N. Bats, A. Tuel, *Chem. Mater.* 28 (2016) 5205.
- [30] S. Li, A. Tuel, F. Meunier, M. Aouine, D. Farrusseng, *J. Catal.* 332 (2015) 25.
- [31] D. Laprune, A. Tuel, D. Farrusseng, F.C. Meunier, submitted, given as supplementary information.
- [32] S. Li, L. Burel, C. Aquino, A. Tuel, F. Morfin, J.-L. Rousset, D. Farrusseng, *Chem. Commun.* 49 (2013) 8507.
- [33] N. Novruzova, A. Tuel, D. Farrusseng, F. Meunier, *Microporous Mesoporous Mater.* 228 (2016) 147.
- [34] S. Li, C. Aquino, L. Gueudré, A. Tuel, Y. Schuurman, D. Farrusseng, *ACS Catal.* 4 (2014) 4299.
- [35] S. Li, A. Tuel, J. Rousset, F. Morfin, M. Aouine, L. Burel, F. Meunier, D. Farrusseng, *ChemNanoMat* 2 (2016) 534.
- [36] ASTM D5758-01, Standard Test Method for Determination of Relative Crystallinity of Zeolite ZSM-5 by X-Ray Diffraction, ASTM, International, West Conshohocken, PA, 2001.
- [37] H.G. Merkus, *Particle Size Measurements: Fundamentals, Practice, Quality*, Springer Ed., 2009, ISBN 978-1-4020-9016-5.
- [38] R. Van Hardeveld, F. Hartog, *Surf. Sci.* 15 (1969) 189.
- [39] J. Wei, E. Iglesia, *J. Catal.* 224 (2004) 370.
- [40] C.H. Bartholomew, R.B. Pannell, *J. Catal.* 65 (1980) 390.
- [41] J.P. Candy, A. Elmansour, O.A. Ferretti, G. Mabilon, J.P. Bournonville, J.M. Basset, G. Martino, *J. Catal.* 112 (1988) 201.
- [42] H. Liu, *Ammonia Synthesis Catalysts: Innovation and Practice*, 7, World Scientific Publishing, 2013, pp. 586.
- [43] M. van der Meijden, P.C.A. Bergman, A. van der Drift, B.J. Vreugdenhil, Preparations for a 10 MWth bio-CHP, in: 18th European Biomass Conference and Exhibition, Lyon, France, 2010, pp. 3–7.
- [44] <http://eurokin.tudelft.nl/>.
- [45] S.P. Zhdanov, N.N. Feoktistova, N.I. Kozlova, I.G. Polyakova, *Bull. Acad. Sci. USSR Div. Chem. Sci.* 34 (1985) 2467.
- [46] M.C.J. Bradford, M.A. Vannice, *Appl. Catal. A* 142 (1996) 73.
- [47] H.M. Swaan, V.C.H. Kroll, G.A. Martin, C. Mirodatos, *Catal. Today* 21 (1994) 571.
- [48] D.L. Trimm, *Catal. Today* 49 (1999) 3.
- [49] J. Jae, G.A. Tompsett, A.J. Foster, K.D. Hammond, S.M. Auerbach, R.F. Lobo, G.W. Huber, *J. Catal.* 279 (2011) 257.



Selective removal of external Ni nanoparticles on Ni@silicalite-1 single crystal nanoboxes: Application to size-selective arene hydrogenation



D. Laprune, A. Tuel, D. Farrusseng, F.C. Meunier*

Institut de Recherches sur la Catalyse et l'Environnement de Lyon, IRCELYON, Université Lyon 1, CNRS, 2, Av. Albert Einstein F-69626, Villeurbanne, France

ARTICLE INFO

Article history:

Received 18 November 2016
Received in revised form 18 January 2017
Accepted 13 February 2017
Available online 16 February 2017

Keywords:

Hollow zeolite
Hydrogenation
Silicalite-1
Citric acid
Size selectivity

ABSTRACT

Undesired metal nanoparticles located outside zeolite nanoboxes (hollow zeolites) can be formed during the preparation of zeolite-embedded metal nanoparticles. The present work demonstrates that it is possible to use citric acid to selectively leach out most of the external Ni nanoparticles from a Ni@silicalite-1 material. The leached sample exhibited an improved selectivity in the hydrogenation of toluene as compared to that of the bulkier mesitylene.

© 2017 Elsevier B.V. All rights reserved.

1. Introduction

Size-selective membranes and catalysts find important applications in separation, sensing and catalytic technologies. Catalytic hydrogenation is an ubiquitous reaction and is used for instance in the synthesis of fine chemicals and fuel upgrading [1–5], with substrate sizes that are similar to that of zeolite pores. The possibility to prepare nanoparticles of metals embedded inside zeolite single crystal nanoboxes was recently reported by our group [6–12] and others [13–15]. The total size exclusion of mesitylene (kinetic diameter = 0.87 nm) from the silicalite-1 (purely siliceous zeolite with MFI topology) hollow nanocrystals was demonstrated and led to a Pt-based catalyst that was highly active for the hydrogenation of toluene (kinetic diameter = 0.58 nm) and totally inactive for that of mesitylene [6]. In addition, we also have reported that these nanoboxes act as nanoreactors [8,9] in which the nanoparticles are encapsulated and protected from sintering by coalescence [10]. We recently reported during an investigation of the effect of tars on methane steam reforming that these silicalite-1-based nanoboxes can retain their structural integrity up to 900 °C [16].

The use of noble metals typically led to single nanoparticles with a well-defined size embedded in silicalite-1 nanoboxes [11,12]. In contrast, the method applied to base metals led in most cases to a large number of nanoparticles present in each nanobox [7]. In the present work dealing with Ni, we show that metal nanoparti-

cles can also be formed outside of the silicalite-1 nanoboxes when attempting to prepare high metal loadings, leading to less size-selective catalysts. The presence of metal nanoparticles outside the nanoboxes can be particularly detrimental if the reactants are converted into deactivating molecules that can poison or block the nanobox surface or pores, as when dealing with reforming or dehydrogenation reactions.

Obuchi and co-workers have previously reported a method to selectively remove Pt nanoparticles located outside ZSM-5 (aluminosilicate zeolite with MFI-type framework) crystals based on a complex procedure involving the use of tetraethylammonium halide salts and halogens [17]. We demonstrate here that a simple citric acid-based treatment can selectively leach out most external Ni nanoparticles, while leaving a significant amount of nanoparticles located inside the nanoboxes. The leached sample exhibited an improved selectivity in the hydrogenation of toluene as compared to that of the bulkier mesitylene.

2. Experimental section

2.1. Sample synthesis

Silicalite-1 was prepared using tetraethylorthosilicate (TEOS, Aldrich, 98%) and 1 M TPAOH (tetrapropyl ammonium hydroxide) solutions obtained from aqueous TPABr (tetrapropyl ammonium bromide) by exchange with Ag₂O. The gel of composition SiO₂-0.4TPAOH-35H₂O was stirred at room temperature overnight to fully hydrolyze the TEOS, then transferred into a Teflon-lined autoclave and heated at 170 °C under static conditions for 3 days.

* Corresponding author.

E-mail address: fcm@ircelyon.univ-lyon1.fr (F.C. Meunier).

The autoclave was then cooled to room temperature and the solid was centrifuged, washed with water until pH=7 and dried overnight at 90 °C. Finally, the resulting solid was calcined for 12 h at 525 °C in air yielding silicalite-1 crystals of approximately 200 nm × 150 nm × 140 nm in size.

Ni@silicalite-1 materials were synthesized following the previously described generic method for the encapsulation of transition metal nanoparticles in hollow silicalite-1 single crystals [7,10,18,19]. In brief, the 5%Ni@sil-1 was prepared by wet impregnation: 2 mL of an aqueous solution of Ni(NO₃)₂·6(H₂O) (99.999%, Sigma-Aldrich) with a concentration of 426 mmol/L was added to 1 g of silicalite-1, which had been outgassed at 300 °C overnight. The mixture was stirred at 50 °C until complete evaporation of water to obtain a Ni(NO₃)₂/sil-1. The hollow structure was then obtained by treating 1 g of this material in a TPAOH aqueous solution (7.5 mL; 0.55 M) in a Teflon-lined autoclave at 170 °C under rotating conditions for 24 h. The solution was then cooled down, washed with water until pH=7, dried overnight at 90 °C and calcined in air at 450 °C for 6 h to obtain a NiO@silicalite-1. Finally the solid was reduced at 750 °C under H₂ for 3 h with a heating rate of 2.5 °C min⁻¹ to yield the sample referred to as 5%Ni@sil-1.

The citric acid post-treatment was carried out as follows. 0.5 g of NiO@silicalite-1 was added to 50 mL of a 0.5 mol/L aqueous solution of citric acid (≥99.0%, Sigma-Aldrich). The mixture was stirred vigorously at 80 °C for 2 h. The solution was then centrifuged and washed with water until pH=7 and dried overnight at 90 °C. Finally the solid was reduced at 750 °C under H₂ for 2 h to yield a sample referred to as CitAc Ni@sil-1. This sample was further calcined in air at 550 °C for 6 h to obtain the calc-CitAc Ni@sil-1. A reference catalyst named 5%Ni/sil-1 was produced by direct calcination and reduction of Ni(NO₃)₂/sil-1 under the same conditions as 5%Ni@sil-1.

2.2. Sample characterization

Powder X-ray diffraction patterns (XRD) were recorded to assess the crystallinity of the samples. Diffractograms were collected between 4 and 90° (2θ) with steps of 0.02° and 1 s per step with a Bruker D5005 diffractometer using CuKα radiation at λ = 1.5418 Å.

Elemental analysis of the catalysts was performed using an ICP-OES ACTIVA from HORIBA Jobin Yvon equipped with a CCD detector for the determination of metal loadings. Nitrogen adsorption isotherms were measured at 77 K on a Belsorp-mini from BEL-Japan. Samples were first outgassed under vacuum at 300 °C for 4 h. The *t*-plot analysis was not considered here, in view of the debate on the validity of the *t*-plot method to assess microporosity in hierarchical materials [20].

TEM pictures were obtained using a Jeol 2010 LaB6 microscope operating at 200 kV. Nanoparticle size distributions of zeolite-based materials were obtained by counting 500 nanoparticles using Image J software [21]. Both number-weighted ($d_{NW} = \sum n_i d_i / \sum n_i$) and surface-weighted ($d_{SW} = \sum n_i d_i^2 / \sum n_i d_i^3$) mean diameters were calculated from the nanoparticle size distributions. Each distribution was then modeled using a normal law centered on the corresponding d_{NW} . Metal dispersions were deduced from the corresponding d_{SW} considering a cuboctahedral model and a calculation method described by Van Hardeveld and Hartog [22]. EDX measurements were performed using an EDX Link ISIS analyzer from Oxford Instruments to identify the elements present in the samples.

2.3. Catalytic tests

Toluene and mesitylene (i.e. 1,3,5-trimethylbenzene) hydrogenation tests were carried out using a fixed-bed continuous-flow reactor consisting of a quartz tube (length 400 mm, 4 mm ID, 6 mm

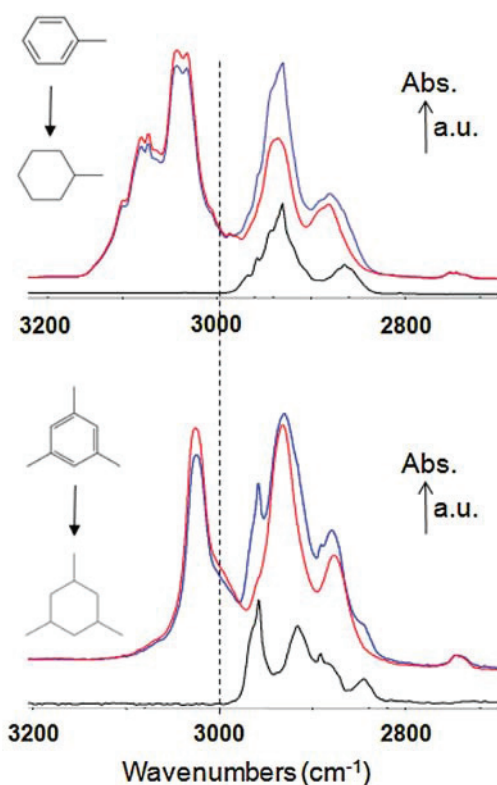


Fig. 1. FT-IR transmission spectra recorded in the 10 cm pathlength gas-cell during the hydrogenation of (top) toluene and (bottom) mesitylene. The spectra in red are those of the reactants. The blue spectra were collected after the reactor at a conversion level of about 9%. The spectra in black are obtained from removing the contribution of the reactant (red) from that of the reactor effluent (blue) and corresponded to (top) methylcyclohexane and (bottom) the two stereoisomers of 1,3,5-trimethylcyclohexane. The area of the bands between 3200 and 3000 cm⁻¹ were used to quantify arene concentrations. (For interpretation of the references to colour in this figure legend, the reader is referred to the web version of this article.)

OD) containing the powdered catalyst held between quartz wool plugs. The system was operated at atmospheric pressure and the samples were reduced *in situ* at 500 °C in pure H₂ for 60 min before the catalytic tests. Aromatic reactants were fed individually using a saturator kept at 0 °C, leading to partial pressures of 912 and 62 Pa for toluene and mesitylene, respectively. A flow of 20 mL/min of pure H₂ was used as reactant carrier gas and fed through one saturator at a time. The catalyst powders were crushed and sieved and the fraction 100–200 μm was selected. Between 60–180 mg of catalyst was used, depending on the activity of the sample, to remain under differential conditions. The gas hourly space velocity was so varied between 6700 and 20000 h⁻¹, approximating the catalyst density as being unity.

The reactor effluent was then analyzed using a 10 cm path-length FT-IR gas cell fitted in a Tensor 27 FT-IR spectrophotometer from Bruker. Typically 32 scans were collected at a resolution of 4 cm⁻¹ and averaged. The conversion of the arene reactants was determined through integration of spectral regions corresponding to the C–H stretching vibration modes [6,23,24]. Note that FT-IR spectroscopy is commonly used as an analytical technique to investigate complex reaction mixtures as found during alkane dehydrogenation [25] and NO_x reduction [26]. The IR spectra of toluene and mesitylene are shown in Fig. 1 (spectra in red). The spectra in blue are those of the corresponding reactor effluents at a conversion of ca. 9%. The spectra of the reaction products (black spectra) could be obtained by removing the contribution of the reactants and corresponded to that of methylcyclohexane in the case of toluene (Fig. 1, top) and to that of the two stereoisomers

Table 1Composition and textural properties of the samples based on plain and hollow silicalite-1. Metal surface area, diameter and dispersion are based on the corresponding d_{sw} .^a

Catalyst	Support	Metal loading (wt.%)	Metal surface area ($m^2 g^{-1}$)	Mean metal nanoparticle diameter (nm) ^a	Metal dispersion (%)
5%Ni/sil-1	silicalite-1	4.5	0.85 ± 0.5	46 ± 16	2.8 ± 1.4
5%Ni@sil-1	hollow silicalite-1	6.2	6.6 ± 3	7.9 ± 3	16 ± 7
CitAc Ni@sil-1	hollow silicalite-1	1.5	2.6 ± 0.7	4.6 ± 1	26 ± 7

^a Surface-weighted mean diameter (the given precision is based on the standard deviation of the distribution – 500 nanoparticles counted).**Table 2**

Porosity of the different samples.

Catalyst	S_{BET} ^a	V_{micro} ^b	V_{cavity} ^c	V_{total} ^d
	($m^2 g^{-1}$)	($cm^3 g^{-1}$)	($cm^3 g^{-1}$)	($cm^3 g^{-1}$)
5%Ni/sil-1	369	0.14	0	0.20
5%Ni@sil-1	338	0.12	0.15	0.38
CitAc Ni@sil-1	272	0.10	0.11	0.29
calc-CitAc Ni@sil-1	315	0.12	0.15	0.34

^a BET method.^b Volume of N_2 adsorbed when the slope of the adsorption branch becomes lower than $10^3 cm^3 g^{-1}$.^c Difference in N_2 uptake between the adsorption and the desorption branches of the isotherms at $p/p_0 = 0.5$.^d Volume of N_2 adsorbed at $p/p_0 = 0.9$ from desorption branch.

of 1,3,5-trimethylcyclohexane in the case of mesitylene (Fig. 1, bottom). No other reaction products could be observed in the conditions used.

The area comprised over the range $3000\text{--}3200 cm^{-1}$ was integrated to quantify the concentration of the reactants, as this region only contained a contribution from the arenes (Fig. 1). The change of arene concentration was then calculated, also taking into account

the reduction of number of moles of gases according to Eqs. (1) and (2). This IR-based method appeared to be significantly more precise than a GC-based analysis (data not shown). Only data points for which the arene conversion was below 20% were considered to calculate rates, apparent activation energies and turn-over frequencies (TOF).



3. Results and discussion

3.1. Sample characterizations

The exact Ni loadings measured by ICP on the 5%Ni/sil-1 and 5%Ni@sil-1 were close to the nominal values (Table 1). The loss of Ni due to the citric acid treatment was extensive, resulting in the Ni loading dropping from 6.2 down to ca. 1.5 wt.%. The N_2 isotherms of the various samples are shown in Fig. 2 and the textural properties are summarized in Table 2.

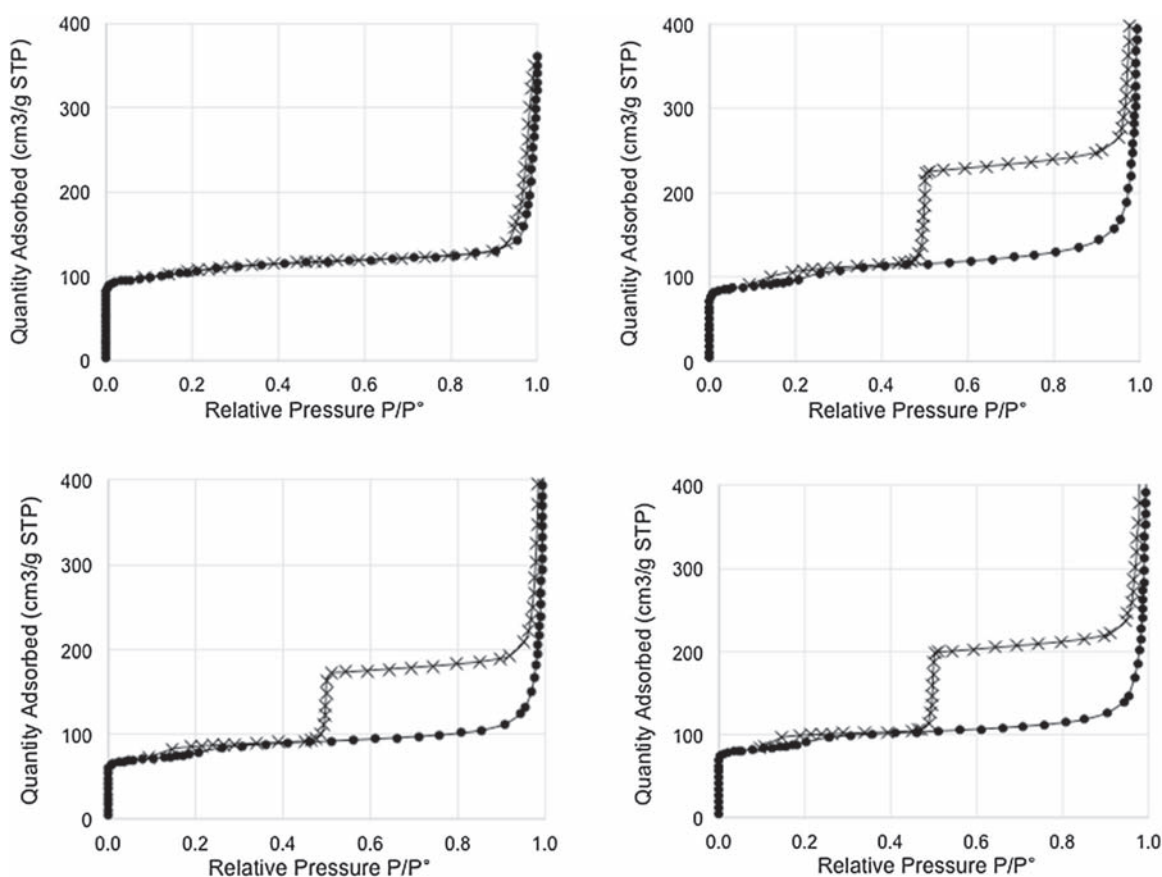


Fig. 2. N_2 adsorption (circle) and desorption (cross) isotherms at 77 K for the: 5%Ni/sil-1 (top left), 5%Ni@sil-1 (top right), CitAc 5%Ni@sil-1 (bottom left) and calc-CitAc Ni@sil-1 (bottom right).

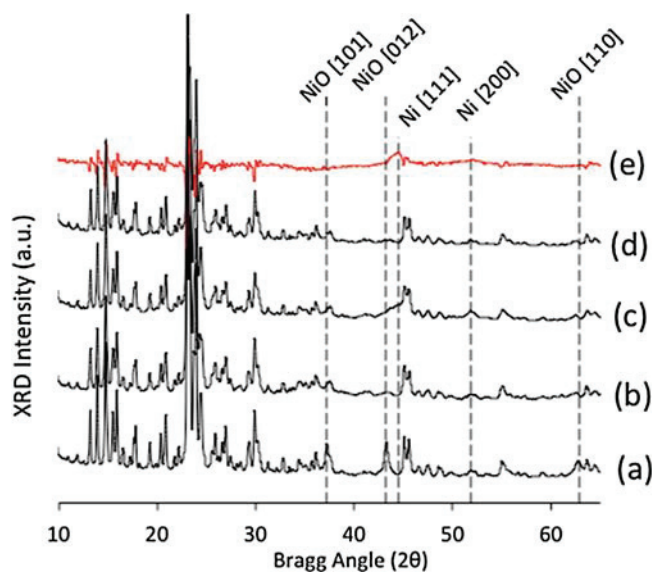


Fig. 3. XRD patterns of (a) calcined 5%Ni/sil-1, (b) calcined 5%Ni@sil-1, (c) reduced 5%Ni@sil-1 and (d) reduced CitAc Ni@sil-1. Pattern (e) was obtained by subtracting (b) from (c). The positions of the main characteristic XRD peaks of NiO (JCPDS: 47-1049) and Ni (JCPDS: 87-0712) are represented by dashed lines. All other peaks are consistent with those of silicalite-1 (JCPDS: 48-0136).

The 5%Ni/sil-1 sample exhibited a type-I isotherm (Fig. 2, top, left), which is a fingerprint of purely microporous compounds. The micropore volume ($0.14 \text{ cm}^3 \text{ g}^{-1}$) was defined as the volume of N_2 adsorbed at the point at which the derivative of the adsorption branch (measured from two consecutive points) became lower than $10^3 \text{ cm}^3 \text{ g}^{-1}$. This value is consistent with those generally reported for MFI-type zeolites [18,27]. The total pore volume was estimated from the nitrogen uptake on the desorption branch at $p/p_0 = 0.9$. Note that the isotherm of 5%Ni/sil-1 was similar to that of the parent silicalite-1 (data not shown), meaning that the sample porosity was not affected by the Ni impregnation and subsequent thermal treatments.

5%Ni@sil-1 (Fig. 2, top right) exhibited a combination of type-I and IV isotherms [28]. The adsorption branch was similar to that of 5%Ni/sil-1, indicating that the microporous nature of the sample was preserved following the formation of the hollow core. The minor hysteresis at $p/p_0 = 0.2$ is commonly attributed to a phase transition of adsorbed N_2 in highly crystalline silicalite-1 [29,30]. The TPAOH-based hierarchization actually proceeds through a dissolution/recrystallization during which the defect-rich core of the zeolite crystal is preferentially dissolved and the resulting sil-

ica species are recrystallized on the crystal outer surface upon hydrothermal treatment to form a crack-free zeolite shell [8].

The nickel cations, when present, may react with dissolved silica species yielding fibrous nickel phyllosilicates attached to the zeolite [7]. The formation of these fibers partly hinders the recrystallization step, explaining the somewhat lower V_{micro} ($0.12 \text{ cm}^3 \text{ g}^{-1}$) as compared to the case of the 5%Ni/sil-1 sample ($0.14 \text{ cm}^3 \text{ g}^{-1}$) (Table 2). The phyllosilicates are then decomposed during the reduction step, leading to well-dispersed Ni nanoparticles strongly bound to the zeolite walls.

The large H2-type hysteresis loop with a steep closure at $p/p_0 = 0.45$, known as “cavitation” phenomenon is characteristic of crack-free shells only accessible via pores smaller than 4 nm [31,32]. The desorption branch was parallel to the adsorption branch, the difference between the two branches corresponding to the amount of N_2 adsorbed in internal cavities. The volume of this entrapped macroporous cavity was $0.15 \text{ cm}^3 \text{ g}^{-1}$.

The textural properties of the citric acid-treated sample (i.e. CitAc Ni@sil-1) were similar to those of the parent sample 5%Ni@sil-1 (Table 2). The lower S_{BET} and pore volumes values obtained were presumably due to carbonaceous deposits created during the treatment with citric acid and the subsequent reduction. Shi et al. have shown that large proportions of carbonaceous deposits can be left on samples prepared with citric acid-based methods [33]. As a matter of fact, additional calcination of the sample CitAc Ni@sil-1 at 550°C during 6 h led to increased porosity (Table 2, sample calc-CitAc Ni@sil-1).

The XRD patterns of all samples were consistent with the presence of well-crystallised silicalite-1 (Fig. 3). Weak peaks attributed to NiO could also be noted in the cases of the calcined 5%Ni/sil-1 (Fig. 3a) and 5%Ni@sil-1 (Fig. 3b). No XRD pattern associated with Ni phyllosilicate could be observed. The reduction of the samples at 750°C resulted in the conversion of the NiO into metallic Ni, as shown for instance in the case of the reduced 5%Ni@sil-1 (Fig. 3c), better seen in the corresponding difference diffractogramme (Fig. 3e). The CitAc Ni@sil-1 sample (Fig. 3d) only exhibited peaks typical of silicalite-1, the Ni phases were not detected by XRD, due to the low Ni loading of this sample (Table 2).

Fig. 4 shows some TEM pictures of the calcined NiO@sil-1 prior to the treatment with citric acid. Layered domains could be observed (inset of Fig. 4b) and corresponded to Ni phyllosilicates. We reported earlier on the formation of phyllosilicates during dissolution/recrystallization of silicalite-1 impregnated with transition metal (Co, Cu, Ni) precursors in the presence of TPAOH [7]. These layered compounds could be converted to metal nanoparticles upon reduction at high temperature, yielding yolk-shell type materials. Nickel phyllosilicates can be formed under hydrothermal

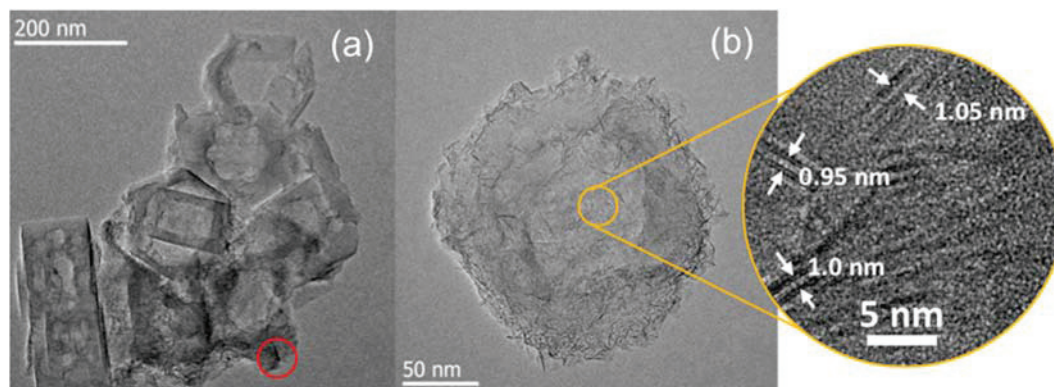


Fig. 4. TEM images of NiO@sil-1 using a magnification of $\times 15000$ (a) and $\times 45000$ (b). The zone analyzed by EDX in (a) is indicated by a red circle. The zoom in on a region of (b) reveals the nickel phyllosilicates: white arrows indicate the silicate layers used for interlayer distance determination. (For interpretation of the references to colour in this figure legend, the reader is referred to the web version of this article.)

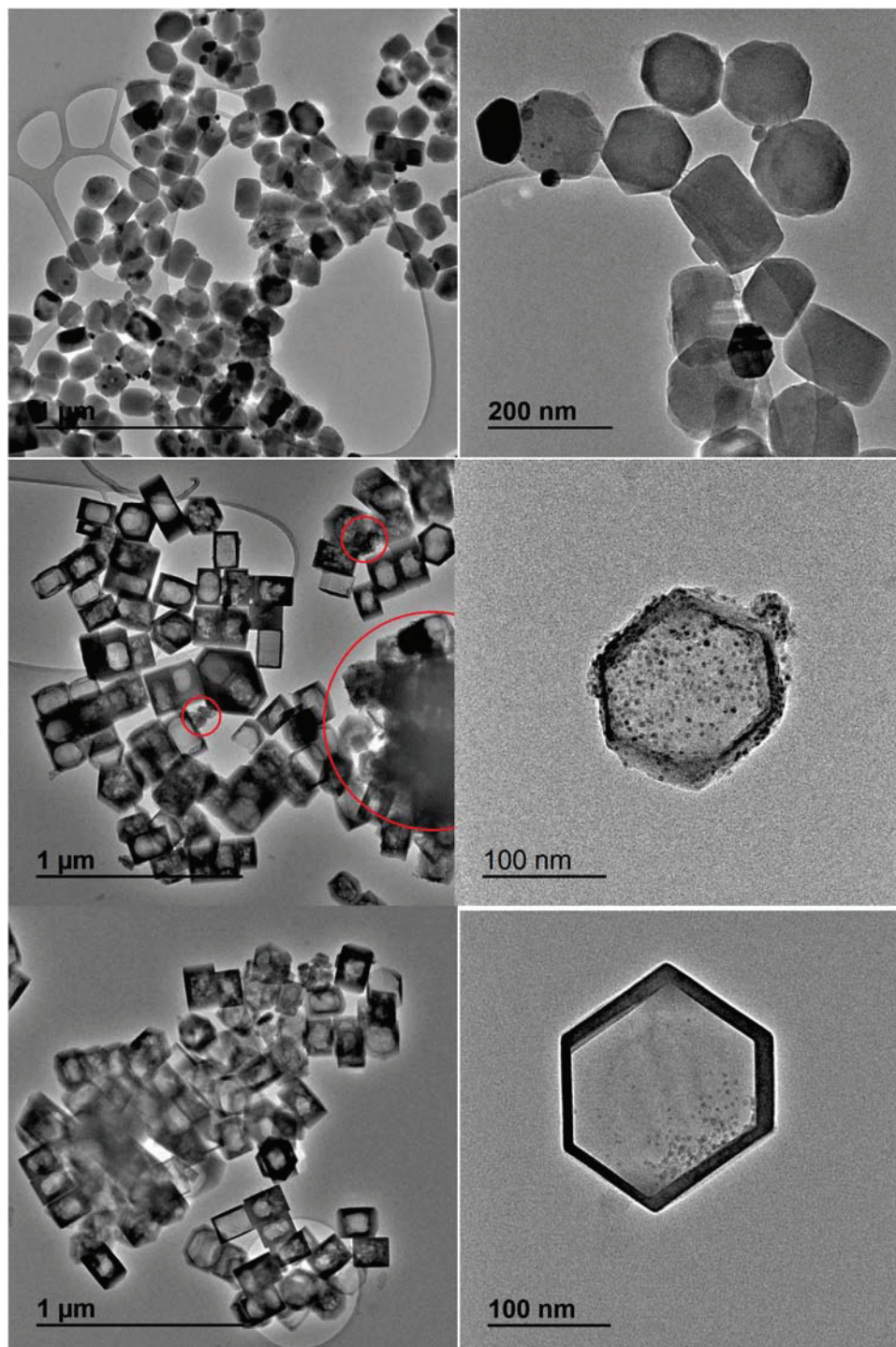


Fig. 5. TEM images of reduced 5%Ni/sil-1 (top), 5%Ni@sil-1 (middle) and CitAc Ni@sil-1 (bottom) using magnification of $\times 5000$ (left), $\times 15000$ (top right) and $\times 30000$ (middle and bottom right). Red circles indicate the presence of nickel nanoparticles (confirmed by EDX analysis) outside the zeolite nanoboxes. (For interpretation of the references to colour in this figure legend, the reader is referred to the web version of this article.)

conditions in basic media leading various compounds depending on subsequent thermal treatment [34,35]. An EDX analysis realized on NiO@silicalite-1 on layers remotely located from the nanoboxes (Fig. 4a) indicated a weight composition of 31% Ni, 30% Si and 39% O, corresponding to NiSi_2O_5 , the $\text{Si}_2\text{O}_5^{2-}$ unit being characteristic of phyllosilicates according to the Nickel-Strunz classification [36]. The nickel phyllosilicate structure was confirmed by high-resolution TEM measurements of the interlayer distance of

1.00 ± 0.05 nm, which corresponds to the value generally reported for these structures (inset of Fig. 4b) [37].

Fig. 5 shows some typical TEM micrographs of the reduced samples and the corresponding Ni nanoparticle size distributions are shown in Fig. 6. The silicalite-1 plain crystals and the corresponding nanoboxes exhibited regular shapes with sizes between 100 and 200 nm. Most of the Ni appeared as large nanoparticles (dsw = 46 nm) located outside of the silicalite-1 plain crystals in the case of the 5%Ni/sil-1 (Fig. 5, top). In contrast, the nanobox-based

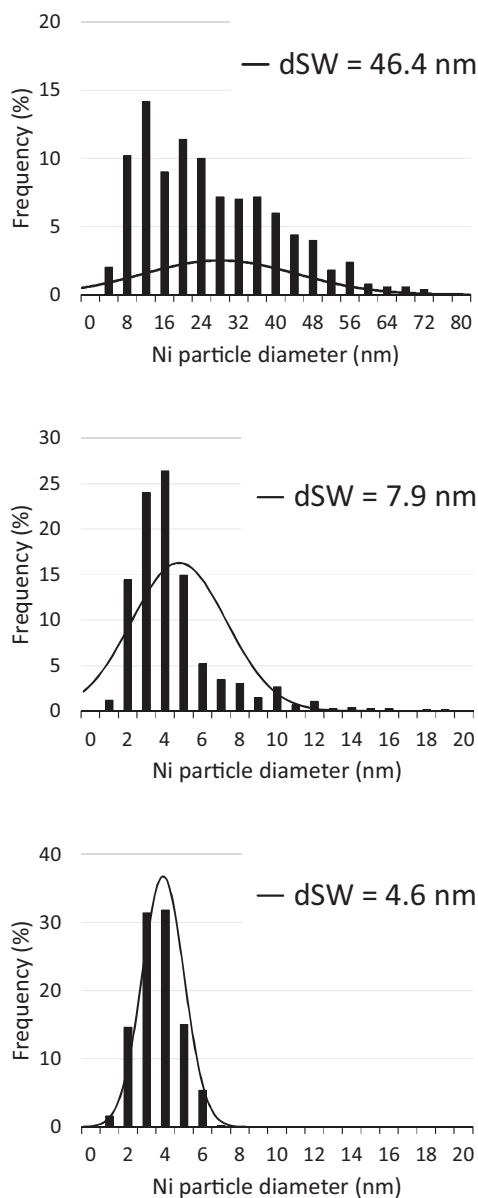


Fig. 6. Particle size distributions of reduced (top) 5%Ni/sil-1, (middle) 5%Ni@sil-1 and (bottom) CitAc Ni@sil-1. 500 nanoparticles were measured for each sample. (d_{sw} = surface-weighted mean diameter).

samples 5%Ni@sil-1 (Fig. 5, middle) and CitAc Ni@sil-1 (Fig. 5, bottom) exhibited significantly smaller nanoparticles, with dsw of 7.9 and 4.6 nm, respectively (Fig. 6).

A large number of Ni nanoparticles clearly appeared to be located outside of the nanoboxes in the case of the 5%Ni@sil-1, such as those visible on the nanobox edges (Fig. 5, middle). These external particles are probably resulting from the reduction of phyllosilicates that were bonded to the external surface of the nanoboxes (Fig. 4). In contrast, almost no nanoparticles were present on the edges of the CitAc Ni@sil-1 (Fig. 5, bottom), suggesting that most of those visible were actually located inside the nanobox. Yet, an analysis of a large number of TEM pictures revealed that some agglomerated Ni nanoparticles could still be observed within the CitAc Ni@sil-1 sample (Fig. 7).

The TEM analysis indicates that the citric acid treatment led to the removal of most of the larger Ni nanoparticles located outside of the nanoboxes, while leaving a significant amount of smaller Ni nanoparticles inside the nanobox. TEM measurements indicated

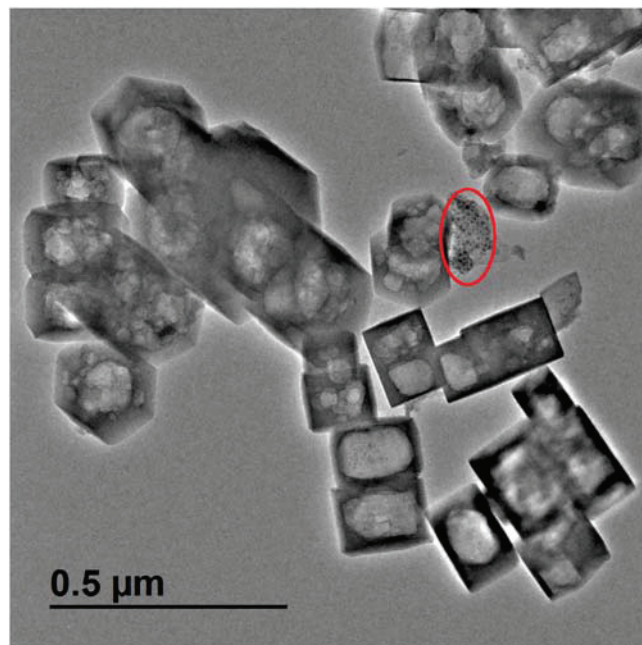


Fig. 7. TEM images of reduced CitAc Ni@sil-1 using magnification of $\times 8000$. The red oval indicates the presence of nickel nanoparticles outside the zeolite nanoboxes. (For interpretation of the references to colour in this figure legend, the reader is referred to the web version of this article.)

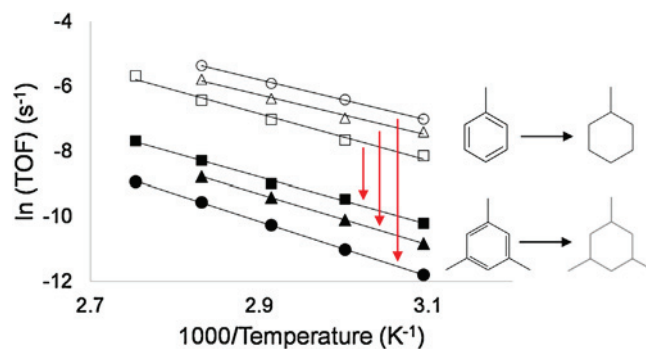


Fig. 8. Arrhenius plots relating to the TOF of toluene hydrogenation (empty symbols) and that of mesitylene (full symbols) over 5%Ni/sil-1 (square), 5%Ni@sil-1 (triangle) and CitAc Ni@sil-1 (circle).

that the quantity of encapsulated nickel nanoparticles was ca. 52 per nanobox for CitAc Ni@sil-1 (counting 20 nanoboxes). It is yet difficult to conclude whether or not some of the Ni located inside the 5%Ni@sil-1 nanoboxes was also leached out during the citric acid treatment. The catalytic study described in the following section was performed using two reactants with markedly different sizes to get a better insight at the proportion of external and internal Ni nanoparticles that were removed during the citric acid treatment.

3.2. Catalytic tests

The catalytic activity of the samples for the hydrogenation of toluene (kinetic diameter ca. 0.58 nm) and mesitylene (i.e. 1,3,5-trimethylbenzene, kinetic diameter ca. 0.87 nm) was measured between 50 and 100 °C (Table 3 and Fig. 8). Note that the silicalite-1 support did not exhibit any catalytic activity. The only product detected in each case was the corresponding cycloalkane. These two model reactants were chosen because the transport of mesitylene through the silicalite-1 pores (MFI-type framework) was

Table 3
Arene hydrogenation activity for the Ni-based samples.

	Toluene hydrogenation rate			Mesitylene hydrogenation rate			Toluene/Mesitylene hydrogenation rate ratio at 80 °C
	Rate at 80 °C ($\mu\text{mol s}^{-1} \text{g}^{-1} \text{Ni}$)	TOF at 80 °C ^a (10^{-3}s^{-1})	E_{app} (kJ mol^{-1})	Rate at 80 °C ($\mu\text{mol s}^{-1} \text{g}^{-1} \text{Ni}$)	TOF at 80 °C ^a (10^{-3}s^{-1})	E_{app} (kJ mol^{-1})	
5%Ni/sil-1	0.58	1.2 ± 0.5	54.5 ± 3	0.09	0.19 ± 0.06	60 ± 4	6
5%Ni@sil-1	7.7	2.8 ± 1	55 ± 3	0.38	0.14 ± 0.05	64 ± 4	20
CitAc Ni@sil-1	19	4.3 ± 1.5	56 ± 3	0.28	0.06 ± 0.02	69 ± 5	67

^a TOF: Turn Over Frequency, expressed as molecules of reactant converted per second per surface Ni atoms.

shown to be totally blocked under these experimental conditions, in contrast to that of toluene, which was unrestricted [6,10]. Therefore, any mesitylene hydrogenation activity will be associated with Ni nanoparticles that are not fully coated by a MFI-type membrane.

It should be stressed that the three catalysts exhibited similar apparent activation energies (E_{app}) of ca. 55 kJ mol^{-1} for toluene hydrogenation (Table 3), in line with those reported in the literature for silica-supported Ni under similar experimental conditions [38,39]. This result indicates that the reaction for both 5%Ni@sil-1 and CitAc Ni@sil-1 was not limited by toluene transport in the micropores of the zeolite membrane, as a much lower (possibly halved) E_{app} would otherwise be expected.

The TOFs for toluene hydrogenation were of the same order of magnitude for the three Ni-based samples (Table 3) and appeared to decrease slightly with increasing Ni nanoparticle size (Table 1), probably due the mild structure-sensitivity of arene hydrogenation over Ni [40]. These TOF were close to those reported in the literature, i.e. a TOF value of $1.2 \times 10^{-3} \text{s}^{-1}$ was calculated at 80 °C from the toluene hydrogenation work on nickel reported by Keane and Patterson [41].

The TOF for the hydrogenation of mesitylene measured over the 5%Ni/sil-1, in which the Ni nanoparticles are not coated by the silicalite-1, were lower than those of toluene (Table 3 and Fig. 8). The lower TOF of mesitylene was primarily due to the lower reactivity of this bulkier molecule [42], and also possibly due to the lower partial pressure used. Interestingly, the decays of the TOFs observed in the case of mesitylene were markedly larger in the cases of the 5%Ni@sil-1 (triangles) and especially in that of the CitAc Ni@sil-1 (circles) catalysts (Fig. 8). This observation is explained by the fact that a significant fraction of the nickel nanoparticles were embedded in the silicalite-1 nanoboxes for these two materials and were not accessible to mesitylene. Since the CitAc Ni@sil-1 catalyst was still active in mesitylene hydrogenation, one must conclude that the citric acid treatment did not remove all external nickel nanoparticles. In fact, some Ni nanoparticles could still be observed by TEM after citric acid treatment (Fig. 7).

The fraction of nickel surface atoms accessible to mesitylene can be estimated from the ratios between the hydrogenation rate of toluene and mesitylene measured on the various samples (Table 3). In the case of the 5%Ni/sil-1, all the Ni nanoparticles are located outside the zeolite plain crystals and therefore all surface Ni atoms were also accessible to mesitylene. The toluene/mesitylene rate ratio was 6 in this case. The 5%Ni@sil-1 and CitAc Ni@sil-1 would then only contain about 30% (=6/20) and 9% (=6/67) of Ni sites accessible to mesitylene, respectively. The latter figure thus indicates that the citric acid treatment led to a catalyst in which more than 90% of Ni sites were embedded in silicalite-1.

Further work is under way in which the experimental conditions of the citric acid treatment or the nature of the complexing agent is varied with a view at determining improved methods for removing external Ni nanoparticles while leaving those embedded essentially untouched.

4. Conclusions

The present work based on TEM and catalytic data demonstrates that it is possible to use citric acid to selectively leach out most of the external Ni nanoparticles from a Ni@silicalite-1 material. The leached sample exhibited an improved selectivity in the hydrogenation of toluene as compared to that of the bulkier mesitylene.

Acknowledgment

This work was partly supported by the European Union Seventh Framework Programme FP7-NMP-2013, under Grant Agreement number 604277 (acronym FASTCARD).

References

- [1] M. Takahashi, T. Imaoka, Y. Hongo, K. Yamamoto, *Angew. Chem. Int. Ed.* 52 (2013) 7419.
- [2] G. Vile, B. Bridier, J. Wichert, J. Perez-Ramirez, *Angew. Chem. Int. Ed.* 51 (2012) 8620.
- [3] M. Shokouhimehr, *Catalysts* 5 (2015) 534.
- [4] I. Nakamura, Y. Yamanoi, T. Imaoka, K. Yamamoto, H. Nishihara, *Angew. Chem. Int. Ed.* 50 (2011) 5830.
- [5] J. Scalbert, F.C. Meunier, C. Daniel, Y. Schuurman, *Phys. Chem. Chem. Phys.* 14 (2012) 2159.
- [6] S. Li, T. Boucheron, A. Tuel, D. Farrusseng, F. Meunier, *Chem. Commun.* 50 (2014) 1824.
- [7] S. Li, A. Tuel, D. Laprune, F. Meunier, D. Farrusseng, *Chem. Mater.* 27 (2015) 276.
- [8] D. Farrusseng, A. Tuel, *New J. Chem.* 40 (2016) 3933.
- [9] C. Pagis, A. Morgado Prates, D. Farrusseng, N. Bats, A. Tuel, *Chem. Mater.* 28 (2016) 5205.
- [10] S. Li, A. Tuel, F. Meunier, M. Aouine, D. Farrusseng, *J. Catal.* 332 (2015) 25.
- [11] S. Li, L. Burel, C. Aquino, A. Tuel, F. Morfin, J.-L. Rousset, D. Farrusseng, *Chem. Commun.* 49 (2013) 8507.
- [12] S. Li, A. Tuel, J. Rousset, F. Morfin, M. Aouine, L. Burel, F. Meunier, D. Farrusseng, *ChemNanoMat* 2 (2016) 534.
- [13] J. Gu, Z. Zhang, P. Hu, L. Ding, N. Xue, L. Peng, X. Guo, M. Lin, W. Ding, *ACS Catal.* 5 (2015) 6893.
- [14] C. Liu, J. Liu, S. Yang, C. Cao, W. Song, *ChemCatChem* 8 (2016) 1279.
- [15] D. Fodor, T. Ishikawa, F. Krumeich, J.A. van Bokhoven, *Adv. Mater.* 27 (2015) 1919.
- [16] D. Laprune, A. Tuel, D. Farrusseng, F.C. Meunier, *Appl. Catal. B: Environ.* 204 (2017) 515.
- [17] C. Knapp, A. Obuchi, J.O. Uchisawa, S. Kushiya, P. Avila, *Microporous Mesoporous Mater.* 31 (1999) 23–31.
- [18] N. Novruzova, A. Tuel, D. Farrusseng, F. Meunier, *Microporous Mesoporous Mater.* 228 (2016) 147.
- [19] S. Li, C. Aquino, L. Gueudré, A. Tuel, Y. Schuurman, D. Farrusseng, *ACS Catal.* 4 (2014) 4299.
- [20] A. Galarneau, F. Villemot, J. Rodriguez, F. Fajula, B. Coasne, *Langmuir* 30 (2014) 13266.
- [21] H. Merkus, *Particle Size Measurements: Fundamentals, Practice, Quality*, Springer ed., (c), Dordrecht, 2009, ISBN 9781402090165.
- [22] R. Van Hardeveld, F. Hartog, *Surf. Sci.* 15 (1969) 189.
- [23] A.A. Taimoor, I. Pitault, F.C. Meunier, *J. Catal.* 278 (2011) 153.
- [24] J. Scalbert, C. Daniel, Y. Schuurman, C. Thomas, F.C. Meunier, *J. Catal.* 318 (2014) 61.
- [25] A. Hakuli, A. Kytökivi, E.-L. Lakomaa, A.O.I. Krause, *Anal. Chem.* 67 (1995) 1881.
- [26] F.C. Meunier, J.P. Breen, V. Zuzaniuk, M. Olsson, J.R.H. Ross, *J. Catal.* 187 (1999) 493.

- [27] F. Meunier, D. Verboekend, J. Gilson, J. Groen, J. Perez-Ramirez, *Microporous Mesoporous Mater.* 148 (2012) 115.
- [28] J. Perez-Ramirez, C. Christensen, K. Egeblad, C. Christensen, J. Groen, *Chem. Soc. Rev.* 37 (2008) 2530.
- [29] P. Llewellyn, Y. Grillet, F. Schuth, H. Reichert, K. Unger, *Microporous Mater.* 3 (1994) 345.
- [30] H. Li, Y. Sakamoto, Z. Liu, T. Ohsuna, O. Terasaki, M. Thommes, S. Che, *Microporous Mesoporous Mater.* 106 (2007) 174.
- [31] M. Thommes, B. Smarsly, M. Groenewolt, P. Ravikovitch, A. Neimark, *Langmuir* 22 (2006) 756.
- [32] R. Cimino, K. Cychozb, M. Thommes, A. Neimark, *Colloids Surf. A: Physicochem. Eng. Asp.* 437 (2013) 76.
- [33] L. Shi, K. Tao, T. Kawabata, T. Shimamura, X.J. Zhang, N. Tsubaki, *ACS Catal.* 1 (2011) 1225.
- [34] M. Sivaiaha, S. Petit, J. Barrault, C. Batiot-Dupeyrat, S. Valange, *Catal. Today* 157 (2010) 397.
- [35] M. Sivaiah, S. Petit, M. Beaufort, D. Eyidi, J. Barrault, C. Batiot-Dupeyrat, S. Valange, *Microporous Mesoporous Mater.* 140 (2011) 69.
- [36] H. Strunz, E. Nickel, *Mineralogical Tables: Chemical–Structural Mineral Classification System*, 9th ed., Schweizerbart ed., 2001, ISBN-13: 978-3510651887.
- [37] P. Burattin, M. Che, C. Louis, *J. Phys. Chem. B* 101 (1997) 7060.
- [38] R. Ross, G. Martin, W. Cook, *Ind. Eng. Chem. Prod. Res. Dev.* 14 (1975) 3.
- [39] J. Völter, *J. Catal.* 3 (1964) 297.
- [40] G. Martin, J. Dalmon, *J. Catal.* 75 (1982) 233.
- [41] M. Keane, P. Patterson, *Ind. Eng. Chem. Res.* 38 (1999) 1295.
- [42] M. Keane, M. Patterson, *J. Chem. Soc. Faraday Trans.* 92 (1996) 1413.



Highly Dispersed Nickel Particles Encapsulated in Multi-hollow Silicalite-1 Single Crystal Nanoboxes: Effects of Siliceous Deposits and Phosphorous Species on the Catalytic Performances

David Laprune, Alain Tuel,* David Farrusseng, and Frédéric C. Meunier^[a]

Multi-hollow silicalite-1 single crystals (MH) were prepared for the first time by an original synthesis pathway by using tetrabutylphosphonium hydroxide (TBPOH) as a mild desilicating agent. This new generation of hierarchical zeolite allowed the encapsulation of nanoparticles (NPs) featuring an enhanced confinement of the metallic guest and a thin wall thickness. The MH catalyst exhibited a better stability for methane steam reforming at 700 °C than a single-hollow counterpart (SH). Ni average particle size could be kept lower than 4 nm after 20 h on stream for the MH sample. However, a detailed analysis of

kinetic data of the structure-insensitive CO methanation used as a model reaction revealed that the sample activity was adversely affected by two main factors deriving from the preparation steps. First, a siliceous over-layer derived from the decomposition of intermediate Ni phyllosilicates, which partly covered the resulting Ni nanoparticles. Second, phosphorus from the templates remained in the samples, probably forming a Ni–P compound upon reduction. The overall catalytic activities observed here were therefore a complex interplay of improved dispersion and poisonous effects.

Introduction

Synthesis gas (syngas), a mixture of hydrogen and carbon monoxide, is a key intermediate in the chemical industry that is used as a base feedstock for the manufacturing of a wide range of chemicals and fuels.^[1,2] Nowadays, the steam reforming of fossil resources (coal and natural gas) is the main pathway to obtain syngas.^[3] Biomass gasification is a promising alternative for the production of syngas with respect to non-renewable resource depletion and sustainable development.^[4] In addition to hydrogen and carbon monoxide, light hydrocarbons (mostly methane, named as bio-substitute natural gas) are formed in the biomass gasification process, which should be preferably reformed to increase syngas yield.^[5]

Catalytic steam methane reforming over nickel has been well documented in the literature.^[6–8] Although noble metal catalysts (based on Rh, Ru, Ir, or Pt) show high activity in reforming and moderate sensitivity to deactivation, industrial processes operate in presence of nickel catalysts because of cost and availability concerns.^[9–11] However, the harsh environment inside a steam reformer strongly compromises the stability of the nickel-based catalysts. Among the various deactivation pathways, sintering is important as a result of the high

temperatures and high pressures of steam used.^[12–15] Limiting sintering is crucial to preserving a high nickel surface area, which increases specific reaction rates. In addition, nickel particle growth also influences the resistance toward poisoning by carbon and sulfur. The tendency for coking is affected by the nickel particle size and the ability for sulfur absorption is related to the nickel surface area.^[16] To operate under stable conditions, it is therefore essential to enhance the sintering-resistance of nickel-based catalysts.

For years, strengthening the metal–support interactions (MSI) has been the cornerstone of research to prevent deactivation resulting from particle agglomeration. Thereby, particular attention has been devoted to study the role of the nature of the support,^[13,17–20] the nickel impregnation method,^[21–24] the thermal treatments,^[25–28] and the addition of promoters^[15,19–31] on sintering. Among these different strategies, Burattin et al.^[22,23] studied the reduction of nickel phyllosilicates, prepared by a deposition–precipitation method by using urea hydrolysis, which are promising synthesis intermediates showing a strong MSI property. The advantage of this method is that the resulting nickel particles are small, evenly dispersed, highly loaded (> 20 wt% Ni), and more resistant to sintering than those produced by more conventional syntheses. More recently, Majewsky et al.^[32,33] used this method to prepare core@shell materials that consist of silica spheres covered with a nickel phyllosilicate layer. The catalyst exhibited noteworthy activity and stability for low-temperature steam methane reforming. The authors attributed these performances to coke-resistance properties resulting from the strong interaction of nickel with the support, confirmed by temperature-programmed reduction

[a] D. Laprune, Dr. A. Tuel, Dr. D. Farrusseng, Dr. F. C. Meunier
Université de Lyon
IRCELYON
Institut de Recherches sur la Catalyse et l'Environnement de Lyon
UMR 5256 CNRS-Université de Lyon 1
2 Avenue Albert Einstein, 69626 Villeurbanne Cedex (France)
E-mail: alain.tuel@ircelyon.univ-lyon1.fr

This manuscript is part of a Special Issue on the "French Conference on Catalysis".

(TPR) analysis. However, no information relating to nickel particle size before and after use was given.

Zhang et al.^[24] reported an alternative synthesis of Ni-containing phyllosilicates by the ammonia evaporation method. The reduced catalyst presented both higher activity and stability in the steam reforming of ethanol at 600 °C compared with that prepared by incipient wetness impregnation. The authors associated this feature to hindrance against the formation of a nickel carbide phase, and to a strong MSI-related sintering resistance. However, the authors did not discuss the discrepancies in nickel surface areas measured from TEM observations and H₂ chemisorption tests, which suggests that nickel surface sites were not all accessible.

Sintering resistance can also be significantly enhanced by encapsulating Ni nanoparticles (NPs) in mesoporous amorphous oxide shells or by coating metal-supporting catalysts with zeolite layers.^[34–39] Although very efficient against particle growth, amorphous silica in these shells displays low hydrothermal stability whereas zeolite coatings do not always show perfect size discrimination owing to mesoporous defects resulting from grain boundaries between individual crystals of the layer.

Embedding metallic nanoparticles directly into well-defined cavities or channels of zeolite frameworks often leads to different properties with respect to the conventional supported catalysts.^[40] The confining environment provided by the support not only offers a high surface area for the dispersion of active metals, but also exerts a spatial restriction on the nanoparticles, hampering their sintering. In a recent review, we reported the potential in bifunctional catalysis of using core/yolk-shell materials, which consist of totally encapsulated nanoparticles in thin (< 20 nm) MFI-type zeolite shells.^[41] Besides the opportunities in mass transport and shape-selective catalysis offered by the crack-free hollow zeolite single crystals, embedding of nanoparticles in monocrystalline microcapsules may also offer protection against particle growth under harsh reaction conditions. We have reported the sintering resistance of Pt@silicalite-1 material under hydrogen at 750 °C by assessing the evolution of the mean particle size, which remained unchanged throughout the test.^[42] More recently, Ni@silicalite-1 catalyst was evaluated in high-temperature steam methane reforming in the presence of naphthalene.^[37] The initial decrease in methane conversion was attributed to nickel sintering occurring in

the very first instants following exposure to the steam-containing feed at 700 °C.

In the present work, similar Ni@silicalite-1 single-hollow crystals were used for the steam methane reforming reaction and compared with a newly developed material, consisting of highly dispersed Ni nanoparticles encapsulated in multi-hollow silicalite-1 single crystals. These multi-hollow crystals were prepared for the first time by using tetrabutylphosphonium hydroxide (TBPOH) as a mild desilication agent. In particular, we have examined the influence of the porous architecture on the sintering resistance of the encapsulated catalyst on exposure to high temperatures and to a steam-rich atmosphere.

Results and Discussion

Synthesis and characterization of single-hollow and multi-hollow silicalite-1 crystals

Two different types of hollow silicalite-1 were obtained depending on the nature of templating molecules and crystallization temperature. Single-hollow silicalite-1 crystals (sil-1 SH) were prepared by using TPAOH, as reported in some of our previous publications.^[41–50] Typically, single-crystal regular nanoboxes of approximately 200 nm in size with a wall thickness of around 15–30 nm were obtained after treatment of the pristine crystals at 170 °C for 24 h (Figure 1a and b). Multi-hollow crystals were synthesized by using solutions of tetrabutylphosphonium hydroxide (TBPOH) at a lower temperature, typically 115 °C. TBPOH is not the best templating molecule for the crystallization of MFI-type zeolites. However, under specific crystallization conditions, TBPOH can direct the crystallization of silicalite-1 and ZSM-5 as well as mixtures of MFI/MEL (ZSM-5/ZSM-11) structures. It has been shown that the combination of TBPOH with relatively low hydrothermal synthesis temperatures could lead to MFI-type zeolites with hierarchical structures, consisting of orthogonally connected thin nanosheets of approximately 2 nm thickness. This house-of-cards arrangement of zeolite nanosheets created intercrystalline mesopores that could be used to improve molecular traffic and catalytic activities in etherification reactions.^[51] If applied to silicalite-1 modification, the strategy effectively led to highly mesoporous nanocrystals with many regular voids separated by thin zeolite layers inside the crystals (Figure 1c).

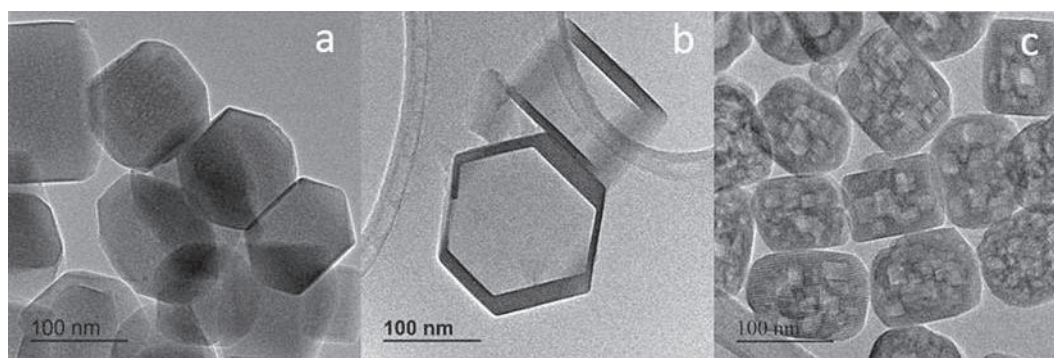



Figure 1. TEM images of plain (a), single-hollow sil-1 SH (b), and multi-hollow sil-1 MH (c) silicalite-1 crystals (magnification $\times 30\,000$).

In contrast to a direct synthesis of silicalite-1, the preparation of nanoboxes involves first the dissolution of the inner part of the crystals followed by recrystallization of dissolved species. In the case of TPAOH, both the dissolution and recrystallization rates are improved at high temperature and the corresponding single-hollow zeolites possess regular external faces similar to those observed on the original bulk crystals. Recrystallization of dissolved species was even confirmed by the slightly larger external dimensions of the crystals, thus supporting our previous model for the formation of hollow structures (Table 1). With TBPOH, the relatively low crystallization temperature means that dissolution and recrystallization were not complete, as evident from the irregular shape of the hollow crystals and their smaller mean size compared with the non-treated material (Table 1).

Crystals	Dimensions L × W × H [nm]
Plain	215 × 175 × 130
Single-hollow	230 × 190 × 145
Multi-hollow	185 × 150 × 115



Ni-loaded silicalite-1 hollow crystals

Either TPAOH or TBPOH were used to prepare silicalite-1 hollow nanocrystals that had been initially loaded with nickel nitrate (see the Experimental Section). In both cases, the presence of Ni in the zeolite (nominal loading = 5 wt%) had no significant influence on the dissolution and recrystallization processes: the structure of the hollow crystals was similar to that obtained in the absence of Ni, that is, a single regular hole with TPAOH and many cavities with TBPOH (Figure 2).

The samples, 5%NiO@sil-1 SH and 5%NiO@sil-1 MH, were obtained by calcination at 450 °C to remove templates and NO_x. The actual Ni loadings obtained in the TPAOH- and TBPOH-treated (and reduced) samples were 6.2 wt% and

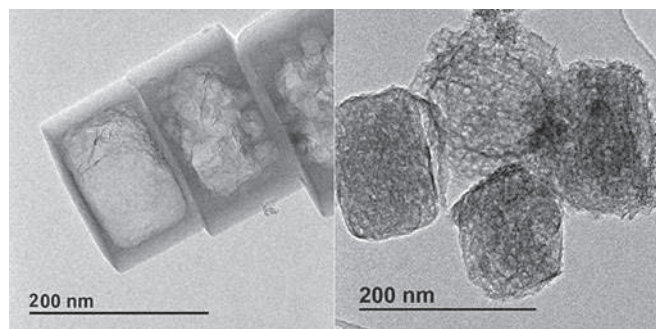


Figure 2. TEM images of 5%NiO@sil-1 SH (left) and 5%NiO@sil-1 MH (right).

Table 2. Nickel loadings in the reduced hollow silicalite-1 catalysts before and after selective removal of external metallic particles with citric acid.

Catalyst	Nickel loading [wt%]		% Ni removed by citric acid treatment
	Before citric acid treatment	After citric acid treatment	
Ni@Sil-1 SH	6.2	1.5	76
Ni@Sil-1 MH	5.1	2.2	57

5.1 wt% for the single- and multi-hollow crystals, respectively (Table 2).

Some of us have previously shown that transition metals did not directly form nanoparticles upon treatment in alkaline solution, as has been shown for the case of noble metals.^[42] Partial dissolution of silica species of the zeolite leads to the formation of stable metal phyllosilicates, located both inside the cavities and on the outer surface of the crystals (Figure 2). Nickel species also appeared in large isolated domains alongside amorphous silica, probably owing to the high Ni loading originally present in bulk crystals (not shown). Upon reduction at high temperature, Ni²⁺ species were reduced and metallic nanoparticles were formed. The corresponding samples are denoted Ni@sil-1 SH and Ni@sil-1 MH for single- and multi-hollow crystals, respectively. In contrast to the cases of noble metals such as Pt or Au, sample reduction did not lead to a single large Ni particle per cavity, but instead to numerous small nanoparticles attached to the zeolite surface (Figure 3).

For both single- and multi-hollow materials, only a fraction of the Ni nanoparticles were located inside the crystals, the rest are encapsulated in large amorphous domains such as those highlighted by yellow circles in Figure 3a and d. Most external Ni species could, however, be removed by treating the as-prepared hollow crystals with citric acid.^[43] Such treatment is expected to remove almost all external Ni species, while leaving a significant number of small Ni nanoparticles inside the cavities. After acid leaching, the original Ni content dropped by 76 and 57% for the single- and multi-hollow materials, respectively. The corresponding catalysts were denoted CitAc Ni@sil-1 SH and CitAc Ni@sil-1 MH in which the Ni nanoparticles were essentially only located in zeolite cavities (Figures 3b, c, d and f). Although the Ni contents were of the same order of magnitude for both samples, the average particle size was significantly larger in the case of CitAc Ni@sil-1 SH (i.e., 3.8 ± 1.1 nm), compared with that of CitAc Ni@sil-1 MH (i.e., 2.25 ± 0.5 nm). This difference could be explained by the fact that approximately the same amount of Ni species was dispersed in many cavities in the case of sil-1 MH crystals and only in one single cavity in the case of sil-1 SH crystals.

X-ray diffraction was used to examine the effect of citric acid treatment on the structural properties of Ni-containing hollow zeolites. As evident from the TEM pictures (Figure 3), the treatment did not significantly affect the crystal habit and the internal mesoporosity remained intact, particularly in the case of multi-hollow crystals. The preservation of the zeolite structure

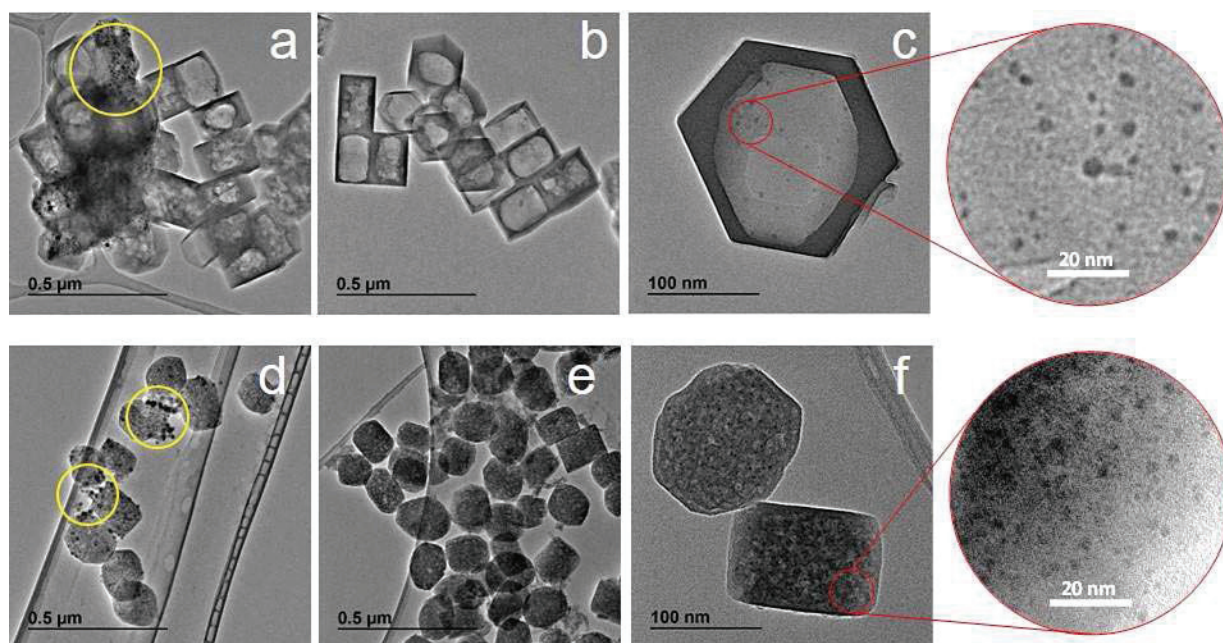


Figure 3. TEM images of reduced Ni-loaded single-hollow Ni@sil-1 SH (a,b,c) and multi-hollow Ni@sil-1 MH (d,e,f) silicalite-1 before (a,d) and after (b,c,e,f) treatment with citric acid. Yellow circles point out external nickel.

was confirmed by the similarity of the XRD patterns of the treated and untreated samples (Figure 4). However, minor modifications could be observed in the region between 23 and 25°. For bulk silicalite-1 crystals, this region contains five main diffraction peaks with a singlet at 24.4° corresponding to the (133) reflection in orthorhombic lattice (see inset in Figure 4). Calcined silicalite-1 exhibits a monoclinic symmetry at room temperature; the persistence of the orthorhombic

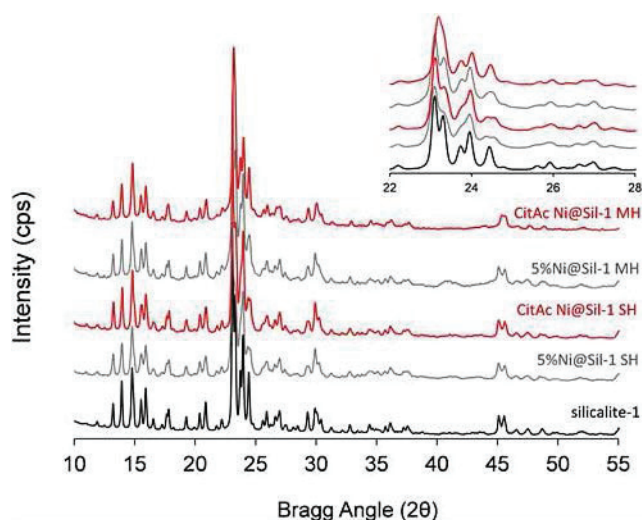


Figure 4. XRD patterns of the parent silicalite-1 (black) and the citric acid treated hollow silicalite-1 catalysts (red). Patterns of the corresponding non-treated samples are presented in grey. For comparative purposes, intensities were normalized by using the area of the silicalite-1 peak centered on $2\theta = 14.8^\circ$. A zoom in on the region $2\theta = 22\text{--}28^\circ$ is shown at the top right corner of the figure.

symmetry has been attributed to the presence of internal framework defects, particularly present in nanocrystals with a size below 500 nm.^[52–56] If the zeolite was treated with TPAOH, most of the inner part of the crystals was removed and the symmetry of the lattice changed with the splitting of the line at 24.4° into a doublet.

This result confirms our previous data suggesting that most of the lattice defects are formed at the early stages of crystal growth and are thus located at the center of the crystals.^[57,58] Using TBPOH at 115 °C to form multi-hollow crystals, removed only partially the inner part of the crystals and the orthorhombic symmetry of the zeolite lattice was preserved. Moreover, the singlet at 24.4° was even more pronounced after citric acid treatment, suggesting that the acid could create additional defects, which could possibly explain why hollow silicalite-1 appeared less stable after acid treatment in the steam reforming of methane at 900 °C.^[43]

The textural properties of acid-treated zeolites have also been studied by nitrogen adsorption at 77 K (Table 3). Bulk

Table 3. Textural properties of the different samples.

Catalyst	$S_{\text{BET}}^{[a]}$ [m ² g ⁻¹]	$V_{\text{micro}}^{[b]}$ [cm ³ g ⁻¹]	$V_{\text{cavity}}^{[c]}$ [cm ³ g ⁻¹]	$V_{\text{total}}^{[d]}$ [cm ³ g ⁻¹]
Silicalite-1	390	0.13	0.00	0.20
CitAc Ni@sil-1 SH	328	0.12	0.15	0.34
CitAc Ni@sil-1 MH	451	0.14	0.06	0.37

[a] BET method. [b] Volume of N₂ adsorbed when the slope of the adsorption branch becomes lower than 10³ cm³ g⁻¹. [c] Difference in N₂ uptake between the adsorption and the desorption branches of the isotherms at $p/p_0 = 0.5$. [d] Volume of N₂ adsorbed at $p/p_0 = 0.9$ from desorption branch.

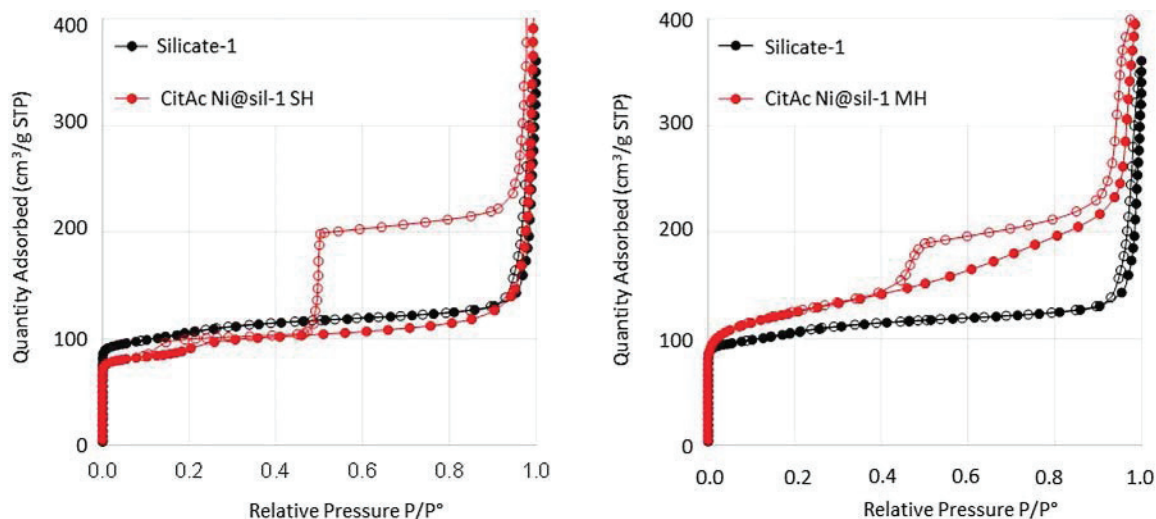


Figure 5. N_2 adsorption (full symbols) and desorption (empty symbols) isotherms at 77 K for the CitAc Ni@sil-1 single hollow (left) and CitAc Ni@sil-1 multi-hollow (right) samples are presented in red. Physisorption branches of the original silicalite-1 are presented in black. Prior to measurement, the Ni-loaded samples were calcined at 500 °C for 6 h for complete removal of carbon traces from the thermal decomposition of the residual citrates.

crystals showed a type I isotherm characteristic of microporous compounds with a large increase at $p/p_0 > 0.95$ corresponding to intercrystalline mesoporosity (Figure 5). Both the Brunauer–Emmett–Teller (BET) surface area and the micropore volume were consistent with values usually reported for ZSM-5 and silicalite-1.^[59] Treatment with TPAOH followed by acid leaching produced type IV isotherms with a hysteresis loop closing at $p/p_0 = 0.45$. This loop is characteristic of internal voids connected to the zeolite surface by apertures smaller than 4 nm.^[60–62] It reflects the hollow structure of the zeolite and the absence of cracks in the zeolite walls.

A small loop was also observed at $p/p_0 = 0.15$, which is not related to internal porosity but to a fluid-to-crystalline-like phase transition observed only in monoclinic MFI-type zeolites.^[63] The BET surface area of the treated zeolite was 15% lower than that of bulk crystals, suggesting that the acid treatment could significantly damage the zeolite structure, in agreement with the increase of framework defect sites deduced from XRD patterns.

The isotherm was quite different for multi-hollow zeolite crystals. In particular, the amount of adsorbed nitrogen continuously increased with pressure for p/p_0 between 0.1 and 0.9, confirming the presence of internal mesopores with different sizes and a wide pore size distribution. The difference compared with the case of single-hollow crystals also confirmed that most mesopores are not interconnected, and are separated from each other by crystalline zeolite walls. The BET surface area of the zeolite increased with respect to the bulk solid owing to the contribution of the external surface of the mesopores (Table 3). However, it has been reported that the measurement of BET surface areas of materials presenting combination of type I and type IV isotherms could be problematic, particularly if the plateau of the isotherm is not horizontal.^[64]

Under such conditions, the differences observed after treatment cannot be considered as real modifications of accessible surface areas but rather to the difficulty in separating the pro-

cesses of monolayer–multilayer adsorption and micropore filling.

The confinement of Ni nanoparticles into zeolite cavities was also confirmed by an investigation based on the hydrogenation of substituted arenes. We had previously reported that Pt or Ni nanoparticles encapsulated in single-hollow silicalite-1 crystals could discriminate between toluene and mesitylene.^[42,44] Toluene was able to diffuse through the micropores of the zeolite walls and be hydrogenated on embedded metal nanoparticles, in contrast to mesitylene, which was fully size-excluded from the silicalite-1 micropores. This led to a high selectivity towards toluene hydrogenation compared with that of mesitylene, the latter being only hydrogenated over a few external metal particles. The results regarding toluene and mesitylene hydrogenations are reported in Table 4 and are compared with those obtained on a standard supported catalyst (HiFUEL R110, Alfa Aesar, 11.4 wt% Ni, 36 nm Ni particle size). Notably the observed apparent activation energies were in line with values reported in the literature.^[65–67] The toluene/mesity-

Table 4. Catalytic activity of the different solids in the hydrogenation of arenes.

Catalyst	Toluene hydrogenation rate		Mesitylene hydrogenation rate		Toluene/mesitylene hydrogenation rate ratio at 100 °C
	Rate at 100 °C [$\mu\text{mol s}^{-1} \text{g}_{\text{Ni}}^{-1}$]	$E_{\text{app}} (\pm 3)$ [kJ mol^{-1}]	Rate at 100 °C [$\mu\text{mol s}^{-1} \text{g}_{\text{Ni}}^{-1}$]	$E_{\text{app}} (\pm 3)$ [kJ mol^{-1}]	
HiFUEL R110	1.3	58	0.09	63	13
CitAc Ni@sil-1 SH	67	53	1.04	63	68
CitAc Ni@sil-1 MH	4.8	51	0.10	62	48

lene hydrogenation rate ratio was equal to 13 on the HiFUEL R110, for which all nanoparticles were accessible and for which there is no molecular sieving mechanism. The rate ratio increased to 48 and 68 for CitAc Ni@sil-1 MH and CitAc Ni@sil-1 SH catalysts, respectively. This clearly demonstrates a preferential hydrogenation of the smaller molecule on the hollow catalysts and proves that most of the Ni nanoparticles were entrapped in the zeolite cavities and accessible only through the zeolite micropores. The finite value of the ratio indicates that both samples still contained external Ni nanoparticles capable of hydrogenating mesitylene, which were not removed during the citric acid treatment. The lower ratio was obtained on the multi-hollow crystals for which the extent of Ni removal was only 57%. This shows that there is room for improving the treatment to leach out external Ni particles.

Steam reforming of methane

The catalytic activity of the acid-treated Ni-containing hollow zeolites for the steam reforming of methane was monitored at 700 °C over 20 h (Figure 6). The single-hollow-based sample was initially more active than that based on multi-hollow crystals. However, the activity of the former decreased significantly with time, before levelling off after approximately 15 h. In contrast, the activity of the multi-hollow-based catalyst remained essentially stable over the whole period.

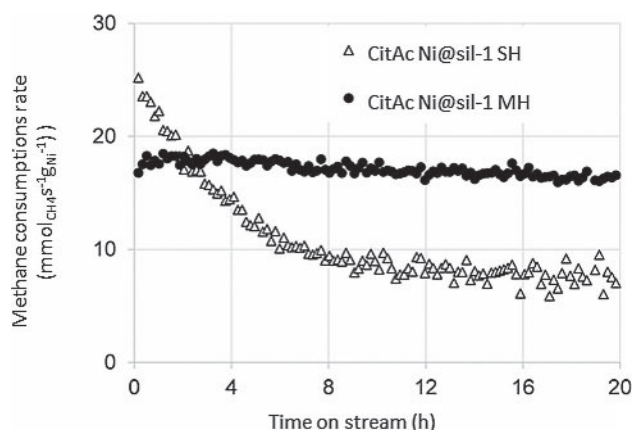


Figure 6. Steam methane reforming rate at 700 °C for the CitAc Ni@sil-1 SH (open triangles) and CitAc Ni@sil-1 MH (full circles). Feed composition is given in Table 7.

Thus, the activity measured after 20 h over CitAc Ni@sil-1 MH was approximately twice that observed on CitAc Ni@sil-1 SH.

Many factors could explain the deactivation of the catalyst with time, for example, coke formation or a gradual loss of dispersion of the catalytic phase. TEM pictures of spent catalysts clearly showed that the average particle size had increased during the catalytic test from 3.8 ± 1.1 nm to 6.0 ± 2.1 nm for CitAc Ni@sil-1 SH and 2.25 ± 0.5 nm to 3.75 ± 0.9 nm for CitAc Ni@sil-1 MH (Figures 7 and 8). The corresponding Ni metal dispersions are given in Table 5.

Table 5. TEM-derived specific metal surface areas, metal dispersions, and proportion of Low Coordination Sites over the total number of surface sites ("LCS", step and corner atoms).^[a]

Catalyst	Fresh samples		Post-reforming samples			Relative decay of dispersion \times LCS after reforming	
	Metal SA ^[b] [m ² g ⁻¹]	Dispersion [%]	LCS [%]	Metal SA ^[b] [m ² g ⁻¹]	Dispersion [%]		LCS [%]
CitAc Ni@sil-1 SH	3.1	31	22	2.1	21	14	2.4
CitAc Ni@sil-1 MH	7.0	48	37	4.6	31	23	2.5

[a] Calculated by using the method reported in Ref. [67]. [b] Specific metal surface area

The increase in average particle size of CitAc Ni@sil-1 SH from 3.8 to 6 nm corresponded to a dispersion decreasing from 31 down to 21%. It has been proposed that the most active sites of metallic nanoparticles for steam methane reforming are those exhibiting low coordination numbers, for example, atoms located at steps, edges, and corners.^[7,68]

Assuming that Ni particles were regular cuboctahedra, it is possible to estimate the proportion of low coordination sites (LCS) over the total number of surface sites for each particle size, typically those on edges and corners.^[69] This proportion decreases from 22% to 14% after the test (Table 5). Therefore, the overall concentration of LCS (= dispersion \times LCS) exhibited an approximately 2.4-fold decrease. The extent of this decay is similar to that of the activity decrease of the CitAc Ni@sil-1 SH catalyst (Figure 6) from the initial value $r_i = 25$ mmol s⁻¹ g_{Ni}⁻¹ to $r_f = 8$ mmol s⁻¹ g_{Ni}⁻¹ after 20 h ($r_i/r_f = 3.1$). Therefore, the activity loss can be mostly attributed to the sintering of the Ni particles in the case of the CitAc Ni@sil-1 SH catalyst.

Sintering was also observed on CitAc Ni@sil-1 MH, although to a lower extent (Figures 7 and 8). The comparison between the initial and final dispersions and LCS (Table 5) indicates that the catalyst activity should have exhibited a 2.5-fold decrease after 20 h, similar to the case of CitAc Ni@sil-1 SH. This was clearly not the case (Figure 6).

The essentially constant value of the activity for the CitAc Ni@sil-1 MH could possibly be explained by the fact that particle sintering could have been compensated for by an almost exactly identical gain in specific activity. Both single- and multi-hollow catalysts were tested for a model reaction, that is, CO methanation at 300 °C, before and after methane reforming to unravel this matter.

CO methanation is known to be structure-insensitive, displaying turnover frequency (TOF) values independent from the size and morphology of Ni particles.^[70-72] The CO methanation experiments performed at 300 °C using various supported catalysts with different Ni loadings and particle size all exhibited a constant TOF of approximately 0.35 s⁻¹ (data not shown), which is well in line with TOF values from the literature.^[73]

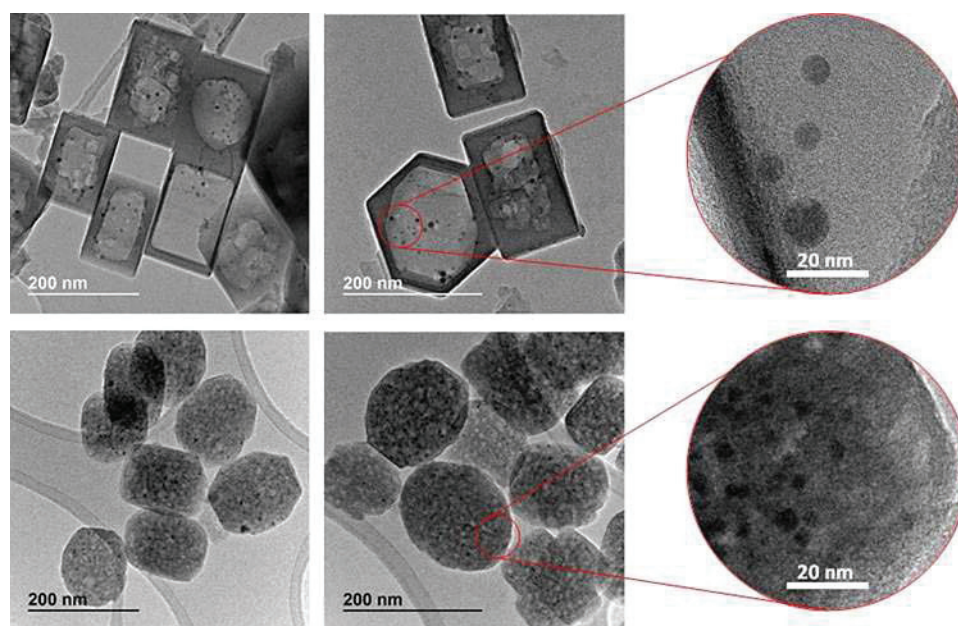


Figure 7. TEM images of the post-reforming CitAc Ni@sil-1 SH (top) and CitAc Ni@sil-1 MH (bottom) samples.

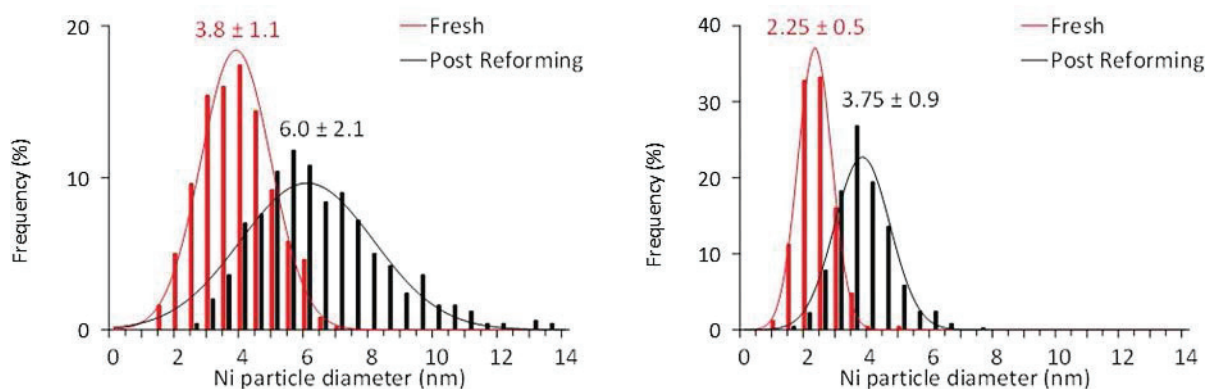


Figure 8. Particle size distributions of fresh (red) and post-reforming (black) CitAc Ni@sil-1 SH (left) and CitAc Ni@sil-1 MH (right). Distributions are modelled by using a Normal law. Based on the measurement of 500 observable particles for each sample.

Prior to the reforming tests, the methanation activity of the fresh single- and multi-hollow catalysts was measured. The CO methanation activity was used to derive the initial metal specific surface area by assuming a TOF of 0.35 s^{-1} for each active site (Table 6).

It appears that the specific metal surface areas determined by CO methanation (Table 6) were significantly lower than those derived from TEM measurements for the fresh samples (Table 5).

This observation indicates that most Ni surface sites were actually not available for CO methanation, possibly because those were in an oxidized state (e.g., as in oxide or silicate compound) or the Ni metal nanoparticles were covered by a layer of, for example, siliceous material. The proportions of “accessible metallic Ni” defined as the fraction of active Ni surface sites participating in the methanation reaction over the total number of Ni surface sites derived by TEM are given in

Table 6 and were markedly small. The two catalysts were prepared by treating Ni-loaded silicalite-1 crystals under alkaline

Table 6. Methanation activity of the fresh samples at 300°C , the corresponding specific metal surface area, and the proportion of accessible metallic Ni.

Catalyst	Methanation activity at 300°C [$\mu\text{mol}_{\text{CH}_4}\text{s}^{-1}\text{g}_{\text{Ni}}^{-1}$]	Specific metal surface area ^[a] [m^2g^{-1}]	Accessible metallic Ni [%]
CitAc Ni@sil-1 SH	110	0.19	6.1
CitAc Ni@sil-1 MH	23	0.06	0.8

[a] Based on CO methanation data, assuming a TOF of 0.35 s^{-1} for each active site and an average area of a surface nickel atom of $6.5 \times 10^{-20} \text{ m}^2$.^[40]

conditions and the formation of Ni-phyllsilicates was observed in both cases (Figure 2). Zhang et al. reported that Ni-phyllsilicates led to Ni particles partially embedded in an amorphous silica matrix upon reduction at 700 °C under H₂.^[24] The percentage of surface Ni atoms titrated by H₂ chemisorption on 3.3 nm nanoparticles obtained by direct reduction of phyllosilicates was only 6%, whereas this percentage increased to 30% if the catalyst was prepared by reduction of Ni impregnated onto silica.^[24]

H₂ chemisorption analysis performed on the present single- and multi-hollow catalysts (data not shown) confirmed that the surface sites able to chemisorb H₂ were scarce, that is, 5.7 and 3.1% of the total number of surface Ni atoms for CitAc Ni@sil-1 SH and CitAc Ni@sil-1 MH, respectively. These values are similar to those based on CO methanation activity, which are reported in Table 6.

The encapsulation (poisoning) of most Ni nanoparticles by amorphous silica cannot account for the whole difference in performance in methane reforming between the CitAc Ni@sil-1 SH and CitAc Ni@sil-1 MH catalysts (Figure 6), as well as the very low fraction of surface atoms accessible in CitAc Ni@sil-1 MH during CO methanation (Table 6). In addition to differences in the size, morphology, and number of mesopores inside the crystals, the SH and MH catalysts also differ in the nature of mineralizing agent that was used to create the porosity. MH crystals were obtained in the presence of phosphonium cations, which are known to contaminate zeolites with phosphorus-containing species upon calcination.^[74] Phosphorus-based compounds are also known as poisons for nickel catalysts.^[75]

Chemical analysis of MH crystals before treatment with citric acid confirmed the presence of phosphorus species in the zeolite with a P/Ni atomic ratio of 0.5 (data not shown). For this sample, the amount of adsorbed hydrogen was below the detection limit, suggesting that P species had reacted with surface Ni atoms and totally prevented H₂ adsorption. In addition, no activity in methanation was detected at 300 °C over this sample. After treatment with citric acid, the P/Ni ratio decreased to 0.15 and the proportion of surface sites chemisorbing H₂ became measurable (ca. 3.1%), thus supporting the poisoning role of P species on the catalyst activity.

A possible explanation for the peculiar behavior of CitAc Ni@sil-1 MH catalyst during steam reforming could be that the phosphorous species initially present were gradually removed from Ni nanoparticles with time on stream, leading to a gradual increase of the proportion of accessible metal Ni atoms. This increase could compensate for the loss of activity resulting from particle sintering inside the zeolite multi-hollow cavities. This assumption is supported by in situ methanation tests realized after reforming: the CO methanation activity was three times higher than that of the fresh catalyst and the fraction of accessible metal increased from 0.8 to 4.3%.

Conclusions

Two different strategies were pursued to create hollow silicalite-1 crystals and to use the corresponding cavities to encapsulate Ni nanoparticles.

While the use of TPAOH and relatively high temperatures led to crystals exhibiting a single, large internal cavity, the use of TBPOH at 115 °C resulted in multi-hollow architectures. During the formation of the porosity, Ni precursors react with dissolved silica species to form Ni phyllosilicates, further reduced into nanoparticles under hydrogen at 700 °C. Even in the case of a unique cavity, this reduction did not lead to a single Ni particle, mainly because of the strong interaction between phyllosilicates and the zeolite surface. Ni nanoparticles displayed sintering with time under steam methane reforming conditions at 700 °C, leading to significant particle growth and catalyst deactivation for both samples. Nonetheless, the dispersion of Ni particles into the numerous cavities of the multi-hollow crystals remained higher after reaction than that obtained in the case of the single-hollow crystals before reaction. Both catalytic activities and hydrogen adsorption data indicate that the fraction of accessible Ni metal atoms was very low, suggesting that the main part of the surface atoms were covered with amorphous silica resulting from the reduction of phyllosilicates. This fraction was even lower in multi-hollow crystals because of the presence of phosphorus-containing species that were formed during calcination of the organic templates. The gradual removal of these phosphorous poisoning species probably explained the apparent constant methane steam reforming activity with time on stream, by compensating for the limited sintering occurring simultaneously almost exactly.

In conclusion, these results indicate that the presence of multi-hollow crystals is effective in keeping highly dispersed Ni nanoparticles, but also that the catalytic performance of the corresponding encapsulated Ni nanoparticles suffered from poisoning originating from the sample preparation method.

Experimental Section

Sample synthesis

Zeolite synthesis

Original silicalite-1 was prepared by using tetraethylorthosilicate (TEOS, Aldrich, 98%) and TPAOH (tetrapropylammonium hydroxide, 1 M in water) obtained by contacting TPABr solutions with Ag₂O in the absence of light. The resulting gel (SiO₂-0.4TPAOH-35H₂O in composition) was stirred at room temperature overnight to fully hydrolyze the TEOS and then transferred into a Teflon-lined autoclave. After heating at 170 °C under static conditions for 72 h, the autoclave was then cooled down to room temperature and the solid was centrifuged, washed with water until pH 7, and dried overnight at 90 °C. Finally, the resulting solid was calcined for 12 h at 525 °C in air, yielding microporous single crystals referred to as silicalite-1.

Nickel-impregnation methods

After degassing overnight at 300 °C, nickel-loaded zeolites denoted Ni(NO₃)₂-silicalite-1 were prepared by incipient wetness impregnation with an aqueous solution of Ni(NO₃)₂·6H₂O (99.999%, Sigma-Aldrich). The metal loading (nominal value 5% in weight) was achieved by impregnating 1 g of the starting silicalite-1 with 2 mL of

an aqueous solution of the metal precursor (426 mmol L⁻¹ in concentration). The mixture was stirred at 50 °C until complete evaporation of water was achieved to reach the Ni(NO₃)₂-silicalite-1. The resulting green powder was dried for 12 h at 90 °C.

Preparation of the single-hollow (SH) structure

5%Ni@sil-1 SH was synthesized by following the generic protocol for the encapsulation of transition metal nanoparticles in the large unique cavity of hollow silicalite-1 single crystals.^[50] The hollow structure was obtained by treating 1 g of Ni(NO₃)₂-silicalite-1 with a homemade TPAOH (tetrapropylammonium hydroxide) aqueous solution (7.5 mL, 0.55 M, pH 13.6) in a Teflon-lined autoclave at 170 °C under rotating conditions for 24 h. The solution was then cooled down, washed with water until pH 7, dried overnight at 90 °C, and calcined in air at 450 °C for 6 h to obtain the 5%NiO@sil-1 SH. Finally, the solid was reduced at 750 °C under H₂ for 3 h with a heating rate of 2.5 °C min⁻¹ to yield the 5%Ni@sil-1 SH.

Preparation of the multi-hollow (MH) structure

Similar to the synthetic approach of the single-hollow material, the multi-hollow structure was formed under hydrothermal conditions in the presence of a phosphonium-containing structure-directing agent. Post-synthesis desilication was conducted by treating Ni(NO₃)₂-silicalite-1 with a commercial TBPOH (tetrabutylphosphonium hydroxide) solution (40 wt% in H₂O, Sigma-Aldrich). The powder (1 g) was added to a solution made of 3.5 mL of the commercial TBPOH mixed with 1 mL of H₂O (4.5 mL, 1.125 M, pH 13.7). The mixture was then transferred into a Teflon-lined autoclave and heated at 115 °C under rotating conditions for 96 h. The solution was then cooled down, washed with water until pH 7, and dried overnight at 90 °C. Finally, the powder was successively calcined in air at 450 °C for 6 h to obtain the 5%NiO@sil-1 MH material and reduced at 750 °C under H₂ for 3 h with a heating rate of 2.5 °C min⁻¹ to yield the 5%Ni@sil-1 MH.

Citric acid treatment

Both single- and multi-hollow samples were treated similarly to remove selectively the nickel particles that were not entrapped during the encapsulation procedure. NiO@silicalite-1 (0.5 g) was added to an aqueous solution (50 mL of 0.5 mol L⁻¹) of citric acid (≥99.0%, Sigma-Aldrich). The mixture was stirred vigorously at 80 °C for 3 h. The solution was then centrifuged and washed with water until pH 7 and dried overnight at 90 °C. Finally, the solid was reduced at 750 °C under H₂ for 2 h to yield samples referred to as CitAc Ni@sil-1 SH and MH. Prior to nitrogen physisorption measurements, these samples were further calcined in air at 550 °C for 6 h to remove carbon traces from the thermal decomposition of the residual citrates.

Characterization techniques

Powder X-ray diffraction patterns (XRD) were recorded to assess the crystallinity of the samples. Diffractograms were collected between 4 and 90° (2θ) with steps of 0.02° and 1 s per step with a Bruker D5005 diffractometer using CuK_α radiation at λ = 1.5418 Å.

Elemental analysis of the catalysts was performed by using an ICP-OES ACTIVA from HORIBA Jobin Yvon equipped with a CCD detector for the determination of metal loadings.

The specific surface area (Brunauer–Emmett–Teller theory) and the porosity of the samples were determined by N₂ adsorption-desorption measurements at 77 K (Belsorp-mini, BEL Japan). Samples were first outgassed under vacuum (<10 Pa) at 300 °C for 4 h (Belprep, BEL-Japan). The maximum *p/p*₀ value was set to be close to 1 to better assess the internal porosity of the hollow materials. The *t*-plot analysis was not considered here, in view of the debate on the validity of the *t*-plot method to assess microporosity in hierarchical materials.^[76]

TEM pictures were obtained by using a Jeol 2010 LaB6 microscope operating at 200 kV. Particle size distributions of zeolite-based materials were obtained by counting 500 particles by using Image J software. Each distribution was then modelled by using a normal law with the maximum position centered on the average particle size $d_{NW} = \sum n_i d_i / \sum n_i$ (in which *n*_{*i*} is the number of particles with diameter *d*_{*i*}) and experimental standard deviation.

Specific nickel surface areas were measured by H₂ chemisorption at 35 °C by using a Micromeritics ASAP 2010. The sample holder was loaded with at least 0.1 g of 5%NiO@sil-1 SH or MH and prior to the measurement the sample was reduced in situ in flowing hydrogen at 750 °C for 3 h. After reduction, the samples were evacuated for 2 h at 350 °C before cooling down to 35 °C. Two successive adsorption isotherms, separated by a second evacuation of 1 h at 35 °C, were then measured, according to the method described by Iglesia and co-workers.^[9] The amount of hydrogen chemisorbed was obtained by correcting the total hydrogen uptake (first isotherm) with that of weakly adsorbed H₂ (second isotherm). Specific surface areas were calculated by assuming a H/Ni surface ratio of 1 and Ni atom area of 6.5 × 10⁻²⁰ m².^[73,77]

Catalytic tests

Arene hydrogenation

Toluene and mesitylene (i.e., 1,3,5-trimethylbenzene) hydrogenation tests were performed using a fixed-bed continuous-flow reactor consisting of a quartz tube (length 400 mm, 4 mm ID, 6 mm OD) containing the powdered catalyst held between quartz wool plugs. The system was operated at atmospheric pressure and the samples were reduced in situ at 500 °C in pure H₂ for 60 min before the catalytic tests. Aromatic reactants were fed individually by using a saturator kept at 0 °C, leading to partial pressures of 912 and 62 Pa for toluene and mesitylene, respectively. A flow of 20 mL min⁻¹ of pure H₂ was used as reactant carrier gas and fed through one saturator at a time. The reactor effluent was then analyzed by using a 10 cm path-length gas cell fitted in a Tensor 27 FTIR spectrophotometer from Bruker. The proportion of the reactant and the corresponding saturated product were determined through integration of two spectral regions corresponding to the C–H stretching vibration mode.^[42] In the case of toluene, methylcyclohexane was the only product observed, whereas trimethylcyclohexane was the only product obtained from the hydrogenation mesitylene. In addition to the hollow zeolites, a commercial Ni-based catalyst (HiFUEL R110, Alfa Aesar, ref. 45465) was used as a reference sample.

Steam methane reforming

Reforming tests were performed using an experimental set-up thoroughly described elsewhere.^[43] In brief, the sample was first crushed and sieved to obtain particle sizes ranging from 100 to 200 microns. The catalyst (10 mg) was then tested in a fixed-bed

continuous-flow reactor consisting of a quartz tube (length 300 mm, 4 mm ID, 6 mm OD). The catalytic bed was held between plugs of quartz wool in the absence of an inert diluent material. Prior to testing, the catalysts were reduced in situ at 700 °C (heating rate of 400 °C h⁻¹) for 2 h under a flow of 200 mL min⁻¹ of 20 vol% H₂/Ar mixture. A model composition made of H₂O, H₂, CH₄, CO, CO₂, N₂, and Ar was used to conduct realistic reforming tests of a bio-derived reformat gas (Table 7). Mass flow controllers (Brooks Instrument) were used to control gas flow rates whereas the steam rate was set by controlling the temperature of the water-containing saturator. The catalytic bed was located in the isothermal region of a tube furnace; this oven was placed in a hotbox for gas pre-heating. The catalysts were tested at 700 °C and maintained for 20 h at this temperature.

Table 7. Feed gas composition for reforming tests.

Compound	CO	H ₂	CO ₂	H ₂ O	CH ₄	N ₂	Ar
Vol [%]	20	16	10	39	9	2	4
mL min ⁻¹	25	20	12.5	48.8	11.3	2.5	5

Online analysis of the reactor effluent was performed with a compact gas chromatograph (Global Analyzer Solutions) by using the N₂ signal as an internal standard for the quantification of gas flow rates (H₂, CO, CO₂, and CH₄). H₂O quantification was not performed. A needle valve was placed downstream in the compact GC to maintain the overall pressure of the system at $P_{\text{total}}=2.2$ bar. The total gas flow rate of reactants was 125 mL min⁻¹. The corresponding gas hourly space velocity (GHSV) was 750 000 h⁻¹, assuming the catalyst density to be unity. This high space velocity was selected to prevent total conversion of methane, providing insights in terms of activity and stability of the hollow zeolites. These conditions also led to an accelerated ageing of the samples on a reasonable timescale.

Acknowledgments

This work was partly supported by the European Union Seventh Framework Programme FP7-NMP-2013, under Grant Agreement number 604277 (acronym FASTCARD).

Keywords: desilication · hollow zeolite crystals · methane reforming · nickel · sintering

- [1] K. Aasberg-Petersen, I. Dybkjaer, C. Ovesen, N. Schjodt, J. Sehested, S. Thomsen, *J. Nat. Gas Sci. Eng.* **2011**, *3*, 423–429.
 [2] M. Economides, D. Wood, *J. Nat. Gas Sci. Eng.* **2009**, *1*, 1–13.
 [3] R. Lan, J. Irvine, S. Tao, *Int. J. Hydrogen Energy* **2012**, *37*, 1482–1494.
 [4] V. Sikarwar, M. Zhao, P. Clough, J. Yao, X. Zhong, M. Memon, N. Shah, E. Anthony, P. Fennell, *Energy Environ. Sci.* **2016**, *9*, 2939–2977.
 [5] D. Sutton, B. Kelleher, J. Ross, *Fuel Process. Technol.* **2001**, *73*, 155–173.
 [6] *Catalytic Steam Reforming*, J. Rostrup-Nielsen, in *Catalysis: Science and Technology* (Eds.: J. R. Anderson, M. Boudart), Vol. 5, Springer-Verlag, Berlin, **1984**, pp. 1–117.
 [7] H. S. Bengaard, J. K. Nørskov, J. Sehested, B. S. Clausen, L. P. Nielsen, A. M. Molenbroek, J. R. Rostrup-Nielsen, *J. Catal.* **2002**, *209*, 365–384.
 [8] J. R. Rostrup-Nielsen, J. Sehested, *Adv. Catal.* **2002**, *47*, 65–139.
 [9] J. Wei, E. Iglesia, *J. Catal.* **2004**, *224*, 370–383.
 [10] J. Wei, E. Iglesia, *J. Phys. Chem. B* **2004**, *108*, 4094–4103.

- [11] G. Jones, J. Jakobsen, S. Shim, J. Kleis, M. Andersson, J. Rossmels, F. Abildpedersen, T. Bligaard, S. Helveg, B. Hinnemann, *J. Catal.* **2008**, *259*, 147–160.
 [12] J. Sehested, *J. Catal.* **2003**, *217*, 417–426.
 [13] K. Christensen, D. Chen, R. Lodeng, A. Holmen, *Appl. Catal. A* **2006**, *314*, 9–22.
 [14] J. Sehested, J. Gelten, I. Remediakis, H. Bengaard, J. Nørskov, *J. Catal.* **2004**, *223*, 432–443.
 [15] J. Sehested, J. Gelten, S. Helveg, *Appl. Catal. A* **2006**, *309*, 237–246.
 [16] J. Sehested, *Catal. Today* **2006**, *111*, 103–110.
 [17] Y. Matsumura, T. Nakamori, *Appl. Catal. A* **2004**, *258*, 107–114.
 [18] K. Urasaki, Y. Sekine, S. Kawabe, E. Kikuchi, M. Matsukata, *Appl. Catal. A* **2005**, *286*, 23–29.
 [19] G. Gallego, F. Mondragon, J. Barrault, J. Tatibouet, C. Batiot-Dupeyrat, *Appl. Catal. A* **2006**, *311*, 164–171.
 [20] A. Gadalla, B. Bower, *Chem. Eng. Sci.* **1988**, *43*, 3049–3062.
 [21] O. Clause, M. Kermarec, L. Bonneviot, F. Villain, M. Che, *J. Am. Chem. Soc.* **1992**, *114*, 4709–4717.
 [22] P. Burattin, M. Che, C. Louis, *J. Phys. Chem. B* **1997**, *101*, 7060–7074.
 [23] P. Burattin, M. Che, C. Louis, *J. Phys. Chem. B* **1998**, *102*, 2722–2732.
 [24] C. Zhang, H. Yue, Z. Huang, S. Li, G. Wu, X. Ma, J. Gong, *ACS Sustainable Chem. Eng.* **2013**, *1*, 161–173.
 [25] P. Turler, H. Praliaud, P. Moral, G. Martin, J. Dalmon, *Appl. Catal.* **1985**, *19*, 287–300.
 [26] L. Alzamora, J. Ross, *J. Chem. Soc. Faraday Trans.* **1981**, *77*, 665–681.
 [27] B. Mile, D. Stirling, M. Zammitt, A. Lovell, M. Webb, *J. Catal.* **1988**, *114*, 217–229.
 [28] C. Courson, E. Makaga, C. Petit, A. Kiennemann, *Catal. Today* **2000**, *63*, 427–437.
 [29] F. Morales-Cano, L. Lundegaard, R. Tiruvalam, H. Falsig, M. Skjoth-Rasmussen, *Appl. Catal. A* **2015**, *498*, 117–125.
 [30] H. Wu, V. La Parola, G. Pantaleo, F. Puleo, A. Venezia, L. Liotta, *Catalysts* **2013**, *3*, 563–583.
 [31] M. Lighthart, J. Pieterse, E. Hensen, *Appl. Catal. A* **2011**, *405*, 108–119.
 [32] A. Majewski, J. Wood, W. Bujalski, *Int. J. Hydrogen Energy* **2013**, *38*, 14531–14541.
 [33] A. Majewski, J. Wood, *Int. J. Hydrogen Energy* **2014**, *39*, 12578–12585.
 [34] W. Yang, H. Liu, Y. Li, J. Zhang, H. Wu, D. He, *Catal. Today* **2016**, *259*, 438–445.
 [35] R. N. Devi, F. C. Meunier, T. Le Goaziou, C. Hardacre, P. J. Collier, S. E. Golunski, L. F. Gladden, M. D. Mantle, *J. Phys. Chem. C* **2008**, *112*, 10968–10975.
 [36] T. D. Gould, A. Izar, A. W. Weimer, J. L. Falconer, J. W. Medlin, *ACS Catal.* **2014**, *4*, 2714–2717.
 [37] U. Cimenler, B. Joseph, J. N. Kuhn, *Energy Fuels* **2016**, *30*, 5300–5308.
 [38] U. Cimenler, B. Joseph, J. N. Kuhn, *AIChE J.* **2017**, *63*, 200–207.
 [39] U. Cimenler, B. Joseph, J. N. Kuhn, *Appl. Catal. A* **2015**, *505*, 494–500.
 [40] S. Li, J. Gong, *Chem. Soc. Rev.* **2014**, *43*, 7245–7256.
 [41] D. Farrusseng, A. Tuel, *New J. Chem.* **2016**, *40*, 3933–3949.
 [42] S. Li, T. Boucheron, A. Tuel, D. Farrusseng, F. Meunier, *Chem. Commun.* **2014**, *50*, 1824–1826.
 [43] D. Laprune, C. Theodoridis, A. Tuel, D. Farrusseng, F. Meunier, *Appl. Catal. B* **2017**, *204*, 515–524.
 [44] S. Li, L. Burel, C. Aquino, A. Tuel, F. Morfin, J.-L. Rousset, D. Farrusseng, *Chem. Commun.* **2013**, *49*, 8507–8509.
 [45] S. Li, A. Tuel, F. Meunier, M. Aouine, D. Farrusseng, *J. Catal.* **2015**, *332*, 25–30.
 [46] S. Li, C. Aquino, L. Gueudré, A. Tuel, Y. Schuurman, D. Farrusseng, *ACS Catal.* **2014**, *4*, 4299–4303.
 [47] N. Novruzova, A. Tuel, D. Farrusseng, F. Meunier, *Microporous Mesoporous Mater.* **2016**, *228*, 147–152.
 [48] S. Li, A. Tuel, J. Rousset, F. Morfin, M. Aouine, L. Burel, F. Meunier, D. Farrusseng, *ChemNanoMat* **2016**, *2*, 534–539.
 [49] C. Pagis, A. Morgado Prates, D. Farrusseng, N. Bats, A. Tuel, *Chem. Mater.* **2016**, *28*, 5205–5223.
 [50] S. Li, A. Tuel, D. Laprune, F. Meunier, D. Farrusseng, *Chem. Mater.* **2015**, *27*, 276–282.
 [51] X. Zhang, D. Liu, D. Xu, S. Asahina, K. Cychosz, K. Agrawal, Y. Al Wahedi, A. Bhan, S. Al Hashimi, O. Terasaki, M. Thommes, M. Tsapatsis, *Science* **2012**, *336*, 1684–1687.

- [52] G. Marra, G. Tozzola, G. Leofanti, M. Padovan, G. Petrini, F. Genoni, B. Venturelli, A. Zecchina, S. Bordiga, G. Ricchiardi, *Stud. Surf. Sci. Catal.* **1994**, *84*, 559–566.
- [53] A. Zecchina, S. Bordiga, G. Spoto, L. Marchese, G. Petrini, G. Leofanti, M. Padovan, *J. Phys. Chem.* **1992**, *96*, 4985–4990.
- [54] A. Zecchina, S. Bordiga, G. Spoto, L. Marchese, G. Petrini, G. Leofanti, M. Padovan, *J. Phys. Chem.* **1992**, *96*, 4991–4997.
- [55] C. Cheng, T. Bae, B. McCool, R. Chance, S. Nair, C. Jones, *J. Phys. Chem. C* **2008**, *112*, 3543–3551.
- [56] E. Mallon, M. Jeon, M. Navarro, A. Bhan, M. Tsapatsis, *Langmuir* **2013**, *29*, 6546–6555.
- [57] Y. Wang, A. Tuel, *Microporous Mesoporous Mater.* **2007**, *102*, 80–85.
- [58] Y. Wang, A. Tuel, *Microporous Mesoporous Mater.* **2008**, *113*, 286–295.
- [59] F. Meunier, D. Verboekend, J. Gilson, J. Groen, J. Perez-Ramirez, *Microporous Mesoporous Mater.* **2012**, *148*, 115–121.
- [60] P. Llewellyn, Y. Grillet, F. Schüth, H. Reichert, K. Unger, *Microporous Mater.* **1994**, *3*, 345–349.
- [61] H. Li, Y. Sakamoto, Z. Liu, T. Ohsuna, O. Terasaki, M. Thommes, S. Che, *Microporous Mesoporous Mater.* **2007**, *106*, 174–179.
- [62] M. Ogura, M. Matsukata in *Mesoporous Zeolites: Preparation, Characterization and Applications* (Eds.: J. Garcia-Martínez, K. Li), Wiley-VCH, **2015**, Chap. 8, pp. 259–294.
- [63] P. L. Llewellyn, J.-P. Coulomb, Y. Grillet, J. Patarin, G. Andre, J. Rouquerol, *Langmuir* **1993**, *9*, 1846–1851.
- [64] M. Thommes, K. Kaneko, A. V. Neimark, J. P. Olivier, F. Rodriguez-Reinoso, J. Rouquerol, K. S. W. Sing, *Pure Appl. Chem.* **2015**, *87*, 1051–1069.
- [65] R. Ross, G. Martin, W. Cook, *Ind. Eng. Chem. Prod. Res. Dev.* **1975**, *14*, 151–154.
- [66] J. Völter, *J. Catal.* **1964**, *3*, 297–298.
- [67] T. Takahashi, K. Yamashita, T. Kai, I. Fujiyoshi, *Can. J. Chem. Eng.* **1986**, *64*, 1008–1013.
- [68] F. Abild-Pedersen, O. Lytken, J. Engbaek, G. Nielsen, I. Chorkendorff, J. Norskov, *Surf. Sci.* **2005**, *590*, 127–137.
- [69] R. Van Hardeveld, F. Hartog, *Surf. Sci.* **1969**, *15*, 189–230.
- [70] D. Goodman, R. Kelley, T. Madey, J. Yates, *J. Catal.* **1980**, *63*, 226–234.
- [71] K. Coulter, X. Xu, D. Goodman, *J. Phys. Chem.* **1994**, *98*, 1245–1249.
- [72] M. Agnelli, H. Swaan, C. Marquez-Alvarez, G. Martin, C. Mirodatos, *J. Catal.* **1998**, *175*, 117–128.
- [73] J. Sehested, S. Dahl, J. Jacobsen, J. Rostrup-Nielsen, *J. Phys. Chem. B* **2005**, *109*, 2432–2438.
- [74] Y. Yamasaki, N. Tsunaji, Y. Takamitsu, M. Sadakane, T. Sano, *Microporous Mesoporous Mater.* **2016**, *223*, 129–139.
- [75] C. Bartholomew, *Appl. Catal. A* **2001**, *212*, 17–60.
- [76] A. Galarneau, F. Villemot, J. Rodriguez, F. Fajula, B. Coasne, *Langmuir*, **2014**, *30*, 13266–13274.
- [77] C. H. Bartholomew, R. B. Pannell, *J. Catal.* **1980**, *65*, 390–401.

Manuscript received: February 3, 2017

Revised manuscript received: February 14, 2017

Accepted manuscript online: February 18, 2017

Version of record online: April 19, 2017